Leen van der Ham

Improving the Second law efficiency of a cryogenic air separation unit

Thesis for the degree of Philosophiae Doctor

Trondheim, December 2011

Norwegian University of Science and Technology
Faculty of Natural Sciences and Technology
Department of Chemistry

NTNU – Trondheim
Norwegian University of
Science and Technology

NTNU
Norwegian University of Science and Technology

Thesis for the degree of Philosophiae Doctor

Faculty of Natural Sciences and Technology
Department of Chemistry

ISBN 978-82-471-3216-6 (printed ver.)
ISBN 978-82-471-3217-3 (electronic ver.)
ISSN 1503-8181

Doctoral theses at NTNU, 2011:318

Printed by NTNU-trykk

Acknowledgements

This Ph.D. thesis is written as a partial fulfilment for the degree of Philosophiae Doctor at the Norwegian University of Science and Technology in Trondheim. The research described in this thesis has been performed at the group of non-equilibrium thermodynamics, which is part of the physical chemistry section at the department of chemistry. The non-equilibrium thermodynamics research group is headed by Signe Kjelstrup. During the past years, Signe has been my thesis supervisor, for which I am very grateful. Without her, I would not have had the opportunity to enjoy living and working in Norway, and without her, this thesis would not have become as diverse and comprehensive as it has. I am still astound by the vast array of subjects and activities that Signe manages to positively contribute to.

Of course, many other people have contributed to this thesis. I want to thank all colleagues with whom I have collaborated as part of the DECARBit project, especially Benoît, Michael, and Petter. I am also grateful to Gunhild, Gunnar, Harald, Helge, and Håvard, who have contributed to the design and realization of the experimental distillation column, which has been an unforeseen but very interesting part of my Ph.D. work. In addition, I want to thank Žarko Olujić, Sigurd Skogestad, Ivar Halvorsen, and Magne Hillestad for useful discussions during the design phase of the experimental set-up. Another great thanks goes to Robert, Audun, and Luigi, for showing interest in my research and for their useful contributions to it.

In addition to the people who have contributed directly to my Ph.D. research, there are many people who contributed indirectly by creating a welcoming and sociable working environment: Thanks to everyone at physical chemistry. I especially appreciate the coffee breaks, cabin trips, board-game evenings, and Friday afternoon drinks that we shared. A special thanks to Diego, Ragnhild, and Katrine: It has been very enjoyable and educational to share office and candies with you.

Luckily, I have not only had the possibility to experience Norway's working environment; exploring the cultural and natural ones has been my pleasure as well. Of course, this is best done in good company. I want to thank my housemates Ane, Siri, Oda, Ellen, and Hanna for creating an open and cosy atmosphere at home and for enduring my re-discovered interest for playing the piano. A big thanks goes as well to all my

friends at NTNUI's underwater rugby and waterpolo teams. It was a nice surprise to win the bronze medal in the national waterpolo championship only a few months after the team's start-up. For an unforgettable trip along the west coast of Norway, I owe my thanks to Anders, Fulong, and my brother Jan. I also want to thank Odne for teaching me how to handle cross-country skis and for numerous other unforgettable experiences.

While slowly acclimatising to the Norwegian environments, it felt good to return to my Dutch roots now and then. This has only been possible thanks to all my friends and family in the Netherlands: they paid me visits in Trondheim and they were always happy to meet me when I was visiting the Netherlands. The monthly drinks with Trondheim's Dutch society have been another appreciated way to keep in tough with the Dutch.

To finish my acknowledgements, I would like to use the European Committee's prescribed sentence to thank them for funding my Ph.D. research:

> "*The research leading to these results has received funding from the European Community's 7th Framework Programme (FP7/2007-2013) under grant agreement No. 211971 (The DECARBit project).*"

In combination with the financial support from several Norwegian funds, this funding has also enabled me to attend various well-situated conferences, where I could exchange research results and ideas with numerous interesting colleagues from all around the world.

Leen van der Ham
Trondheim, September 2011

Summary

One-quarter of the worldwide greenhouse gas emissions is emitted by fossil fuel based power plants. In order to limit future climate changes caused by these emissions, several types of CO_2-capturing power plants are currently being developed. An integrated gasification combined cycle (IGCC) is one of the most promising alternatives. It is the mission of a European collaboration project called DECARBit to enable the commercial use of this type of power plant. One of the main process units of an IGCC is the air separation unit (ASU). It provides both oxygen and nitrogen to the gasifier, and nitrogen to the gas turbine. The main objective of this thesis is to improve the Second law efficiency of a cryogenic ASU, with a focus on the use of novel distillation concepts.

Improving the Second law efficiency of a process is equivalent to improving its exergy efficiency. In this thesis, the exergy efficiency is defined as the desired change in exergy contents of the ASU products divided by the net amount of added work. Using exergy analysis, it is shown that the exergy efficiency of a state-of-the-art two-column ASU with a pumped liquid cycle is approximately 35%. Most of the exergy destruction is located in the compressor after-coolers, the distillation section, and the main heat exchanger.
The irreversibilities in the compressor after-coolers are caused by the use of cooling water. They can almost completely be eliminated by transferring the heat of compression to the ASU products instead of to the cooling water. The achieved reduction in exergy destruction corresponds to almost 1% of the net electric efficiency of the IGCC and it increases the exergy efficiency of the ASU to approximately 70%.
Two alternatives are presented that can improve the distillation section efficiency. The first one is the addition of a third distillation column; it can reduce the exergy destruction in the distillation section by approximately 30%. The second option is to improve the heat integration of the two distillation columns, by using heat-integrated distillation stages (HI stages). These HI stages are the basis of a relatively novel distillation column configuration called a heat-integrated distillation column (HIDiC). In an ASU, the use of HI stages enables a lower operating pressure in the high-pressure column, which reduces the required work input to ASU. Depending on the amount of heat-transfer capacity per HI stage, the exergy destruction in the distillation section can be reduced by 20 to 30% due to the use of HI stages.

HI stages and HIDiCs are not yet in industrial use. So far, only two complete HIDiCs have been built, both using concentrically-integrated columns equipped with structured packing. They have proven the feasibility of the HIDiC concept, but detailed knowledge on the performance of the columns is still very scarce. As a result, simulations of packed concentric HIDiCs still involve several uncertainties. They are related to the achievable overall heat-transfer coefficient, to the performance of a ring-shaped distillation column, and to the effects that a radial heat flux has on the column performance. In order to obtain more insight into these phenomena, two research directions have been pursued: a theoretical one and an experimental one.

The theoretical work concerns the further development of a model for the simultaneous transfer of mass and thermal energy, based on the theory of irreversible thermodynamics. The model describes the vapour–liquid interface region of a mixture as a series of connected control volumes that together represent a vapour film, the interface, and a liquid film. This interface region is located in between the bulk vapour and bulk liquid phases; the conditions at its boundaries are equal to the adjacent bulk phase conditions. A routine has been developed that calculates the thermal and molar fluxes through the interface region, based on input values for the boundary conditions, or driving forces. The film thicknesses ratio is found by requiring consistency between the entropy productions calculated using the entropy balance and using the product-sum of conjugate fluxes and driving forces.
By applying this model to a nitrogen–oxygen mixture, it has been shown that the direct coupling between heat and diffusion fluxes has a considerable influence on the calculated values of the fluxes. The measurable heat flux is most sensitive to the coupling effect, which makes a correct description of the effect especially important when simulating a HIDiC. Another important model parameter is the number of control volumes that is used to represent the films. The effect of the interface resistances on the calculation results was relatively small.

The experimental work concerns the development of a new experimental HIDiC. The designed set-up consists of a cylindrical inner column with a diameter of 14 cm that is surrounded by a ring-shaped outer column with a diameter of 22 cm. A difference in operating pressures causes thermal energy to be transferred from the high-pressure inner column to the low-pressure outer column. Both columns will be equipped with 1.6 m of structured packing and will operate at total reflux conditions. The set-up is designed to operate at cryogenic temperatures, elevated pressures, and high oxygen concentrations. At the top of the set-up, two copper-brazed plate heat exchangers will be used as condensers, using evaporating nitrogen as coolant. Electrical heaters with a maximum duty of 25 kW will be used as reboilers.
Radial and angular temperature and composition gradients inside the columns will be measured directly at several height levels, in both the vapour and liquid phases. These measurements can also be used to determine the separation efficiency of the columns. The total amount of thermal energy transfer will be obtained based on two independent measurements of the condenser and reboiler duties of both columns. The set-up can also be used to assess the coupling between thermal and molar fluxes.

Contents

Chapter 1

Introduction

This Ph.D. thesis is written as part of a large European collaboration project called DECARBit. The main aim of the DECARBit project is to enable the commercialization of an integrated gasification combined cycle (IGCC) with pre-combustion CO_2 capture [Røkke and Langørgen, 2009]. This fossil fuel based power plant emits a reduced amount of greenhouse gas into the atmosphere. The work presented in this thesis focusses on improvements in the cryogenic air separation unit that is typically used to provide the oxygen and nitrogen that are required in such a power plant.

1.1 CO_2 emissions from fossil fuel based power plants

Nowadays, reducing the emissions of greenhouse gases is considered one of the main measures to limit future unsustainable climate changes. According to the International Energy Agency [2010], CO_2 emissions accounted for three-quarters of the worldwide greenhouse gas emissions in 2005. The other two main contributing gases were CH_4 and N_2O. About four-fifths of the total CO_2 emissions are caused by the use of fossil fuels (coal, oil, and natural gas), 16% is caused by deforestation and biomass burning, and about 3% is related to cement production. Two-fifths of these fossil fuels are combusted in electric power plants, one-quarter is used in industry, 22% is used for transportation purposes, and 6% is burned for residential use.
Combining these numbers teaches us that one-quarter of the worldwide greenhouse gas emissions is emitted by fossil fuel based power plants. These power plants are producing about two-thirds of the global electricity consumption. Although the share of electricity that is generated from fossil fuels is expected to become somewhat smaller over the next decades, the absolute number will still increase due to growing electricity consumption. Therefore, reducing the CO_2 emissions from fossil fuel based power plants is considered to be one of the most important actions to limit future climate changes. This motivates research projects such as the DECARBit project to focus

on the capture (and storage) of CO_2 that is originating from fossil fuel based power plants.

1.2 Fossil fuel based power plants with CO_2 capture

In a conventional fossil fuel based power plant (without CO_2 capture), fuel is burned with air in order to release high-temperature thermal energy that subsequently can be used to produce electricity in a series of turbines. The CO_2 that is produced during the combustion reaction leaves the power plant as part of the flue gas, which further mainly consists of nitrogen and water.
For the CO_2 to be suitable for storage, it first needs to be compressed to a high pressure. Because this requires a considerable amount of energy, it is favourable to purify the CO_2 in order to prevent other components from needlessly being compressed. The purification, or capturing, of the CO_2 can be done using various alternative power plant designs. Currently, three types of processes seem to be the most promising ones: post-combustion capture, pre-combustion capture, and oxy-fuel combustion [Rackley, 2010].

1.2.1 Post-combustion capture

A power plant with post-combustion CO_2 capture is very similar to a conventional power plant. The main difference is that a CO_2-capture unit is added at the end of the process, after the combustion step but before the flue gas is vented into the atmosphere. Therefore, this alternative is very suitable for retrofitting of existing power plants.
The main task of the CO_2-capture unit is to separate CO_2, having a concentration typically between 5% and 15%, from nitrogen. The most commonly used technology for this task is absorption using amine-based chemical solvents like monoethanolamine. Other options that are investigated are the use of adsorbents, membranes, and cryogenic temperatures.

1.2.2 Pre-combustion capture

Power plants with pre-combustion CO_2 capture are usually based on an integrated gasification combined cycle (IGCC). The main difference between an IGCC and a conventional power plant is that before combustion, the fuel is first converted into a syngas mixture by partial oxidation with purified oxygen, also known as gasification. The resulting syngas mixture mainly consists of carbon monoxide and hydrogen.
In case of an IGCC with pre-combustion CO_2 capture, an additional water-gas shift unit is used to convert the carbon monoxide in the syngas to carbon dioxide. The obtained process stream has a relatively high pressure with CO_2 concentrations typically between 15% and 40%. Before combusting the hydrogen with air and additional nitrogen, the CO_2 is removed from the process stream, resulting in a carbon-lean flue gas. This is the alternative on which the DECARBit project focusses.
The main task of a CO_2-capture unit that is part of an IGCC is to separate the carbon

dioxide from hydrogen, which is easier than separating it from nitrogen. Similar to post-combustion capture processes, absorption is currently the most commercially developed technology, but using physical solvents instead of chemical ones. A commonly used solvent is Selexol, which is a mixture of the dimethyl ethers of polyethylene glycol. The use of adsorbents, membranes, and cryogenic temperatures is also researched for this separation.
In addition to the separation of carbon dioxide from hydrogen, an IGCC, both with and without CO_2 capture, also involves the separation of air in oxygen and nitrogen. Here, the most commonly used technology is cryogenic distillation. However, other alternatives can also be used, as is discussed in Section 1.3.

1.2.3 Oxy-fuel combustion

In oxy-fuel combustion power plants, the fuel is combusted using oxygen only, resulting in a flue gas that mainly consists of CO_2. In order to control the combustion temperature, a part of the flue gas is recycled into the combustion reactor. The required oxygen can be provided either as a pure gas, obtained using air separation, or as a solid oxide in a chemical looping cycle.

1.3 Air separation

Both IGCCs and oxy-fuel combustion power plants (can) involve an air separation unit. In an IGCC, both purified oxygen and nitrogen are required, whereas an oxy-fuel combustion power plant only requires oxygen, although at a higher purity. Other examples of industrial processes that use large amounts of oxygen are steel production, cement production, and oil refining.
Several types of air separation technologies can be distinguished: adsorption of nitrogen using zeolite materials, adsorption of oxygen using activated carbon molecular sieves or perovskite materials, absorption of oxygen in molten salt solutions, polymer membranes, oxygen-transfer membranes made of solid oxide ceramics, and cryogenic distillation [Smith and Klosek, 2001].
As part of the DECARBit project, the use of oxygen adsorbents, oxygen-transfer membranes, and cryogenic distillation is investigated. The work presented in this thesis focuses on cryogenic distillation only, which currently is the most cost-effective option when large amounts of high-purity products are required.
Various types of cryogenic air separation units exist, as explained in more detail by, for example, Smith and Klosek [2001]. The work in this thesis does not concern a comparison of these different types of processes. Instead, it focuses on the analysis and potential improvement of one of them. The studied process is designed based on the experience of industrial partners within the DECARBit project, it is considered to be a state-of-the-art design for a cryogenic air separation unit as part of an IGCC and is described in more detail in Chapter 4.

1.4 Research objectives

The main objective of this Ph.D. thesis, as defined in the DECARBit project, is to improve the Second law efficiency of a cryogenic air separation unit, with a special focus on the use of novel distillation concepts. The use of the Second law efficiency as performance criterion is motivated and explained in more detail in Chapter 2. More background information on distillation in general and on novel distillation concepts in particular is presented in Chapter 3. Improvements in the efficiency of a cryogenic air separation unit do not only increase the effectiveness of fossil fuel based power plants with CO_2 capture, but they can increase the energy efficiency of any industrial process that makes use of a cryogenic air separation unit. These efficiency improvements will help to limit future climate changes.
A second objective is related to the use of novel distillation concepts, which are based on the integration of elaborate heat transfer possibilities within conventional distillation equipment. In such configurations, considerable amounts of mass and thermal energy are being transferred simultaneously. The interdependency of these transfer processes is not explicitly included in existing distillation models. Therefore, efforts on the development and implementation of a novel transfer model based on the theory of irreversible thermodynamics have been initiated. It is an objective of this thesis to continue the development of this model. Distillation is a widely used separation technology. A more-accurate distillation model is not only useful for novel types of cryogenic air separation units, but for distillation in general and possibly also for other separation techniques like absorption and extraction.
One of the aims of the DECARBit project is to bridge the gap between theoretical ideas and commercial implementations. This is pursued by building several pilot-sized experimental set-ups. It has been a task within the project to propose conceptual designs for such experimental set-ups. A proposal for a set-up concerning the use of heat-integrated air distillation column has been submitted, in close collaboration with SINTEF Energy Research, one of the partners within the DECARBit project. Because the proposed design was selected for realization by the technical advisory committee of the DECARBit project, the development of a detailed design and an experimental plan has also been added to the thesis objectives. The experience and knowledge that is generated by these activities is again not only useful for air distillation columns, but for separation columns in general.

1.5 Thesis outline

This thesis continues with two chapters that provide more background information on Second law analysis and on distillation. In Chapter 2, it is explained how an analysis based on the Second law of thermodynamics can be used to improve the efficiency of processes and process units. The connection of the Second law efficiency with quantities like the 'exergy destruction' and the 'entropy production' is also discussed. Chapter 3 presents more details on various types of distillation column configuration, with a special focus on a novel configuration called a heat-integrated distillation column (HIDiC). Some different models that can be used to simulate distillation columns

are also discussed.
The next seven chapters form the main body of this thesis. In Chapters 4 to 6, Second law analysis is used to suggest and investigate possible improvements of a cryogenic air separation unit. Chapter 4 presents the exergy analysis of two state-of-the-art cryogenic air separation units, one containing two distillation columns and one containing three. Based on the results of this analysis, two possible improvements are identified. The first one is the use of heat-integrated distillation stages. Chapter 5 investigates the effect that the use of these stages has on the performance of the distillation section of a cryogenic air separation unit. In Chapter 6, the effect on the entire air separation unit is investigated. Chapter 6 also assesses the effect of the second possible improvement, which is to make better use of the heat of compression by heating the separation products.
The next two chapters focus on the development and application of a novel approach to the modelling of distillation columns. Chapter 7 presents a thermodynamically consistent model for the simultaneous transfer of mass and thermal energy through a vapour–liquid interface. The model is subsequently applied to a binary oxygen–nitrogen mixture in order to evaluate its properties and in order to assess the effect of coupling between the thermal energy and mass fluxes. This coupling is expected to be significant especially in heat-integrated distillation columns. In Chapter 7, the model is applied to a single set of system conditions, representing a single location in a distillation column. In Chapter 8, it is applied to a range of system conditions that represent an entire distillation column. The obtained results are subsequently compared to the results of a conventional distillation model.
Chapters 9 and 10 concern the development of an experimental set-up that will allow for a more accurate performance evaluation of heat-integrated air distillation columns. These chapters can be regarded as the experimental continuation of the simulation results obtained in Chapters 5, 7 and 8. The detailed design of the set-up, and the rational behind it, are presented in Chapter 9. Descriptions of the instrumentation that is used and of the experiments that are required are all part of Chapter 10.
The thesis is concluded by Chapters 11 and 12, which contains general discussions and conclusions, and Appendix A, which discusses the details of the high-accuracy thermodynamic model that has been used in the calculations presented in Chapters 5, 7, 8 and 10.

1.6 List of publications

All publications that have been used to disseminate the results of the work presented in this thesis are listed in Sections 1.6.1 and 1.6.2. The author of the thesis is the first author of all publications and he has performed the majority of the work. The contributions of the co-authors are discussed in more detail in Section 1.6.3. The seven journal publications listed in Section 1.6.1 correspond to Chapters 4 to 10 of this thesis.

1.6.1 Journal articles

L.V. van der Ham, R. Bock, and S. Kjelstrup. *Modelling the coupled transfer of mass and thermal energy in the vapour–liquid region of a nitrogen–oxygen mixture.* Chemical Engineering Science 65 (2010), 2236–2248.

L.V. van der Ham and S. Kjelstrup. *Exergy analysis of two cryogenic air separation processes.* Energy 35 (2010), 4731–4739.

L.V. van der Ham and S. Kjelstrup. *Improving the heat integration of distillation columns in a cryogenic air separation unit.* Industrial & Engineering Chemistry Research 50 (2011), 9324–9338.

L.V. van der Ham and S. Kjelstrup. *The importance of coupling between thermal and molar fluxes in a nitrogen–oxygen distillation column.* International Journal of Thermodynamics, accepted.

L.V. van der Ham. *Improving the exergy efficiency of a cryogenic air separation unit as part of an integrated gasification combined cycle.* Energy Conversion & Management, submitted.

L.V. van der Ham and M. Drescher. *Cryogenic total reflux experiments in a packed concentric HIDiC. Part A: Background and Design.* In preparation.

L.V. van der Ham and M. Drescher. *Cryogenic total reflux experiments in a packed concentric HIDiC. Part B: Instrumentation and experiments.* In preparation.

1.6.2 Conference presentations

L.V. van der Ham and S. Kjelstrup. *The importance of coupling between thermal and molar fluxes in a nitrogen–oxygen distillation column.* 23^{rd} International Conference on Efficiency, Cost, Optimization, Simulation, and Environmental Impact of Energy Systems; 14-17 June 2010, Lausanne, Switzerland.

L.V. van der Ham, M. Drescher and S. Kjelstrup. *Applying novel distillation techniques to the ASU of an IGCC with pre-combustion CO_2-capture.* 6^{th} Trondheim Conference on CO_2 Capture, Transport and Storage; 14-16 June 2011, Trondheim, Norway.

L.V. van der Ham and S. Kjelstrup. *Distributing the heat integration of distillation columns for air separation.* 24^{th} International Conference on Efficiency, Cost, Optimization, Simulation, and Environmental Impact of Energy Systems; 4-7 July 2011, Novi Sad, Serbia.

L.V. van der Ham and S. Kjelstrup. *Improving the heat integration of distillation columns in a cryogenic air separation unit.* 23^{rd} IIR International Congress of Refrigeration; 21-26 August 2011, Prague, Czech Republic.

L.V. van der Ham, M. Drescher and S. Kjelstrup. *Design of an experimental set-up for performance assessment of heat-integrated air distillation columns.* 23^{rd} IIR International Congress of Refrigeration; 21-26 August 2011, Prague, Czech Republic.

1.6.3 Co-author contributions

Co-author Kjelstrup has been the thesis supervisor. She has contributed to the publications by scientific discussions and by thoroughly reading the manuscripts. Co-author Bock and the author have jointly taken a Ph.D. course under supervision of Kjelstrup, which has resulted in a report that has been the basis for the first journal publication. He has also contributed by reading the manuscript of this publication.
Co-author Drescher has contributed to the detailed design of the experimental set-up and has been the main responsible on behalf of SINTEF Energy Research for the design and construction of the set-up. He has also contributed by thoroughly reading the publications that concern the experimental set-up.

Chapter 2

Second law analysis[1]

Classically, energy conversion processes are evaluated based on amounts of energy. A common way of assessing process performances is to divide the amount of useful energy that is leaving the process by the amount of useful energy that is added to it. The resulting quantity is called the energy efficiency or the First law efficiency.
The energy efficiency is based on quantities of energy alone. Nowadays, it is increasingly argued that processes should be evaluated using criteria that also take the quality of energy into account, such as the exergy efficiency and the Second law efficiency. Contrary to the energy efficiency, these efficiencies always have values between zero and unity. In addition, they can be used to locate process inefficiencies and thus indicate where in the process possible improvements can have the largest impact. A process analysis based on this approach is known as a Second law analysis.
Numerous theoretical as well as practical examples exist that demonstrate the potential of Second law analysis, see for example the monograph by Kotas [1985], the work of Bejan et al. [1996], the work in the research group of Kjelstrup [De Koeijer, 2002, Johannessen, 2004, Røsjorde, 2004], and the work of Leites et al. [2003].

2.1 Exergy destruction, lost work, and entropy production

The exergy of a process stream is defined as its potential to perform work. The ratio between the net exergy output and input of a process is often called the exergy efficiency of the process.
The difference between the exergy inputs and outputs of a process is the amount of work that has been consumed or produced. For each work consuming process, there exists a minimum amount of required work, defined by the Second law of thermodynamics, which is called the ideal or reversible work. This is the minimum amount of

[1] This chapter is based on the introductions of two publications [Van der Ham et al., 2011, 2009] that are written as follow-ups on the M.Sc. thesis of the author. These publications are not included in this Ph.D. thesis.

net exergy input. In practise, the amount of consumed work is always larger than the ideal work, so the actual amount of net exergy input is always larger than the minimum amount. The difference between these two amounts is called the destroyed exergy, or the 'lost work'. The Second law efficiency of a work consuming process is defined as the ratio between the minimum and actual amounts of net exergy input. According to the Gouy–Stodola theorem, the amount of exergy that is destroyed in a process is proportional to the amount of entropy that is produced [Bejan, 1982]. Therefore, optimization of both the exergy efficiency and the Second law efficiency is equivalent to minimization of both the exergy destruction and the entropy production. In an ideal reversible process, the amount of entropy production is equal to zero. However, as given by the Second law of thermodynamics, in real processes it is always positive.

2.2 Calculating the entropy production

Two different methods for calculating the entropy production can be distinguished: the first considers process units as black boxes, the second is based on the theory of irreversible thermodynamics or non-equilibrium thermodynamics.

2.2.1 Black-box approach

The black-box approach is the simplest way to calculate the entropy production. It is based purely on a balance of the ingoing and outgoing process streams. For steady state it is

$$\frac{dS_{irr}}{dt} = \sum_i F_{i,out} s_i - \sum_i F_{i,in} s_i - \sum_i S_{i,add} \tag{2.1}$$

Here $\frac{dS_{irr}}{dt}$ is the total entropy production, $F_{i,out}$ are the outgoing material streams, $F_{i,in}$ are the incoming material streams, s_i are the specific entropies of the material streams and $S_{i,add}$ are the directly added (or removed) amounts of entropy. The last term contains contributions of thermal energy fluxes and radiation. This approach can be applied both to single process units as well as to entire processes.

2.2.2 Irreversible thermodynamics approach

Contrary to the black-box approach, the irreversible thermodynamics approach focuses on the phenomena that are occurring inside a process unit, for example the transfer of mass, the transfer of thermal energy, the transfer of charge, or chemical reactions. According to the theory of irreversible thermodynamics, the local entropy production is the product sum of all the conjugate thermodynamic fluxes and forces that are involved [De Groot and Mazur, 1962, Kjelstrup et al., 2010]. Examples of thermodynamic fluxes (J_i) are a mass flux, a thermal energy flux and a reaction rate; examples of thermodynamic forces (X_i) are a chemical potential gradient, a temperature gradient and a reaction Gibbs energy difference. The local entropy production

(σ) is thus given by

$$\sigma = \sum_i J_i X_i \tag{2.2}$$

Each of the thermodynamic fluxes is given by a linear combination of all thermodynamic driving forces:

$$J_i = \sum_j L_{ij} X_j \tag{2.3}$$

Here L_{ij} is the coupling coefficient that is coupling flux i with driving force j. The coupling coefficients are symmetric, meaning that $L_{ij} = L_{ji}$. The total entropy production of a process unit can be calculated by integrating the local entropy production over the entire volume (V) of the process unit

$$\frac{dS_{irr}}{dt} = \int_0^V \sigma dV \tag{2.4}$$

In comparison with the black-box approach, the irreversible thermodynamics approach requires a more detailed resolution of the transport processes in the process unit. It can only be applied to one process unit at the same time. In the case that an entire process needs to be analysed, first each of the process units need to be analysed separately, then their contributions can be summed to yield the overall entropy production.

2.2.3 Consistent modelling of transfer processes

The fact that the steady state total entropy production can be calculated using the two different approaches discussed above provides excellent means for verifying model and calculation consistencies. This can be especially useful when modelling transfer processes that are occurring simultaneously. Most models for simultaneous transfer processes do not fully take into account the principles of irreversible thermodynamics; they are rather based on extensive sets of empirical correlations. As a result, these models can yield inconsistent results. The transfer model that is described in Chapters 7 and 8 is based on irreversible thermodynamics and makes use of these two ways of calculating the total entropy production in order to ensure a thermodynamically consistent model.

2.3 Improving the Second law efficiency

Two different strategies can be distinguished that aim at improving the Second law efficiency. The first one is called exergy analysis, it uses the black-box approach described in Section 2.2.1 to calculate the entropy production for different process alternatives. The second strategy is based on irreversible thermodynamics, as described in Section 2.2.2. Its main aim is to minimize the total entropy production in a single process unit.

2.3.1 Exergy analysis

When using the exergy analysis approach, the Second law efficiency is improved by comparing the total entropy production, or its equivalent the exergy destruction, of various process alternatives, and selecting the best configuration. Different process alternatives can be created by varying operating conditions and design variables, and by changing the process superstructure and the types of the process units that are used. The investigated process variations and changes are often focussed on the most inefficient process parts; the parts that are producing the most entropy. This is the approach that is pursued in Chapters 4 to 6 of this thesis.

2.3.2 Minimization of entropy production

In order to get more fundamental insight into strategies for the minimization of entropy production in a process unit, the state of minimum entropy production has received considerable attention, for example by Johannessen and Kjelstrup [2005] and by Wilhelmsen et al. [2010]. The state of minimum entropy production of a process unit corresponds to the configuration that results in the lowest possible entropy production, while obeying a given constraint that is related to the function of the process unit. Examples of such constraints are the transfer of a given amount of thermal energy, or the conversion of a given amount of chemicals. An important result of the work by Johannessen and Kjelstrup is a hypothesis stating that "Equipartition of Entropy Production (EoEP), but also Equipartition of Forces (EoF) are good approximations to the state of minimum entropy production in the parts of an optimally controlled system that have sufficient freedom.".

Equipartition of entropy production

EoEP means that the local entropy production is the same at every location in a process unit. In other words, the total entropy production is distributed evenly over the available volume, resulting in a constant entropy production profile. Because EoEP involves the entropy production at a local scale, the use of irreversible thermodynamics is a prerequisite. The theory of irreversible thermodynamics also gives more insight into why EoEP and EoF can minimize the entropy production. If we combine Equations (2.2) and (2.3) for one single conjugate flux–force pair, we see that its local entropy production (σ_i) equals the coupling coefficient times the squared force, or the squared flux divided by the coupling coefficient alternatively

$$\sigma_i = L_{ii} X_i^2 = \frac{J_i^2}{L_{ii}} \tag{2.5}$$

When we consider an even distribution of this single flux and require that the total flux, which is the local flux integrated over its relevant spatial coordinate, remains constant, it becomes plausible that minimum entropy production corresponds to EoEP.

Starting from the even distribution, any local decrease of the flux is then countered by a local increase of the flux elsewhere, in order to maintain the defined total flux. Because the entropy production is proportional to the squared flux, the decrease in entropy production due to the local decrease of the flux is always smaller than the increase in entropy production due to the corresponding local increase of the flux. So any deviation from an even distribution of the flux always increases the entropy production. It can therefore be concluded that the optimal distribution of the flux is an even distribution. This also implies that the driving force and the entropy production of this flux should have an even distribution.
This argument is of course an idealization; we did not consider the influence of the boundary conditions and we assumed that the system indeed has "sufficient degrees of freedom". But the argument helps to understand why EoEP and EoF can be useful strategies to minimize entropy production and it motivates work to develop their application in practise. Both concepts were discussed in more detail by Tondeur and Kvaalen [1987] and by Kjelstrup, Sauar and co-workers [Kjelstrup Ratkje et al., 1995, Sauar et al., 1996].

Practical requirements and examples

The assumption that sufficient degrees of freedom are available can be translated in the requirement that there must be at least one quantity that can be fully controlled along the entire spatial coordinate of the process unit. When such a quantity is available, its profile can be used to approximate EoEP as much as possible.
An example of such quantity is the temperature at which thermal energy is added to a plug-flow reactor in which an endothermic reaction takes place [Johannessen and Kjelstrup, 2004, Van der Ham et al., 2009, Wilhelmsen et al., 2010]. Another example is the thermal energy transfer in distillation columns that involve thermal energy transfer along their entire length, such as diabatic distillation columns [De Koeijer, 2002, Johannessen, 2004, Schaller, 2007] and heat-integrated distillation columns [Røsjorde, 2004]. These types of distillation column are discussed in more detail in Chapter 3.

2.3.3 Economical considerations

For an improvement in the Second law efficiency to be applied in practise, it should result in a higher profitability. An increase in the process efficiency typically translates in lower operating costs. However, in order to achieve the efficiency increase, the investment costs often increase. The net change in costs depends on many factors, which differ from location to location and from time to time. Therefore, the work in this thesis focuses mainly on efficiency improvements. Financial assessments are restricted to qualitative considerations only. The economical consequences that improvements in the Second law efficiency have are not investigated in a quantitative matter.

Chapter 3

Distillation

Distillation is the most widely used technique in chemical industry to separate a feed mixture in two or more purified products. A distillation column is a process unit that separates a mixture based on differences in boiling temperatures, or volatilities, of its components. Several types of distillation column configurations can be distinguished.

3.1 Distillation column configurations

Figure 3.1a shows a schematic overview of a conventional distillation column. A feed mixture, which can be vapour, liquid, or both, is fed to column at a height that is determined by the feed composition and by the product purities. Within the column, liquid is continuously flowing down and vapour is continuously flowing up.
A vapour stream rich in the most volatile component (having the lowest boiling temperature) leaves the top of the column. A part of this stream is condensed in a condenser and recycled to the column as liquid (the reflux); the remainder forms the top product (the distillate). The ratio between the reflux and the distillate is called the reflux ratio.
A liquid stream rich in the least volatile component (having the highest boiling temperature) leaves at the bottom of the column. A part of this stream is evaporated in a reboiler and recycled to the column as vapour; the remainder forms the bottom product.
The height of the column is determined by the feed composition, by the required product purities, by the reflux ratio, and by the type of column internal that is used. The most common column internals are physical trays, random packing, and structured packing.

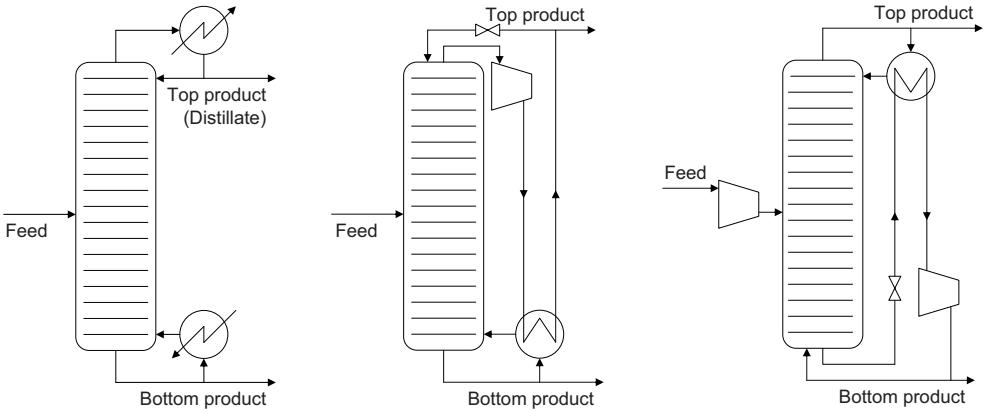

(a) Conventional distillation column

(b) Vapour recompression distillation column

(c) Liquid re-expansion distillation column

Figure 3.1: Schematics of a conventional (a), a vapour re-compression (b), and a liquid re-expansion (c) distillation column.

3.1.1 Heat-pump assisted configurations

Most distillation processes take place at temperatures above the ambient temperature. High quality heat is then added to the bottom of the column by the reboiler, and heat of a lower quality is removed at the top of the column by the condenser. Because this conventional configuration proved to be thermodynamically very inefficient, alternative configurations have been developed [Freshwater, 1951].
One of the first approaches to increase the efficiency was to re-use the energy removed in the condenser by using the top-product as heat source in the reboiler. Since the reboiler operates at a higher temperature than the condenser, the temperature of the top product needs to be increased first. This can be done by compressing it. The resulting concept is called a vapour recompression column and it is shown in Figure 3.1b. The compression ratio depends on the required temperature increase. Vapour recompression is especially feasible for close boiling mixtures. If the temperature difference becomes too large, the energy associated with the required compression ratio surpasses the reduction in external energy input of the reboiler.
The distillation step of an air separation unit takes place at temperatures far below the ambient temperature. In this case, high quality cold is added to the column in the condenser and cold of a lower quality is removed at the reboiler. Therefore, more-efficient distillation configurations aim at the re-use of the cold removed at the reboiler. Upgrading the quality of this cold stream can be done by expanding it, yielding a cryogenic variant of the vapour recompression configuration. A schematic of this liquid re-expansion configuration is shown in Figure 3.1c. To enable expansion of the bottom product, an elevated column pressure is required. Therefore, the feed needs to be compressed before it is added to the column.

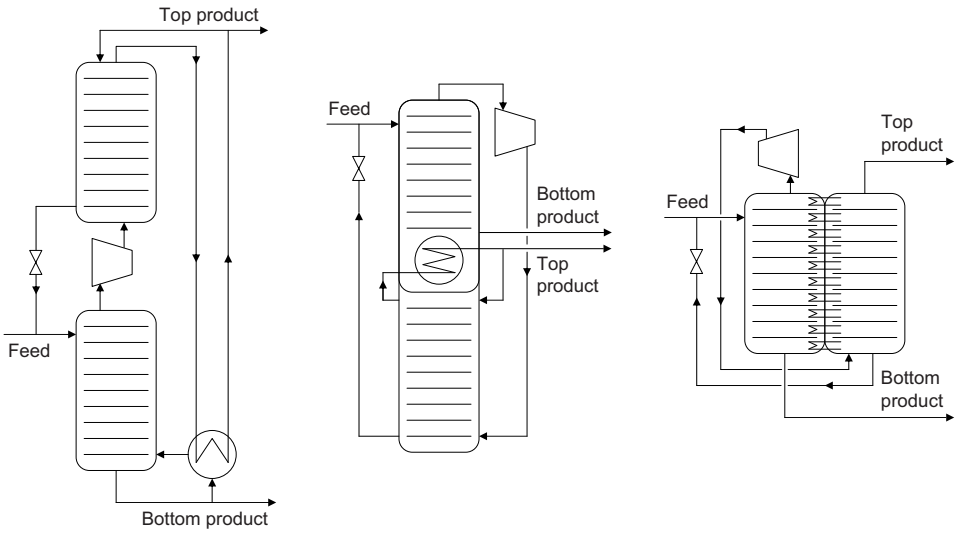

(a) Pressure-swing distillation column

(b) One-shell pressure-swing distillation column

(c) Ideal heat-integrated distillation column

Figure 3.2: Schematics of a pressure swing (a), a one-shell pressure-swing (b), and an ideal heat-integrated (c) distillation column.

3.1.2 Pressure-swing configurations

A variation to the vapour recompression and liquid re-expansion configurations is the pressure-swing concept. In this case, the single column is split in two parts, which are now operated at different pressures. The compressor and expander are positioned between the two column parts. The new configuration is shown in Figure 3.2a.
Instead of using two separate columns, the pressure-swing configuration is often integrated into one single column shell. The heat exchanger that is replacing the condenser and reboiler is also incorporated in this shell. The top half of the conventional distillation column is now the bottom half and vice versa. This one-shell configuration is shown in Figure 3.2b. Cryogenic air distillation processes are usually based on this type of column configuration. More details on the actual configuration are discussed in Section 3.1.4.
In a relatively novel distillation concept, the two column halves are positioned next to each other instead of on top of each other (see, for example Nakaiwa et al. [2003]. In this way, heat can be exchanged between the two columns along their heights, instead of in the central heat exchanger only. This configuration is called a heat-integrated distillation column (HIDiC). In an ideal situation, a HIDiC can operate without reboiler and condenser, as is shown in Figure 3.2c. In practise however, they are often still necessary. The HIDiC is discussed in more detail in Section 3.2.

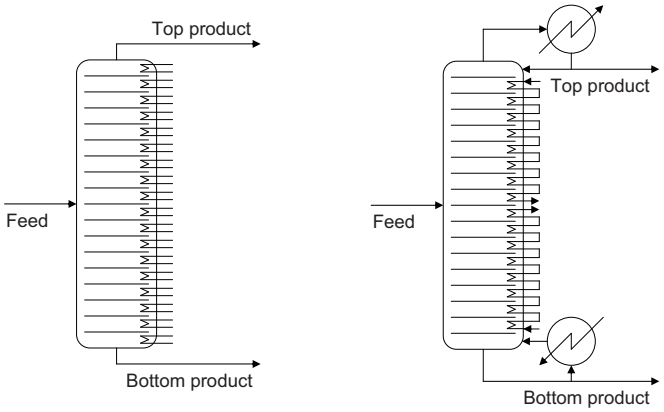

(a) Ideal diabatic distillation column

(b) Sequential diabatic distillation column

Figure 3.3: Schematics of an ideal diabatic (a) and a sequential diabatic (b) distillation column.

3.1.3 Diabatic configurations

Another relatively novel distillation concept that uses heat exchangers along the entire column height is called diabatic distillation. The heat exchangers can be considered to distribute the reboiler and condenser duties over the entire columns height, see, for example, the work of Fonyó [1974a,b]. In the ideal case, an independently operating heat exchanger is present at each tray of the column, as shown in Figure 3.3a.
In more practical designs, the heat exchangers are coupled in the top and the bottom parts of the column, yielding a diabatic distillation column with sequential heat exchangers, see, for example, the work by Jimenez et al. [2004]. For easier operation, a small separate reboiler and condenser can also be installed. Figure 3.3b shows a diabatic distillation column with sequential heat exchangers and a separate reboiler and condenser.

3.1.4 Two-column air distillation configuration

The column configuration that is the basis for most air distillation processes is based on the one-shell pressure-swing configuration shown in Figure 3.2b. However, the two column parts are connected to each other in a different way. They are rather operated as two columns in series, than as one column that is split into two parts.
In the simplest version of this configuration, pressurized and super-heated air is fed to the bottom of the bottom column. The top product, high-purity nitrogen, is withdrawn from the top of the bottom column. The liquid that is leaving the bottom of this column is cooled, throttled down in pressure, and fed to the top column at an intermediate height. Another liquid stream is withdrawn from the bottom column

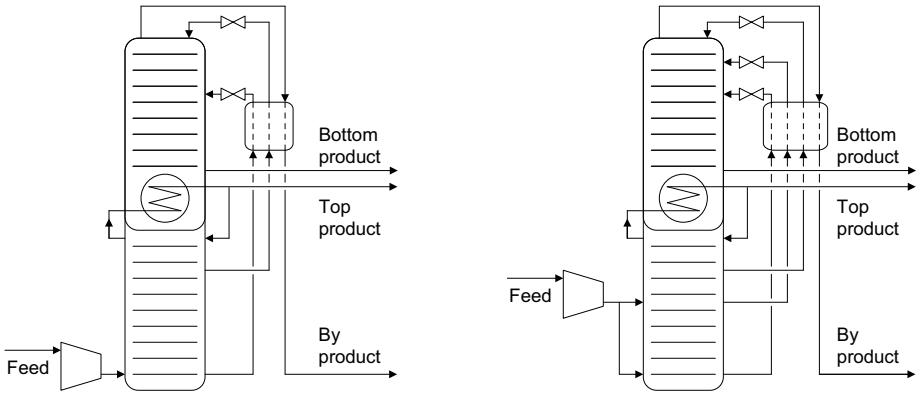

(a) Basic two-column air distillation configuration

(b) Advanced two-column air distillation configuration

Figure 3.4: Schematics of a basic (a) and an advanced (b) two-column configuration used for air distillation.

at an intermediate height, sub-cooled, throttled down in pressure, and fed to the top of the top column. The top column produces high-purity oxygen, which is the bottom product of the column configuration, and a low-purity nitrogen by-product, which is used to cool the liquid streams that are fed to the top column. This basic configuration is shown in Figure 3.4a.
In more advanced configurations, the air can be fed to the columns at several locations, both as vapour and as liquid. In addition, more liquid streams can be used to connect the two columns. An example of an advanced two-column configuration is shown in Figure 3.4b. This is the configuration that is used in Chapters 4 to 6. More details on the other process units that are part of a cryogenic air separation process included in Chapters 4 and 6.

3.2 Heat-integrated distillation columns

Nakaiwa and Ohmori [2009] showed that the thermodynamically optimal way of operating a distillation column involves the transfer of thermal energy along the entire length of the column. In a conventional distillation column, the addition and removal of thermal energy is limited to three locations only: the top, the bottom, and the feed location. The number of locations can be increased by using additional feed and product locations, and by adding intermediate heat exchangers. However, in order to achieve thermal energy transfer at every location, a different type of distillation column is required. Both diabatic distillation columns and heat-integrated distillation columns (HIDiC) allow for this type of thermal energy transfer. This thesis focuses mainly on the HIDiC option.
As discussed in Section 3.1.2, a HIDiC can be regarded as a conventional distillation

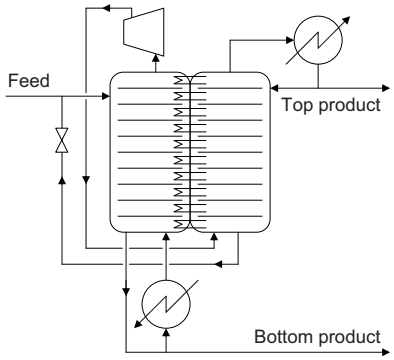

Figure 3.5: Schematic representation of a heat-integrated distillation column with a reboiler and a condenser.

column that is split into two at its feed location. By operating the two parts at different pressures and by positioning them next to each other, thermal energy can be transferred from the high-pressure part to the low-pressure part along the entire length of the integrated column. Figure 3.5 shows a schematic of a practical implementation of a HIDiC, it is equipped with both a reboiler and a condenser, as opposed to the ideal HIDiC shown in Figure 3.2c.
Compared to a conventional distillation column, a HIDiC has two big advantages. The first one is the possibility for thermal energy transfer along the entire height of the columns, which can enable a thermodynamically more efficient design. The second one is a reduction in the required condenser and reboiler duties, caused by thermal energy transfer along the column height. However, in order to realize these advantages, an additional compressor and throttle valve are required, as shown in Figure 3.5. The net effect of reducing the condenser and reboiler duties but adding compressor duty is often used to determine the thermodynamic feasibility of a HIDiC design, an overview of reported efficiency gains is given in Section 3.2.1. From an economic point of view, the feasibility of a HIDiC is determined by the increase in investment costs, related to the addition of a compressor, and by the change in operational costs, related to the changing energy duties.
Applying this type of heat integration to air distillation columns has a big advantage when compared to the use of a HIDiC for other applications. Because the current state-of-the-art air distillation processes already involve different operating pressures, no additional compressor is required.

3.2.1 Reported efficiency gains

Various theoretical and experimental studies that are comparing HIDiCs to conventional columns report considerable efficiency gains. Table 3.1 shows a chronological overview of the reported efficiency gains, represented by the reduction in the total energy input. The total energy input is given by the sum of the reboiler and compressor

duties, it is chosen because it is the only quantity available for all studies.
In addition to the changes in the total energy input, Mah et al. [1977] also calculated the changes in the steam and cooling water requirements for the three separation cases they studied. This was done in order to take the changes in the temperatures at which energy is added and removed into account. For the trans-2-butene–cis-2-butene case, they found comparable results; a reduction of 15% in the steam consumption and of 35% in the cooling water consumption. The propylene–propane case showed utility requirements that were quite different from the changes in the energy input; a 70% increase in the steam consumption and a 60% decrease in the cooling water consumption. The third case, the ethylene–ethane separation, performed much better in terms of utilities; the steam consumption decreased by 55% and the cooling water by 75%.
Røsjorde [2004] also reports the efficiency gain in terms of a reduced amount of lost exergy. He found possible reductions of 35% and 45%, depending on the allowed type of heat-transfer area distribution. For the case of a propylene–propane splitter, De Rijke [2007] reports a decrease in the exergy requirement of approximately 40%. For a similar case, but operated at higher pressures, Olujić et al. [2003] reported a possible decrease in the exergy losses of 75%.
All the reductions in energy input that are listed in Table 3.1 concern comparisons between a HIDiC and a conventional distillation column. According to Shenvi et al. [2011], a configuration based on the use of a heat pump (as shown in Figure 3.1b), potentially equipped with one or two additional intermediate heat exchangers, should also be considered. Such a configuration can be the most effective one, depending on the temperature profiles in the two heat-integrated columns.

3.2.2 Heat-integrated air distillation columns

Detailed performance evaluations of heat-integrated air distillation columns have not been found in the open literature. However, the use of such a column configuration has been mentioned.
Nakaiwa et al. [1996] describe an energy supply system that uses purified oxygen, which is obtained using air distillation. They state that the use of column configuration with two reboiler–condensers that are enclosing a heat-integrated column part can reduce the energy requirement of the air separation unit by 30%. This reduction is related to a decrease in the operating pressure of the high-pressure column, which lowers the required feed pressure.
Iwakabe et al. [2006a] report a study that predicts a reduction in the energy input of 40% when using a plate-fin type HIDiC as part of a cryogenic air separation unit.
In order to place these efficiency gains in a wider perspective, detailed information is needed on both the suggested process flow sheets, the processes to which they are compared, and the practical implementation of the heat integration. Unfortunately, insufficient data is available for this purpose. Detailed numerical performance assessments of heat-integrated air distillation columns are included in Chapters 5 and 6 of this thesis.

Table 3.1: Reported efficiency gains when comparing a HIDiC with a conventional distillation column. The efficiency gains are here given as the reduction in the sum of the reboiler and compressor duties.

Mixture	Efficiency gain	Study type	Reference
trans-2-butene – cis-2-butene	25%	Numerical	Mah et al. [1977]
propylene – propane	45%	Numerical	Mah et al. [1977]
ethylene – ethane	20%	Numerical	Mah et al. [1977]
benzene – toluene	60%	Numerical	Nakaiwa et al. [1997]
benzene – toluene	50%	Numerical	Liu and Qian [2000]
benzene – toluene	40%	Experimental	Naito et al. [2000]
benzene – toluene	75%	Numerical	Røsjorde [2004]
benzene – toluene – ethyl-benzene	40%	Numerical	Matsuda et al. [2006]
benzene – toluene – p-xylene	30%	Numerical	Iwakabe et al. [2006b,c]
n-pentane – cyclopentane – 2-methylpentane [a]	50%	Numerical	Iwakabe et al. [2006c]
12-component hydrocarbon mixture	50%	Numerical	Iwakabe et al. [2006b]
propylene – propane [b]	90%	Numerical	De Rijke [2007]
water – methanol	50%	Numerical	De Rijke [2007]
ethylbenzene – styrene [b]	90%	Numerical	De Rijke [2007]
hypothetical close-boiling ternary mixture [c]	60%	Numerical	Huang et al. [2007]
acetic acid – acetic anhydride [b]	60%	Numerical	Campbell et al. [2008]
12-component hydrocarbon mixture	60%	Experimental	Horiuchi et al. [2008]
ethylene – ethane	90%	Numerical	Chen et al. [2010]
benzene – toluene	55%	Numerical	Chen et al. [2010]
benzene – toluene – o-xylene [a,c]	35%	Numerical	Cabrera-Ruiz et al. [2011]
butane – isopentane – pentane [a,c]	25%	Numerical	Cabrera-Ruiz et al. [2011]

[a] Multiple feed compositions have been evaluated. The average reduction is shown.
[b] A comparison with a vapour recompression column is also included.
[c] A series of two HIDiCs is compared with a series of two conventional distillation columns.

3.2.3 Existing HIDiC installations

HIDiCs are not yet in industrial use; they are still under development. At the moment, only two complete experimental HIDiC configurations are described in the open literature. Both have been built and operated successfully as part of Japanese national research projects and both used concentrically-integrated columns equipped with structured packing. In a concentric HIDiC, one of the column parts is positioned inside the other column part, yielding a configuration with a regular cylindrical inner column and an annular or ring-shaped outer column. The first Japanese HIDiC was about 20 m high and had an outer diameter of about 25 cm [Naito et al., 2000]. The second Japanese HIDiC was 27 m high and contained 7 parallel columns with an outer diameter of 41 cm that were positioned in a single shell of 1.4 m diameter [Horiuchi et al., 2008]. In both designs, three different inner column diameters were used to account for the changing vapour flow rates.
The most important European experimental efforts aiming at the development of a HIDiC are done by a Dutch research consortium. Their initial experimental work has been focused on the properties of an annular sieve tray equipped with heat transfer panels [De Rijke, 2007]. More recently, they have also started experimental efforts on a plate-fin type HIDiC.

3.2.4 Designing a HIDiC

The key design variables of a HIDiC are the ratio between the pressures in two column parts, the available heat-transfer area, and the overall heat-transfer coefficient. The pressure ratio determines the required compressor duty and the temperature difference between the two columns. This temperature difference, in combination with the heat-transfer area and the overall heat-transfer coefficient, determines the thermal energy transfer, and thus the reduction in reboiler and condenser duties. The pressure ratio is relatively straightforward to model. However, the heat-transfer area and especially the overall heat-transfer coefficient are more complicated.

Heat-transfer area

The amount of available heat-transfer area depends a lot on the type of column internals that is used: either trays or (structured) packing.
When using packing, heat integration can be realized by using concentrically-integrated columns, as explained in Section 3.2.3. The inner column wall forms the basis of the heat-transfer equipment in such a configuration. The amount of heat-transfer area is mainly defined by the diameter of the inner column and the number of parallel columns that is used. The design described by Horiuchi et al. [2008] used a wire that was wound around the inner column wall. Such surface or flow enhancements increase the overall heat-transfer coefficient, but make it harder to define the heat-transfer area accurately. Good thermal contact between the inner column wall and the packing in the columns is advantageous for the thermal energy transfer between the columns,

but it also makes it harder to define the heat-transfer area.
When using trays, additional heat-transfer equipment is often used to connect the two column parts thermally . It can be placed in the downcomer area or in the active tray area. When it is placed in the active tray area, the active heat-transfer area can depend on the flow conditions and the froth height on the tray [De Rijke, 2007]. The active area can also decrease during operation due to the accumulation of incondensables in the heat-transfer equipment.

Overall heat-transfer coefficient

HIDiC designs are usually modelled and evaluated using a constant value for the overall heat-transfer coefficient, which is used for the entire column. In reality, the overall heat-transfer coefficient is not constant. In case of packed columns, it depends for example on the properties of the liquid films that are flowing down on both sides of the wall. Table 3.2 gives an overview of reported experimental overall heat-transfer coefficients in distillation columns equipped with structured packing.

Table 3.2: Reported experimental overall heat-transfer coefficients in distillation columns with structured packing.

Overall heat-transfer coefficient	Reference
670 W/(m^{2}K)	Horiuchi et al. [2008]
700 W/(m^{2}K)	Niggemann et al. [2010]
1100 W/(m^{2}K)	Nakanishi et al. [2008]

According to Iwakabe et al. [2006a], it was found that the overall heat-transfer coefficient in a trayed column does not depend on the compression ratio. But an experimental investigation by De Rijke [2007] showed that the overall heat-transfer coefficient does depend on the temperature difference between the two columns, because of the effect that this temperature difference has on the flow conditions of the liquid films. This suggests that different types of heat-transfer coefficient models should be used, depending on type of condensation and evaporation mechanisms.
Based on this information, we can conclude that it is not yet straightforward to make a reliable prediction for the overall heat-transfer coefficient in a specific HIDiC design. For an accurate HIDiC model, more-detailed experimental data on the overall heat-transfer coefficient is required.

3.2.5 Properties of a packed HIDiC

The properties of a packed HIDiC cannot be described by simply combining the properties of two conventional packed columns. Some additional effects need to be taken into account. Firstly, the amount of wall area per column volume is higher in a HIDiC than in a conventional column. Secondly, the transfer of thermal energy within

a HIDiC promotes radial gradients and affects the mass transfer characteristics. Both effects can influence the separation efficiency of the packing.

Increased wall effects

In conventional packed distillation columns, it is a well-known phenomenon that a part of the liquid flows down along the wall of the column, thus bypassing the packing. Such a radial liquid flow maldistribution causes maldistributions in the temperature and compositions, eventually decreasing the separation efficiency of the packing [Huber and Hiltbrunner, 1966]. Columns with structured packing use wall scrapers to reduce this effect; they redirect the liquid flow back into the packing. However, these wall-scrapers do not completely prevent an increase of liquid flow in the wall zone of the column [Olujić et al., 2006].
There are two reasons why the wall effects are more severe in a packed concentric HIDiC. First, several parallel columns with a small diameter are used instead of a single column with a large diameter. This is done in order to accommodate sufficient heat-transfer area and it results in more wall area per total column volume. The column diameter also affects the pressure drop and the capacity of structured packing [Olujić, 1999].
The second reason for increased wall effects is related to the concentric integration of the two column parts. The inner column has the same amount of wall area per column volume as a conventional column, but the outer annular part contains more wall area per column volume. So the wall effects can be expected to be more severe in the outer column, possibly causing the outer column to have lower separation efficiency than the inner column. At the moment, no experimental or numerical data is publicly available on the performance of annular columns.

Effect of heat integration

The transfer of thermal energy from the high-pressure part of a HIDiC to its low-pressure part causes several operational differences compared to a conventional distillation column.

Firstly, it creates radial temperature gradients in both columns. These gradients will be steepest in the near-wall zones of the inner column wall, but they might also affect the other zones in the columns.
The heat flux through the inner wall will also cause an increase in the evaporation at the low-pressure side of the wall, and an increase in condensation at the high-pressure side. So the wall-zone liquid flow can be expected to decrease in the low-pressure column, and it can be expected to increase in the high-pressure column. This means that the reduction in separation efficiency due to wall flow can be expected to be lower at the low-pressure side of the inner wall than at its high-pressure side. The evaporation and condensation at the inner column wall will also affect the separation

efficiency of the two columns directly, because light components tend to evaporate easier than heavy components. As a result, radial composition gradients might be observed.
To what extent the temperature and concentration gradients will be present, and to what extent the separation performance will be affected is currently unknown. It is therefore interesting to investigate these phenomena experimentally.

The fact that a change in the heat flux causes changes in the diffusional fluxes is described by the theory of irreversible thermodynamics. According to this theory, there exists a direct coupling between thermal and molar fluxes, see Section 2.2.2. In previous studies, based on conventional columns separating an ethanol–water mixture [De Koeijer and Kjelstrup, 2004, Kjelstrup and De Koeijer, 2003], it was found that this coupling effect can be significant and should be included in detailed distillation models. It can be expected that the importance of this effect is even more pronounced in a HIDiC, because of the additional heat flux through the inner wall.
The importance of the coupling can be quantified using various quantities that all describe the same effect: the heat of transfer, the thermal diffusion coefficient, the Soret coefficient, the Dufour coefficient, the thermal diffusion factor, and the thermal diffusion ratio. For air-like mixtures, some of these quantities have been investigated experimentally for the vapour phase [Ibbs et al., 1929, Nakano and Maeda, 2008, Rastogi and Madan, 1966, Van Itterbeek and De Rop, 1956, Waldmann, 1944, 1949]. But for the liquid phase, no experimental data is available. According to Kjelstrup and De Koeijer [2003], the coupling effect is the strongest in the liquid phase. This gives a rational for doing additional experiments to elucidate these phenomena.

3.2.6 The need for experimental investigations

The data presented in Sections 3.2.1 and 3.2.2 show that the use of heat-integrated (air) distillation columns has a high potential to improve the efficiency of distillation processes. So far, the only practical implementations of a HIDiC use concentrically-integrated columns that are equipped with structured packing. Section 3.2.3 shows that the amount and level of detail of the publicly available experimental data of such configurations is very limited. As a results, there exist several uncertainties in the model parameters that are used when simulating these configuration, as explained in Sections 3.2.4 and 3.2.5. In order to obtain more accurate efficiency improvement estimates, experimental investigations are needed that focus on four aspects of a packed concentric HIDiC:

1. The overall heat-transfer coefficient, its dependency on operating conditions and its variation along the column height.
2. The separation efficiency and capacity limits of an annular column, compared to a cylindrical one.
3. The severity of radial temperature and composition gradients under varying operating conditions.

4. The effect of the additional heat flux on the diffusion fluxes, as a result of their direct coupling.

The experimental set-up that is developed in Chapters 9 and 10 aims to address these four issues.

3.3 Distillation column models

The building and operation of industrial-scale distillation columns involves substantial amounts of money. As a natural result, considerable efforts have been made to develop predictive distillation column models that allow for an accurate simulation of column performances.
The models that are commonly used to simulate distillation columns can be considered to consist of two parts: a theoretical part and an empirical part. Two main types of theoretical models can be distinguished: the theoretical equilibrium stage model and the rate-based model. The theoretical equilibrium stage model is the simplest one; thermodynamic data is required as main input, which can be supplemented with empirical correlations in order to improve the predictive accuracy. The rate-based model is more elaborate and requires both thermodynamic data and empirical correlations as input.
The main assumptions of these models and their differences are discussed below in a qualitative manner. More elaborate descriptions of the models, including relevant equations and calculation routines, can be found, for example, in the monographs by Taylor and Krishna [1993], by Seader and Henley [1998], and by Asano [2006].

3.3.1 Theoretical equilibrium stage model

In the theoretical equilibrium stage model, a distillation column is assumed to consist of a series of connected theoretical equilibrium stages. The main assumption that is made in the model is that the vapour and liquid streams that are leaving a distillation stage are in thermodynamic equilibrium. This means that their temperature, pressure and chemical potentials are equal. The transfer processes that are occurring within the distillation stage are not modelled explicitly.
The origin of this model can be best understood when considering distillation columns that are equipped with physical trays. In a properly designed tray, thermodynamic equilibrium between the outgoing streams can indeed be achieved. A physical tray is in such a case equal to a theoretical equilibrium stage. However, this is not always true. The difference in performance of physical trays compared to theoretical equilibrium stages can be captured using tray or point efficiencies. These efficiencies are calculated using correlations that are developed based on past experimental experience, they use various design variables as input.
In case of a distillation column that is equipped with packing, a theoretical equilibrium stage is assumed to correspond to a certain height of packing. The exact height depends on the type of packing that is used and on the operating conditions. It can again be calculated using empirical correlations.

3.3.2 Rate-based model

In the rate-based model, equilibrium is assumed to exist at the vapour–liquid interface instead of between the streams leaving a theoretical stage. In order to calculate the properties of the streams that are leaving a physical tray or a section of packing, additional relations for the interfacial area and the rates of mass and thermal energy transfer are required. These transfer rates can be calculated using two different ways of modelling the vapour–liquid interface region: the four-film approach [Taylor and Krishna, 1993], which is most commonly used, and the integrated-interface approach [Bedeaux and Kjelstrup, 2004, Kjelstrup and De Koeijer, 2003], which is still under development. The second approach is the one that this thesis will focus on, in Chapters 7 and 8.
In both approaches, the interface region is a hypothetical region in which all transfer resistance is assumed to be located. It is positioned between the bulk liquid and the bulk vapour phases, as shown in Figure 3.6. The physical properties at the liquid and vapour boundaries of the region are assumed to be equal to the bulk properties. The two model approaches differ mainly in their definitions for the thickness(es) of the interface region(s) and in the structure of their transfer equations.

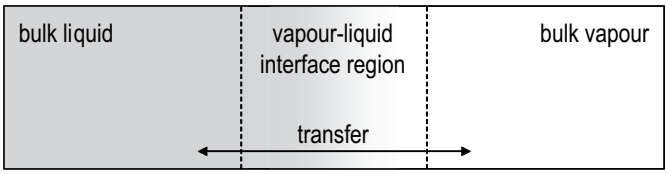

Figure 3.6: Schematic overview of the transfer processes through a vapour–liquid interface region.

Four-film approach

In the four-film approach, two partly-overlapping interface regions are distinguished: one containing the resistance against mass transfer, and one containing the resistance against thermal energy transfer. Both regions consist of a liquid film and a vapour film that meet each other at the vapour–liquid interface, resulting in a total of four films. The transfer rates through the interface regions are functions of transfer coefficients and of the differences in temperature or composition between the interface and the bulk phases.
The thicknesses of the four films can be calculated using correlations for the transfer coefficients, which are developed using past experimental observations. Because these empirical correlations contain correction factors that dependent on the transfer rates, some interdependency between the mass and thermal energy transfer processes can be present in the model, although included implicitly.

Empirical correlations are often not available for all four transfer coefficients or film thicknesses. To cope with this problem, different types of assumptions are being used. A first approach is to estimate heat-transfer coefficients based on mass transfer coefficient relations, using an analogy between thermal energy and mass transfer. A second approach is to estimate liquid phase coefficients by multiplying vapour phase coefficients by a certain fixed value. Sometimes the liquid phase resistance is assumed negligible, which corresponds to multiplication by infinity, or to assuming a film thickness that is equal to zero.

Integrated-interface approach

The integrated-interface approach is based on the theory of irreversible thermodynamics (see Section 2.2.2). According to this theory, there exists direct coupling between the mass and thermal energy transfer rates. Therefore, the region containing the resistance against mass transfer and the region containing the resistance against thermal energy transfer are by definition the same. Furthermore, the thicknesses of the liquid and the vapour parts of the interface region are dependent on each other, in order to ensure a thermodynamically consistent transfer model, as discussed in Section 2.2.3. As a result, the entire vapour–liquid interface region is considered as a single integrated system, which is defined by a single thickness. In theory, this thickness only depends on the flow conditions, but this has not yet been verified experimentally. The experimental efforts described in Chapters 9 and 10 aim to elucidate this.
Another property of the integrated-interface approach is the addition of the interface transfer resistance. In the four-film approach, this resistance is assumed negligible, resulting in, for example, a constant temperature on both sides of the interface. Including the resistance of the vapour–liquid interface creates a temperature jump over the interface.

3.3.3 Simulations of air distillation columns

Several approaches to the simulation of air distillation columns have been published during the past five decades. They reflect the transition from the use of theoretical equilibrium stage models to the use of rate-based models, and from the use of physical trays to the use of structured packing.

Latimer [1967] gave an extensive description of various air distillation configurations in terms of common operating conditions, numbers of theoretical equilibrium stages, and achieved purities. Based on one of these configurations, Biddulph [1975] investigated the use of experimentally obtained point efficiencies as part of a multi-component distillation simulation. He found a number of required distillation stages that was close the number mentioned by Latimer.

Krishnamurty and Andrecovich [1989] made a numerical comparison between the use of an efficiency modified equilibrium stage model and a rate-based model for the

simulation of an argon-producing air distillation process using physical trays. They stated that the rate-based model yielded more-accurate results. However, they did not include a comparison of the simulation results with experimental data. Numerical results that can be related to the film thicknesses were neither reported.
Agrawal et al. [1993] presented experimental performance data for an air distillation column equipped with structured packing. Based on their measurements on a nitrogen–oxygen system, they developed empirical correlations for liquid and vapour mass transfer coefficients. Using these correlations, they were able to predict the separation performance for a nitrogen–oxygen mixture quite well. However, when applying them to an oxygen–argon mixture, the accuracy of the predictions was worse. Agrawal et al. were not able to identify a clear reason for this difference and concluded that more research is needed to explain the variation in performance.

Recently, Egoshi et al. published a series of articles [Egoshi et al., 1999, 2000, 2001, 2002, 1997] on the development of a simplified four-film transfer model for mixtures of nitrogen, argon, and oxygen based on experimental data.
In the first article [Egoshi et al., 1997], an empirical mass transfer coefficient correlation was developed based on experimental data for nitrogen–oxygen and argon–oxygen mixtures in a wetted-wall column. High vapour flow rates were used, resulting in turbulent vapour flow. The transfer process was assumed to be completely vapour-controlled and mass fraction differences were used to represent the driving forces. Both the diffusional fluxes and the total mass fluxes were found to depend linearly on these driving forces. It was observed that, in the absence of driving forces, the diffusional fluxes became zero, but the total mass fluxes did not.
The second article [Egoshi et al., 1999] extended the model from binary mixtures to ternary mixtures, based on experimental investigations of a nitrogen–argon–oxygen mixture in a wetted-wall column. The combination of an effective diffusion coefficient and the empirical correlation for binary mixtures was found to predict the separation efficiency of the ternary mixture satisfactory. It was concluded that the interaction between the diffusional fluxes was negligibly small for the distillation of air.
In the third article [Egoshi et al., 2000], binary experimental data was obtained for a structured packing column (instead of a wetted-wall column) and subsequently used to develop new empirical mass transfer coefficient correlations. A penetration model was included in the model, which was used to estimate the liquid interface composition based on the bulk liquid composition. It was observed that the total mass fluxes depended on the amount of thermal energy that was transferred through the wall of the column.
The last two articles [Egoshi et al., 2001, 2002] are very similar to each other. They compared simulations based on the correlations developed in the third paper [Egoshi et al., 2000] with experimental values obtained from pilot-scale air distillation columns. The used heat-transfer coefficients were based on the mass transfer coefficients, using an analogy between mass and thermal energy transfer. The reported experimental data consisted of a limited number of mole fraction measurements in the vapour phase, which did not cover the entire column for all components. Although the predictions sometimes differed by a factor of two from the measurements, it was concluded that

the predicted separation performance and concentration profiles showed good agreement with the observed data. No temperature measurements were reported.

The work presented in Chapters 7 and 8, in combination with the experiments described in Chapters 9 and 10, is a first effort to use the integrated-interface approach described in Section 3.3.2 for the simulation of air distillation column.

Chapter 4

Exergy analysis of two cryogenic air separation processes

L.V. van der Ham[1] and S. Kjelstrup[1,2]

1. Department of Chemistry
Norwegian University of Science and Technology
7491 Trondheim, Norway

2. Department of Process and Energy
Delft University of Technology
2628 CA Delft, The Netherlands

This chapter has been published in
Energy – The International Journal
Volume 35 (2010), pages 4731 - 4739

It is an extended version of a report written for the PhD-course
EP8110 – Exergy Analysis
NTNU, December 2009

Abstract

Two process designs of a cryogenic ASU (air separation unit) have been evaluated using exergy analysis. The ASU is part of an IGCC (integrated gasification combined cycle); it is supplying oxygen and nitrogen to the gasifier and nitrogen to the gas turbine. The two process designs separate the same feed into products with the same specifications. They differ in the number of distillation columns that are used; either two or three. Addition of the third column reduced the exergy destruction in the distillation section with 31%. Overall, the three-column design destroyed 12% less exergy than the two-column design. The rational exergy efficiency is defined as the desired exergy change divided by the total exergy change; it is 38% for the three-column design and 35% for the two-column design. Almost half of the exergy destruction is located in compressor after-coolers. Using this heat of compression elsewhere in the IGCC can be an important way to increase the IGCC efficiency. It is proposed to use it for the pre-heating of ASU products or for the production of steam, which can be used as part of the steam turbine cycle.

4.1 Introduction

The current work is part of a study that aims at improving the Second law efficiency of air distillation processes. Distillation of air is currently the most commonly used technique for production of pure oxygen and nitrogen on an industrial scale. An example of an industrial process that requires pure oxygen and nitrogen is an IGCC (integrated gasification combined cycle), where the oxygen is fed to a gasifier and the nitrogen to a gas turbine. Our study is part of an international collaboration project called DECARBit, which aims at developing an IGCC with pre-combustion CO_2 capture [Røkke and Langørgen, 2009]. We focus on a cryogenic air separation process within this context, and in particular on its distillation section.

4.1.1 Integrated gasification combined cycle

A schematic overview of the main process steps of a coal-based IGCC with pre-combustion CO_2 capture is given in Figure 4.1. The first step of an IGCC is the gasification of a hydrocarbon feedstock using pure oxygen. The coal is fed to the gasifier using pressurized nitrogen. Both the oxygen and nitrogen are produced in an ASU (air separation unit), which separates air into oxygen and nitrogen. The outlet stream of the gasifier consists mainly of hydrogen, carbon monoxide and steam, which are converted into a carbon dioxide and hydrogen mixture in the water–gas shift unit. The carbon dioxide is separated from the hydrogen in a subsequent separation unit, and prepared for storage. Next, the hydrogen is fed to a gas turbine, where it is burnt with air to produce electricity. A part of the air that leaves the compressor of the gas turbine can be fed to the ASU, which can return a part of its produced nitrogen to the burner of the gas turbine to be used as diluent. The outlet stream of the gas turbine consists mainly of steam and nitrogen. This hot flue gas is used in a steam turbine to produce more electricity and leaves the process afterwards.

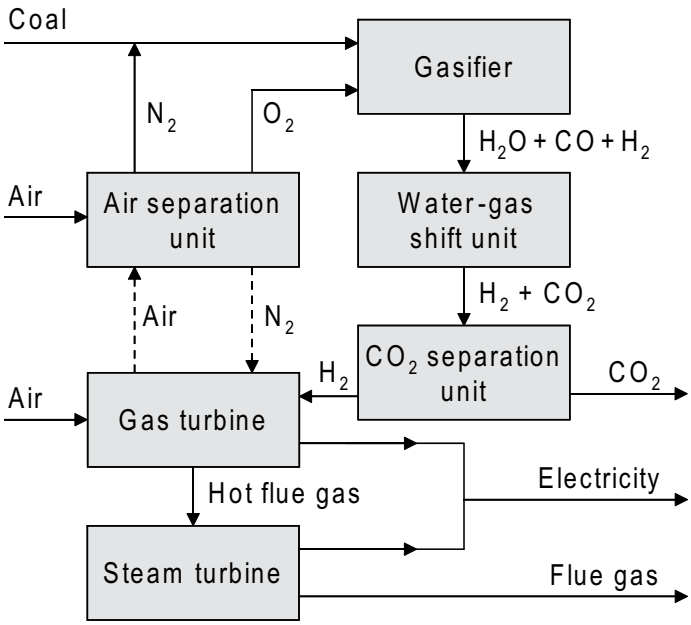

Figure 4.1: A schematic overview of a coal-based integrated gasification combined cycle (IGCC) with pre-combustion CO_2 capture.

4.1.2 Integrating the ASU and gas turbine

One of the advantages of an IGCC is the possibility to integrate the ASU and the gas turbine. The most important integration options are discussed in more detail by Smith and Klosek [2001]. The two most obvious options are to extract (a part) of the feed to the ASU from the gas turbine compressor, and to feed (a part) of the nitrogen that is produced in the ASU to the gas turbine. These options have already been realized in commercial processes and are indicated in Figure 4.1 using dotted lines. Another integration option is to warm the nitrogen that is fed to the gas turbine using the compressed air that is extracted from it. In this way, the heat of compression is used within the process instead of removed with cooling water.
The fraction of the feed air to the ASU that is extracted from the gas turbine compressor is often used to characterize the degree of air integration between the ASU and gas turbine. The fraction of the produced nitrogen that is fed to the gas turbine can in a similar way be used to characterize the nitrogen integration between the ASU and gas turbine. Frey and Zhu [2006] examined how different combinations of air and nitrogen integration affect the IGCC efficiency. They concluded that air integration only is the worst option, no integration at all is the second worst option, both air and nitrogen integration is the second best option, and nitrogen integration only is the best option. The difference between nitrogen only and both air and nitrogen was small and depended on the degrees of integration. Emun et al. [2010] also investi-

gated the effect of the degree of nitrogen integration on the efficiency of an IGCC and concluded that it should be as high as possible.

4.1.3 Cryogenic air separation

Separation of air can be achieved using various technologies, for example distillation, adsorption or membranes. When large volumes of high purity products are required, distillation at cryogenic conditions is the first choice [Smith and Klosek, 2001, Thorogood, 1991]. The first steps in a cryogenic ASU are to compress the feed air and remove water, carbon dioxide and other hydrocarbon contaminants from it. The resulting mixture consists of nitrogen, oxygen, argon and some traces of other noble gases. Next, the cleaned air is cooled to cryogenic conditions in the MHX (main heat exchanger) and subsequently fed to the distillation unit. The distillation unit separates the air into an oxygen stream and a nitrogen stream; sometimes an argon stream is produced as well. The product streams are passed again through the MHX and compressed or pumped to pressures that are required downstream of the ASU.
There exists a wide variety of process designs for the cryogenic separation of air. The main differences are related to the method used for providing refrigeration, to the method used for pressurizing the products, to the operating pressures, and to the column configuration in the distillation section. The type of process that is chosen depends usually on the feed and product specifications of the specific application.
In this work, we will assess two processes that are both designed to be part of an IGCC, but differ in their column configurations. For a process that is not producing any argon, the most common configuration contains two columns, see for example Raney and Thorogood [1997] and Kerry [2007]. Another type of configuration, that has not received much attention in the academic literature so far, contains three columns, see for example Higginbotham et al. [2001] and Shah [2003]. We will analyse and compare a two-column and a three-column design. In addition to the distillation section, the designs contain a feed pre-processing part, the MHX and a product post-processing part.

4.1.4 Exergy analysis of cryogenic air separation processes

The Second law or exergy efficiencies of various cryogenic ASUs have been investigated in the past. Agrawal and Woodward [1991] and Raney and Thorogood [1997] both looked at the effect that the addition of intermediate heat exchangers has on the exergy efficiency of a two-column ASU. Agrawal and Woodward assessed a process for the production of high purity nitrogen, focussing on the cryogenic part of the process. They investigated processes using either liquid air or liquid nitrogen as cold fluid in the additional heat exchanger. Raney and Thorogood considered a process for the production of low purity oxygen, and focused on the optimal positioning of a first and a second additional heat exchanger.
Cornelissen [1997] made a detailed exergy analysis of an air separation and liquefaction process. The process produced both gaseous and liquid nitrogen, oxygen and argon in a three-column configuration, where the third column was used for purification of

argon.
Yong et al. [2002] looked at a single column configuration used for the production of high purity nitrogen. They compared the efficiencies of the cryogenic part of the process when providing refrigeration either by expansion or by using liquid nitrogen. In addition, they compared the efficiencies of sieve trays and of structured packing, both by simulation and experiments.

4.1.5 Aim of the work

The aim of this work is to assess two designs of an ASU that is part of an IGCC using exergy analysis. The main difference between the two designs is the number of columns used in their distillation sections; either two or three. The assessment serves two main purposes. First of all, it will give more insight in typical efficiencies of current air separation processes, and in the location of their inefficiencies. Secondly, it will be used to compare the performances and properties of the two processes and in particular their distillation sections.
Previous exergy analysis of ASUs cover processes for several applications and with various product specifications. An ASU as part of an IGCC has not yet been analysed. A three-column design that is not producing any argon has not been analysed either.

4.2 Theoretical background on exergy analysis

The theory that is used in this work is based on the monograph by Kotas [1985]. Relevant relations are here shortly repeated for convenience.

4.2.1 Exergy contents of a stream of matter

In the current study, the kinetic and the potential exergy of streams of matter are assumed to be negligible. This means that the total molar exergy (ε_{tot}) is given by the sum of the physical molar exergy (ε_{ph}) and the chemical molar exergy (ε_0) only:

$$\varepsilon_{tot} = \varepsilon_{ph} + \varepsilon_0 \tag{4.1}$$

The physical molar exergy of a mixture can be calculated from the molar enthalpy (h) and molar entropy (s) of the mixture at the actual conditions, in combination with the molar enthalpy (h^0) and molar entropy (s^0) of the mixture at the environmental temperature ($T^0 = 298.15$ K) and pressure ($P^0 = 1$ atm):

$$\varepsilon_{ph} = \left(h_{T,P} - h_{T^0,P^0}\right) - T^0 \left(s_{T,P} - s_{T^0,P^0}\right) \tag{4.2}$$

The chemical molar exergy of an ideal gas mixture can be calculated from the standard chemical exergies of the components ($\varepsilon_{0,i}$) and their mole fractions (x_i):

$$\varepsilon_0 = \sum_i x_i \varepsilon_{0,i} + RT^0 \sum_i x_i \ln x_i \tag{4.3}$$

Here, R is the molar gas constant. The total exergy of a stream of matter (E_{tot}) can be calculated by multiplying its total molar exergy with its molar flow rate (F):

$$E_{tot} = F\varepsilon_{tot} \tag{4.4}$$

4.2.2 Standard chemical exergies

In this work we consider the streams of matter to consist of nitrogen, argon and oxygen only. In reality, other noble gases such as helium, krypton, neon and xenon are also part of the mixture. The standard chemical exergies of gaseous atmospheric reference substances listed by Kotas [1985] are calculated based on a mixture containing these noble gases. In order to use standard chemical exergies that are consistent with the considered substances, they have been recalculated for a hypothetical atmosphere that consists of nitrogen, argon, oxygen, carbon dioxide and water.
The partial pressure of water was set at the value that Kotas uses; it is assumed that this value captures both the vapour pressure that water has at the environmental temperature and the average relative humidity of air. The partial pressures (P_i^{00}) of the other four substances were calculated by distributing the difference between the environmental pressure and the partial pressure of water over them, while keeping the ratios in mole fractions constant at the values they have in dry air. The standard chemical exergies can subsequently be calculated using the formula provided by Kotas, assuming ideal gas behaviour:

$$\varepsilon_i^0 = -RT^0 \ln \frac{P_i^{00}}{P^0} \tag{4.5}$$

The resulting values are shown in Table 4.1; they show small deviations compared to the values from Kotas. The differences between the values are partly caused by the

Table 4.1: Comparison between the standard chemical exergies used in this work and the ones listed by Kotas [1985], in J/mol.

Substance	H_2O	CO_2	N_2	Ar	O_2
Current work	11766	20130	636	11609	3891
Kotas	11760	20170	720	11690	3970

fact that the partial pressures that Kotas uses do not sum up to the environmental pressure. The partial pressure for water that he uses indicates a low relative humidity. Since there are no chemical reactions occurring in the current process, these deviations will have no practical importance for the cases studied in this work.

4.2.3 Exergy efficiency definitions

Several exergy efficiencies exist. Two common ones are the simple and the rational exergy efficiencies. The simple exergy efficiency (η) is given by dividing the total

exergy output by the total exergy input:

$$\eta = \frac{E^{out}}{E^{in}} \tag{4.6}$$

The rational exergy efficiency (ψ) of a process or process unit can be calculated by dividing the desired exergy change by the total used exergy.

$$\psi = \frac{\Delta E^{desired}}{\Delta E^{used}} \tag{4.7}$$

It depends on the process or process unit that is considered what exactly the desired exergy change and total used exergy are. Agrawal and Woodward [1991] suggested that a similar criterion can also be used to characterize the efficiency of a part of a distillation column. The rational efficiency is closely related to the exergy efficiency without transiting exergy.

4.3 Two ASU flow sheets

The two ASU designs that are analysed in this work are designed as part of an IGCC. Integration between the ASU and the gas turbine of the IGCC is limited to nitrogen only, in this respect we follow Frey and Zhu [2006]. The ASU product specifications that we use are the same for both designs. They are determined by the the gasifier and gas turbine operating conditions and are listed in Table 4.2. Oxygen (O_2) and

Table 4.2: Product specifications

O_2 mole fraction	95.0	%
O_2 pressure	48.0	bar
HP N_2 mole fraction	99.9	%
HP N_2 pressure	88.0	bar
MP N_2 mole fraction	99.0	%
MP N_2 pressure	25.0	bar
O_2-to-HP N_2 flow ratio	3.20	-

high pressure nitrogen (HP N_2) are used in the gasification step of the IGCC. They are pressurized using a pumped liquid cycle. Medium pressure nitrogen (MP N_2) is fed to the gas turbine. All products are gaseous and no argon is produced. Because the air pre-purification step is the same for both designs, it is not included in the current comparison. The feed stream that both designs use is therefore assumed to be a mixture of nitrogen, argon and oxygen at an elevated pressure.

4.3.1 Two-column design

Figure 4.2 shows the flow sheet of the ASU that is using two distillation columns. The most important process units in the flow sheet are the MHX, the high-pressure

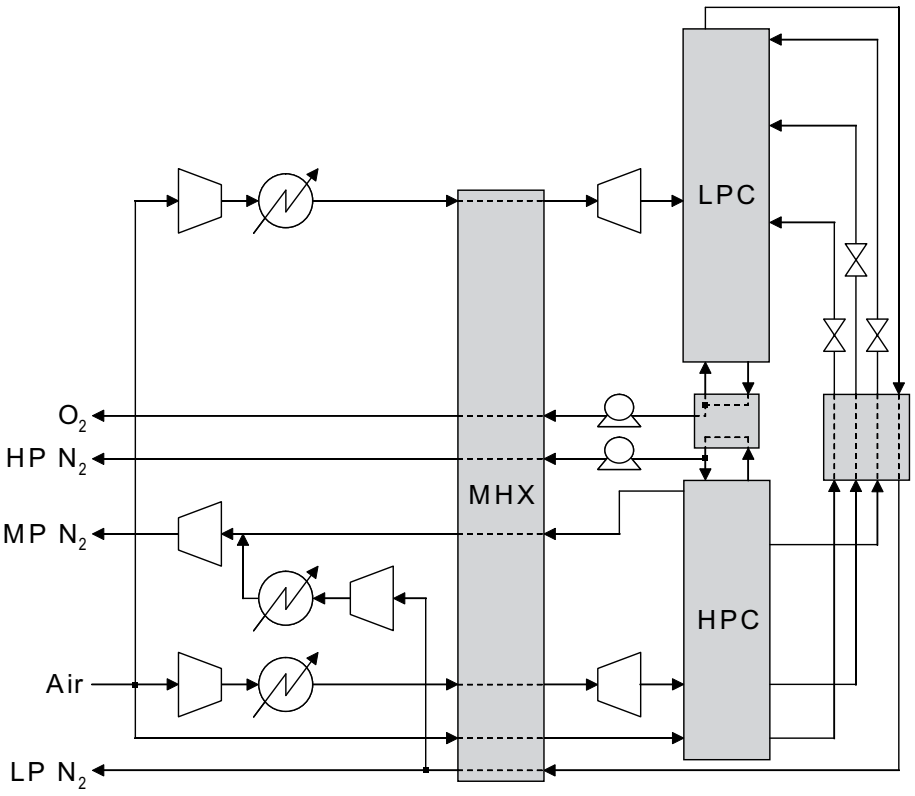

Figure 4.2: A schematic process flow sheet of the two-column ASU design.

column (HPC, 4.8 bar and 50 stages) and the low-pressure column (LPC, 1.3 bar and 55 stages). The two columns are thermally coupled by a heat exchanger, which is functioning as reboiler for the low-pressure column and as condenser for the high-pressure column.
Cleaned and pressurized air enters the process and is split into three streams. The first stream is compressed, cooled to an ambient temperature, subsequently cooled and liquefied in the MHX, expanded, and finally fed to the high-pressure column. The second stream is directly cooled to a cryogenic temperature and is also fed to the high-pressure column. The third and relatively smallest stream is compressed, cooled, expanded and fed to the low-pressure column.
The high-pressure column has five outlet streams. Three of them are inputs to the low-pressure column. They are first cooled and throttled before they enter the second column. The other two outlets are nitrogen product streams. The liquid stream is first pumped to a higher pressure, than vaporised and heated in the MHX and finally delivered as HP N_2 (high pressure nitrogen) product. The vapour stream is heated in the MHX, compressed and delivered as MP N_2 (medium pressure nitrogen) product.
The low-pressure column has two outlets. The top product is first used to cool the three streams coming from the high-pressure column. Subsequently it passes through the MHX. Depending on the amount of required medium pressure nitrogen, a part of it is mixed with the gaseous nitrogen product from the high-pressure column. It is first compressed and cooled before the two streams are combined. The other part leaves the process as LP N_2 (low pressure nitrogen) by-product with a pressure slightly above the environmental pressure. The liquid bottom product is pumped to a higher pressure, vaporised and heated in the main heat exchanger, and finally delivered as oxygen product (O_2).

4.3.2 Three-column design

Figure 4.3 shows the flow sheet of the ASU that is using three distillation columns. This three-column design is very similar to the two-column design. The main difference is the addition of the third distillation column, which operates at a pressure in between the high and low-pressure columns (MPC (medium-pressure column), 2.8 bar and 40 stages). The bottom of the MPC is thermally coupled to top of the high-pressure column, similar to the low-pressure column.
The condenser at the top of the MPC uses its throttled bottom product as cooling fluid. The MPC receives it feed from the bottom of the high-pressure column and delivers its products to the low-pressure column. Its top product is first cooled and throttled before it enters the low-pressure column.

4.3.3 Flow sheet simulations

Both flow sheets have been simulated with the process simulator HYSYS, using the Peng–Robinsons equation of state, modified by Stryjek and Vera and using Lee–Kessler vapour pressures (PRSV-LK). The three-column design was simulated first. The amount of medium pressure nitrogen that was produced by this design was sub-

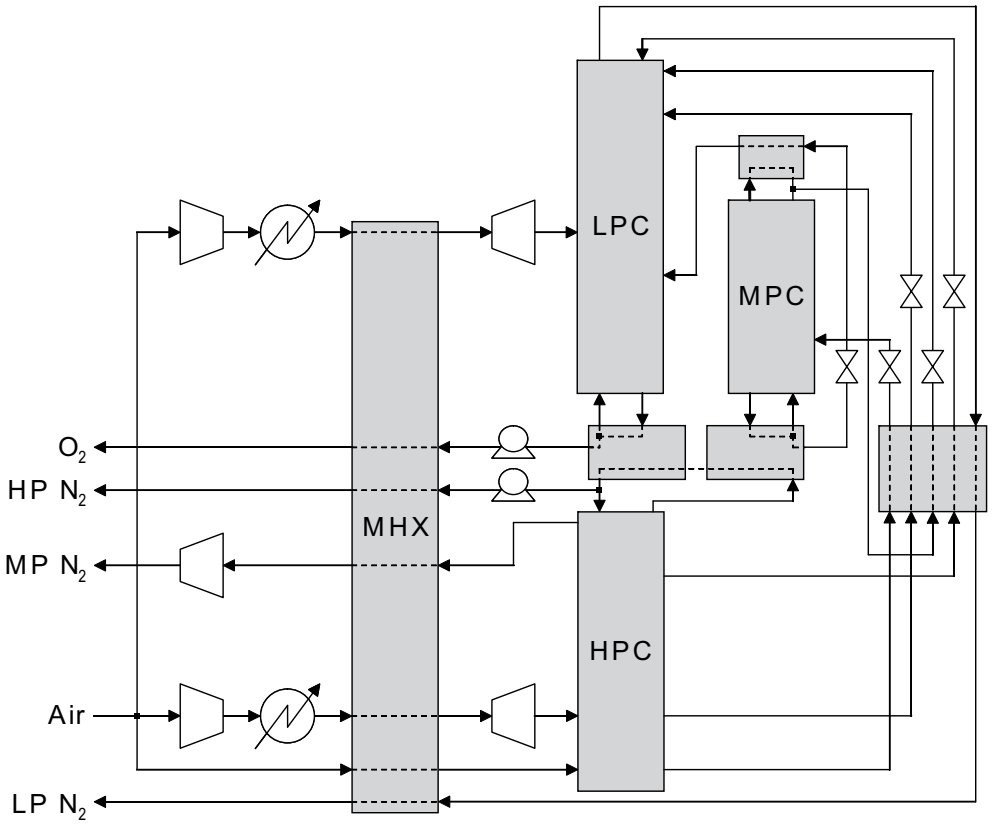

Figure 4.3: A schematic process flow sheet of the three-column ASU design.

sequently used as target for the two-column design.
During the simulation of the three-column design, the product pressures were fixed at their specification values. The feed flow rate, the oxygen purity and the flow rate of HP N_2 were fixed too. The oxygen fraction of the two top streams entering the low-pressure column was fixed at 0.012 and a minimum approach temperature of 2.5 K was used for the sub-cooler. The flow rate of air entering the low-pressure column was fixed at 1.5% of the total feed flow rate. Losses of low temperature thermal energy to the environment were included for all columns and heat exchangers. The pumps are modelled with efficiency of 50%, the compressors with an efficiency of 87%, the liquid expander before the high-pressure column with an efficiency of 75%, and the booster compressor and expander with efficiencies of 80% and 87%. All efficiencies are adiabatic efficiencies. These efficiencies are used for both designs and affect them in a similar manner. The exact values have therefore little influence on the comparison between the two designs.
Three flow rates were varied in order to find the most efficient design, while taking into account the specified oxygen flow rate and a minimum approach temperature in the MHX of 2.0 K: the flow rate of the compressed and expanded air entering the high-pressure column, the flow rate of the gaseous product leaving the high-pressure column, and the flow rate of the stream from the high to the low-pressure column with the lowest nitrogen fraction. The purities of the MP and HP N_2 products proved to be above their specified minima for all studied cases.
The two-column design was simulated using the same specifications and variables as the three-column design. One exception is the oxygen fraction of the top streams entering the low-pressure column, which was fixed at 0.02. The flow rate of the MP N_2 was additionally required to match the flow rate obtained in the three-column model. This was achieved by compressing a part of the nitrogen leaving the low-pressure column and mixing it with the gaseous nitrogen product from the high-pressure column. Before mixing, the compressed nitrogen is first cooled to match the temperature of the nitrogen coming from the high-pressure column.

4.4 Exergy calculations

The exergy calculations have been done based on the HYSYS simulations of the two process designs. All process stream properties required for the exergy analysis were extracted from HYSYS simulations and imported into Excel, which was used to perform the actual analysis.

4.4.1 Extracting process data

The magnitudes of all the energy streams could be extracted directly from HYSYS. The energy that is added to the compressors and pumps, and extracted from the expanders has the form of work, which is equivalent to exergy. Thermal energy is leaving the process in the coolers, which use cooling water. It is assumed that this cooling water is taken from and returned to a large reservoir at ambient temperature. Thermal energy is added to the heat exchangers and columns to represent losses from

the environment. Because all the thermal energy streams enter or leave at the environmental temperature, their exergy contents is zero.
The properties of the streams of matter that were extracted from the HYSYS simulation are the molar flow rate, the composition (nitrogen, argon and oxygen mole fractions), the temperature, the pressure, the molar enthalpy and the molar entropy. For all the compositions in the process, reference molar enthalpies and entropies were calculated by creating new process streams with the same compositions but at the environmental temperature and pressure. Using these quantities it is possible to calculate the exergy contents of the streams, as explained in Section 4.2.

4.4.2 Checking data consistency

After importing all process data in Excel, the first step was to check their consistency. This has been done by calculating mole, component and energy balances, both over the total process and over each of the process units separately. The mole and component balances proved to be completely consistent. The energy balances showed some minor inconsistencies in the order of magnitude of the simulation accuracy; they were below 0.001% of the net work input.

4.4.3 Calculating exergy destruction

After calculating mole, component and energy balances over all process units, the next step was to set up their exergy balances and calculate the destroyed exergy in each of them. An exergy balance over the total process was also used to check the consistency of the calculations. The total amount of destroyed exergy should be equal to net work input minus the increase in exergy contents of the streams of matter. This was indeed true. The destroyed exergy should also be positive in all process units, which was the case.

4.5 Results

In order to facilitate a direct and quantitative comparison between the two designs, we have chosen to present all results using tables rather than graphs. We have also decided to focus more on the localization and distribution of the total exergy destruction, rather than on the total exergy streams in the process. This is related to the relatively large amount of 'exergy in transit' in the processes, as is discussed in more detail in Section 4.5.3. This large amount of exergy in transit, in combination with the process structure, is also the reason why we have omitted Grassmann diagrams; they present the results in an overcomplicated way for the processes that are studied in this work.

4.5.1 Two-column design

Table 4.3 gives an overview of the composition, pressure, and temperature of all feed and products streams. By comparing with Table 4.2 it can be verified that all product

Table 4.3: Feed and product properties of the two-column design. The molar flow rates are given as fraction of the feed flow rate.

Stream		Air	O_2	HP N_2	MP N_2	LP N_2
F	-	1	0.212	0.066	0.262	0.459
x_{N_2}	-	0.781	0.017	1.000	0.991	0.982
x_{O_2}	-	0.009	0.950	0.000	0.002	0.004
x_{Ar}	-	0.210	0.033	0.000	0.007	0.014
P	bar	5.07	48.0	88.0	25.0	1.15
T	K	293	295	295	500	295

specifications have been met.
The total exergy destruction amounts to 4.76 kJ/mol air. Table 4.4 shows how much of the total exergy destruction is destroyed in which part of the process. The process is subdivided into four separate parts; feed pre-processing, the MHX, the distillation section, and product post-processing. The first column of numbers gives the contributions of the process units and the last column gives the contributions of the four process parts. All process parts are responsible for a considerable part of the total

Table 4.4: Break-down of the total exergy destruction over the different process parts and process units of the two-column design.

Feed pre-processing		47.1%
Compressors	6.3%	
Coolers	38.7%	
Expanders	2.1%	
Main heat exchanger		16.7%
Distillation section		26.5%
HP column	5.7%	
LP column	14.1%	
Heat exchangers	4.4%	
Throttle valves	2.2%	
Product post-processing		9.8%
Pumps	3.3%	
Compressors	3.8%	
Cooler	2.5%	
Mixer	0.1%	
Total exergy destruction		100.0%

exergy destruction. The feed pre-processing part, representing compression, cooling and expansion of the air feed, has the biggest contribution; almost half of the total exergy destruction is located in this process part. The distillation section accounts for about one-quarter of the total, the MHX destroys one-sixth, and around 10% of the total exergy destruction is located in the product post-processing part.

Within the feed pre-processing section, the coolers destroy by far the most exergy; almost 40% of the total exergy destruction. This exergy destruction is mainly caused by the use of water as cooling fluid. The thermal energy that is transferred to the cooling water becomes useless, which means that its exergy is reduced to zero. Within the distillation section, the two columns are destroying most of the exergy; about 20% of the total exergy destruction. The heat exchangers in the process, including the reboiler/condenser, destroy 20 %, and the compressors destroy about 10% of the total. The expanders, throttle valves, pumps, and mixer have relatively small contributions.

4.5.2 Three-column design

Table 4.5 gives an overview of the composition, pressure, and temperature of all feed and products streams. The total exergy destruction amounts to 4.12 kJ/mol air.

Table 4.5: Feed and product properties of the three-column design. The molar flow rates are given as fraction of the feed flow rate.

Stream		Air	O_2	HP N_2	MP N_2	LP N_2
F	-	1	0.212	0.066	0.262	0.459
x_{N_2}	-	0.781	0.022	0.999	0.999	0.975
x_{O_2}	-	0.009	0.950	0.000	0.000	0.018
x_{Ar}	-	0.210	0.028	0.001	0.001	0.007
P	bar	5.03	48.0	88.0	25.0	1.15
T	K	293	295	295	502	295

Table 4.6 shows again how much of the total exergy destruction is destroyed in which part of the process. The feed pre-processing part has again the biggest contribution; over half of the total exergy destruction is located in this process part. The distillation section and the MHX both account for about one-fifth of the total, and around 7% of the total exergy destruction is located in the product post-processing part.
Within the feed pre-processing section, the coolers destroy again by far the most exergy; almost 45% of the total exergy destruction. Within the distillation section, the three columns are destroying most of the exergy; around 13% of the total exergy destruction. The heat exchangers destroy 25 %, and the compressors destroy about 10% of the total. The expanders, throttle valves, and pumps have relatively small contributions.

4.5.3 Comparison between the two designs

By comparing Tables 4.3 and 4.5, it can be seen that the two process designs deliver practically the same products. There are some minor differences in the product compositions, in the feed pressure, and in the temperature of the medium pressure nitrogen. The effect of these differences on the exergy contents of these streams is very small however, as will be shown below.

Table 4.6: Break-down of the total exergy destruction over the different process parts and process units of the three-column design.

Feed pre-processing		54.1%
Compressors	7.2%	
Coolers	44.5%	
Expanders	2.4%	
Main heat exchanger		18.3%
Distillation section		20.8%
HP column	5.9%	
MP column	0.7%	
LP column	6.1%	
Heat exchangers	6.5%	
Throttle valves	1.6%	
Product post-processing		6.8%
Pumps	3.7%	
Compressors	3.1%	
Total exergy destruction		100.0%

Distribution of the exergy destruction

Table 4.7 gives an overview of the differences in exergy destruction localization between the two- and three-column designs. In order to make a proper comparison between the two designs, the exergy destruction contributions are given per amount of feed air instead of percentage of the total destruction. When comparing the contributions of the four process parts, we see that the feed pre-processing and MHX perform comparable. The main differences are located in the distillation section and the product post-processing part; they represent 68% and 32% of the total difference in exergy destruction.

Within the distillation section, the addition of the MPC reduces the exergy destruction in the low-pressure column with more than 60%. The exergy destruction in the MPC itself is small, but the condenser and reboiler of the column also cause an increase in the exergy destruction of the heat exchangers. Because more product is recovered from the high-pressure column in the three-column design, less throttling is required. This causes less exergy destruction in the throttle valves.

The recovery of more product from the high-pressure column is also the main reason for less exergy destruction in the post-processing part of the three-column design. In the two-column design, the lower quantity of product from the high-pressure column has to be compensated for by compressing some low pressure product. The additional compression, and the cooling that is related to it, causes an increase in the exergy destruction. This increase represents about one-third of the total difference in exergy destruction. So even if we would not compress the low pressure product, and thus allow a lower MP N_2 production rate, the two-column design would still perform worse than the three-column design.

Table 4.7: Comparison between the exergy destruction per amount of feed (kJ/mol) of the two- and three-column designs.

Process design	2-column		3-column	
Feed pre-processing		2.20		2.23
Compressors	0.29		0.30	
Coolers	1.81		1.83	
Expanders	0.10		0.10	
Main heat exchanger		0.78		0.75
Distillation section		1.24		0.86
HP column	0.27		0.24	
MP column	–		0.03	
LP column	0.66		0.25	
Heat exchangers	0.21		0.27	
Throttle valves	0.10		0.07	
Product post-processing		0.46		0.28
Pumps	0.15		0.15	
Compressors	0.18		0.13	
Cooler	0.12		–	
Mixer	0.00		–	
Total exergy destruction		4.67		4.12

Total exergy inputs and outputs

Overall, the three-column design destroys 12% less exergy than the two-column design. Table 4.8 shows how the amounts of exergy destruction are related to the total exergy inputs and outputs of the two designs. A first observation is that the exergy in the feed and products is practically the same for both designs. Another interesting thing to look at is the distribution of those exergies over their physical and chemical components. In the feed, only 0.6% of the exergy is chemical exergy. This is logical because the composition of the feed is almost equal to the environmental composition. In the products, the chemical exergy amounts to 18%. The amount of added chemical exergy corresponds to approximately 16% of the net work input. Because the total standard chemical exergy is equal in the feed and the products, this increase is only caused by an increase in the chemical exergy of mixing. An increasing exergy of mixing means that the products are less mixed than the feed, which is the primary aim of separation processes like distillation.

Exergy efficiencies

At the bottom of Table 4.8, the simple and rational exergy efficiencies of the two designs are given. The simple exergy efficiency relates the exergy destruction to the total exergy input, including the exergy in the feed. Because a part of the exergy in

Table 4.8: Comparison between the exergy inputs and outputs per amount of feed (kJ/mol) of the two- and three-column designs.

Process design	2-column	3-column
Physical exergy in feed	3.99	3.97
Chemical exergy in feed	0.02	0.02
Work input	7.26	6.73
Physical exergy in products	5.35	5.35
Chemical exergy in products	1.15	1.14
Work output	0.10	0.10
Destroyed exergy	4.67	4.12
Simple exergy efficiency	58.6 %	61.5 %
Rational exergy efficiency	34.7 %	37.8 %

the feed simply passes through the process, this can be argued to give a false picture. In a process with a very large exergy in transit, the exergy destruction will always be small compared to the total exergy input. A similar thing can be said about the work terms; when the total work input is used as exergy input and the total work output as exergy output, a large amount of work in transit will give a false picture. In order to avoid potentially misleading numbers, the exergy destruction can be related to the net work input instead of the total exergy input. If we consider the changes in both physical and chemical exergy of all products to be desirable, this is equal to the rational exergy efficiency.
The simple efficiencies of both designs are about 60%, while the rational ones are about 35%. This clearly shows that there is a big difference between the two types of efficiencies. When comparing the two designs, both efficiencies suggest that the three-column design performs approximately 3% better than the two-column design. In case of the simple efficiency this means a 5% improvement, but when using the rational efficiency it corresponds to an improvement of 9%. Based on the amount of destroyed exergy, the three-column design performs 12% better. When looking purely at the required net work inputs, which can be used as measure for the energy efficiency, the three-column design is 7% more efficient. The additional work that is required in the two-column design is mainly used for compressing a part of the low pressure product.

4.6 Discussion

4.6.1 Comparison with results from other works

Although the details of the previously studied air separation processes that are discussed in Section 4.1.4 are quite different from the ones studies in this work, it can still be interesting to compare some general characteristics.

Agrawal and Woodward

Agrawal and Woodward [1991] analysed a process that shows similarities with the two-column design that is discussed in this work. They did not include any feed pre-processing or product post-processing steps in their analysis. In the process they analysed, the major part of the exergy destruction was located in the MHX, the low-pressure column and the integrated reboiler/condenser. The total exergy destruction per amount of produced nitrogen was about 2.2 kJ/mol. Using a nitrogen recovery of 90%, this corresponds to an exergy destruction of approximately 1.6 kJ/mol air. This is very close to the sum of the exergy destruction in the MHX and distillation section of the three-column design.
More than half of the exergy destruction in the MHX was related to pressure drop. Within the low-pressure column, especially the bottom part was inefficient. By adding an intermediate heat exchanger in the bottom part of the low-pressure column, Agrawal and Woodward were able to reduce the exergy destruction in the process with about 9%. This increased the efficiency of the process from 36% to 38%. These improvements are comparable to the performance difference between the two- and three-column designs.

Raney and Thorogood

Raney and Thorogood [1997] used the decrease in exergy destruction caused by adding intermediate heat exchangers as guideline to optimize their locations within the bottom of the low-pressure column. They concluded that the work input per amount of oxygen product can be decreased with 5% or 10% when adding one or two intermediate heat exchangers. This corresponds to a decrease in the work input from 7.09 to 6.28 or 6.20 kJ/mol air. These improvements are also in the same order as the performance difference between the two- and three-column designs.

Cornelissen

The analysis of a cryogenic air separation and liquefaction process performed by Cornelissen [1997] yielded a rational efficiency for the total process of 28%. The exergy destruction was 15.57 kJ/mol air, which is much higher than in the processes studied in this work. The difference is mostly related to the fact that Cornelissen analysed a different type of process; it included the feed pre-purification step and the turbines that are driving the compressors, and it was producing liquid products and argon as well. The exergy destruction in the MHX and distillation section were 0.59 and 1.39 kJ/mol, yielding a rational efficiency of 41%. These values are much closer to the values found in this work. Within the distillation section, the combination of the low pressure and argon columns destroyed most of the exergy.

Yong, Moon and Yi

The process analysed by Yong et al. [2002] produced nitrogen with a relatively low recovery of 55%. The total exergy destruction in the MHX and distillation section of their base case amounts to 2.03 kJ/mol air. This is again comparable to the values found in this work. Most of the losses are located in the MHX however, followed by the distillation column. Yong et al. also mention the pressure drop as one of the main causes for exergy destruction in the MHX. The work input is 7.44 kJ/mol air. Their case that is using liquid nitrogen as refrigeration source is hard to evaluate, because they did not include the liquid nitrogen and its exergy contents in their analysis.

Common findings

Based on the results of the current work and the other works discussed in this section, some common findings can be identified. The rational exergy efficiency of cryogenic air separation processes is typically in the order of 35-40%. The exergy destruction in the MHX and distillation section together is about 1.6-2.0 kJ/mol air. The required work input for a process with gaseous products is in the range of 6.0-7.5 kJ/mol air. In addition to being destroyed within the process, a part of this work is added to its products and waste streams. These numbers are rough estimates, the exact values depend to a large extent on the details of a specific process and do not necessarily have to be within the indicated ranges.
Within the cold part of the process, the main exergy destroying pieces of equipment are the MHX and the distillation columns. An important part of the exergy destruction in the MHX is related to its pressure drop. Within the distillation section of a two-column configuration, a large part of the exergy destruction occurs in the bottom part of the low-pressure column. This inefficiency can be reduced by adding intermediate heat exchangers in the low-pressure column, or by adding the third column to the process. These changes can have a significant effect on the required work input of the process.

4.6.2 Improving distillation efficiency

Conventional distillation columns use a single reboiler at their bottom and a single condenser at their top, concentrating the thermal energy transfer at two single points in the column. It is discussed by Nakaiwa and Ohmori [2009] that the theoretically optimal way of operating a distillation column involves thermal energy transfer along its entire length. So attempts to improve the efficiency of a distillation column should focus on providing more thermal energy transfer points along the length of the column.
One example of this approach is the addition of intermediate heat exchangers, as studied by Agrawal and Woodward [1991] and Raney and Thorogood [1997]. Another good example, explained in detail by Nakaiwa and Ohmori, is a heat-integrated

distillation column (HIDiC). A HIDiC can be regarded as conventional column that is split into two parts at a certain point along its length. By position one part inside the other part and by operating them at different pressures, thermal energy can be transferred from the high pressure part to the low pressure part along the entire length of the integrated column. Applying this type of heat integration to (a part of) an air distillation section could be an interesting option to further improve its efficiency.

4.6.3 Evaluating distillation section efficiency

The evaluation of the distillation section efficiency shows why using an exergy-based criterion can be better than using the conventional energy efficiency. The energy efficiency is based on amounts of added and removed energy. When looking at the distillation sections shown in Figures 4.2 and 4.3, we see that there is no energy added or removed within this process part, except for losses to the environment. Using the energy efficiency to characterize the distillation section performance is therefore completely meaningless. The desired separation of air into nitrogen and oxygen is paid for by a decrease in the pressure of the process streams. The efficiency of this conversion can easily be evaluated using exergy efficiencies.

4.6.4 Integration with the gas turbine

As discussed in Section 4.1.2, it can be advantageous to integrate the ASU and gas turbine of an IGCC as much as possible with respect to nitrogen. The process designs discussed in this work deliver 8% of the nitrogen products at high pressure, 33% at medium pressure and 58% at low pressure. Only the MP N_2 product is fed to the gas turbine. If more MP N_2 is required, a part of the low pressure product can be upgraded to a medium pressure, as is already done to some extent in the two-column design. The exergy losses that are related to this additional compression are the same for both process designs.
The ASU and gas turbine can also be integrated with respect to air. In the current process designs, a part of the air feed is further compressed. This stream is especially suitable to be replaced by air that is extracted from the gas turbine compressor. In the current designs, its flow rate amounts to about 42% of the total air feed. The degree of air integration affects the two designs in a similar manner.

4.6.5 Making use of the heat of compression

A large part of the exergy destruction is caused by the use of cooling water to remove heat of compression from compressed process streams. Smith and Klosek [2001] already suggested to use the heat of compression in a better way. As possible uses, they mentioned the regeneration steps of adsorption or solvent based processes elsewhere in the IGCC, or the production and heating of steam for the humidification of the nitrogen stream to the gas turbine.
Emun et al. [2010] suggested to pre-heat the oxygen that is fed to the gasifier with a stream from the CO_2 separation unit. The heat of compression from an ASU could

also be used for this purpose, and the nitrogen that is fed to the gasifier could be pre-heated as well. The effect of pre-heating these streams would be to lower the amount of hydrocarbon feed that normally would be oxidized to heat them within the gasifier. This can lower both the hydrocarbon consumption and the oxygen demand. The maximum temperature of the feed air after adiabatic compression is about 410 °C. Because this is higher than the temperature of the MP N_2 product, it can also partially be used to further increase the temperature of this stream. In the case of the two-column design, the after-cooler that is used when upgrading a part of the low pressure product to a medium pressure product can simply be removed.
Another option to use the heat of compression in a better way could be to generate or upgrade steam. This steam can be used in the steam turbine cycle of the IGCC, increasing the electricity output of the process.

4.7 Conclusions

A two- and a three-column design of a cryogenic ASU have been evaluated using exergy analysis. Both designs were separating the same feed into products with the same specifications. The three-column design performed better than the two-column design; their exergy destructions amounted to 4.12 and 4.67 kJ/mol air. This means that the three-column design destroyed 12% less exergy, which was coupled to a 7% lower net work input requirement. The rational exergy efficiencies of the two designs are 35% and 38%.
Almost half of the exergy destruction was caused by the compressor after-coolers, which are using water as cooling fluid. The distillation sections and the MHXs also have considerable contributions. The exergy destruction within the cold section of a cryogenic ASU is typically around 1.6-2.0 kJ/mol air. The product post-processing part accounted for a relatively small part of the total exergy destruction.
Making better use of the heat of compression can be an important step towards a higher efficiency of the IGCC. Possible uses are to pre-heat the ASU products before they are fed to the gasifier or gas turbine, or to create steam that can be used to humidify the nitrogen stream that is fed to the gas turbine or as part of the steam turbine cycle.
The distillation section of the three-column design destroyed 31% less exergy than the distillation section of the two-column design. This is the result of adding the third column. Other works showed that the efficiency of the distillation section can also be improved by adding intermediate heat exchangers in the bottom of the low-pressure column. Using the HIDiC-concept in (a part of) the distillation section can be another important way to improve its efficiency. Evaluating the performance of the distillation section requires an exergy based criterion. It is impossible to use the energy efficiency for this purpose.

Nomenclature

ASU	air separation unit
E_{tot}	total exergy flow, J/s

F	molar flow rate, mol/s
h	molar enthalpy, J/mol
HIDiC	heat-integrated distillation column
HP	high pressure
IGCC	integrated gasification combined cycle
LP	low pressure
MHX	main heat exchanger
MP	medium pressure
P	pressure, bar
R	universal gas constant, 8.3145 J/(K mol)
s	molar entropy, J/(K mol)
T	temperature, K
x	mole fraction, dimensionless

Greek symbols

ε_0	chemical molar exergy, J/mol
ε_{ph}	physical molar exergy, J/mol
ε_{tot}	total molar exergy, J/mol
η	simple exergy efficiency, dimensionless
ψ	rational exergy efficiency, dimensionless

Sub- and superscripts

0	ambient or reference conditions
i	component index

Acknowledgements

The research leading to these results has received funding from the European Community's 7th Framework Programme (FP7/2007-2013) under grant agreement number 211971 (The DECARBit project).

Chapter 5

Improving the heat integration of distillation columns in a cryogenic air separation unit

L.V. van der Ham[1] and S. Kjelstrup[1,2]

1. Department of Chemistry
Norwegian University of Science and Technology
7491 Trondheim, Norway

2. Department of Process and Energy
Delft University of Technology
2628 CA Delft, The Netherlands

This chapter has been published in
Industrial & Engineering Chemistry Research
Volume 50 (2011), pages 9324 - 9338

Parts of this chapter have been published in
Proceedings of ECOS 2011, Novi Sad, Serbia
and
Proceedings of ICR 2011, Prague, Czech Republic

Is not included due to copyright

Chapter 6

Improving the exergy efficiency of a cryogenic air separation unit as part of an integrated gasification combined cycle

L.V. van der Ham

Department of Chemistry
Norwegian University of Science and Technology
7491 Trondheim, Norway

This chapter has been submitted to
Energy Conversion and Management

Abstract

The efficiency of a two-column cryogenic ASU (air separation unit) that is part of an IGCC (integrated gasification combined cycle) can be increased significantly by making better use of the heat of compression and by improving the heat integration of the distillation columns. The rational exergy efficiency of the ASU, which is defined as the desired increase in exergy content of the products divided by the amount of work that is added to the process, can be increased from 35% to over 70%. The exergy destruction per amount of feed is reduced with 1.6 kJ/mol air, corresponding to a 0.74% increase in the net electric efficiency of the IGCC. The efficiencies are expected to increase further because the full potential of using heat-integrated distillation columns is not yet achieved.

6.1 Introduction

DECARBit is a European collaboration project whose main aim is to develop a coal-based IGCC (integrated gasification combined cycle) with pre-combustion CO_2 capture [Røkke and Langørgen, 2009]. Figure 6.1 shows a schematic overview of the main process units in such an IGCC.

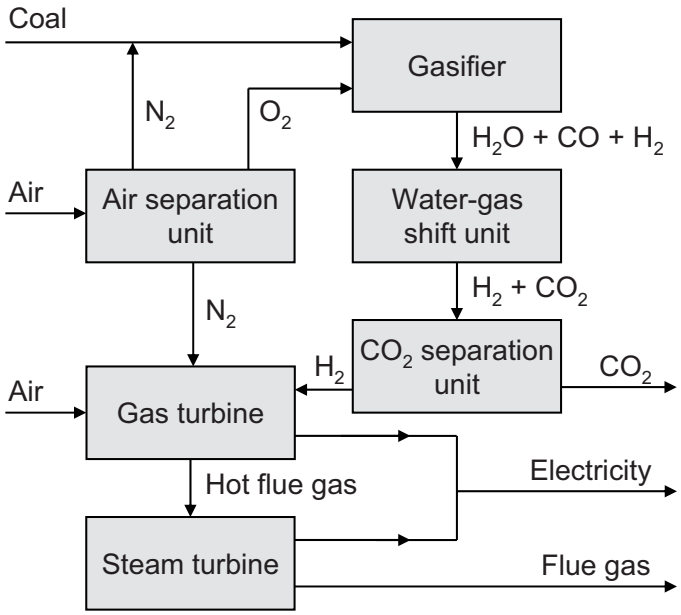

Figure 6.1: A schematic overview of a coal-based IGCC (integrated gasification combined cycle) with pre-combustion CO_2 capture.

Pulverized and dried coal is transported to the gasifier using high pressure nitrogen. In the gasifier, the coal is partly oxidized using a purified oxygen stream. The oxidation

is completed in the water-gas shift reactors, which convert carbon monoxide and water into carbon dioxide and hydrogen. The carbon dioxide is subsequently separated from the hydrogen and transported away for storage. The hydrogen is diluted with nitrogen and burnt with compressed air to generate electricity in the gas and steam turbines.

6.1.1 Air separation units

An IGCC uses both purified oxygen and nitrogen, which are usually obtained by separating air. Within the DECARBit project, three different air separation technologies are investigated: high-temperature ceramic membranes, pressure-swing or temperature-swing adsorption, and cryogenic distillation. The current work is part of an effort to improve the Second law (or exergy) efficiency of cryogenic air separation processes.
A cryogenic ASU (air separation unit) typically consists of four main process sections: a feed compression and purification section, a main heat exchanger, a distillation section, and a product compression and pumping section, see for example Thorogood [1991] and Smith and Klosek [2001] for more details.

6.1.2 Improving the efficiency of a cryogenic ASU

In a previous work [Van der Ham and Kjelstrup, 2010], we used exergy analysis to evaluate two low pressure pumped liquid cycle ASUs that were designed as part of an IGCC. The two processes delivered the same products, but differed in the number of distillation columns that were used: either two or three. A two-column design is commonly used when no argon product is required.
The study showed amongst others that the compressor after-coolers, the distillation columns, and the main heat exchanger are responsible for most of the exergy destruction in both processes. Exergy is the potential to do work, so the destruction or loss of exergy can be regarded as a loss in work potential. Two strategies were suggested in order to try and decrease the exergy destruction: making better use of the heat of compression, and improving the distillation section efficiency by applying the type of heat integration used in a HIDiC (heat-integrated distillation column). The first strategy involves changes in the process flow sheet, while the second focuses on altering a single process unit.

Making use of the heat of compression

The ASU designs studied by Van der Ham and Kjelstrup [2010] use cooling water to remove thermal energy from compressed process streams. This reduces the temperature of the thermal energy from over 400 °C to the ambient temperature, rendering the thermal energy useless. This degradation of the thermal energy quality is equivalent to the destruction of exergy.
In the current process, the nitrogen and oxygen streams enter the gasifier at approximately ambient temperatures. The nitrogen stream that is fed to the gas turbine

has a temperature of about 200 °C. Both the gasifier and the gas turbine operate at temperatures above 1000 °C. So it might be possible to use the heat of compression more efficiently by using it to heat the ASU products in an additional heat exchanger. Several patents have been filed that pursue this approach, see for example Shah et al. [2001], Briesch et al. [2007] and Günster et al. [2010]. However, no detailed studies of this alternative are currently available in the academic literature. In the current work, we assess what effect the addition of this heat exchanger has on the product temperatures, and how these temperature changes affect the performances of the ASU, the gasifier and the gas turbine.

Improving distillation efficiency

A HIDiC (heat-integrated distillation column) can be considered as a conventional distillation column that is split into two parts at its feed point. The two column parts are operated at different pressures and positioned next to each other, enabling thermal energy transfer from the HPC (high-pressure column) to the LPC (low-pressure column) along the entire height of the integrated column. The duties of the original reboiler and condenser are in this way spread out over a larger part of the column height. This can reduce the irreversibilities within the distillation columns and it reduces the reboiler and condenser duties.
The distillation section of a conventional two-column ASU contains two distillation column that operate at different pressures. They are thermally integrated by a single heat exchanger that is functioning as condenser for the HPC and as reboiler for the LPC.
In a previous study [Van der Ham et al., 2011], we investigated how the performance of the distillation section changes when the LPC is moved down along the HPC, thereby creating a HIDiC-type heat-integrated column part. It was shown that the exergy destruction in the distillation section can be reduced with 23% when using such a configuration. The reduction in exergy destruction can be translated into a lower operating pressure of the HPC, which means that the feed air can be provided at a lower pressure, or into a higher operating pressure of the LPC, which means that some products are delivered at a higher pressure. In the current study, we investigate how such a change in configuration and operating pressure affects the efficiency of the entire ASU.

6.1.3 Aim of the work

The aim of this work is to assess how heating of the ASU products and using a HIDiC-type heat integration affect the Second law efficiency of a cryogenic ASU that is part of an IGCC.

6.2 Theoretical background on exergy analysis

The Second law efficiency of the ASU is evaluated using exergy analysis. The theoretical background and use of exergy analysis are explained in detail in for example the monograph by Kotas [1985]. Relevant relations are here shortly repeated for convenience.

6.2.1 Exergy contents of a stream of matter

The exergy content of a stream of matter is given by the amount of work that ideally can be extracted when the stream is brought into equilibrium with the environment. In the current study, the kinetic and the potential exergy of streams of matter are assumed to be negligible. This means that the total molar exergy (ε_{tot}) is given by the sum of the physical molar exergy (ε_{ph}) and the chemical molar exergy (ε_0) only:

$$\varepsilon_{tot} = \varepsilon_{ph} + \varepsilon_0 \tag{6.1}$$

The physical molar exergy of a mixture can be calculated from the molar enthalpy (h) and molar entropy (s) of the mixture at the actual conditions, in combination with the molar enthalpy (h^0) and molar entropy (s^0) of the mixture at the environmental temperature ($T^0 = 298.15$ K) and pressure ($P^0 = 1$ atm):

$$\varepsilon_{ph} = \left(h_{T,P} - h_{T^0,P^0}\right) - T^0 \left(s_{T,P} - s_{T^0,P^0}\right) \tag{6.2}$$

The chemical molar exergy of an ideal gas mixture can be calculated from the standard chemical exergies of the components ($\varepsilon_{0,i}$) and their mole fractions (x_i):

$$\varepsilon_0 = \sum_i x_i \varepsilon_{0,i} + RT^0 \sum_i x_i \ln x_i \tag{6.3}$$

Here, R is the molar gas constant. The standard chemical exergies are defined based on the atmospheric concentrations of reference substances. The values that are used in the current study are shown in Table 6.1, they are based on a hypothetical atmosphere consisting of nitrogen, argon, oxygen, carbon dioxide and water only, see Van der Ham and Kjelstrup [2010] for more details.

Table 6.1: Standard chemical exergies used in this work, in J/mol.

Substance	$\varepsilon_{0,i}$
N_2	636
Ar	11609
O_2	3891

The total exergy of a stream of matter (E_{tot}) can finally be calculated by multiplying its total molar exergy with its molar flow rate (F):

$$E_{tot} = F\varepsilon_{tot} \tag{6.4}$$

6.2.2 Rational exergy efficiency

The current study uses the rational exergy efficiency (ψ) as performance criterion. It is a measure for the thermodynamic perfection of a process or process unit and can be calculated by dividing the desired exergy change by the total used exergy.

$$\psi = \frac{\Delta E^{desired}}{\Delta E^{used}} \tag{6.5}$$

A rational exergy efficiency of unity corresponds to complete perfection or reversibility. Completely irreversible processes or process units have a rational exergy efficiency of zero.
The definitions of the desired exergy change and total used exergy depend on the process or process unit that is being considered. In the current study, the desired exergy change is given by the amount of exergy that is added to the process streams, it can be calculated by subtracting the exergy contents of the feed air (E^{feed}) from the exergy contents of the separation products ($E^{products}$). The total used exergy is given by the net work input to the process (E^{work}).

6.3 Process unit descriptions

Three parts of the IGCC process shown in Figure 6.1 are considered in more detail in this study: the ASU, the gasifier, and the gas turbine. The process unit operating conditions that are relevant for the current study are based on the values that are used in the DECARBit project [Bolland et al., 2009]. The gasifier and gas turbine are discussed first, because their characteristics define the product specifications of the ASU. The proposed changes in the flow sheet and column configuration of the ASU are also discussed in more detail.

6.3.1 Coal gasifier

The gasifier is assumed to operate at a pressure of 44 bar and a temperature of 1550 °C . It is fed with bituminous Douglas Premium coal, having a higher heating value of 26.23 MJ/kg and a lower heating value of 25.17 MJ/kg. The assumed coal properties are listed in Table 6.2.
The specifications of the required nitrogen and oxygen streams are listed in Table 6.3.

6.3.2 Gas turbine

The use of a generic F class gas turbine is assumed. It operates with a pressure ratio of 18 and has a turbine inlet temperature of 1350 °C. The diluted synthesis gas is fed to the unit at a pressure of 25 bar and 200 °C. A minimum mole fraction of 0.99 is required for the nitrogen streams that is used as diluent.

Table 6.2: Properties of bituminous Douglas Premium coal

Proximate analysis		Ultimate analysis	
Fixed carbon	54.95 %	Carbon	66.52 %
Volatiles	22.90 %	Ash	14.15 %
Ash	14.15 %	Oxygen	5.46 %
Moisture	8.00 %	Hydrogen	3.78 %
		Nitrogen	1.56 %
		Sulphur	0.52 %
		Chlorine	0.01 %
Total	100.00 %	Total	100.00 %

Table 6.3: Gasifier input specifications

Stream		N_2	O_2
Mole fraction	-	0.999	0.950
Pressure	bar	88	48
Flow rate per kg coal	kg	0.221	0.812

6.3.3 Two-column ASU

The ASU design that is used as base case in the current work is similar to the two-column design that was previously analysed [Van der Ham and Kjelstrup, 2010] and that was used as basis when assessing the performance increase of the distillation section due to improved heat integration of the distillation columns [Van der Ham et al., 2011]. Figure 6.2 shows the process flow sheet of the base case ASU.

The three most important process units are the HPC (high-pressure column), the LPC (low-pressure column), and the MHX (main heat exchanger). The air pre-purification step of the ASU is not included in the current design.
Purified and compressed air enters the process and is split into three parts. Almost half of the air is further compressed to a high pressure, cooled to an ambient temperature, liquefied in the MHX, expanded, and fed to the HPC. More than half of the air is cooled in the MHX and fed to the bottom of the HPC as a vapour. A very small portion of the air is compressed in the booster air compressor, cooled, expanded, and fed to the LPC.
The HPC is assumed to have 51 theoretical equilibrium stages, including condenser. The liquid feed enters the column at stage 42, counting from top to bottom. Two products are withdrawn from the top of the HPC: a liquid stream which is subsequently pumped to a high pressure and vaporised in the MHX to yield HP N_2 (high pressure nitrogen), and a gaseous stream that passes through the MHX and is compressed to yield MP N_2 (medium pressure nitrogen). Both products have the same composition. Three liquid streams are withdrawn from the HPC, sub-cooled, throt-

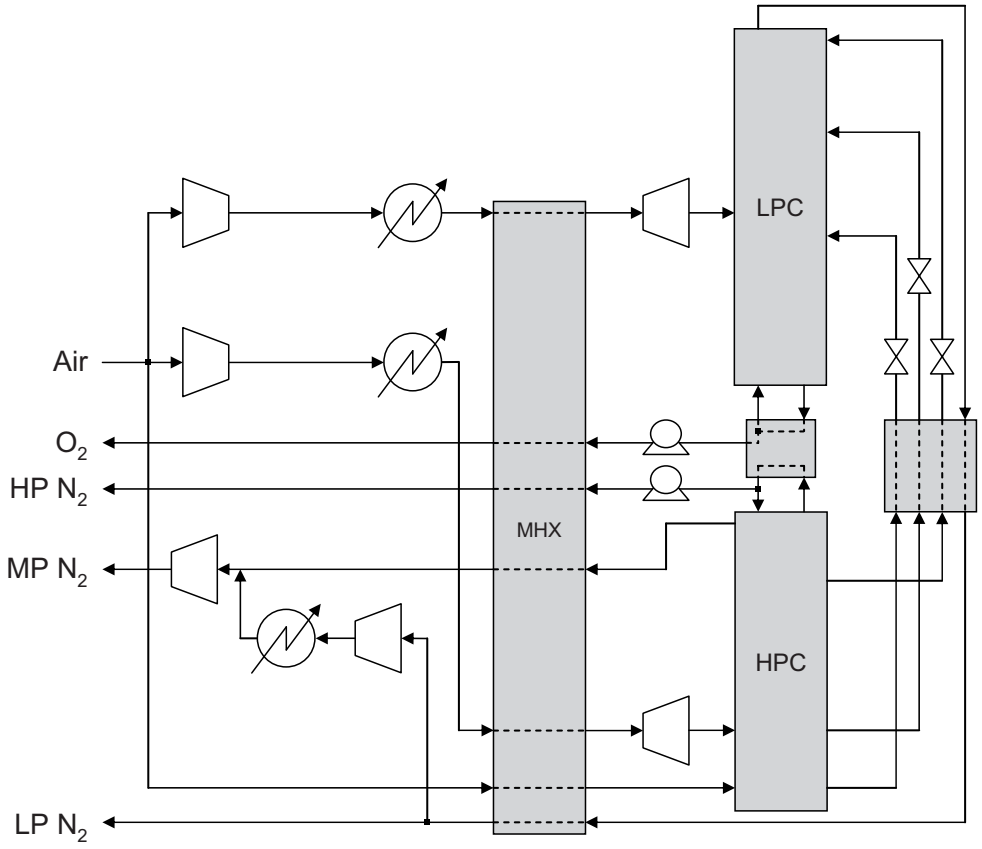

Figure 6.2: Process flow sheet of the base case two-column ASU design.

tled, and fed to the LPC. They are withdrawn from stage 11, stage 42 and the bottom stage.
The LPC has 56 theoretical equilibrium stages, including reboiler. The air stream is fed to stage 25, counting from top to bottom. The liquid parts of the streams originating from HPC are fed to the top stage, stage 16 and stage 28; the vapour parts are fed to the top stage, stage 15 and stage 27. The top product is first used to sub-cool the streams originating from the HPC and subsequently warmed in the MHX. A part of this stream is compressed, cooled and added to the gaseous nitrogen product from the HPC before it is compressed to yield MP N_2. The remaining part leaves the process as LP N_2 (low pressure nitrogen), which is used for regeneration purposes in the feed pre-purification step of the ASU.
Previous studies [Van der Ham et al., 2011, Van der Ham and Kjelstrup, 2010] used an oxygen recovery of 96.0% and a ratio of 3.20 between the O_2 and HP N_2 molar flow rates. The amount of produced MP N_2 was 26.2% of the molar feed flow rate. In combination with the specification originating from the gasifier and gas turbine, this results in the ASU product specification listed in Table 6.4.

Table 6.4: ASU product specifications.

Stream		O_2	HP N_2	MP N_2
Flow per mole feed	mol	0.212	0.066	0.262
Purity	-	0.950	0.999	0.990
Pressure	bar	48.0	88.0	25.0

Additional heat exchanger

As discussed in Section 6.1.2, the efficiency of the ASU might be improved by adding a heat exchanger that uses heat of compression to heat some of the ASU products. The O_2, HP N_2, and MP N_2 are all used at high temperatures downstream of the ASU. They are therefore good candidates to be heated. Any combination of these three streams can be heated. In the current study we investigate two combinations: heating of the O_2 and the HP N_2 only, and heating of all three streams. Heating of the MP N_2 stream is combined with removal of the cooler that is used after the nitrogen compressor. Figure 6.3 shows the process flow sheet for the case where all three streams are heated.

Improved heat integration of distillation columns

The second strategy to try and increase the ASU efficiency is by improving the heat integration of the distillation columns, as discussed in Section 6.1.2. The proposed change in the configuration of the columns is illustrated schematically in Figure 6.4. In

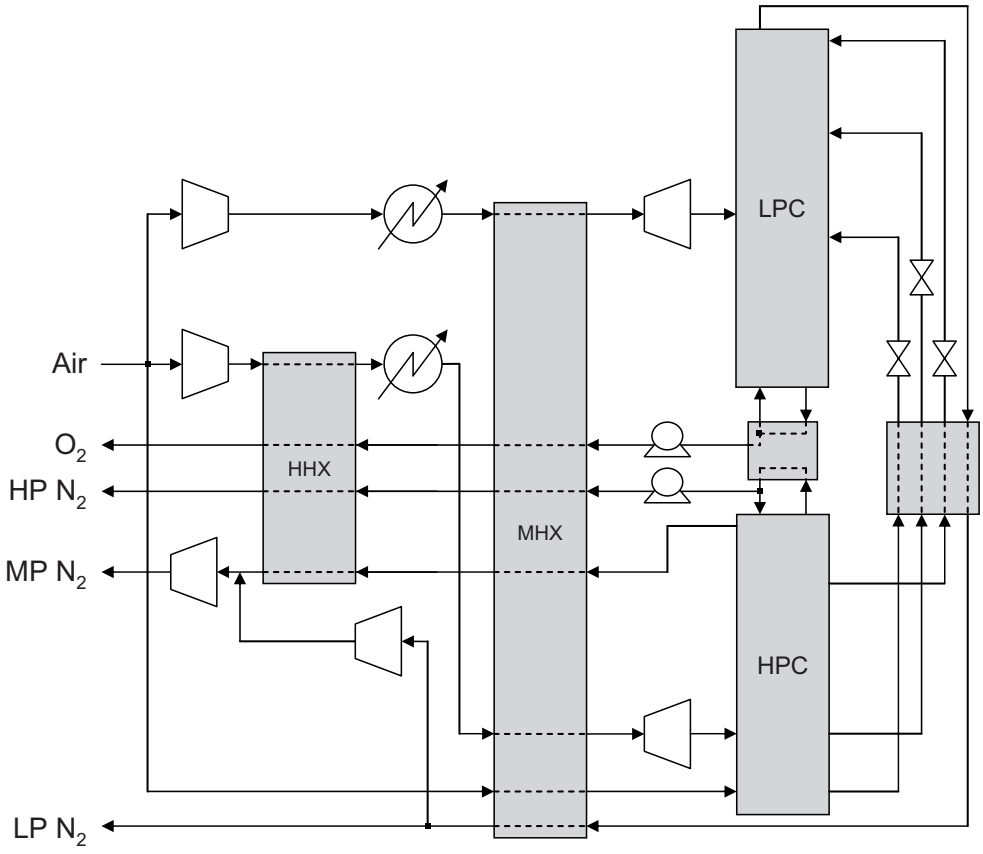

Figure 6.3: Process flow sheet of the two-column ASU design with an additional heat exchanger that is used to heat all product streams that are used in the gasifier and gas turbine.

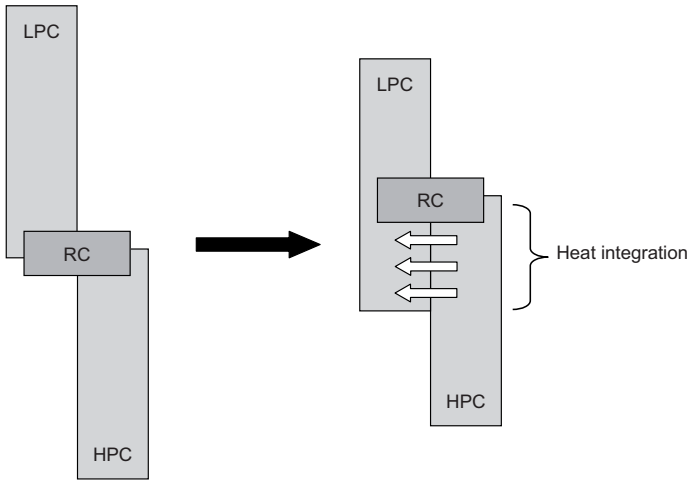

Figure 6.4: Schematic illustration of the proposed change in distillation column configuration: the HPC (high-pressure column) and RC (reboiler-condenser) are moved up along the LPC (low-pressure column), enabling heat integration of a larger part of the column heights.

a previous study [Van der Ham et al., 2011], it was found that the gain in performance increases as the height of the heat-integrated column part is increased. The maximum height of the heat-integrated column part is determined by the required product specifications; if the height becomes too large, it is no longer possible to produce the required amounts of product. The maximum feasible number of HI-stages (heat-integrated stages) was found to be 26, which is approximately half of the column height. This is the number of HI-stages that is used in the current study as well.
The use of HI-stages makes it possible to decrease the ratio between the operating pressure of the two columns, while keeping the temperature difference in the RC (reboiler-condenser) unchanged. A decrease in pressure ratio can be realized either by increasing the pressure in the LPC or by decreasing the pressure in the HPC. Both alternatives are investigated in the current study.

6.4 Simulations and calculations

6.4.1 Coal gasifier

The coal gasifier is simulated using the process simulator Aspen PLUS V7.1, using the Soave–Redlich–Kwong equation of state.
A series of two reactors is used to model the gasifier. The first one is a 'yield reactor'; it decomposes the coal feedstock into the components listed in the ultimate analysis in Table 6.2. The reactor operates at the temperature and pressure of the coal feed: 15 °C and 1 atm. The coal properties listed in Table 6.2 need to be converted to a

dry basis before they are used in Aspen PLUS. The heat of combustion is specified directly, based on the higher heating value of the coal. The reaction products and the thermal energy that is liberated during the decomposition reactions are fed to the second reactor, together with the nitrogen and oxygen streams.
The second reactor is a 'Gibbs reactor'; it is used to find the equilibrium composition and temperature at the gasifier outlet for the operating pressure listed in Section 6.3.1. The allowed outlet components are N_2, O_2, Ar, H_2O, CO, CO_2, ash, C, S, SO_2, SO_3, NO, NO_2, H_2, HCl, CL_2, CH_4, NH_3, COS and HCN. The nitrogen flow rate is fixed at the value given in Table 6.3, while the oxygen flow rate is used to obtain the desired outlet temperature.

6.4.2 Gas turbine

The gas turbine calculations are done in the process simulator Aspen HYSYS V7.1, using the Soave–Redlich–Kwong equation of state.
The main function of the nitrogen that is used as diluent in the gas turbine is to make sure that the TIT (turbine inlet temperature) does not become too high. The total amount of thermal energy that is absorbed by the nitrogen stream is given by the nitrogen inlet temperature, the TIT and the nitrogen flow rate. When increasing the nitrogen inlet temperature, the temperature difference decreases. In order to keep the total amount of energy that is absorbed by the nitrogen unchanged, the nitrogen flow rate needs to increase. The required increase in flow rate can be calculate using specific enthalpy (h) values:

$$\frac{F^{new}}{F^{old}} = \frac{h\left(TIT\right) - h\left(T_{N_2}^{old}\right)}{h\left(TIT\right) - h\left(T_{N_2}^{new}\right)} \tag{6.6}$$

An increase in the nitrogen flow rate means that more nitrogen has to be compressed, requiring more work input. But since the amount of matter that is entering the turbine also increases, more work is extracted as well. The net effect can be estimated by subtracting the work required for compression from a pressure of 1 atm and a temperature of 20 °C to a pressure of 25 bar, from the work obtained when expanding from a pressure of 18 bar and a temperature of 1350 °C to a pressure of 1 atm. Using adiabatic efficiencies of 87% for the compressor and expander, this yields a net work output of approximately 10 kJ/mol nitrogen. So an increase in the nitrogen temperature has a positive effect on the net work output, even without including the additional work output from the steam cycle.

6.4.3 Two-column ASU

The ASU flow sheet is simulated with the process simulator Aspen HYSYS V7.1, using the Peng-Robinsons equation of state modified by Stryjek and Vera and using Lee-Kessler vapour pressures (PRSV-LK).

Fixed operating conditions

All simulations use a total air feed flow rate of 1 mol, at a temperature of 20 °C and with mole fractions of 0.781, 0.009 and 0.210 for nitrogen, argon and oxygen respectively. The pressures of the O_2, HP N_2 and MP N_2 products are set are their specification values as listed in Section 6.3.3. The pressure of the LP N_2 is set at 0.14 bar above the minimum pressure level. The minimum pressure level is equal to 1 atm, except when using HI-stages in combination with an increased pressure in the LPC.
The flow rate of the air that is fed to the LPC is fixed at 1.5% of the total feed; its temperature is specified at 30 °C at the inlet of the MHX and at -125 °C at its outlet. The liquid air that is fed to the HPC has a temperature of -176 °C at the MHX outlet; it is compressed to a pressure of 80 bar and cooled to a temperature of 30 °C before entering the MHX. All streams leaving the hot side of the MHX have the same temperature.
The flow rate of the liquid nitrogen product from the HPC is fixed at the product specification for the HP N_2. Liquid is leaving the HPC at stage 42 with a flow rate equal to 13.0% of the total feed. The liquid withdrawn from stage 11 has a oxygen mole fraction of 0.020. Sub-cooling of the liquid streams from the HPC to the LPC is done in two heat exchangers that have a minimum approach temperature of 2.5 °C.
The purity of the liquid oxygen leaving the LPC is set at its specification value.
The adiabatic efficiencies of the compressors are 87%; they are 50% for the liquid pumps, 75% for the liquid expander, 80% for the booster compressor and 87% for the turbo-expander. Pressure drop and losses of low temperature thermal energy to the environment were included for all columns and heat exchangers.

Varying operating conditions

When solving the process flow sheet, the feed pressure is used to ensure a temperature difference of 0.80 °C in the RC (reboiler-condenser). In the case of HI-stages in combination with an increased pressure in the LPC, the LP N_2 pressure is used to control the RC temperature difference. A minimum approach temperature of 2.0 °C in the MHX is realized by adjusting the flow rate of the liquid air; it amounts to approximately 42% of the total feed. The flow rate of the gaseous air that is fed to the HPC is set such that the total feed flow rate remains constant. Its temperature when leaving the MHX is found using the energy balance of the RC (reboiler-condenser). The pressure after the booster compressor is defined by the work input of the compressor, which is set at 96% of the turbo-expander work output. The required oxygen flow rate is obtained by varying the flow rate of the gaseous HPC product. The pressure and temperature of the nitrogen that is upgraded from LP N_2 to MP N_2 are set to match the values of the gaseous nitrogen from the HPC. Its flow rate is chosen such that the flow rate of the total MP N_2 equals the product specification.

Additional heat exchanger

The additional heat exchanger is modelled with a minimum approach temperature of 25 °C. All hot outlet streams have the same temperature. For simplicity, no pressure drop and heat losses are assumed for this heat exchanger.

Heat-integrated distillation stages

The heat duties of the HI-stages are calculated using the spreadsheet functionality that is part of HYSYS. Based on the stage temperatures and a fixed value for the heat-transfer capacity per stage, the heat duties can be calculated. These duties are added to the relevant stages of the LPC and removed from the relevant stages of the HPC. Heat-transfer capacity is defined as the available heat-transfer area multiplied with the overall heat-transfer coefficient; a value of 17 W/°C per stage is used. This value is based on assumptions concerning the column diameter, the type of structured packing that is used, the overall heat-transfer coefficient, the vapour density, and the maximum vapour flow rate; see Van der Ham et al. [2011].

Exergy calculations

The exergy contents of the feed and products is calculated according to the relations given in Section 6.2.1, using the spreadsheet functionality of HYSYS. The exergy contents of the thermal energy streams that are entering and leaving the process are equal to zero, because the temperature of the energy is equal to the environmental temperature. Work is by definition equal to exergy.

6.4.4 Case descriptions

Several ASU cases are simulated. The first case is the base case (case 0), which is also discussed in [Van der Ham and Kjelstrup, 2010]. Next, the HI-stages are added to the design. The effects of both increasing the pressure in the LPC (case 1L) and decreasing the pressure in the HPC (1H) are evaluated.
The additional heat exchanger is subsequently added to both designs. Two more cases are considered for each of them: heating of the products to the gasifier only (case 2L & 2H), and heating of the products to both the gasifier and gas turbine (case 3L & 3H).
In the next six cases, the interaction of the gasifier and gas turbine with the ASU is included. The interaction with the gasifier involves a change in the flow ratio between the O_2 and HP N_2 products. Both changing the O_2 flow rate (case 4L & 4H) and changing the HP N_2 flow rate (case 5L & 5H) are assessed. The most promising alternatives are used for the two final designs, which add the interaction with the gas turbine (case 6L & 6H) to the ASU design.

6.5 Simulation results

The simulation results of the cases described in Section 6.4.4 are first shown and discussed separately. A summarizing overview of the performance improvements is given at the end of the section.

6.5.1 Case 0: Base case

The resulting properties of the feed and products of the base case ASU design are shown in Table 6.5.

Table 6.5: Feed and product properties of the base case ASU design. Molar flow rates are given as fraction of the total feed flow rate.

Stream		Air	O_2	HP N_2	MP N_2	LP N_2
F	-	1	0.212	0.066	0.262	0.459
x_{N_2}	-	0.781	0.017	1.000	0.992	0.982
x_{Ar}	-	0.009	0.033	0.000	0.002	0.004
x_{O_2}	-	0.210	0.950	0.000	0.006	0.014
P	bar	5.08	48.0	88.0	25.0	1.15
T	°C	20	22	22	226	22

The values found in this work are very similar to ones previously found [Van der Ham and Kjelstrup, 2010][1]. There are some very minor differences in the air pressure and in the MP N_2 mole fractions. They are caused by the use of different versions of Aspen HYSYS in the two works, either 2006.5 or V7.1. Table 6.6 contains a comparison between the found exergy characteristics of the two works, it also shows some minor differences.

Table 6.6: Comparison between the exergy inputs and outputs per amount of feed (kJ/mol) of the two-column designs evaluated in the current work and in a previous work [Van der Ham and Kjelstrup, 2010].

Study	Current	Previous
Physical exergy in feed	3.99	3.99
Chemical exergy in feed	0.02	0.02
Work input	7.22	7.26
Physical exergy in products	5.34	5.35
Chemical exergy in products	1.15	1.15
Work output	0.10	0.10
Destroyed exergy	4.64	4.67
Rational exergy efficiency	0.348	0.347

[1] In Table 3 of the previous work [Van der Ham and Kjelstrup, 2010], the argon and oxygen mole fractions of the Air, MP N_2 and LP N_2 streams were accidentally interchanged.

6.5.2 Case 1L & 1H: Adding heat-integrated stages

Figure 6.5 shows how the temperature profile of the columns change when HI-stages are added to the base case ASU design (case 0).

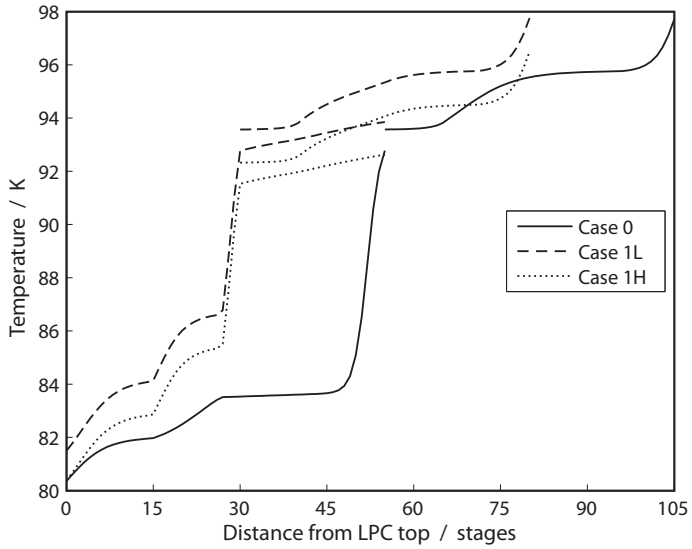

Figure 6.5: Column temperatures as function of the distance from the top of the low-pressure column (LPC) for column configurations without (case 0) and with (case 1L and 1H) heat-integrated stages. Case 1L maintains the base case temperature difference in the reboiler-condenser by increasing the pressure in the LPC, while case 1H achieves this by decreasing the pressure in the high-pressure column.

Increasing the pressure in the LPC (case 1L) causes an increase in the LPC temperatures, thus maintain the base case temperature difference in the reboiler-condenser. Decreasing the pressure in the HPC (case 1H) achieves the same result by decreasing the HPC temperatures. The fraction of the total heat duty that is accommodated by the HI-stages is 13% for both cases; Van der Ham et al. [2011] found 22% for comparable cases.
Table 6.7 shows how the operating pressures and product temperatures change when HI-stages are added to the base case ASU design.
In order to keep the temperature difference at the base case value, the pressure in the LPC needs to be increased with 13% or the pressure in the HPC needs to be decreased with 10%. The resulting decreases in the pressure ratio are smaller than the ones found in Van der Ham et al. [2011]. Only the temperature of the MP N_2 product is affected by the pressure changes; it increases with 0.3 °C for case 1L and with 16 °C for case 1H. The effect that these temperature increases have on the MP N_2 flow rate required by the gas turbine is included in Section 6.5.5.

Table 6.7: Product temperatures for different cases of HI-stages.

Case	Pressures (bar)		Temperatures (°C)	
	Feed	LP N_2	O_2 & HP N_2	MP N_2
0	5.08	1.15	22	226
1L	5.08	1.33	22	227
1H	4.62	1.15	22	242

Table 6.8 shows how the exergy characteristics of the ASU change when HI-stages are added to the base case design.

Table 6.8: Exergy characteristics per amount of feed (kJ/mol) for different cases of HI-stages.

Case	E^{work}	E^{feed}	$E^{products}$	$E^{destroyed}$	ψ (-)
0	7.12	4.01	6.49	4.64	0.348
1L	7.24	4.01	6.63	4.63	0.361
1H	7.55	3.78	6.52	4.81	0.363

Both cases with HI-stages require more work input than the base case. For case 1L, only the compressor that is upgrading LP N_2 to MP N_2 requires more work. The main air compressor is responsible for most of the extra work in case 1H. This makes sense because the air is entering the process at a lower pressure, while still being compressed to a pressure of 80 bar. The decreased feed pressure is also the reason for the decreased exergy content of the feed. The increasing exergy content of the products is caused by the increased product temperatures, and for case 1L also by an increase in the LP N_2 pressure.
Overall, the rational efficiency of both cases is higher than the one of the base case, with case 1H performing slightly better than case 1L. These efficiency increases are approximately half of the efficiency increase that can achieved by adding a third distillation column to the ASU design, as discussed in more detail in Van der Ham and Kjelstrup [2010].

6.5.3 Case 2L, 3L, 2H & 3H: Adding the hot heat exchanger

The effect of adding the proposed heat exchanger is evaluated in two steps. First it is used to only heat the O_2 and HP N_2 streams, which are the ASU products that are fed to the gasifier (case 2L & 2H). Subsequently, heating of the MP N_2 stream, which is fed to the gas turbine, is included as well (case 3L & and 3H).
Table 6.9 shows how the product temperatures change when the hot heat exchanger is added to the ASU design. Heating of products that are fed to the gasifier does not affect the temperature of the stream to the gas turbine, and vice versa. The temperature increases for the cases with an increased LPC pressure (denoted with L) are smaller than the ones for cases with a decreased HPC pressure (denoted with H).

Table 6.9: Product temperatures for different cases of product heating.

Case	Product heating		Temperatures (°C)	
	O_2 & HP N_2	MP N_2	O_2 & HP N_2	MP N_2
1L	No	No	22	227
2L	Yes	No	383	227
3L	Yes	Yes	383	580
1H	No	No	22	242
2H	Yes	No	402	242
3H	Yes	Yes	402	657

This was also the case when adding the HI-stages.
Table 6.10 shows how the exergy characteristics of the ASU change when the hot heat exchanger is added to the design. Heating of the streams to gasifier increases

Table 6.10: Exergy characteristics per amount of feed (kJ/mol) for different cases of product heating.

Case	E^{work}	E^{feed}	$E^{products}$	$E^{destroyed}$	ψ (-)
1L	7.24	4.01	6.63	4.63	0.361
2L	7.24	4.01	7.71	3.55	0.510
3L	8.41	4.01	9.30	3.12	0.628
1H	7.55	3.78	6.52	4.81	0.363
2H	7.55	3.78	7.69	3.64	0.518
3H	8.98	3.78	9.66	3.11	0.654

the exergy content of the products, caused by the increase in their temperatures. The amount of destroyed exergy decreases significantly, since the exergy added to the process remains unchanged, resulting in a considerable increase in the rational exergy efficiency.
Heating the stream to the gas turbine increases the exergy content of the products even further, but an increase in the work input is now required. All of the additional work is used in the MP N_2 compressor, related to the increase of its operating temperature. The net effect is another decrease in the amount of destroyed exergy, resulting in a second large increase in the rational exergy efficiency.
When comparing the L-cases with the H-cases, it can be concluded that the H-cases are more extreme in all the increases and decreases that occur. The difference between the rational efficiencies of the two design variants becomes larger when adding the hot heat exchanger to the design.

6.5.4 Case 4L, 5L, 4H & 5H: Including gasifier interaction

In Section 6.5.3 it is shown that adding the HI-stages and the hot heat exchanger increases the temperatures of the oxygen and nitrogen streams that are fed to the gasifier. Because the nitrogen stream is used for coal transportation, its flow rate depends on the coal flow rate only. So the temperature change will only affect the amount of oxygen that is required in the gasifier. The extent of this effect is evaluated by first performing the calculations described in Section 6.5.3 based on the base case temperature, and subsequently based on the temperatures found in Section 6.5.2. Compositional changes are neglected.
Due to the found change in oxygen flow rate, the ratio between the nitrogen and oxygen flow rates changes. This change can be translated back to the ASU by either adjusting the oxygen flow rate (case 4L & 4H) or by adjusting the nitrogen flow rate (case 5L & 5H). When adjusting the nitrogen flow rate, the entire ASU should subsequently be scaled with the relative change in nitrogen flow rate in order to keep the ratio between the nitrogen and coal flow rates unchanged. This means that the amount of air feed changes. The ASU flow rate adjustments cause small changes in some operating temperatures and pressures. They converge after a few iteration steps. Table 6.11 shows the converged product temperatures and flow rates when interaction with the gasifier is included.

Table 6.11: Product temperatures for different cases of adjusted O_2 or HP N_2 flow rates. The flow rates are given as fraction of their base case values listed in Table 6.5.

Case	Flow rates (-)		Temperatures (°C)	
	O_2	HP N_2	O_2 & HP N_2	MP N_2
3L	1	1	383	580
4L	0.967	1	383	617
5L	1	1.034	383	575
3H	1	1	402	657
4H	0.966	1	398	696
5H	1	1.036	402	651

For case 4L, the pressure in the LPC had to be increased with 0.3% in order to keep the temperature difference in the RC constant. The HPC pressure had to be decreased with 0.3% for case 4H. These pressure changes cause small decreases in the O_2 and HP N_2 temperatures. The MP N_2 temperature increases when adjusting the O_2 flowrate and decreases when adjusting the HP N_2 flow rate. Table 6.12 shows how the oxygen flow rate and the gasifier outlet flow rate and composition change for the different cases.
The oxygen mass flow rate found for the base case is slightly higher than the specification value taken from Bolland et al. [2009]. That is why it has been decided to use the relative change in oxygen flow rate as basis for the ASU flow rate adjustments, rather than the absolute change.

Table 6.12: Oxygen and outlet mass flow rates for different temperatures of the oxygen and nitrogen streams entering the gasifier, given per mass of coal. The shown O_2/N_2 ratio is based on molar flow rates and relative to the base case ratio.

Case	0	4L & 5L	4H	5H
Temperature (°C)	22	383	398	402
O_2 flow rate	0.845	0.818	0.816	0.816
Relative O_2/N_2 ratio	1	0.967	0.966	0.965
Outlet flow rate	2.066	2.038	2.037	2.037
CO	1.516	1.533	1.534	1.534
N_2	0.250	0.250	0.250	0.250
Ash	0.142	0.142	0.142	0.142
CO_2	0.047	0.018	0.017	0.017
H_2	0.043	0.045	0.045	0.045
H_2O	0.029	0.012	0.011	0.011
Ar	0.028	0.027	0.027	0.027
COS	0.010	0.010	0.010	0.010
Other	0.001	0.001	0.002	0.002

Table 6.12 shows that the oxygen requirement of the gasifier indeed decreases when the temperature of the oxygen and nitrogen streams increases. It also reveals how an increase in temperature is translated into an efficiency increase of the IGCC. When comparing the CO, CO_2, H_2 and H_2O mass flow rates of the different cases, it can be seen that the outlet composition becomes less oxidized when the temperature increases; there is more CO and H_2 and less CO_2 and H_2O. This means that more H_2O is needed in the water-gas shift unit in order to oxidise the remaining CO, increasing the H_2 flow rate even more. So in the end, the increase in oxygen and nitrogen temperature results into a higher H_2 flow rate into the gas turbine, increasing the work output of both the gas and steam turbines.
Table 6.13 shows how the exergy characteristics of the ASU change when interaction with the gasifier is included. When using the HP N_2 flow rate to adjust the O_2/N_2

Table 6.13: Exergy characteristics (in kJ) based on the base case amount of HP N_2 product, for different cases of adjusted O_2 or HP N_2 flow rates.

Case	E^{work}	E^{feed}	$E^{products}$	$E^{destroyed}$	ψ (-)
3L	8.41	4.01	9.30	3.12	0.628
4L	8.64	4.01	9.35	3.30	0.618
5L	8.16	3.88	9.00	3.05	0.627
3H	8.98	3.78	9.66	3.11	0.654
4H	8.86	3.77	9.70	2.93	0.669
5H	8.70	3.65	9.33	3.03	0.652

ratio (case 5L & 5H), both cases behave similarly. The required work input, the exergy contents of the feed and products, and the resulting exergy destruction all show a small decrease. This decrease is mainly caused by the decrease in feed flow rate. The net effect is a minor decrease in the rational efficiency, which is independent on the amount of feed flow rate.
When using the O_2 flow rate to adjust the O_2/N_2 ratio (case 4L & 4H), the two cases behave differently. For case 4L, the work input increases, while it decreases for case 4H. These changes are mainly caused by changing flow rates of the stream going through the main air compressor. The exergy content of the products increases slightly for both cases, related to the higher temperature of the MP N_2. The overall effect is a decrease in the rational efficiency of case 4L, and an increase in the rational efficiency of case 4H.
Because we can choose ourselves whether we want to adjust the HP N_2 flow rate or the O_2 flow rate, we select the HP N_2 flow rate for the L-variant (case 5L) and the O_2 flow rate for the H-variant (case 4H).

6.5.5 Case 6L & 6H: Including gas turbine interaction

By adding HI-stages, adding the hot heat exchanger and including the interaction with the gasifier, the MP N_2 temperature has increased from its base case value of 226 °C to 575 °C for case 5L and 696 °C for case 4H. Using these temperatures and the gas turbine inlet temperature specified in Section 6.3.2, a new MP N_2 flow rate can be calculated. Adjusting the ASU flow rate specification to this values causes a small change in the MP N_2 temperature. After several iteration steps, the MP N_2 flow rate and temperature converge to the values listed in Table 6.14. Including interaction

Table 6.14: MP N_2 temperatures for adjusted MP N_2 flow rates. The flow rate is given as fraction of the base case values listed in Table 6.5.

Case	Flow rate (-)	Temperatures (°C)
5L	1	575
6L	1.357	545
4H	1	696
6H	1.501	628

with the gas turbine increases the MP N_2 flow rate and decreases its temperature. The changes are again more extreme for the H-variant than for the L-variant of the ASU design. The resulting ASU exergy characteristics when including the interaction with the gasifier are shown in Table 6.15. Both case 6L and 6H require more work input, caused by the increased MP N_2 flow rate. The exergy content of the products increase with a slightly smaller amount; a small part of the additional work input is destroyed. Including the gas turbine interaction in the ASU design results in a higher rational efficiency. The final efficiency of the H-variant is considerably higher than the one of the L-variant.

Table 6.15: Exergy characteristics (in kJ) based on the base case amount of HP N_2 product, for an adjusted MP N_2 flow rate.

Case	E^{work}	E^{feed}	$E^{products}$	$E^{destroyed}$	ψ (-)
5L	8.16	3.88	9.00	3.05	0.627
6L	9.36	3.88	10.11	3.13	0.665
4H	8.86	3.77	9.70	2.93	0.669
6H	10.73	3.77	11.43	3.07	0.713

6.5.6 Overall efficiency improvements

The overall effect of adding the HI-stages and the hot heat exchanger, while including the interaction of the ASU with the gasifier and gas turbine, is graphically depicted in Figure 6.6; it shows the exergy characteristics of the base case design (case 0) and the two final designs (case 6L & 6H).

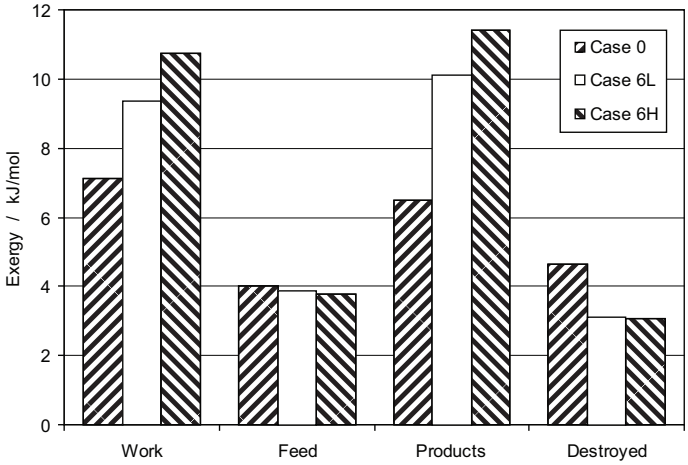

Figure 6.6: Comparison between the exergy characteristics of the base case ASU design (case 0) and the final ASU designs (case 6L & 6H). The amounts of exergy are given based on the base case amount of HP N_2 product.

It can be seen that the exergy content of the feed hardly changes. There is a minor decrease for case 6H, related to a decrease in pressure, and an even smaller decrease in case 6L, related to the decrease in feed flow rate. The work input of both final cases is substantially larger than for the base case. This is mainly related to increased duties of the two nitrogen compressors. The majority of the additional work is transformed into thermal exergy of the products. But this is not the only cause for the increased exergy content of the products. Addition of the HI-stages and the hot heat exchanger makes the process more efficient, resulting in less exergy destruction which also translates into a higher exergy content of the products.

When comparing the two final ASU variants, it shows that the H-variant destroys less exergy than the L-variant. Case 6H is therefore the most promising variant. Table 6.16 gives the feed and products properties of this case.

Table 6.16: Feed and product properties of case 6H, the final ASU design. Molar flow rates are given as fraction of the total feed flow rate.

Stream		Air	O_2	HP N_2	MP N_2	LP N_2
F	-	1	0.205	0.066	0.393	0.336
x_{N_2}	-	0.781	0.024	1.000	0.979	0.967
x_{Ar}	-	0.009	0.026	0.000	0.004	0.007
x_{O_2}	-	0.210	0.950	0.000	0.016	0.026
P	bar	4.61	48.0	88.0	25.0	1.15
T	°C	20	398	398	628	22

These numbers can be compared to their base case values given in Table 6.5. Apart from the changes in pressure, temperatures and flow rates discussed in the previous sections, there are some minor changes in the product mole fractions. The oxygen product contains a bit more nitrogen, which is compensated for by a decrease in the argon content. This change is not expected to have a notable effect on the process performance. The decreased flow rate of the oxygen product causes increased oxygen fractions in both the MP N_2 and LP N_2 products. In combination with a small increase in their argon fractions, this results in lower nitrogen fractions. The MP N_2 nitrogen fraction is now below its specification given in Section 6.3.2. An excess of air is normally fed to the gas turbine. The decreased nitrogen fraction is therefore not expected to cause any problems, as long as the turbine inlet temperature not exceeds its maximum.

Table 6.17 gives a comparison between the distribution of the exergy destruction over the different process parts and process units of case 0 and case 6H. The exergy destruction in the feed pre-processing part of the ASU decreases with more than 80%, caused by an almost disappearing contribution of the coolers. This huge reduction is mainly realized by the addition of the hot heat exchanger, which is taking over a large part of the cooling duty. The extra heat exchanger itself adds some exergy destruction to the heat exchanger process part, but the net effect is still a large reduction. The distillation section is now the process part that destroys most of the exergy, although its efficiency has increased a little bit. For the product post-processing part we can see an increase in the exergy destruction. The overall result is a decrease of 34% in the exergy destruction.

Looking at the process unit types, it can be concluded that the contribution of the coolers decreases from 41% to below 1%. The main exergy destroying types of equipment are now the heat exchangers, the distillation columns and the compressors, accounting for 38%, 30% and 19 % of the total destruction.

Table 6.17: Comparison between the exergy destruction per amount of feed (kJ/mol) of the base case (case 0) and final case (case 6H) designs.

Process design	Base case		Final case	
Feed pre-processing		2.20		0.40
Compressors	0.29		0.29	
Coolers	1.80		0.01	
Expanders	0.10		0.09	
Heat exchangers		0.78		0.98
Main heat exchanger	0.78		0.81	
Hot heat exchanger	–		0.18	
Distillation section		1.21		1.16
HP column	0.26		0.25	
LP column	0.65		0.66	
HI-stages	0.11		0.08	
Sub-coolers	0.10		0.09	
Throttle valves	0.10		0.08	
Product post-processing		0.45		0.53
Pumps	0.15		0.15	
Compressors	0.18		0.30	
Cooler	0.11		–	
Mixer	0.00		0.08	
Total exergy destruction		4.64		3.07

6.6 Discussion

6.6.1 Effect on the IGCC efficiency

We have seen in Section 6.5 that the efficiency of the ASU can be increased substantially. If we keep the amount of feed coal fixed, then this performance improvement should in the end translate into an increased net work output of the IGCC. There are two ways in which the work output is increased. The first one is an increase in the amount of nitrogen that is passing through the turbine as discussed in Section 6.4.2, the second one is an increase in the amount of hydrogen that is entering the gas turbine, as discussed in Section 6.5.4.
In order to quantify the efficiency improvement of the IGCC, we need to calculate the amount of air that is required per amount of coal. This can be done using the HP N_2 flow rates in Tables 6.3 and 6.5 and the molar mass of nitrogen, yielding an air requirement of 119 mol/kg coal. Per mole of air, we can reduce the exergy destruction with 1.57 kJ. So per kilogram of coal, the exergy destruction can be reduced with 187 kJ. Since exergy is equal to potential work, this means that the net work output of the IGCC can be increased with 187 kJ/kg coal. If we relate this number to the lower heating value of the coal, as given in Section 6.3.1, we obtain a possible increase of 0.74% in the net electric efficieny of the IGCC.
This efficiency increase is calculated based on the ASU and its interaction with the gasifier and gas turbine only. All other process units will most likely also be affected by the changes in amounts of hydrogen and nitrogen that are fed to the gas turbine. In order to fully capture all process unit interdependencies properly, the entire IGCC should be simulated as a whole. This is outside the scope of the current work.

6.6.2 Further ASU improvements

The main process irreversibilities of the base case were located in the coolers. This work has shown that they almost completely can be prevented by the addition of an extra heat exchanger. The remaining irreversibilities are mainly located in the heat exchangers, the distillation columns and the compressors, so this is where efforts for further improvements should focus at. Of these three areas, the distillation columns have the highest potential for improvements. Both heat exchangers and compressors are relatively mature process units for which currently no substantial performance improvements are expected. But there are indications that the distillation column efficiency can be further increased.
In a previous work [Van der Ham et al., 2011], the use of HI-stages decreased the exergy destruction of the distillation section with 21% when increasing the pressure in the LPC, and with 23% when decreasing the pressure in the HPC. The LPC was in both cases responsible for approximately 75% of the reduction. In the current work, the exergy destruction of the distillation secion decreases with only 5%, and the contribution of the LPC remains almost unchanged. It is discussed in Section 6.5.2 that the HI-stages in the current work seem to affect the design to a lesser extent; their total heat duty is smaller and the required decrease in pressure ratio is smaller.

This suggests that the potential performance improvements of using heat-integrated distillation columns is not yet fully achieved in the current ASU design.
In the current work, we have implemented the HI-stages in an existing flow sheet without attempting to optimize the flow sheet for the use of HI-stages. There are several design parameters that could be varied in order to try and improved the performance of the distillation section. Some are related to the distillation section itself, like the flow rates, compositions, and/or draw locations of the HPC side-draws. The locations at which the HPC bottom product and its lowest side-draw are fed to the LPC are also good candidates. Some other design parameters are rather related to the MHX, like the cold outlet temperatures and the flow rate through the turbo-expander. In order to increase the heat duties of the HI-stages, it is also possible to increase the pressure ratio. The effects that such changes have on the distillation section and ASU efficiency would be a very interesting subject for future studies. More structural changes in the process flow sheet can also be considered.

6.6.3 Relevance for other processes

The advantages of adding the hot heat exchanger and using HI-stages are not limited to the ASU design that is studied in this work, they can be used in various other designs and processes as well.
The hot heat exchanger can be used in any process where products from the ASU are used at elevated temperatures, for example in an oxy-fuel combustion process [Brugerolle and Ha, 2009, Darde et al., 2009]. The efficiency of the three-column ASU studied in Van der Ham and Kjelstrup [2010] can also be increased using the extra heat exchanger.
Adding HI-stages to the three-column design is less straightforward, because the addition of the third column already reduces the exergy destruction in the distillation section considerably. Rather than adding HI-stages to the three-column design, it might be possible to replace the third column with a HIDiC. A related design is presented by Arman et al. [2001], who are describing the use of heat-integrated rectifying and stripping sections as part of the MHX.

6.6.4 On the use of exergy analysis

Exergy analysis has been the basis for the current and previous [Van der Ham and Kjelstrup, 2010] ASU studies. First, it was used to characterize the process and locate the largest inefficiencies. Subsequently, it was used to evaluate the effect of measures aiming to reduce these inefficiencies. According to the exergy efficiency, the process can be improved considerably. Section 6.6.1 discusses how this improvement translates into a higher net work output of the entire IGCC.
Energy conversion processes are often evaluated based on amounts of energy, without taking into account the quality of the energy. If such a performance criterion had been used to evaluate the ASU performance, then it would have been concluded that the ASU performs worse because the amount of net work input increases. The entire IGCC would have to be simulated in order to show that the changed design actually

has a positive effect, which is much more demanding.
This shows that, when evaluating the performance of a part of a larger process, performance criteria based on the Second law of thermodynamics are more suitable than criteria based on the First law of thermodynamics. However, increasing the Second law efficiency of a process part or unit should not become a goal on its own. It is important to always make sure that the improvement of this single process part can also be translated into a higher Second law efficiency of the entire process. In case of an energy conversion processes like an IGCC, this means that the First law efficiency should increase as well.

6.7 Conclusions

The effect that the addition of HI-stages and a hot heat exchanger has on the Second law efficiency of an ASU as part of an IGCC has been studied. Adding the HI-stages increases the rational exergy efficiency with 1 to 2 %, while adding the heat exchanger increases it with 30 to 35 %. When adding HI-stages, decreasing the pressure in the HPC results in a thermodynamically better process than increasing the pressure in the LPC. The reduction in exergy destruction of the final case, which also includes the interaction of the ASU with the gasifier and gas turbine, amounts to 1.6 kJ/mol air. This corresponds to an increase in the net electric IGCC efficiency of 0.74%.
The improved ASU performance translates into a higher IGCC efficiency by increasing the net work output of the combined cycle. An increase in the temperatures of the oxygen and nitrogen streams that are fed to the gasifier result in a lower oxygen demand per amount of coal, which eventually increases the amount hydrogen that can be fed to the gas turbine. Increasing the temperature of the nitrogen stream that is fed to the gas turbine allows for a larger nitrogen flow rate through the gas turbine. Addition of the hot heat exchanger removes the largest source of exergy destruction from base case ASU. The most important remaining sources are the heat exchangers, the distillation columns and the compressors. The distillation columns have the largest potential for improvements; future efforts should aim at reducing the exergy destruction in the distillation section of the ASU. The ASU flow sheet can be optimized in order to make better use of the HI-stages.

Nomenclature

ASU	air separation unit
E	exergy flow, J/s
F	molar flow rate, mol/s
h	molar enthalpy, J/mol
HI-stage	heat-integrated stage
HIDiC	heat-integrated distillation column
HP	high pressure
HPC	high-pressure column
IGCC	integrated gasification combined cycle
LP	low pressure

LPC	low-pressure column
MHX	main heat exchanger
MP	medium pressure
P	pressure, bar
R	universal gas constant, 8.3145 J/(K mol)
RC	reboiler-condenser
s	molar entropy, J/(K mol)
TIT	turbine inlet temperature
x	mole fraction, dimensionless

Greek symbols

ε_0	chemical molar exergy, J/mol
ε_{ph}	physical molar exergy, J/mol
ε_{tot}	total molar exergy, J/mol
ψ	rational exergy efficiency, dimensionless

Sub- and superscripts

0	ambient or reference conditions
i	component index

Acknowledgements

The research leading to these results has received funding from the European Community's 7th Framework Programme (FP7/2007-2013) under grant agreement number 211971 (The DECARBit project).

Chapter 7

Modelling the coupled transfer of mass and thermal energy in the vapour–liquid region of a nitrogen–oxygen mixture

L.V. van der Ham[1], R. Bock[1] and S. Kjelstrup[1,2]

1. Department of Chemistry
Norwegian University of Science and Technology
7491 Trondheim, Norway

2. Department of Process and Energy
Delft University of Technology
2628 CA Delft, The Netherlands

This chapter has been published in
Chemical Engineering Science
Volume 65 (2010), pages 2236 - 2248

It is an extended version of a report written for the PhD-course
KJ8208 – Advanced Irreversible Thermodynamics
NTNU, May 2009

Abstract

Current non-equilibrium distillation models do not explicitly include the coupling between thermal and mass fluxes. We present a calculation model for the coupled transfer of mass and thermal energy in the vapour–liquid region of a binary mixture. The region is modelled as a vapour–liquid interface in between two homogeneous films. The entropy production in the vapour–liquid region can be calculated using both irreversible thermodynamics and the entropy balance. The film thickness ratio is found by requiring the entropy production calculated with the two methods to be equal, while keeping the vapour film thickness fixed. Using a nitrogen–oxygen mixture as example, we show that neglecting the coupling between thermal and mass fluxes can have a large impact on the magnitude and direction of the theoretical (net) fluxes. The size of the impact depends on the vapour film thickness, but it is significant for all thicknesses. By increasing the number of control volumes that is used to represent the liquid and vapour films, we also show that the fluxes depend highly on the resistivity profiles in the films. They depend slightly on the interface resistance. A sensitivity analysis of the transport properties shows that accurate values of the Maxwell–Stefan diffusion coefficients in both homogeneous phases and of the liquid phase heat of transfer are most important. Especially the measurable heat flux at the liquid boundary of the system is sensitive to neglect of coupling, to neglect of the interface resistance and to uncertainties in the transfer properties.

7.1 Introduction

The current work is part of a study that aims at improving the Second law efficiency of an cryogenic air distillation process. Distillation of air is currently the most commonly used technique for the production of pure oxygen and nitrogen on an industrial scale. An example of an industrial process that requires pure oxygen and nitrogen is an integrated gasification combined cycle (IGCC), where the oxygen is fed to a gasifier and the nitrogen to a gas turbine. Our study on a cryogenic air separation unit is part of an international collaboration project called DECARBit, which aims at developing an IGCC with pre-combustion CO_2 capture [Røkke and Langørgen, 2009].
Most efforts to increase the energy and exergy efficiencies of distillation columns involve improved strategies for energy addition and removal. In traditional designs, energy is only added to the bottom of a column and it is removed only at the top. Alternative designs like diabatic distillation columns and heat-integrated distillation columns increase the efficiencies by transferring thermal energy along the entire length of the column. When optimising the efficiencies of such columns, it is essential to model the thermal energy flows inside the column as accurately as possible.

7.1.1 Conventional distillation column models

Distillation columns are classically modelled using the equilibrium stage concept. The main assumption of this concept is that the vapour and liquid streams that are leaving a stage are at equilibrium. Or in other words, it is assumed that the mass and energy transfer processes are fast enough to reach equilibrium within the available time

frame. Thermodynamic data are in this case sufficient to calculate the conditions of the streams leaving a stage. The equilibrium stage assumption, in combination with mass and energy balances over the entire column and over each stage separately, makes it relatively straightforward to model a distillation column, see for example Seader and Henley [1998].
When the transfer processes are too slow to reach equilibrium within the available time frame, a different procedure can be used; the non-equilibrium approach. This approach, also known as the rate-based approach, assumes equilibrium at the vapour–liquid interface, but not between the streams leaving a stage [Seader and Henley, 1998]. In combination with adding mass and thermal energy transfer relations, this assumption results in a much more realistic model. But it also requires more detailed input, for example on tray or packing hydraulics and expressions for the mass-transfer and heat-transfer coefficients. The difference between the equilibrium and non-equilibrium approaches is especially profound in multi-component mixture models.

7.1.2 Modelling distillation using irreversible thermodynamics

The rate-based approach to model multi-component mixtures includes the interdependency of all component mass transfer rates, but the mass and thermal energy transfer rates are assumed to be independent [Taylor and Krishna, 1993]. The theory of irreversible thermodynamics provides a rigorous method for the determination of the mass and thermal fluxes that also takes into account the coupling between the different types of fluxes. According to this theory, every flux is a linear combination of all the driving forces. So the component fluxes are not only dependent on chemical potential differences, which are their direct driving forces, but also on the temperature difference, which is the direct driving force for the thermal flux. And in parallel, the thermal flux depends on both the temperature difference and the chemical potential differences [Kjelstrup and Bedeaux, 2008].
The design of a distillation column is based on a theoretical model in combination with a set of empirical relations. Current theoretical distillation models neglect the coupling between thermal and mass fluxes. As a result, the coupling effects are implicitly included in the empirical part of the design, for example using efficiencies. Kjelstrup and De Koeijer [2003] were the first to explicitly include coupling in the theoretical model. They assessed the importance of the coupling contributions using an ethanol–water distillation column as case study. Based on a film model, they derived a set of transport equations for the coupled transfer of mass and thermal energy and showed that coupling can have considerable contributions to the theoretical transfer rates.
According to irreversible thermodynamics, the local entropy production in a system is given by the product sum of its conjugate fluxes and driving forces. The entropy production in a process is directly related to its Second law efficiency. This is another reason for describing the system using irreversible thermodynamics.

7.1.3 Aim of the work

Accurate values of the thermal energy flux are essential when evaluating the energy and exergy efficiencies of distillation columns. The aim of the current work is to gain more insight into the contribution of coupling to the theoretical transfer rates in an air distillation column. Kjelstrup and De Koeijer [2003] assumed that the resistance to mass and thermal energy transfer is constant throughout the liquid and vapour films. To assess the validity of this assumption, a model will be presented that enables a description of these resistances as function of position in the films.

7.2 Modelling the vapour–liquid region

We model the vapour–liquid region at one single point in a distillation column. In the case of a packed column with negligible wall-effects, this corresponds to a single position on the length-axis of the column. Modern air distillation columns use structured packings as contacting equipment [Kerry, 2007]. In the case of a trayed column, this single point corresponds to the interface of a droplet or bubble at a single position on a tray.
Kjelstrup and De Koeijer [2003] modelled the vapour–liquid region as an interface film with a negligible thickness in between a liquid film of thickness d_l and a vapour film of thickness d_v. Each of these three films was modelled as a single control volume. It was assumed that the resistance to mass and thermal energy transfer is located in these films only; the bulk liquid and vapour phases next to the films have uniform temperatures and compositions. The model was described in more detail by Bedeaux and Kjelstrup [2004]. In the current work, we want to model the liquid and vapour films as series of connected control volumes while keeping the possibility to calculate the total entropy production in the system. This requires a change in the earlier description.

7.2.1 Entropy production

The starting point for the description of our system is a general expression for the local entropy production σ caused by heat transfer and diffusion:

$$\sigma = J'_q \left(\frac{\partial}{\partial x} \frac{1}{T} \right) + \sum_{j=1}^{n} J_j \left(-\frac{1}{T} \frac{\partial \mu_{j,T}}{\partial x} \right) \tag{7.1}$$

Here, J'_q is the measurable heat flux, J_j are the molar fluxes of the n components, the first bracketed term is the inverse temperature gradient and the last bracketed term contains the gradients of the chemical potentials evaluated at a constant temperature. The local entropy production of the interface σ^s, going from the liquid to the vapour,

is given by

$$\begin{aligned}\sigma^s &= J'_{q,v}\left(\frac{1}{T_v}-\frac{1}{T_l}\right) + \sum_{j=1}^{n} J_j\left(-\frac{\mu_{j,v}\left(T_l\right)-\mu_{j,l}\left(T_l\right)}{T_l}\right)\\ &= J'_{q,v}\left(\Delta_{lv}\frac{1}{T}\right) \quad + \sum_{j=1}^{n} J_j\left(-\frac{\Delta_{lv}\mu_j\left(T_l\right)}{T_l}\right)\end{aligned} \tag{7.2}$$

The subscript v indicates the vapour phase directly next to the interface and the subscript l indicates the liquid phase directly next to the interface. This expression assumes that the molar fluxes are equal on both sides of the interface, i.e. a steady state. When we write Equation (7.1) for the case of a one-dimensional difference d_x between the points a and b, we obtain a general expression similar to Equation (7.2):

$$d_x\sigma = J'_{q,b}\left(\Delta_{ab}\frac{1}{T}\right) + \sum_{j=1}^{n} J_j\left(-\frac{\Delta_{ab}\mu_j\left(T_a\right)}{T_a}\right) \tag{7.3}$$

When the liquid and vapour films each consist of m equally sized control volumes, the total local entropy production per unit of surface area is given by

$$\sigma^{tot} = \frac{d_l}{m}\sum_{k=1}^{m}\sigma_k^l + \sigma^s + \frac{d_v}{m}\sum_{k=1}^{m}\sigma_k^v \tag{7.4}$$

Alternatively, the total local entropy production can be calculated from the entropy balance using the partial molar entropies of the components S_j:

$$\sigma^{tot} = \sum_{j=1}^{n} J_j\left(S_{j,out}-S_{j,in}\right) + \left(\frac{J'_{q,out}}{T_{out}}-\frac{J'_{q,in}}{T_{in}}\right) \tag{7.5}$$

7.2.2 Force–flux relations

Equation (7.3) leads to the following force–flux relations for the liquid and vapour control volumes:

$$\Delta_{ab}\frac{1}{T} = r_{qq}^{ab}J'_{q,b} + \sum_{j=1}^{n} r_{qj}^{ab}J_j \tag{7.6}$$

$$-\frac{\Delta_{ab}\mu_i\left(T_a\right)}{T_a} = r_{iq}^{ab}J'_{q,b} + \sum_{j=1}^{n} r_{ij}^{ab}J_j \tag{7.7}$$

where r_{mn}^{ab} is the resistivity of the control volume between points a and b that is coupling driving force m with flux n, where $m,n \in q,i,j$. The resistivity matrix is symmetric, which means that $r_{mn} = r_{nm}$. For the interface, Equation (7.2) yields the

following force–flux relations:

$$\Delta_{lv}\frac{1}{T} = r_{qq}^{s,v}J'_{q,v} + \sum_{j=1}^{n} r_{qj}^{s,v}J_j \tag{7.8}$$

$$-\frac{\Delta_{lv}\mu_i\left(T_l\right)}{T_l} = r_{iq}^{s,v}J'_{q,v} + \sum_{j=1}^{n} r_{ij}^{s,v}J_j \tag{7.9}$$

In this formulation, the interface resistivities $r_{mn}^{s,v}$ are based on properties of the vapour phase directly next to the interface, where again $m, n \in q, i, j$.

7.2.3 Generalized force–flux relations

Both sets of force–flux relations in Section 7.2.2 describe one single control volume only. A control volume can be the liquid or the vapour film, a part of one of these films or the interface. Instead of modelling separate control volumes, we want to model a series of connected control volumes. When we apply the force–flux relations to each of the control volumes, the temperature differences can be directly combined to yield the total temperature difference. But each set of relations uses a different measurable heat flux and the chemical potentials are evaluated at different temperatures. It proves to be convenient to use the same measurable heat flux in all control volumes and to evaluate all chemical potentials at the same temperature. In order to accomplish this, we use the energy balance at stationary state to write a given measurable heat flux $J'_{q,c}$ in terms of another measurable heat flux:

$$J'_{q,0} = J'_{q,c} + \sum_{j=1}^{n} \Delta_{0c}H_jJ_j \tag{7.10}$$

Here, H_j are the partial molar enthalpies of the components. The subscript 0 refers to a certain reference point. When we assume that the partial molar enthalpies are independent of temperature within the temperature interval that is considered, we can write a difference in chemical potentials evaluated at a given temperature T_d in terms of a difference in chemical potentials evaluated at another temperature using:

$$-\frac{\Delta_{ab}\mu_j\left(T_0\right)}{T_0} = -\frac{\Delta_{ab}\mu_j\left(T_d\right)}{T_d} + \Delta_{ab}H_j\Delta_{0d}\frac{1}{T} \tag{7.11}$$

When applying Equations (7.10) and (7.11) to the force–flux relations, we obtain the following generalized expressions:

$$\Delta_{ab}\frac{1}{T} = r_{qq}^{ab}J'_{q,0} + \sum_{j=1}^{n}\left(r_{qj}^{ab} + r_{qq}^{ab}\Delta_{0b}H_j\right)J_j \tag{7.12}$$

$$-\frac{\Delta_{ab}\mu_i\left(T_0\right)}{T_0} = r_{iq}^{ab}J'_{q,0} + \sum_{j=1}^{n}\left(r_{ij}^{ab} + r_{iq}^{ab}\Delta_{0b}H_j\right)J_j + \Delta_{ab}H_i\Delta_{0a}\frac{1}{T} \tag{7.13}$$

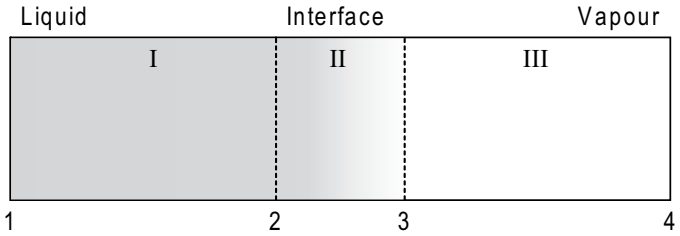

Figure 7.1: A schematic of a system containing three control volumes; one liquid volume, the vapour–liquid interface and one vapour volume.

Contrary to the sets of force–flux relations in Section 7.2.2, the fluxes and forces of the generalized expression are non-conjugate and the resistivity matrix is no longer symmetric.

7.2.4 Total resistivities

The next step is to use the generalized force–flux equations for the description of a series of connected control volumes. We will apply them to the system shown in Figure 7.1, consisting of three control volumes. We chose the reference temperature T_0 at the liquid boundary of the system, so at T_1. And we chose the reference measurable heat flux $J'_{q,0}$ at the vapour boundary of the system, so at $J'_{q,4}$. The generalized force–flux equations of the three control volumes are now given by

$$\Delta_{12}\frac{1}{T} = r^I_{qq}J'_{q,4} + \sum_{j=1}^{n}\left(r^I_{qj} + r^I_{qq}\Delta_{42}H_j\right)J_j \tag{7.14}$$

$$-\frac{\Delta_{12}\mu_i\left(T_1\right)}{T_1} = r^I_{iq}J'_{q,4} + \sum_{j=1}^{n}\left(r^I_{ij} + r^I_{iq}\Delta_{42}H_j\right)J_j \tag{7.15}$$

$$\Delta_{23}\frac{1}{T} = r^{II}_{qq}J'_{q,4} + \sum_{j=1}^{n}\left(r^{II}_{qj} + r^{II}_{qq}\Delta_{43}H_j\right)J_j \tag{7.16}$$

$$-\frac{\Delta_{23}\mu_i\left(T_1\right)}{T_1} = r^{II}_{iq}J'_{q,4} + \sum_{j=1}^{n}\left(r^{II}_{ij} + r^{II}_{iq}\Delta_{43}H_j\right)J_j + \Delta_{23}H_i\Delta_{12}\frac{1}{T} \tag{7.17}$$

$$\Delta_{34}\frac{1}{T} = r^{III}_{qq}J'_{q,4} + \sum_{j=1}^{n}r^{III}_{qj}J_j \tag{7.18}$$

$$-\frac{\Delta_{34}\mu_i\left(T_1\right)}{T_1} = r^{III}_{iq}J'_{q,4} + \sum_{j=1}^{n}r^{III}_{ij}J_j + \Delta_{34}H_i\Delta_{13}\frac{1}{T} \tag{7.19}$$

All driving forces of the control volumes can directly be added to yield the total driving forces of the system. Because we are considering a steady state, the molar fluxes are constant throughout the system. And since we have replaced all measurable heat fluxes with one single measurable heat flux, all fluxes are constant in the current description. Furthermore, it is important to note that the inverse temperature difference on the right-hand side of Figure 7.1 is given by Figure 7.1, and that the inverse temperature difference on the right-hand side of Figure 7.1 is given by the sum of Figures 7.1 and 7.1. Our last step is to find an expression for the total resistivity matrix of the system that corresponds to the fluxes and total driving forces. We can do this by calculating the sum of each matrix element over the control volumes:

$$r_{qq}^{tot} = r_{qq}^{I} + r_{qq}^{II} + r_{qq}^{III} = \sum_{k=I}^{III} r_{qq}^{k} \tag{7.20}$$

$$r_{qj}^{tot} = \sum_{k=I}^{III} r_{qj}^{k} + r_{qq}^{I}\Delta_{24}H_j + r_{qq}^{II}\Delta_{34}H_j \tag{7.21}$$

$$\begin{aligned} r_{jq}^{tot} &= \sum_{k=I}^{III} r_{jq}^{k} + r_{qq}^{I}\Delta_{23}H_j + \left(r_{qq}^{I} + r_{qq}^{II}\right)\Delta_{34}H_j \\ &= \sum_{k=I}^{III} r_{jq}^{k} + r_{qq}^{I}\Delta_{24}H_j + r_{qq}^{II}\Delta_{34}H_j = r_{qj}^{tot} \end{aligned} \tag{7.22}$$

$$\begin{aligned} r_{ij}^{tot} &= \sum_{k=I}^{III} r_{ij}^{k} + r_{iq}^{I}\Delta_{24}H_j + r_{iq}^{II}\Delta_{34}H_j + \left(r_{qj}^{I} + r_{qq}^{I}\Delta_{24}H_j\right)\Delta_{23}H_i \\ &\quad + \left(r_{qj}^{I} + r_{qj}^{II} + r_{qq}^{I}\Delta_{24}H_j + r_{qq}^{II}\Delta_{34}H_j\right)\Delta_{34}H_i \\ &= \sum_{k=I}^{III} r_{ij}^{k} + r_{iq}^{I}\Delta_{24}H_j + \left(r_{qj}^{I} + r_{qq}^{I}\Delta_{24}H_j\right)\Delta_{24}H_i \\ &\quad + r_{iq}^{II}\Delta_{34}H_j + \left(r_{qj}^{II} + r_{qq}^{II}\Delta_{34}H_j\right)\Delta_{34}H_i = r_{ji}^{tot} \end{aligned} \tag{7.23}$$

These equations show that the total resistivity matrix is symmetric again. The description can be extended to any number of connected control volumes. The number of control volumes can be increased by splitting up the liquid and vapour control volumes, see for example Figure 7.2.

7.3 Calculating resistivities

The air that is fed to an air distillation column can in practise be considered to be a mixture of nitrogen, oxygen and argon. Because the fraction of argon is very small, air is often assumed to be a mixture of nitrogen and oxygen only. In this work, we will model air as a binary mixture of nitrogen and oxygen.

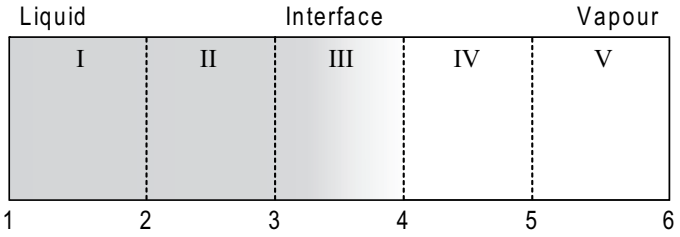

Figure 7.2: A schematic of a system containing five control volumes; two liquid volumes, the vapour–liquid interface and two vapour volumes.

7.3.1 Liquid and vapour phase resistivities

The resistivities of both homogeneous phases can be calculated from the thermal conductivity λ, the heat of transfer q^* and the Maxwell–Stefan interdiffusion coefficient $Đ$ [Kjelstrup and Bedeaux, 2008]. The required formulae, applied to a binary mixture of nitrogen and oxygen, are:

$$r_{qq} = \frac{1}{\lambda T^2} \tag{7.24}$$

$$r_{qN_2} = r_{N_2q} = -q^*_{N_2} r_{qq} \tag{7.25}$$

$$r_{qO_2} = r_{O_2q} = -\frac{x_{N_2}}{x_{O_2}} r_{qN_2} \tag{7.26}$$

$$r_{N_2N_2} = \frac{R}{cĐ}\frac{x_{O_2}}{x_{N_2}} + \frac{r_{qN_2} r_{N_2q}}{r_{qq}} \tag{7.27}$$

$$r_{N_2O_2} = r_{O_2N_2} = -\frac{x_{N_2}}{x_{O_2}} r_{N_2N_2} \tag{7.28}$$

$$r_{O_2O_2} = \frac{x^2_{N_2}}{x^2_{O_2}} r_{N_2N_2} \tag{7.29}$$

Here, x_j is the mole fraction of component j, R is the universal gas constant and c is the total molar concentration. These expressions are similar to the ones Kjelstrup and De Koeijer [2003] used, with two exceptions. The first exception is the use of the heat of transfer; Kjelstrup and De Koeijer used the Soret-coefficient S_T multiplied with a thermodynamic non-ideality factor instead. In a binary mixture, these two quantities are related to each other by

$$q^*_1 = x_2 S_T R T^2 \left(1 + x_1 \frac{\partial \ln \gamma_1}{\partial x_1}\right) = x_1 x_2 S_T T \frac{\partial \mu_1}{\partial x_1} \tag{7.30}$$

where γ_j is the activity coefficient of component j. The second exception is that we do take into account the coupling between thermal and molar fluxes in the vapour phase. Kjelstrup and De Koeijer neglected this coupling effect because the Soret-coefficient is much smaller in the vapour phase than in the liquid phase. However, the calculation of r_{qj} also involves r_{qq}. Because the latter is larger in the vapour phase,

the difference in r_{qj} is smaller than the difference in Soret-coefficients. Especially in a vapour controlled system, where the vapour film is much thicker than the liquid film, setting r^v_{qj} equal to zero can be a poor approximation.

Thermal conductivities

Thermal conductivities in the liquid phase can be calculated as a function of temperature, density and composition using the work of Lemmon and Jacobsen [2004] and Shan et al. [2000]. Lemmon and Jacobsen [2004] give formulae for calculating the pure component thermal conductivities of nitrogen, oxygen and argon. Shan et al. [2000] describe how these pure component thermal conductivities can be combined to yield the thermal conductivity of a mixture.
The vapour phase thermal conductivities can be calculated using the kinetic theory of gases, as described in the book by Hirschfelder et al. [1964]. Based on a 6-12 Lennard-Jones potential model, various mixture properties can be calculated as function of temperature, pressure and composition. More information on the calculation of the required collision integrals and related quantities is presented in Section 7.A.

Heats of transfer

The heats of transfer of both the liquid and the vapour phases are calculated based on the work of Kempers [2001]. He provides a relation for the thermal diffusion factor $\alpha_T = S_T T$ in terms of thermodynamic quantities:

$$\alpha_T = \frac{V_1 V_2}{x_1 V_1 + x_2 V_2} \frac{\frac{H_2 - H_2^0}{V_2} - \frac{H_1 - H_1^0}{V_1}}{x_1 \left(\frac{\partial \mu_1}{\partial x_1}\right)_{p,T}} + \frac{RT\alpha_T^0}{x_1 \left(\frac{\partial \mu_1}{\partial x_1}\right)_{p,T}} \tag{7.31}$$

where V_j is the partial molar volume of component j and the superscript 0 refers to the ideal gas state. The ideal gas thermal diffusion factor can be calculated from the thermal diffusion ratio $k_T = \alpha_T x_1 x_2$ using the kinetic theory of gases, see Section 7.A for more details. When we compare Equations (7.30) and (7.31), we see that the heat of transfer is given by

$$q_1^* = \left(\frac{V_1 V_2}{x_1 V_1 + x_2 V_2} \frac{\frac{H_2 - H_2^0}{V_2} - \frac{H_1 - H_1^0}{V_1}}{1} + \frac{RT\alpha_T^0}{1} \right) x_2 \tag{7.32}$$

Equation (7.31) requires accurate input values for the partial molar enthalpies and volumes. These quantities have been calculated using a thermodynamic model for mixtures of nitrogen, oxygen and argon by Lemmon et al. [2000]. This empirical thermodynamic model describes the Helmholtz energy of any mixture of the three components as a function of temperature and density. Combinations of derivatives of

the Helmholtz energy with respect to the temperature and density yield other thermodynamic quantities of the mixture, for example the enthalpy, the Gibbs energy or the entropy. Partial molar quantities of component j can be calculated by numerically evaluating the derivatives of these quantities with respect to the number of moles of component j, at constant temperature, pressure and numbers of moles of all other components. Some typical values of the quantities involved in the calculation of heats of transfer are given in Section 7.B.

Maxwell–Stefan diffusion coefficients

Liquid phase Maxwell–Stefan interdiffusion coefficients can be calculated following the work of Rutten [1992]. He proposes to use a modified Stokes–Einstein equation to calculate the diffusion coefficients at infinite dilution $Đ_{ij}^{i\to 0}$:

$$Đ_{ij}^{i\to 0} = \frac{kT}{n_{SE}^{o}\pi\eta_j R_i}\frac{R_j}{R_i} \tag{7.33}$$

Here, k is the Boltzmann constant, n_{SE}^{o} is an empirically determined constant which depends on the type of molecules involved, η_j is the viscosity of component j and R_j is its molecular diameter. The value of n_{SE}^{o} for non-associating mixtures is 2.40, based on critical molecular diameters. The viscosities of the pure components can be calculated based on the work of Lemmon and Jacobsen [2004]. The viscosity of a mixture can again be calculated using the mixture model of Shan et al. [2000]. Critical molecular diameters can be calculated from the critical volumes of the pure components. The diffusion coefficients at infinite dilution can subsequently be used to calculate the diffusion coefficient as function of the composition. Rutten [1992] describes the following interpolation scheme:

$$Đ = \frac{x_1\left(Đ^{2\to 0}\eta_1 R_2\right) + x_2\left(Đ^{1\to 0}\eta_2 R_1\right)}{\eta\left(x_1 R_2 + x_2 R_1\right)} \tag{7.34}$$

Vapour phase Maxwell–Stefan diffusion coefficients have been calculated using both the kinetic theory of gases and the thermodynamic model by Lemmon et al. [2000]. Kinetic theory has been used to calculate the more common Fick diffusion coefficients D. The thermodynamic model has been used to calculate the thermodynamic non-ideality factor that is required to relate Maxwell–Stefan diffusion coefficients to Fick diffusion coefficients:

$$D = Đ\left(1 + x_1\frac{\partial \ln\gamma_1}{\partial x_1}\right) \tag{7.35}$$

7.3.2 Interface resistivities

Obtaining the resistivities of the interface needs a different approach, because properties like the thermal conductivity and Maxwell–Stefan diffusion coefficients are generally not known for interfaces. Instead, the resistivities are calculated directly using the

kinetic theory gases. Kjelstrup and De Koeijer [2003] list the necessary equations for a binary mixture, they are derived from the more general formula for multi-component mixtures by Cipolla Jr. et al. [1974]. We use the relations given by Kjelstrup and De Koeijer with one modification. The temperature at the liquid side of the interface is used instead of the temperature at the vapour side of interface, as suggested by Kjelstrup and Bedeaux [2008, Chapter 22]. The vapour phase thermal conductivity values that are required in the calculations are obtained using kinetic theory, see Section 7.A for more details.

7.4 Solving the model

Now that we know how to model the vapour–liquid region using irreversible thermodynamics and how to calculate all resistivities required for a nitrogen–oxygen mixture, the final step is to combine this knowledge in a calculation.

7.4.1 Calculating fluxes

The main aim of the calculations is to find the values of the molar fluxes and the measurable heat flux, when the conditions at the liquid and vapour boundaries of the system are known. In order to do so, we have developed the following calculation routine:

1. Define the liquid and vapour boundary conditions.
2. Calculate the total driving forces ΔX_i^{tot} from the boundary conditions.
3. Choose a vapour film thickness, the number of control volumes per film, and an initial film thickness ratio.
4. Calculate initial guesses for the temperature profile $\boldsymbol{T}$, and mole fraction profiles $\boldsymbol{x_j}$.
5. Calculate the resistivities $\boldsymbol{r_{ij}^{cv}}$ of all control volumes and the partial molar enthalpies $\boldsymbol{H_j}$ at all control volume boundaries, using $\boldsymbol{T}$, $\boldsymbol{x_j}$ and the control volume thicknesses.
6. Calculate the total resistivity matrix R^{tot}, using $\boldsymbol{r_{ij}^{cv}}$ and $\boldsymbol{H_j}$.
7. Calculate the fluxes $J'_{q,0}$, J_{N_2} and J_{O_2}, using ΔX_i^{tot} and R^{tot}.
8. Calculate the measurable heat flux profile $\boldsymbol{J'_q}$, using $J'_{q,0}$ and $\boldsymbol{H_j}$.
9. Calculate the control volume driving forces $\boldsymbol{\Delta X_i^{cv}}$, using $\boldsymbol{r_{ij}^{cv}}$, $\boldsymbol{J'_q}$, J_{N_2} and J_{O_2}.
10. Calculate a new temperature profile $\boldsymbol{T}$, using $\boldsymbol{\Delta X_T^{cv}}$.
11. Calculate new mole fraction profiles $\boldsymbol{x_j}$, using $\boldsymbol{\Delta X_{\mu_j}^{cv}}$, $\boldsymbol{T}$ and $\boldsymbol{H_j}$.

12. Repeat steps 5 to 11 until the fluxes have converged.
13. Calculate the total entropy production, using $\boldsymbol{\Delta X_i^{cv}}$, $\boldsymbol{J'_q}$, J_{N_2} and J_{O_2}, and using the entropy balance.
14. Determine a new film thickness ratio that reduces the difference between the two total entropy productions.
15. Repeat steps 5 to 14 until the two total entropy productions are equal.
16. The model is now consistent.

Linear profiles between the two system boundaries are used as initial guesses for the temperature and mole fraction profiles. The control volume resistivities are calculated as described in Section 7.3. The liquid and vapour phase resistivities are calculated using the average control volume temperatures and mole fractions. They are subsequently multiplied with their control volume thicknesses. The interface resistivities refer to the interface thickness already, so they do not need to be multiplied with any thickness. Because we have assumed that the partial molar enthalpies are independent of temperature, we must evaluate all of them at the same temperature. We have chosen to use the average system temperature in our calculations.
The total resistivity matrix is calculated as described in Section 7.2.4. The flux vector can then easily be calculated by multiplying the inverse total resistivity matrix with the total driving force vector. Once the reference measurable heat flux is known, Equation (7.10) can be used to calculate the measurable heat flux profile. In combination with the molar fluxes and the control volume resistivities, the measurable heat flux profile can subsequently be used to obtain the driving forces of all control volumes using the equations in Section 7.2.2. A new temperature profile can then be calculated using the thermal driving forces.
The calculation of new mole fraction profiles consists of two sub-steps. First, the temperature at which the chemical potential differences are evaluated is changed from the control volume boundary temperature to the system boundary temperature that is used as reference temperature using Equation (7.11). This is the sub-step that requires the temperature and partial molar enthalpy profiles as input. During the second sub-step, the new composition profiles are obtained from the chemical potential differences by interpolation. We use a pre-generated table of chemical potentials as function of mole fractions. A one-dimensional interpolation is sufficient because there are only two components and because the temperature and pressure at which the chemical potentials are calculated are constant.
The fluxes are considered to have converged when the maximum relative change in the fluxes between to subsequent iterations is below a certain threshold value:

$$\max \left| 1 - \frac{J_i^{new}}{J_i^{old}} \right| < 10^{-4} \tag{7.36}$$

The entropy production of each control volume can be calculated using the final values of the fluxes and the control volume driving forces, as given by Equation (7.3). The

total entropy production can be calculated both using the final values of the fluxes and the total driving forces, and by summing over the entropy production of the separate control volumes. Because the entropy production can be calculated using these two methods, we have a way to check the consistency of the calculations.
A third way to calculate the total entropy production is by using the entropy balance, as given by Equation (7.5). In a consistent model, all calculated total entropy productions should be equal. We are using the difference between Equations (7.4) and (7.5) to find the film thickness ratio that results into a consistent model. The results of these two equations are considered to be equal when:

$$\left| 1 - \frac{\sigma^{tot}_{balance}}{\sigma^{tot}_{force-flux}} \right| < 10^{-4} \tag{7.37}$$

7.4.2 Input data

The calculation requires the system pressure and the temperatures and compositions at the system boundaries as input. We have obtained estimates for these values by simulating a simple one column design for the separation of air, using a standard equilibrium stage model. The maximum driving forces of a stage are defined by the temperatures and compositions of the incoming liquid and vapour streams. The minimum driving forces are related to the outgoing streams; they are zero in the case of an equilibrium stage. For each phase, we have used the average stage temperatures and compositions as input to our calculations. We have selected a stage around the centre of the top part of the column, where the driving forces are relatively constant. The vapour film thickness, the number of control volumes per film and the initial film thickness ratio need to be set as well. Taylor and Krishna [1993] give estimates for both film thicknesses; the vapour phase film thickness usually varies between 10^{-3} and 10^{-4} m, and the liquid film thickness between 10^{-4} and 10^{-5} m. The thickness of the interface is several orders of magnitude smaller. Kjelstrup and De Koeijer [2003] use a film thickness ratio of 1000 for the case of a vapour controlled system.
In this work we fix the vapour film thickness at a value of $5 \cdot 10^{-4}$ m and use an initial film thickness ratio of 500. The sensitivity of the final film thickness ratio to the chosen vapour film thickness is discussed in Section 7.5.3. The number of control volumes per film will be varied in order to investigate the effect that non-uniform film resistivities have on the results. The input data are summarized in Table 7.1.

7.4.3 Three model modifications

We will use three modifications to the routine that is described in Section 7.4.1. In the first modification, we set all control volume resistivities that couple a thermal and a molar flux to zero. This does not mean that the total resistivities coupling thermal and molar fluxes are zero, however, see Figures 7.1 and 7.1. We will use this modification to investigate the effect of neglecting coupling between thermal and molar fluxes. Because we want to investigate the effect it has on a given system, and not the effect it has on the solution method, the film thickness ratio must be the same

Table 7.1: Calculation input data

Input quantity	Value	
System pressure	1.40	(bar)
Liquid boundary temperature	82.05	(K)
Liquid boundary N_2 mole fraction	0.759	(-)
Vapour boundary temperature	82.61	(K)
Vapour boundary N_2 mole fraction	0.893	(-)
Vapour film thickness	$5.00 \cdot 10^{-4}$	(m)
Initial liquid film thickness	$1.00 \cdot 10^{-6}$	(m)

when comparing systems with and without coupling. This means that steps 14 and 15 from the routine described in Section 7.4.1 are skipped. The entropy production calculated using Equation (7.4) and using Equation (7.5) are not equal any more as a result.
In the second modification, we set all interface resistivities equal to zero. This will allow us to investigate the effect of neglecting the interface resistance. The film thickness ratio must again be the same when comparing systems with and without interface resistivities.
In the third modification, we invert the order of the control volumes. Instead of going from the liquid boundary to the vapour boundary, as shown in Figure 7.2, we now go from the vapour boundary to the liquid boundary. In theory, this change should not influence the results. So this modification offers us another way of checking the consistency of the calculations. The third modification will always be combined with the second modification. The reason for this is that the interface resistivities calculated from the kinetic theory of gases are only compatible with a description that is going from the liquid to vapour boundary, as given by Section 7.2.2. When going from the vapour to the liquid, we cannot use the same resistivities. So in order to make a fair comparison, we must compare descriptions that both neglect the interface resistance.

7.5 Results

The results of the calculations are divided into three parts. The first part discusses the characteristics of a base case system. In the second part, the base case system is used to investigate the effects of changing the number of control volumes, neglecting the coupling between thermal and molar fluxes and neglecting the interface resistance. In the third part we assess the sensitivity of the results with respect to the vapour film thickness, with respect to the transport properties that are used to calculate the resistivities and with respect to the order of the control volumes.

7.5.1 Base case system

The base case system is modelled as described in Section 7.4.1 and using the data presented in Section 7.4.2. The resulting film thickness ratio is dependent on the number of control volumes per film that is used. As will be shown in Section 7.5.2, the value of the ratio converges to a fixed value when increasing the number of control volumes. The base case system uses a number of 32 control volumes per film for both the liquid and the vapour film. This number ensures that the film thickness ratio deviates from its final value of 154.1 with less than 0.1%.

Transport properties and resistivities

Table 7.2 presents average values of the transport properties and resistivities in the homogeneous liquid and vapour phases. In order to facilitate a comparison between the two phases it also contains the V/L-ratios, which are the ratios between the values that the properties have in the vapour phase and the values they have in the liquid phase. When we compare the transport properties of the two phases, we see that they

Table 7.2: Typical values of the transport properties and resistivities in the liquid phase and in the vapour phase. The last column gives a comparison of these properties in the two phases, by showing the ratios between them.

Property		Liquid	Vapour	V/L-ratio
λ	$\left(\frac{J}{mKs}\right)$	$1.4 \cdot 10^{-1}$	$8.6 \cdot 10^{-3}$	1/16
$q^*_{N_2}$	$\left(\frac{J}{mol}\right)$	$-7.4 \cdot 10^{2}$	$-2.1 \cdot 10^{0}$	1/350
$Đ$	$\left(\frac{m^2}{s}\right)$	$4.3 \cdot 10^{-9}$	$1.3 \cdot 10^{-6}$	300
r_{qq}	$\left(\frac{ms}{JK}\right)$	$1.0 \cdot 10^{-3}$	$1.7 \cdot 10^{-2}$	17
r_{qN_2}	$\left(\frac{ms}{molK}\right)$	$7.7 \cdot 10^{-1}$	$3.5 \cdot 10^{-2}$	1/22
r_{qO_2}	$\left(\frac{ms}{molK}\right)$	$-2.4 \cdot 10^{-0}$	$-3.4 \cdot 10^{-1}$	1/7.1
$r_{N_2N_2}$	$\left(\frac{Jms}{mol^2K}\right)$	$2.9 \cdot 10^{4}$	$3.1 \cdot 10^{3}$	1/9.4
$r_{N_2O_2}$	$\left(\frac{Jms}{mol^2K}\right)$	$-9.0 \cdot 10^{4}$	$-3.0 \cdot 10^{4}$	1/3.3
$r_{O_2O_2}$	$\left(\frac{Jms}{mol^2K}\right)$	$2.8 \cdot 10^{5}$	$2.9 \cdot 10^{5}$	1.0

differ by several orders of magnitude. The ratios between the resulting resistivities are much smaller. The V/L-ratios of the r_{qj} are much smaller than the V/L ratio of the heats of transfer because of the multiplication with the thermal conductivity. The V/L-ratios of the r_{ij} are much smaller than the V/L-ratio of the Maxwell–Stefan diffusion coefficients because the two phases have very different total molar concentrations. The local resistance against heat transfer is the highest in the vapour phase. The local resistance against diffusion and the local coupling resistances are the highest

in the liquid phase.
The second Law of thermodynamics imposes two bounds on the value of the resistivities. The first bound requires that all diagonal resistivity matrix elements are non-negative. It can easily be verified that this is indeed the case. The second bound requires that the product of two diagonal elements is not smaller than the product of the corresponding off-diagonal elements: $r_{ii}r_{jj} \geq r_{ij}r_{ji}$. All resistivities calculated in this work satisfy this bound as well.
Table 7.3 presents the total resistivities of the three sub-systems: the liquid film, the interface and the vapour film. We see that all resistivities are largest in the vapour

Table 7.3: Comparison between the total resistivities of the liquid film, the interface and the vapour film.

Property		Liquid	Interface	Vapour
r^{cv}_{qq}	$\left(\frac{m^2 s}{JK}\right)$	$3.4 \cdot 10^{-9}$	$1.3 \cdot 10^{-8}$	$8.5 \cdot 10^{-6}$
$r^{cv}_{qN_2}$	$\left(\frac{m^2 s}{molK}\right)$	$2.5 \cdot 10^{-6}$	$3.5 \cdot 10^{-6}$	$1.8 \cdot 10^{-5}$
$r^{cv}_{qO_2}$	$\left(\frac{m^2 s}{molK}\right)$	$-7.9 \cdot 10^{-6}$	$4.8 \cdot 10^{-6}$	$-1.7 \cdot 10^{-4}$
$r^{cv}_{N_2N_2}$	$\left(\frac{Jm^2 s}{mol^2 K}\right)$	$9.3 \cdot 10^{-2}$	$1.8 \cdot 10^{-2}$	$1.6 \cdot 10^{0}$
$r^{cv}_{N_2O_2}$	$\left(\frac{Jm^2 s}{mol^2 K}\right)$	$-2.9 \cdot 10^{-1}$	$6.1 \cdot 10^{-4}$	$-1.5 \cdot 10^{1}$
$r^{cv}_{O_2O_2}$	$\left(\frac{Jm^2 s}{mol^2 K}\right)$	$9.2 \cdot 10^{-1}$	$2.1 \cdot 10^{-1}$	$1.5 \cdot 10^{2}$

film. The fact that the r^{cv}_{qj} are the largest in the vapour phase shows that neglecting them can introduce serious errors. The magnitudes of the liquid film and interface resistivities are of the same order, with the exception of $r^{cv}_{N_2O_2}$. Contrary to the liquid and vapour film resistivities, all interface resistivities are positive.

Fluxes, forces and entropy production

For the selected input data, the fluxes amount to $J_{N_2} = 14.1$ mmol/m^{2}s, $J_{O_2} = -14.9$ mmol/m^{2}s and $J'_{q,0} = -9.98$ J/m^{2}s. The reference measurable heat flux is the flux at the vapour boundary of the system. The measurable heat flux at the liquid boundary of the system amounts to $J'_{q,l} = -35.9$ J/m^{2}s. A positive sign means that a flux is going from the liquid to the vapour phase and a negative sign indicates the opposite direction. The total molar flux is negative, so condensation is the overall effect. At the vapour boundary thermal energy is entering the system and at the liquid boundary it is leaving the system. So overall, thermal energy is leaving the system. Thermal energy is usually being released during condensation, so the thermal and molar fluxes are in agreement with each other.
Table 7.4 presents the driving forces of the three separate sub-systems and of the total system. This table suggests that the vapour film controls the system; the changes in

Table 7.4: Comparison between the driving force of the liquid film, the interface, the vapour film and the total system.

System	$\Delta\frac{1}{T}\ \left(\frac{1}{K}\right)$	$-\frac{\Delta\mu_{N_2}}{T_0}\ \left(\frac{J}{molK}\right)$	$-\frac{\Delta\mu_{O_2}}{T_0}\ \left(\frac{J}{molK}\right)$
Liquid film	$3.13 \cdot 10^{-8}$	$5.58 \cdot 10^{-3}$	$-1.75 \cdot 10^{-2}$
Interface	$-1.47 \cdot 10^{-7}$	$3.79 \cdot 10^{-4}$	$-2.91 \cdot 10^{-3}$
Vapour film	$-8.25 \cdot 10^{-5}$	$2.46 \cdot 10^{-1}$	$-2.40 \cdot 10^{-0}$
Total	$-8.26 \cdot 10^{-5}$	$2.52 \cdot 10^{-1}$	$-2.42 \cdot 10^{-0}$

the temperature and chemical potentials are almost completely located in the vapour film. The liquid film accounts for a small part of the total diffusional driving forces, but its contribution to the thermal driving force is practically zero. For the interface it is the other way around; its influence on the diffusional forces is negligible and it accounts for a small part of the total thermal force.
The total entropy production in the system amounts to $\sigma_{tot} = 4.04 \cdot 10^{-2}$ J/sKm^2. Table 7.5 presents how it is distributed over the three sub-systems and over the three entropy production components. When comparing the total contributions of

Table 7.5: Distributions of the total entropy production over its three components and over the three sub-systems.

System	σ_q^{cv}	$\sigma_{N_2}^{cv}$	$\sigma_{O_2}^{cv}$	σ_{tot}^{cv}
Liquid film	−0.00 %	0.19 %	0.65 %	0.84 %
Interface	0.00 %	0.00 %	0.12 %	0.13 %
Vapour film	2.04 %	8.58 %	88.42 %	99.04 %
Total	2.04 %	8.78 %	89.18 %	100.00 %

the three components, we see that the thermal component amounts to only 2% of the total entropy production. The oxygen component seems to contribute the most, but since the two molar fluxes are dependent it is probably better to consider their contributions as one single diffusion contribution. When we look at the contributions of the three sub-systems, we see that the interface hardly produces entropy and that the entropy production in the liquid film is small as well. The vapour film controls the entropy production, as expected from Tables 7.3 and 7.4. Diffusion in the vapour film is responsible for the major part of the entropy production, it produces 97% of the total production.

7.5.2 System modifications

The film thickness ratio was fixed at the base case value while assessing the effects of increasing the number of control volumes and of the first two system modifications

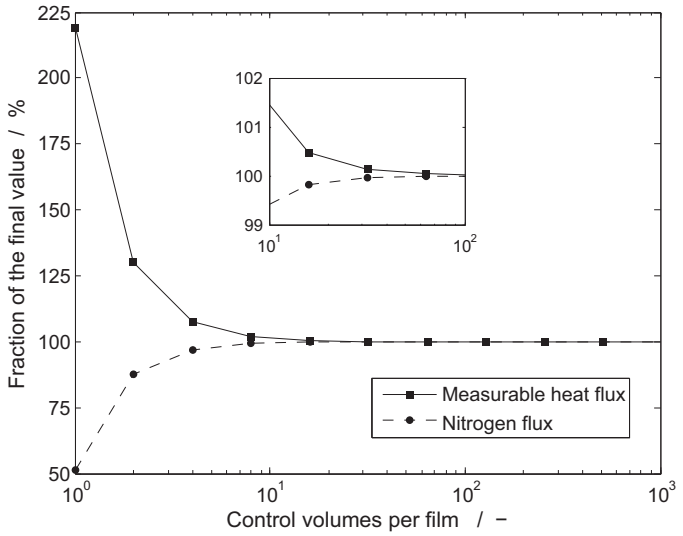

Figure 7.3: The measurable heat flux at the liquid boundary and the nitrogen flux as percentage of the values they attain when increasing the number of control volumes to a very high value. The inset shows a magnification of the region between 10 and 100 control volumes per film.

presented in Section 7.4.3.

Increasing the number of control volumes

Figure 7.3 shows how the measurable heat flux at the liquid boundary and the nitrogen flux change when the number of control volumes per film is increased from one up to 1024. The values of the fluxes converge to constant values when the number of control volumes is increased. Using only one control volume per film yields values that are a factor two different from the converged values. So using a small number of control volumes can cause serious errors in the results, because the dependency of the resistivities on temperature and composition is not properly accounted for. Using 32 control volumes per film ensures that the difference between the results and the final values is within 0.1%. This number has been used in all other calculations.
The measurable heat flux at the vapour boundary and the oxygen flux are not shown in Figure 7.3. They show similar trends, but the magnitude of the deviation is smaller. The values of these fluxes when using one control volume per film are 99.85% and 105.4% of the values they attain when using 1024 control volumes per film.
Figure 7.4 illustrates how increasing the number of control volumes affects the profiles of the film resistivities, r^v_{qq} has been used as example. When only one control volume per film is used, the resistivities have constant values throughout a film. Upon in-

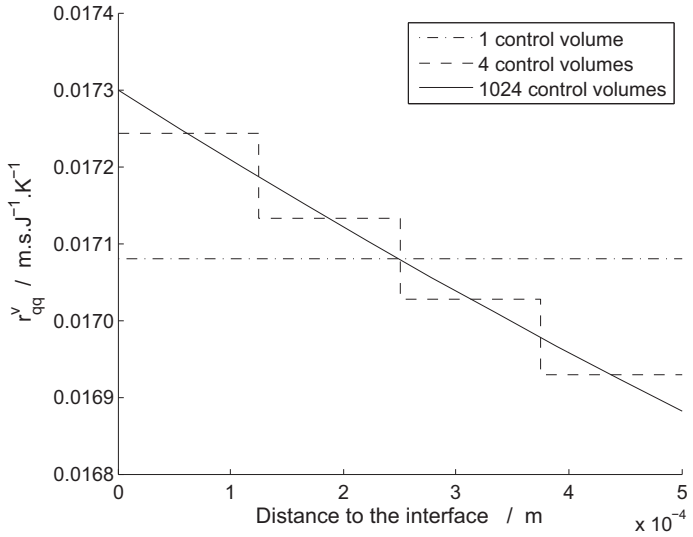

Figure 7.4: Typical resistivity profiles in systems consisting of 1, 4 or 1024 control volumes per film.

creasing the number of control volumes, the resistivity profiles adopt a stairlike shape as is the case for a system with 4 control volumes per film. When the number of control volumes reaches a very high value, for example 1024, the stairlike shape starts looking like a continuous, but no longer horizontal, line.

Neglecting coupling and interface resistances

Table 7.6 presents the effects of neglecting the coupling between thermal and molar fluxes and neglecting the interface resistance. Neglect of coupling in the films has a

Table 7.6: The molar and measurable heat fluxes for systems with and without coupling and interface resistances.

Coupling?		Yes	No	Yes	No
Interface?		Yes	Yes	No	No
J_{N_2}	$\left(\frac{mmol}{m^2 s}\right)$	14.1	18.3	13.8	18.7
J_{O_2}	$\left(\frac{mmol}{m^2 s}\right)$	-14.9	-14.4	-15.0	-14.4
$J'_{q,l}$	$\left(\frac{J}{m^2 s}\right)$	-35.9	-9.43	-38.1	-7.36
$J'_{q,v}$	$\left(\frac{J}{m^2 s}\right)$	-9.98	-9.65	-10.0	-9.67

big effect on the calculated fluxes. The nitrogen flux becomes 30% bigger and the measurable heat flux at the liquid boundary decreases with 75%. Both the oxygen flux and the measurable heat flux at the vapour boundary decrease with 3%. The sign of the total molar flux changes from negative to positive in the systems without coupling, so the net effect is now evaporation instead of condensation. The measurable heat flux at the vapour boundary is bigger than the measurable heat flux at the liquid boundary in these systems. So thermal energy is added, which corresponds to evaporation.
Neglecting the interface resistances also has a considerable effect on the calculated fluxes, but it is less profound than the effect of neglecting coupling. The nitrogen flux decreases with 2% and the measurable heat flux at the liquid boundary increases with 6%. The oxygen flux and the measurable heat flux at the vapour boundary increase with less than half a percent.
In both system modifications, the change in nitrogen flux has the opposite sign of the changes in the other three fluxes.

7.5.3 Sensitivity analysis

We have investigated the dependency of the results shown in Sections 7.5.1 and 7.5.2 on the values of the transport properties, on the vapour film thickness and on the order of the control volumes.

Transport properties

The film thickness ratio is fixed at the base case value while assessing the effects of possible errors in the values of the transport properties of the homogeneous phases and in the interface resistivities. Table 7.7 presents the deviations of the calculation results with respect to the base case values when errors of +5% are introduced. The

Table 7.7: Sensitivity of the results to +5 % deviations in the transport properties.

	J_{N_2}	J_{O_2}	$J'_{q,l}$	$J'_{q,v}$	σ_{tot}
λ_l	−0.3 %	0.0 %	0.8 %	0.0 %	0.0 %
λ_v	−0.4 %	0.0 %	−0.3 %	−4.8 %	−0.1 %
$q^*_{N_2,l}$	1.7 %	−0.2 %	−4.1 %	0.0 %	0.0 %
$q^*_{N_2,v}$	−0.0 %	0.0 %	−0.0 %	−0.2 %	−0.0 %
$Đ_l$	−6.8 %	0.6 %	16.2 %	−0.0 %	−0.0 %
$Đ_v$	2.4 %	−5.7 %	−21.4 %	−0.1 %	−4.9 %
$r^{s,v}_{ij}$	−0.1 %	0.0 %	0.3 %	0.0 %	0.0 %

results are relatively insensitive to errors in the interface resistivities and in the vapour phase heat of transfer. Errors in the thermal conductivities of both phases mainly

influence their corresponding measurable heat fluxes, but they also have a small effect on the nitrogen flux. Errors in the liquid phase heat of transfer and in both Maxwell–Stefan diffusion coefficients have considerable effects on the molar fluxes and on the measurable heat flux at the liquid boundary. The value of the measurable heat flux at the vapour boundary is almost only dependent on the vapour phase thermal conductivity. The total entropy production practically only depends on the vapour phase Maxwell–Stefan diffusion coefficient.
Kempers [2001] estimates the uncertainty in the vapour phase thermal diffusion factor around 25% and the uncertainty in the liquid phase thermal diffusion factor is even higher. The accuracy of the calculated thermal diffusion factors is highly dependent on the accuracy of the thermodynamic model that is used, especially in the liquid phase. This work uses a very accurate thermodynamic model, uncertainties in the thermodynamic properties are below 0.1% [Lemmon et al., 2000]. So it can be expected that the uncertainty in the calculated heats of transfer is lower.
The uncertainties in the interface resistivities are not important, because the results are relatively insensitive to errors in these resistivities. The uncertainty in the liquid phase Maxwell–Stefan diffusion coefficient is around 5%. This has a considerable effect on the accuracy of the nitrogen flux and of the liquid boundary measurable heat flux. The uncertainties in the other transport properties are around 2%. This means that accurate values of the vapour phase Maxwell–Stefan diffusion coefficient are still important for the quality of the results.
Overall, it is most important to use accurate values of the liquid phase heat of transfer and of the two Maxwell–Stefan diffusion coefficients. The liquid boundary measurable heat flux is most sensitive to errors in the transport properties.

Vapour film thickness

Taylor and Krishna [1993] estimate the vapour film thickness to be in between 10^{-4} and 10^{-3} m. The base case system presented in Section 7.5.1 uses a value of $5 \cdot 10^{-4}$ m, resulting in a final film thickness ratio of 154.1. Figure 7.5 shows how the film thickness ratio changes when other vapour film thicknesses are used. Doubling the vapour film thickness increases the film thickness ratio with 1% and halving it decreases the film thickness ratio with 2%. The vapour film thickness range estimated by Taylor and Krishna [1993], which spans one order of magnitude, corresponds to a film thickness ratio range from 145 to 155. So the film thickness ratio is relatively insensitive to the chosen vapour film thickness.
Figure 7.6 shows how the effects of neglecting coupling and neglecting the interface resistance depend on the vapour film thickness. Only the two fluxes that are most sensitive to these neglects are shown. The effect of neglecting the coupling between the thermal and molar fluxes becomes smaller as the vapour film thickness decreases, but it is considerable in the entire range of vapour film thicknesses. Combining this observation with the trend shown in Figure 7.5 leads to the conclusion that the coupling is mainly located in the vapour film. The effect of neglecting the interface resistance increases when the vapour film thickness becomes smaller. This is logical,

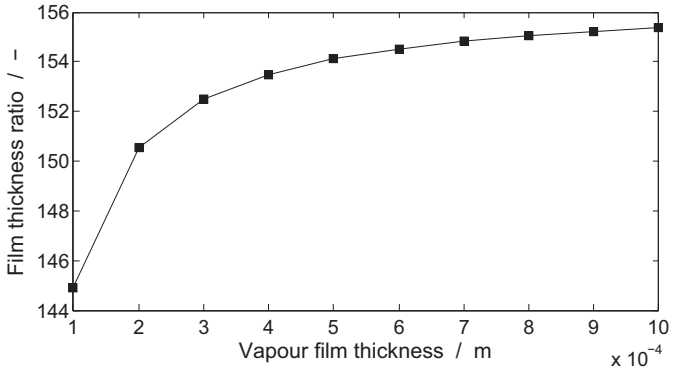

Figure 7.5: The calculated film thickness ratio as function of the fixed value of the vapour film thickness.

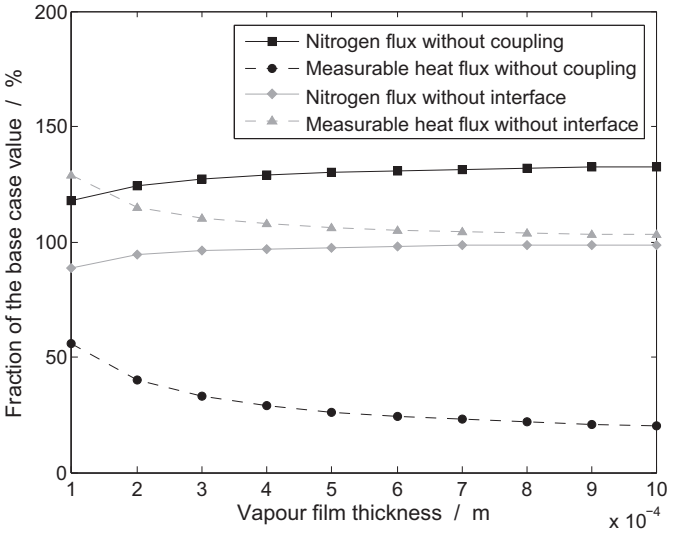

Figure 7.6: The nitrogen flux and the measurable heat flux at the liquid boundary for a system without coupling and a system without interface resistance. The fluxes are given as percentage of the values they have in base case system, which includes both coupling and the interface resistance.

because the contribution of the interface resistance to the total resistance increases as the vapour phase resistivity decreases. Neglecting the interface resistivity might be acceptable in the case of a large vapour film thickness, but the coupling between thermal and molar fluxes should never be neglected.

Inverting the control volume order

As explained in Section 7.4.3, the order of the control volumes should not influence the results. Table 7.8 presents a comparison between calculations using the two possible control volumes orders. The film thickness ratio is not fixed during these calculations. Systems with and without coupling between the thermal and molar fluxes are considered. Table 7.8 presents that changing the control volume order, so starting at the

Table 7.8: Comparison between the results of systems with a control volume order going from the liquid boundary to the vapour boundary (L-V) and systems with a control volume order going from the vapour boundary to the liquid boundary (V-L).

Order:		$L-V$	$V-L$	$L-V$	$V-L$
Coupling?		Yes	Yes	No	No
J_{N_2}	$\left(\frac{mmol}{m^2 s}\right)$	14.11	14.11	14.07	14.07
J_{O_2}	$\left(\frac{mmol}{m^2 s}\right)$	−14.92	−14.92	−14.87	−14.87
$J'_{q,l}$	$\left(\frac{J}{m^2 s}\right)$	−35.94	−35.94	−35.52	−35.52
$J'_{q,v}$	$\left(\frac{J}{m^2 s}\right)$	−10.00	−10.00	−9.652	−9.652
d_v/d_l	$(-)$	156.6	156.6	125.1	125.0

vapour boundary and going to the liquid boundary (V-L) instead of the other way around (L-V), does indeed not influence the results. This confirms the consistency of the calculation method. The results of the L-V systems are different from the ones presented in Table 7.6 because the film thickness ratio is fixed to the base case value during the calculations of the latter.

7.6 Discussion

7.6.1 Comparison with the work of Kjelstrup and de Koeijer

The current work can be seen as a continuation of the work of Kjelstrup and De Koeijer [2003]. It is therefore useful to give a clear overview of the main similarities and differences between the two works. This work concerns the vapour–liquid region of a nitrogen–oxygen mixture at one single location in a distillation column. Starting from values for the bulk-phase properties next to the vapour–liquid region, we have been able to calculate the thermal energy and molar fluxes through the interface.

Using the values of these fluxes, we have subsequently been able to calculate the local entropy production in the system.
The calculations done by Kjelstrup and De Koeijer were based on experimental data of an ethanol–water separation column. Starting from measured values for all compositions, the vapour and liquid rates and the temperatures in the liquid, they calculated the resistivities and entropy productions of all trays in the column.

Calculating local fluxes instead of average tray forces

The first big difference between the two works is the size of the system that is modelled. In the current work we consider the vapour–liquid region at one single location only, while Kjelstrup and De Koeijer considered entire trays. The aim of their calculations was to find average tray driving forces, starting from the total transfer rates on a tray. We do the calculation the other way around; starting from the driving forces, we calculate the fluxes. Both approaches require values for the resistivities as input, and both allow the calculation of the entropy production from the fluxes and forces in the end.

Film thickness ratio

Another important difference is the method used for calculating the film thicknesses and the film thickness ratio. Kjelstrup and De Koeijer fixed the film thickness ratio and used the difference between the entropy production from an entropy balance and from the fluxes and forces to find a liquid film thickness. They used vapour-to-liquid film thickness ratios of 1000 and 0.1, resulting in vapour film thicknesses of $2 \cdot 10^{-4}$ and $1 \cdot 10^{-3}$ m.
In this work, we fix the vapour film thickness and find the film thickness ratio using the difference between the entropy production from an entropy balance and from the fluxes and forces. We use a vapour film thickness of $5 \cdot 10^{-4}$ m. The resulting film thickness ratio was about 150, and a sensitivity analysis showed that it hardly changes when varying the vapour film thickness.
The vapour film thicknesses used in both works are comparable, but the dependencies between the film thickness ratio and the vapour film thickness are very different. This difference is probably related to the sizes of the systems that are considered. In this work we are considering one vapour–liquid region only. We calculate the film thickness ratio for this specific region by requiring the entropy productions calculated from the entropy balance and from the fluxes and forces to match exactly. Kjelstrup and De Koeijer considered a series of trays. They calculated one liquid film thickness for all trays by minimising the sum of the squared differences between the entropy productions calculated from the entropy balance and from the fluxes and forces. As a result, the entropy productions do not match exactly for any of the trays. So by using one single liquid film thickness for all trays, they were forced to allow inconsistencies

in the entropy productions on every tray. These inconsistencies translate into wrong film thicknesses, which can explain the difference in dependencies between the film thickness ratio and the vapour film thickness.

Including coupling in the vapour phase

As has already been discussed in Section 7.3.1, Kjelstrup and De Koeijer neglect the coupling between thermal and molar fluxes in the vapour phase. In this work we include this coupling effect as well. In Section 7.5.1 we show that the resistivity coefficient that is coupling these two fluxes can be bigger in the vapour phase than in the liquid phase. This supports our choice for including it in the model.

Varying film resistivities

One of the research aims of this work was to investigate the influence of modelling the film resistivities as function of the position in the film. In Section 7.5.3 we show that allowing varying film resistivities can make a big difference on the calculated fluxes, compared to fixing them at constant values as was done by Kjelstrup and De Koeijer.

Common conclusions

Both works agree very well on what the main contributions to the total entropy production in the system are. Diffusion was the most important entropy producing process in both system, the contribution of heat was small. And in both cases, the entropy production of the interface was very small. Another important shared conclusion is that the coupling between thermal and molar fluxes should not be neglected.

7.6.2 Sensitivity of the measurable heat fluxes

The results presented in Sections 7.5.1 to 7.5.3 show that especially the measurable heat flux at the liquid boundary is very sensitive to the correctness of the model and the accuracy of input data. As explained in the introduction, accurate values of the heat fluxes are important when optimising distillation columns designs. Especially in the case of heat-integrated and diabatic columns it is essential to accurately predict the local thermal effects. This underlines the importance of using a model that properly captures all contributions to the heat fluxes.

7.6.3 Alternative interface resistivities

Recent work by Glavatskiy [2009] suggests that the off-diagonal interface resistivities given by kinetic theory are underestimates. In addition, he predicts that the off-diagonal resistivity that is coupling the two molar fluxes is negative instead of positive.

As can be seen in Table 7.3, this corresponds well with the relative magnitudes and the signs of these resistivities in the homogeneous phases. Table 7.9 presents the effect of neglecting the interface resistances for the base case system and for a system in which $r^{s,v}_{qN_2}$ and $r^{s,v}_{qO_2}$ are 5 times their base case values and $r^{s,v}_{N_2O_2}$ is -50 times its base case value. When using the changes in off-diagonal resistivities suggested by the

Table 7.9: The molar and measurable heat fluxes of systems without interface resistances, relative to their values in systems with interface resistances.

System	J_{N_2}	J_{O_2}	$J'_{q,l}$	$J'_{q,v}$
Base case	97.6%	100.4%	106.1%	100.2%
Adjusted $r^{s,v}_{nm}$	108.2%	99.3%	80.9%	100.3%

results of Glavatskiy, the influence of the interface resistance on the fluxes becomes a factor two larger. The effect of neglecting the interface resistance is still smaller than the effect of neglecting coupling, but it is now significant even in the case of a large vapour film thickness.

7.6.4 Predictive use of the model

In this work, the presented model is used to assess the contribution of coupling. The model uses the vapour film thickness as input. Although the vapour film thickness has little influence on the coupling contribution, it does influence the magnitude of the calculated fluxes. In order to use the model as a predictive tool, an empirically determined value for the vapour film thickness is required.
Current rate-based models use empirical relations to calculate mass-transfer and heat-transfer coefficients. When using a film model, these coefficients can be used to obtain values for the film thicknesses. The current empirical relations can not directly be used to calculate film thicknesses for the presented model. The existing relations must account for the effects of coupling, but in the presented model these contributions are brought out specifically. This means that new empirical relations for the film thicknesses are required. Relations for only one film thickness are required, however, because the thickness of the other film is an output of the model.

7.6.5 Applicability of the model

The model presented in this work describes one single point in a distillation column. A logical next step is to extend the model to an entire tray or column. Such an extension requires the interfacial area and the liquid and vapour flow rates as additional variables. The variation in these variables depends on the type of contacting equipment that is used. When using structured packing, the variables are relatively well-defined. In the case of trayed columns, the situation becomes more complicated. The different flow regimes that can be observed make it much harder to accurately predict these variables at every point on the tray.

In this work, the presented model is used to describe transport through a vapour–liquid interface. The model can also be used to describe transport through liquid–liquid interfaces. So when the model is extended from a single point to an entire tray or column, it will be possible to model a wide variety of separation columns.
Similar to other rate-based models, the current model is most useful in situations where the transfer processes are too slow to reach equilibrium within the available time frame. This means that it is useful for all packed columns. In the case of trayed columns, it depends on the tray design. If the trays are designed in such a way that the outgoing streams are practically at equilibrium, the use of a rate-based method is not necessary.

7.7 Conclusions

A calculation method has been presented that can be used to model the coupled transfer of mass and thermal energy in the vapour–liquid region of a binary mixture. The entropy production calculated as the product-sum of the conjugate fluxes and driving forces and the entropy production calculated from the entropy balance is used to determine ratio between the vapour and liquid film thicknesses. Both the vapour and liquid films are modelled as series of multiple connected control volumes.
The calculation method has been applied to a nitrogen–oxygen mixture, using boundaries conditions based on simplified air distillation data. The calculated values of the thermal and molar fluxes are highly dependent on the coupling between the thermal and molar fluxes. They are slightly dependent on the interface resistance. By increasing the number of control volumes that is used to represent the liquid and vapour films, it has been shown that the resistivity profiles in the films can have a large influence on the calculated values of the fluxes.
The resistivities in the vapour film dominate the system; the vapour film resistivities that are coupling the thermal and molar fluxes should not be neglected. Diffusion in the vapour phase is responsible for most of the entropy production. The calculated film thickness ratio of 154 is insensitive to changes in the vapour film thickness. The effects of neglecting coupling and neglecting the interface resistance depend on the vapour film thickness. The latter might be acceptable in the case of a large vapour film thickness, but the former should never be done.
The accuracy of the calculation results is especially sensitive to uncertainties in the Maxwell–Stefan diffusion coefficients and in the liquid phase heat of transfer. The measurable heat flux at the liquid boundary of the system is the flux that is most sensitive to uncertainties in the transfer properties, to the neglect of coupling and to the neglect of the interface resistance. These results provide useful insights for the modelling and optimisation of air distillation columns, especially in the case of heat-integrated and diabatic designs.

Notation

c	total molar concentration, $\mathrm{mol/m^3}$
D	Fick diffusion coefficient, $\mathrm{m^2/s}$

$Đ$	Maxwell-Stefan diffusion coefficient, m^2/s
d_l	liquid film thickness, m
d_v	vapour film thickness, m
H_j	partial molar enthalpy of component j, J/mol
J_j	molar flux of component j, mol/s m^2
J'_q	measurable heat flux, J/s m^2
k	Boltzmann constant, $1.3807 \cdot 10^{-23}$ kg m^2/s^2 K
k_T	thermal diffusion ratio, dimensionless
m	number of control volumes per film, dimensionless
n	number of components, dimensionless
n^o_{SE}	empirical constant of 2.40, dimensionless
S_j	partial molar entropy of component j, J/K mol
S_T	Soret coefficient, 1/K
q^*	heat of transfer, J/mol
R	universal gas constant, 8.3145 J/K mol
R_j	molecular diameter of component j, m
R^{tot}	resistivity matrix of the total system
r_{mn}	local resistivity coupling driving force m with flux n, where $m, n \in q, N_2, O_2$
r^k	resistivity of control volume k
T	temperature, K
V_j	partial molar volume of component j, m^3/mol
x	spatial coordinate, m
x_j	mole fraction of component j, dimensionless
ΔX_i	driving force of type i

Greek symbols

α_T	thermal diffusion factor, dimensionless
γ_j	activity coefficient of component j, dimensionless
$\Delta_{ab}Y$	difference in property Y: $Y_b - Y_a$
η	viscosity, kg / m s
λ	thermal conductivity, J/s K m^2
μ_j	chemical potential of component j, J/mol
σ	local entropy production, J/K m^3 or J/K m^2

Sub- and superscripts

0	reference point or ideal gas state
a, b, c, d	points on the x-axis
cv	control volumes
i, j	component indices
k	control volume index
l	liquid
q	thermal energy
s	interface
T	(constant) temperature
tot	total

v vapour

Acknowledgements

The research leading to these results has received funding from the European Community's 7th Framework Programme (FP7/2007-2013) under grant agreement number 211971 (The DECARBit project).

7.A Polynomial fits for kinetic theory calculations

We calculate the vapour phase thermal conductivities, thermal diffusion ratios and Fick diffusion coefficients using the kinetic theory of gases, as described in the book by Hirschfelder et al. [1964]. A 6–12 Lennard-Jones potential model is used to calculate these properties as function of temperature, pressure and composition. In order to obtain values for the required collision integrals and related quantities, Hirschfelder et al. provide tables with their values as function of the reduced temperature T_r. The reduced temperature is given by the actual temperature divided by the force constant of a component. To facilitate the interpolation of these data, we have fitted polynomial functions through the data points as functions of the natural logarithm of the reduced temperature. Use of the natural logarithm was suggested by Shan et al. [2000] and proved to give a more accurate fit through the data points. The fitting was done using Excel. Five polynomial term were needed to represent the values of Hirschfelder et al. satisfactory. All of the quantities Q that were required for the transport property calculations can be calculated using the following equation:

$$Q = c_0 + c_1 \ln T_r + c_2 \left(\ln T_r\right)^2 + c_3 \left(\ln T_r\right)^3 + c_4 \left(\ln T_r\right)^4 \tag{7.38}$$

The values of the coefficients c_i are given in Table 7.10 along with the R^2 values provided by Excel. We only used the data points for the reduced temperature range from 0.5 to 5.0 as a basis for the fit, which corresponds to 61 values of the reduced temperature. All temperatures relevant for our calculations are within this range. Figure 7.7 shows how the polynomial functions of the two fits with the lowest R^2 values match the data points from Hirschfelder et al..

7.B Contributions to the heats of transfer

In Section 7.3.1 we present an equation that can be used for the calculation of heats of transfer. Applied to a nitrogen–oxygen mixture, this equation looks as follows:

$$q^*_{N_2} = \left(\frac{V_{N_2} V_{O_2}}{x_{N_2} V_{N_2} + x_{O_2} V_{O_2}} \frac{\frac{H_{O_2} - H^0_{O_2}}{V_{O_2}} - \frac{H_{N_2} - H^0_{N_2}}{V_{N_2}}}{1} + \frac{RT\alpha^0_T}{1} \right) x_{O_2} \tag{7.39}$$

Calculating heats of transfer is not very common and in order to provide more insight into the contributions to the heats of transfer, we have listed values of all input

Table 7.10: Polynomial fit coefficients for calculation of the transport properties using a Lennard-Jones (6-12) potential.

Q	c_0	c_1	c_2	c_3	c_4	R^2
$\Omega^{(1,1)\star}$	$1.4401 \cdot 10^{-0}$	$-7.029 \cdot 10^{-1}$	$2.773 \cdot 10^{-1}$	$-3.132 \cdot 10^{-2}$	$-8.305 \cdot 10^{-3}$	1.0000
$\Omega^{(1,2)\star}$	$1.2044 \cdot 10^{-0}$	$-5.114 \cdot 10^{-1}$	$2.544 \cdot 10^{-1}$	$-7.207 \cdot 10^{-2}$	$6.619 \cdot 10^{-3}$	1.0000
$\Omega^{(1,3)\star}$	$1.0761 \cdot 10^{-0}$	$-3.818 \cdot 10^{-1}$	$2.049 \cdot 10^{-1}$	$-7.817 \cdot 10^{-2}$	$1.263 \cdot 10^{-2}$	1.0000
$\Omega^{(2,2)\star}$	$1.5885 \cdot 10^{-0}$	$-7.908 \cdot 10^{-1}$	$2.813 \cdot 10^{-1}$	$1.320 \cdot 10^{-2}$	$-2.614 \cdot 10^{-2}$	1.0000
$A^\star$	$1.1028 \cdot 10^{-0}$	$-1.294 \cdot 10^{-2}$	$-1.547 \cdot 10^{-2}$	$2.897 \cdot 10^{-2}$	$-9.280 \cdot 10^{-3}$	0.9846
$B^\star$	$1.1924 \cdot 10^{-0}$	$-1.342 \cdot 10^{-1}$	$2.661 \cdot 10^{-2}$	$3.025 \cdot 10^{-2}$	$-1.188 \cdot 10^{-2}$	0.9995
$C^\star$	$8.3678 \cdot 10^{-1}$	$5.505 \cdot 10^{-2}$	$3.581 \cdot 10^{-2}$	$-2.709 \cdot 10^{-2}$	$3.900 \cdot 10^{-3}$	0.9999

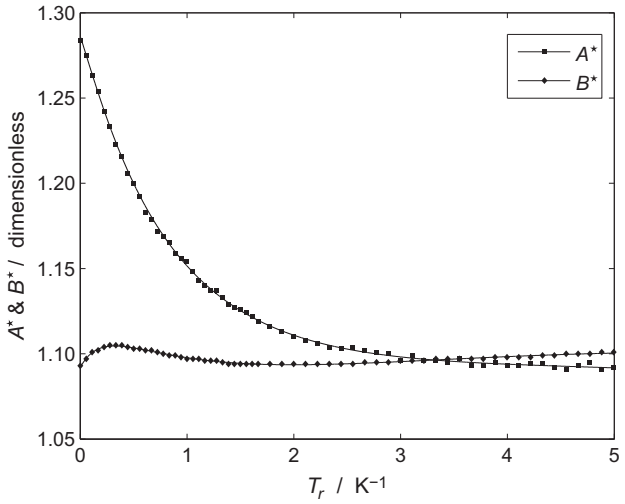

Figure 7.7: Comparison between the polynomial functions and data points of the quantities $A^\star$ and $B^\star$.

Table 7.11: Typical values of the properties that are required when calculating heats of transfer in a nitrogen–oxygen mixture at a pressure of 1.40 bar.

Property		Liquid	Vapour
T	(K)	$8.21 \cdot 10^{1}$	$8.23 \cdot 10^{1}$
x_{N_2}	$(-)$	$7.59 \cdot 10^{-1}$	$9.06 \cdot 10^{-1}$
x_{O_2}	$(-)$	$2.41 \cdot 10^{-1}$	$9.37 \cdot 10^{-2}$
V_{N_2}	$\left(\frac{m^3}{mol}\right)$	$3.56 \cdot 10^{-5}$	$4.65 \cdot 10^{-3}$
V_{O_2}	$\left(\frac{m^3}{mol}\right)$	$2.65 \cdot 10^{-5}$	$4.59 \cdot 10^{-3}$
H_{N_2}	$\left(\frac{J}{mol}\right)$	$-3.14 \cdot 10^{3}$	$2.29 \cdot 10^{3}$
H_{O_2}	$\left(\frac{J}{mol}\right)$	$-1.33 \cdot 10^{4}$	$-6.41 \cdot 10^{3}$
$H^0_{N_2}$	$\left(\frac{J}{mol}\right)$	$2.38 \cdot 10^{3}$	$2.39 \cdot 10^{3}$
$H^0_{O_2}$	$\left(\frac{J}{mol}\right)$	$-6.30 \cdot 10^{3}$	$-6.29 \cdot 10^{3}$
α^0_T	$(-)$	$-2.05 \cdot 10^{-3}$	$-2.02 \cdot 10^{-3}$
$\frac{V_{N_2} V_{O_2}}{x_{N_2} V_{N_2} + x_{O_2} V_{O_2}}$	$\left(\frac{m^3}{mol}\right)$	$2.82 \cdot 10^{-5}$	$4.59 \cdot 10^{-3}$
$\frac{H_{O_2} - H^0_{O_2}}{V_{O_2}} - \frac{H_{N_2} - H^0_{N_2}}{V_{N_2}}$	$\left(\frac{J}{m^3}\right)$	$-1.09 \cdot 10^{8}$	$-4.52 \cdot 10^{3}$
$RT\alpha^0_T$	$\left(\frac{J}{mol}\right)$	$-1.40 \cdot 10^{0}$	$-1.38 \cdot 10^{0}$
$q^*_{N_2}$	$\left(\frac{J}{mol}\right)$	$-7.41 \cdot 10^{2}$	$-2.07 \cdot 10^{0}$

properties in Table 7.11. The thermodynamic term is the most important one in both phases. In the vapour phase, the ideal gas term represents 6% of the total heat of transfer. In the liquid phase, the ideal gas term is negligible; it represents only 0.05% of the total heat of transfer.

Chapter 8

The importance of coupling between thermal and molar fluxes in a nitrogen–oxygen distillation column

L.V. van der Ham[1] and S. Kjelstrup[1,2]

1. Department of Chemistry
Norwegian University of Science and Technology
7491 Trondheim, Norway

2. Department of Process and Energy
Delft University of Technology
2628 CA Delft, The Netherlands

This chapter has been accepted for publication in
International Journal of Thermodynamics

A preliminary version of the chapter has been published in
Proceedings of ECOS 2010, Lausanne, Swiss

Abstract

A model for the transfer of mass and thermal energy in a vapour–liquid region is used to investigate the influence of neglecting coupling on the transfer rates. As an example, we studied a nitrogen–oxygen distillation column. Using a combination of stage and point boundary conditions, a nitrogen transfer profile is obtained that shows the same trend as a profile based on an equilibrium stage distillation model. The distribution of the total transfer over the two column halves is not in agreement, however. This disagreement can be expected to decrease when the dependency of the vapour film thickness on the vapour flow rate and the vapour viscosity is included in the model. The effect of neglecting coupling on the calculated transfer rates changes along the length of the column. The total effect is considerable and should be taken into account in models for the transfer of mass and thermal energy through an interface.

8.1 Introduction

The energy and exergy efficiencies of conventional distillation columns can be increased by distributing the thermal energy addition and removal over the entire length of the column, instead of concentrating it at the top and the bottom [Fonyó, 1974a,b]. When optimizing the efficiencies of such columns, it is essential to model the thermal energy flows inside the column as accurately as possible. According to the theory of irreversible thermodynamics, a thermal flux is not only dependent on a temperature difference, but also on concentration differences. In general, each flux is a linear combination of all driving forces. More details on the theory of irreversible thermodynamics can be found, for example, in the monograph by Kjelstrup and Bedeaux [2008].
Current non-equilibrium distillation models do not explicitly include the coupling between thermal and mass fluxes [Taylor and Krishna, 1993]. Using an ethanol–water distillation column as case study, De Koeijer and Kjelstrup showed that coupling can have a considerable effect [De Koeijer and Kjelstrup, 2004, Kjelstrup and De Koeijer, 2003]. This is confirmed by a recent study by Van der Ham et al. [2010] based on a single point in a cryogenic nitrogen–oxygen column.

8.1.1 Objectives

The aim of the current work is to gain more insight into the influence of coupling between thermal and mass fluxes on the calculated transfer rates in a nitrogen–oxygen distillation column. We investigate how this influence changes along the length of the column. We also provide more premises on the thermodynamic description of the transfer of mass and thermal energy through an interface.

8.2 Model of the interface region

The model we use to characterize the coupled transfer of mass and thermal energy in a vapour–liquid region is described by Van der Ham et al. [2010]. In this model,

the interface region is located in between the bulk liquid and bulk vapour phases; the conditions at its boundaries are equal to the properties of the adjacent bulk phases. The region itself consists of an interface layer in between a liquid and a vapour film. Both the liquid and the vapour film can be represented by multiple control volumes, but the interface is always given by a single control volume. Figure 8.1 gives a schematic representation of a system consisting of five control volumes.

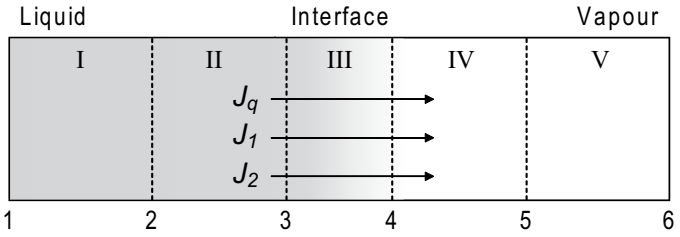

Figure 8.1: Schematic a vapour–liquid interface region consisting of five control volumes: two liquid volumes (I and II), the vapour–liquid interface (III) and two vapour volumes (IV and V). Point 1 is the liquid boundary of the system and point 6 is its vapour boundary.

The model uses the interface frame of reference, which is also know as the laboratory frame of reference. This corresponds to a system with a non-moving center-of-volume. Using a matrix of total resistivity coefficients, the model can be used to calculate the thermal and molar fluxes for a given set of boundary conditions, or driving forces. This section elaborates on the model formulation that was chosen in Van der Ham et al..

8.2.1 Choosing the set of fluxes and forces

The basis of the model is an expression for the local entropy production σ of a control volume that is located between points a and b. According to the theory of irreversible thermodynamics, the local entropy production is given by the product-sum of conjugate fluxes and driving forces. Different sets of fluxes and driving forces can be used. Bedeaux and Kjelstrup [2004] describe two possible sets for a system with only thermal and molar fluxes. One can choose to use the total heat flux J_q in combination with the chemical potentials μ_j divided by temperature T, as shown in Equation (8.1), or one can use the measurable heat flux J'_q in combination with the chemical potentials, evaluated at a constant temperature, divided by the temperature, as shown in

Equations (8.2) and (8.3).

$$\sigma = \quad J_q \left(\Delta_{ab} \frac{1}{T} \right) + \sum_{j=1}^{n} J_j \left(-\Delta_{ab} \frac{\mu_j}{T} \right) \tag{8.1}$$

$$\sigma = J'_{q,b} \left(\Delta_{ab} \frac{1}{T} \right) + \sum_{j=1}^{n} J_j \left(-\frac{\Delta_{ab} \mu_j \left(T_a \right)}{T_a} \right) \tag{8.2}$$

$$\sigma = J'_{q,a} \left(\Delta_{ab} \frac{1}{T} \right) + \sum_{j=1}^{n} J_j \left(-\frac{\Delta_{ab} \mu_j \left(T_b \right)}{T_b} \right) \tag{8.3}$$

From a theoretical perspective, the three sets of fluxes and forces are equivalent. But from a practical perspective, there are some clear differences. The measurable heat flux, also known as the sensible heat flux, is a quantity that can be measured in practise. Experimental values for resistivities are always related to the measurable heat flux. The measurable and total heat fluxes are can related via the partial molar enthalpies H_j multiplied by the molar fluxes J_j:

$$J_q = J'_q + \sum_{j=1}^{n} H_j J_j \tag{8.4}$$

In practise we calculate enthalpy differences, or relative enthalpies, rather than absolute enthalpies. It is therefore very hard to link the total heat flux to practical situations. Similar to the enthalpy, we also calculate chemical potential differences rather than absolute chemical potentials. The driving forces in Equations (8.2) and (8.3) are therefore more practical to use than the ones in Equation (8.1). These are three reasons to favour the measurable heat flux formulation over the total heat flux formulation.

The system consists of at least three control volumes: one liquid control volume, one interface control volume and one vapour control volume. It was found by Van der Ham et al. [2010] that more control volumes should be used to describe the liquid and vapour films. The driving forces and fluxes in a control volume can be gathered by a driving force vector and a flux vector. The driving force vector of each control volume is then given by the product of a resistivity matrix and the flux vector. The sum of the driving force vectors of all control volumes yields the total driving force vector of the system. If the flux vector is exactly the same in all control volumes, which means that the fluxes are constant throughout the system, it is straightforward to calculate them once the total resistivity matrix is known. The differences in chemical potential divided by temperature can be summed directly. But this is not possible for the differences in chemical potential evaluated in Equations (8.2) and (8.3), because they are all evaluated at different constant temperatures. At steady state, the total heat flux is constant throughout the system, similar to the molar fluxes. But the

measurable heat flux is not constant. These are two reasons to favour the total heat flux formulation over the measurable heat flux formulation.

Instead of selecting one of these two formulations, a new formulation is introduced that uses the measurable heat flux at a certain reference location $J'_{q,0}$ and evaluates all chemical potential differences at a certain reference temperature T_0. The choice of using such reference points must be compensated for in the resistivity matrix of the control volume. Replacing the measurable heat flux at one location by the measurable heat flux at another location can be done using the energy balance shown given by Equation (8.4):

$$J'_{q,a} = J'_{q,b} + \sum_{j=1}^{n} \Delta_{ab} H_j J_j \tag{8.5}$$

8.2.2 Assuming constant enthalpy

Replacing a chemical potential difference at one temperature by a chemical potential difference at another temperature requires an assumption. First, the difference in chemical potential divided by temperature is rewritten in terms of a chemical potential difference at a constant temperature T_a:

$$\begin{aligned} -\Delta_{ab}\left(\frac{\mu_j}{T}\right) &= -\left(\frac{\mu_j\left(T_b, x_{j,b}\right)}{T_b} - \frac{\mu_j\left(T_a, x_{j,a}\right)}{T_a}\right) \\ &= -\left(\frac{\mu_j\left(T_a, x_{j,b}\right)}{T_a} - \frac{\mu_j\left(T_a, x_{j,a}\right)}{T_a}\right) \\ &\quad + \frac{\mu_j\left(T_a, x_{j,b}\right)}{T_a} - \frac{\mu_j\left(T_b, x_{j,b}\right)}{T_b} \\ &= -\frac{\Delta_{ab}\mu_{j,T_a}}{T_a} - \int_{T_a}^{T_b} \frac{d}{dT}\left(\frac{\mu_{j,x_{j,b}}}{T}\right) dT \end{aligned} \tag{8.6}$$

The partial derivative of the chemical potential divided by temperature with respect to temperature is given by the Gibbs–Helmholtz equation:

$$\frac{\partial}{\partial T}\left(\frac{\mu_j}{T}\right) = -\frac{H_j}{T^2} \tag{8.7}$$

The partial enthalpy is a function of temperature. Including this temperature dependency into the equations will eventually result into third order temperature difference terms in the entropy production expression. The theory of irreversible thermodynamics only uses terms up to the second order. So in order to avoid introducing any third order term, we assume that the partial enthalpies are independent of temperature within the control volume we are considering. If we introduce Equation (8.7) into Equation (8.6) with this in mind we obtain:

$$-\Delta_{ab}\left(\frac{\mu_j}{T}\right) = -\frac{\Delta_{ab}\mu_{j,T_a}}{T_a} - H_{j,x_{j,b}}\Delta_{ab}\frac{1}{T} \tag{8.8}$$

Instead of going to an expression containing the chemical potential at constant temperature T_a, we can also go to an expression at constant temperature T_b. The difference between the expressions for the two constant temperatures is the composition at which the partial enthalpy is evaluated. Equation (8.8) will be used to obtain an expression for going directly from one constant temperature to another:

$$-\frac{\Delta_{ab}\mu_{j,T_b}}{T_b} = -\frac{\Delta_{ab}\mu_{j,T_a}}{T_a} - \Delta_{ab}H_j\Delta_{ab}\frac{1}{T} \tag{8.9}$$

Although the partial enthalpies are considered to be independent of temperature within the control volume, we still need to choose at which constant temperature we evaluate them. This temperature must be the same for all volumes.

8.2.3 Formulae for total resistivities

Based on Equation (8.3), the following force–flux relations can be written for a single control volume:

$$\Delta_{ab}\frac{1}{T} = r^{ab}_{qq}J'_{q,a} + \sum_{j=1}^{n} r^{ab}_{qj}\ J_j \tag{8.10}$$

$$-\frac{\Delta_{ab}\mu_i\left(T_b\right)}{T_b} = r^{ab}_{iq}J'_{q,a} + \sum_{j=1}^{n} r^{ab}_{ij}\ J_j \tag{8.11}$$

Here, r^{ab}_{mn} represents the resistivity in the control volume between points a and b that is coupling driving force m with flux n, where $m, n \in q, i, j$. The subscript q indicates the thermal driving force or flux, and the subscripts i and j indicate component driving forces or fluxes. The resistivity r_{qq} is related to the thermal conductivity, the resistivities $r_{ij} = r_{ji}$, r_{ii}, and r_{jj} are related to diffusion, and the resistivities $r_{iq} = r_{qi}$ and $r_{jq} = r_{qj}$ are related to the coupling between thermal and component fluxes, also known as the Soret and Dufour effects.
Equations (8.10) and (8.11) can be rewritten using Equations (8.5) and (8.9) in order to replace $J'_{q,a}$ with the measurable heat flux at the vapour boundary of the system ($J'_{q,v}$) and in order to evaluate the chemical potential differences at the temperature of the liquid boundary of the system (T_l) instead of at T_b:

$$\Delta_{ab}\frac{1}{T} = r^{ab}_{qq}J'_{q,v} + \sum_{j=1}^{n}\left(r^{ab}_{qj} + r^{ab}_{qq}\Delta_{vb}H_j\right)\ J_j \tag{8.12}$$

$$-\frac{\Delta_{ab}\mu_i\left(T_l\right)}{T_l} = r^{ab}_{iq}J'_{q,v} + \sum_{j=1}^{n}\left(r^{ab}_{ij} + r^{ab}_{iq}\Delta_{vb}H_j\right)\ J_j + \Delta_{ab}H_i\Delta_{la}\frac{1}{T} \tag{8.13}$$

Kjelstrup and De Koeijer [2003] and Bedeaux and Kjelstrup [2004] give formulae for the total resistivities of a system that consists of three connected control volumes. It is shown by Van der Ham et al. [2010] how the force–flux relations given by Equations (8.12) and (8.13) can be used to derive general formulae for the total resistivities of a system consisting of a series of m connected control volumes:

$$r_{qq}^{tot} = \sum_{k=1}^{m} r_{qq}^{k} \tag{8.14}$$

$$r_{qj}^{tot} = r_{jq}^{tot} = \sum_{k=1}^{m} r_{qj}^{k} + r_{qq}^{k} \Delta_{k_v v} H_j \tag{8.15}$$

$$r_{ij}^{tot} = r_{ji}^{tot} = \sum_{k=1}^{m} r_{ij}^{k} + r_{iq}^{k} \Delta_{k_v v} H_j + r_{qj}^{k} \Delta_{k_v v} H_i + r_{qq}^{k} \Delta_{k_v v} H_j \Delta_{k_v v} H_i \tag{8.16}$$

Where $\Delta_{k_v v}$ indicates the difference between the vapour boundary of the system and the boundary of control volume k that is closest to the system vapour boundary.

8.3 Calculations

The routine described by Van der Ham et al. [2010] allows the calculation of values for the molar fluxes and the measurable heat flux when the conditions at the liquid and vapour boundaries of the system are known. A thermodynamically consistent solution is found by requiring the entropy productions calculated using both irreversible thermodynamics and the entropy balance to be equal. This requirement is used to find the liquid film thickness for a fixed vapour film thickness. All calculations reported in this work were done using this calculation routine.

It is discussed in detail by Van der Ham et al. how to calculate all relevant resistivities. The influence of inaccuracies in their values on the calculation results was described in a sensitivity analysis. The influence of the number of control volumes per film, of the interface resistances, of the chosen vapour film thickness and of the order of the control volumes was also investigated. In the current study we always: used a minimum of 32 control volumes per film, included the interface resistances, used a vapour film thickness of 5×10^{-4} m and described the system from the liquid to the vapour boundary.

8.3.1 Distillation column design

The work by Van der Ham et al. discussed the influence of coupling between thermal and mass fluxes on the transfer rates in a nitrogen–oxygen mixture at one single point in a distillation column. In this work, we investigated how this influence changes along the length of the distillation column. In order to obtain sets of boundary conditions that represent positions along the entire length of the column, we started by defining a base case distillation column design.

Column specifications

The distillation column design we used as base case is separating a binary nitrogen–oxygen mixture with a nitrogen mole fraction of 0.80 into products with purities of 0.99. The feed and the top product are vapours at their dew points and the bottom product is a liquid at its bubble point. It is assumed that the column operates at a constant pressure of 1.4 bar. The total number of stages is 18, excluding reboiler and total condenser. At stage 11, counting from top to bottom, a feed with a flow rate of 1 mol/s enters the column. An equilibrium stage model was used to simulate the column; it was solved using the bubble point method as described by Seader and Henley [1998]. A high accuracy thermodynamic model was used to calculate the required thermodynamic properties; it is described by Lemmon et al. [2000]. This model was used for all thermodynamic calculations that were done in this work.

Column profiles

Table 8.1 gives an overview of how the characteristic column properties change within the column. The temperature, liquid mole fraction x, vapour mole fraction y, liquid flow rate L and vapour flow rate V are given as function of the stage number n. The condenser and reboiler are represented by stage numbers C and R.

Stage and point boundary conditions

The point in the distillation column that was used as base case by Van der Ham et al. was defined by calculating average temperatures and mole fractions for a certain stage. The considered stage was located around the centre of the top part of the column, which corresponds to a position in between stages 5 and 6 in the column that was used in this work. The vapour and liquid boundary conditions based on stage n can be calculated using the following formula:

$$T_l^{n,s} = \frac{1}{2}\left(T^{n-1} + T^n\right) \tag{8.17}$$

$$T_v^{n,s} = \frac{1}{2}\left(T^n + T^{n+1}\right) \tag{8.18}$$

$$x_{N_2}^{n,s} = \frac{1}{2}\left(x_{N_2}^{n-1} + x_{N_2}^n\right) \tag{8.19}$$

$$y_{N_2}^{n,s} = \frac{1}{2}\left(y_{N_2}^n + y_{N_2}^{n+1}\right) \tag{8.20}$$

Instead of using boundary conditions based on average stage values, it is also possible to select boundary conditions based on the point in between two stages. In a packed

Table 8.1: Column profiles of the temperature, the nitrogen mole fractions, the liquid flow and the vapour flow.

n	T	x_{N_2}	y_{N_2}	L	V
(-)	(K)	(-)	(-)	(mol/s)	(mol/s)
C	80.28	0.9900	–	0.639	–
1	80.45	0.9652	0.9900	0.634	1.445
2	80.72	0.9289	0.9791	0.627	1.440
3	81.09	0.8793	0.9633	0.618	1.433
4	81.57	0.8174	0.9420	0.607	1.424
5	82.13	0.7485	0.9159	0.595	1.413
6	82.72	0.6812	0.8874	0.585	1.401
7	83.25	0.6237	0.8602	0.576	1.391
8	83.68	0.5798	0.8373	0.570	1.382
9	83.99	0.5492	0.8201	0.565	1.376
10	84.20	0.5291	0.8082	0.563	1.372
11	84.34	0.5165	0.8005	0.561	1.369
12	84.62	0.4907	0.7839	0.558	0.367
13	85.23	0.4380	0.7468	0.551	0.364
14	86.39	0.3478	0.6702	0.541	0.357
15	88.17	0.2322	0.5363	0.530	0.347
16	90.15	0.1290	0.3603	0.523	0.337
17	91.71	0.0618	0.1991	0.519	0.329
18	92.64	0.0265	0.0926	0.517	0.325
R	93.11	0.0100	0.0364	0.194	0.323

column, the liquid flowing down from a stage meets the vapour rising up from the stage below at this point. These point boundary conditions are given by:

$$T_l^{n,p} = T^{n-1} \tag{8.21}$$
$$T_v^{n,p} = T^n \tag{8.22}$$
$$x_{N_2}^{n,p} = x_{N_2}^{n-1} \tag{8.23}$$
$$y_{N_2}^{n,p} = y_{N_2}^n \tag{8.24}$$

A schematic overview of stage n is shown in Figure 8.2, including the quantities that are required to determine the boundary conditions sets for stage n and for points n and $n+1$.

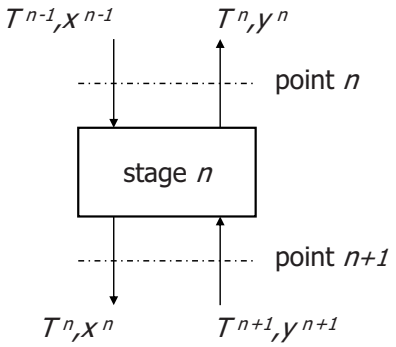

Figure 8.2: Schematic overview of stage n, depicting the quantities that are required to calculate the boundary conditions sets for stage n and for points n and $n+1$.

Using the column design presented in this section, it is possible to calculate 18 sets of stage boundary conditions. Because the points above stage 1 and below stage 18 can also be used as a set of boundary conditions, there exist 19 sets of point boundary conditions. When plotted as function of position in the column, each of the stage boundary conditions is located in between two point boundary conditions.

8.4 Results and discussion

8.4.1 Nitrogen flux profile

Using the temperature and mole fraction data given in Table 8.1 and using Equations (8.17) to (8.20) and Equations (8.21) to (8.24), 37 sets of system boundary conditions have been determined; 18 sets of stage boundary conditions and 19 sets of point boundary conditions. Each of these sets has been used as input to the calculation model for coupled transfer of mass and thermal energy. Figure 8.3 gives an overview of the calculated nitrogen fluxes as function of position in the column.

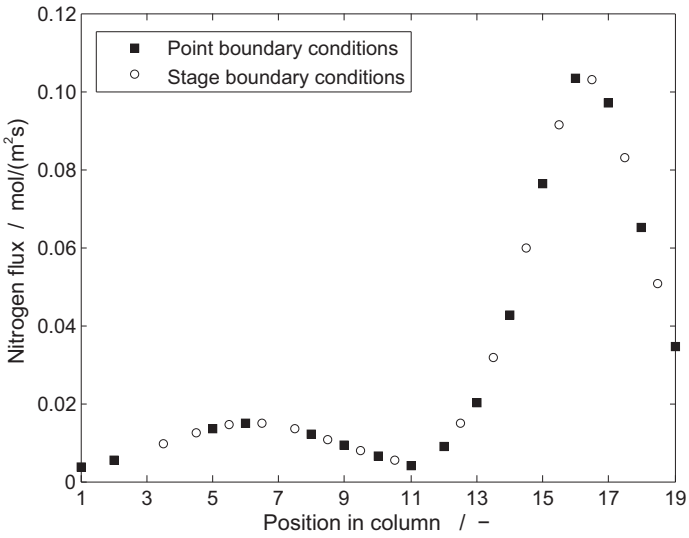

Figure 8.3: Comparison between the calculated nitrogen flux as function of the position in the column for both point and stage boundary conditions.

Only the profile of the nitrogen flux is shown in Figure 8.3; the profiles of the other fluxes and of the entropy production are comparable. Although we used 37 sets of boundary conditions as input, the figure contains only 31 data points. It proved impossible to find a liquid film thickness that yielded a thermodynamically consistent system for the other 6 sets of boundary conditions.
There can be different reasons why it might be impossible to solve the model for some specific cases. It might be caused by the fixed vapour film thickness we use, or it could be related to possible inaccuracies in the calculated resistivities. It can also be related to the fact that we are using boundary conditions originating from an equilibrium stage model as input to our rather rate-based like model. At the moment we do not have sufficient understanding to predict beforehand which cases are impossible to solve.
The data points from the two different types of boundary conditions are very well in agreement with each other. The combination of the two gives a good representation of how the calculated nitrogen flux changes along the entire length of the column.

8.4.2 Nitrogen transfer profiles

Based on the mole fraction and flow data in Table 8.1, it is possible to calculate how much nitrogen is transferred on each of the stages. It does not make any sense to make a direct comparison between the amounts of transferred nitrogen and the calculated nitrogen fluxes shown in Figure 8.3. The calculated fluxes are values at a single point and they are given per amount of interfacial area, while the transferred amounts are the totals of complete stages. But if we assume that the interfacial area is constant

along the length of the column and express the fluxes and transferred amounts as percentages of their column averages, we can still compare how the two quantities change along the length of the column. This comparison is shown in Figure 8.4.

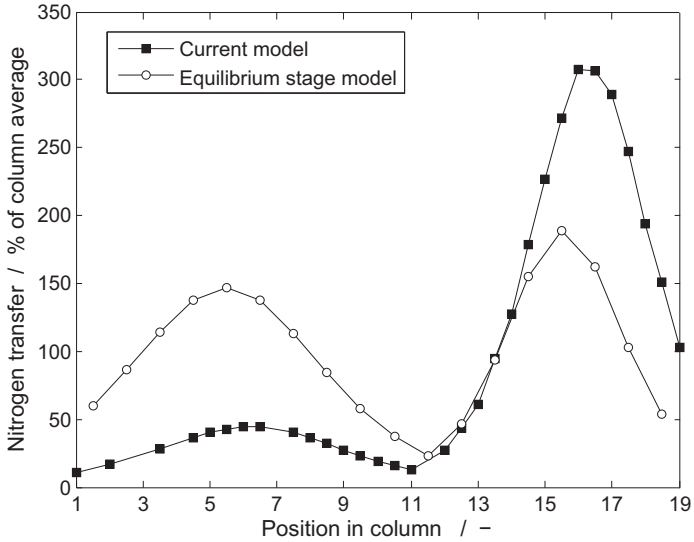

Figure 8.4: Comparison between the nitrogen fluxes calculated with the model presented in this work and the total amounts of transferred nitrogen calculated from the equilibrium stage model.

The comparison between the two nitrogen transfer profiles shows that they follow the same trend; both have a minimum around the feed stage and maxima around the centres of the top and bottom parts. But the relative magnitudes of the two maxima are different. The maxima are comparable in the equilibrium stage model profile. But in the profile based on the calculations done in this work, the bottom part maximum is almost seven times bigger than the top part maximum. A part of this difference can be related to the constant vapour film thickness that we have used in our calculations. An increase in the vapour film thickness would translate into an increase in the total resistivities, which means that a fixed set of boundary conditions yields smaller fluxes. There are two reasons why we expect the vapour film thickness to be larger in the bottom part of the column. The first one is related to the vapour flow rates in the column. As can be seen in Table 8.1, the vapour flow rate is about four times larger in the top part of the column. A larger vapour flow rate corresponds to a larger superficial vapour velocity, which means a smaller vapour film thickness. The second reason is related to the viscosity of the vapour phase. When going from the top to the bottom of the column, the temperature and the oxygen fraction increase. Because oxygen has a higher viscosity than nitrogen and because the viscosity increases with an increasing temperature, the viscosity must be higher in the bottom part of the column.

A higher vapour viscosity corresponds to a larger vapour film thickness. How much these two effects exactly affect the vapour film thickness should be investigated in future studies.

8.4.3 Neglecting coupling resistances

Similar to Van der Ham et al. [2010], we have investigated the effect of neglecting coupling between thermal and molar fluxes. This can be done by setting all control volume resistivities that couple a thermal and a molar flux equal to zero, while fixing the film thickness ratio at the value found for the coupled case. We have done this for all data points shown in Figure 8.3 and calculated the relative differences between the fluxes obtained from uncoupled systems and the fluxes obtained from coupled systems. Table 8.2 gives the averages and standard deviations of these relative differences, summarizing the effect of neglecting coupling for the entire column.

Table 8.2: The average and standard deviation of the influence that neglecting coupling resistances has on the different fluxes.

	J_{N_2}	J_{O_2}	$J'_{q,l}$	$J'_{q,v}$
Average (%)	11	−4.2	−39	−3.3
Standard deviation (%)	11	5.4	29	0.2

Similar to what was found by Van der Ham et al. for a single stage, the neglect of coupling mostly affects the nitrogen flux and the measurable heat flux at the liquid boundary. The column average values are lower than the values found for the single stage investigated by Van der Ham et al.. The standard deviations in the effects on the molar fluxes and on the measurable heat flux at the liquid boundary are of the order of their averages. There is no clear relation between these effects and the position in the column. The deviations are mainly caused by deviations in the liquid film thicknesses that were found. The vapour film thickness was fixed at the same value for all systems, which partly explains the relatively constant and small effect that neglecting coupling has on the measurable heat flux at the vapour boundary. Figure 8.5 shows how this effect changes along the length of the column.

The effect that neglecting coupling between thermal and molar fluxes has on the measurable heat flux at the vapour boundary is relatively constant along the length of the column. It increases slowly in the top part of the column, but towards the bottom of the column it starts decreasing.

The thermal and molar fluxes are central variables in the minimization of entropy production in distillation columns. It is therefore essential to have accurate models to calculate them.

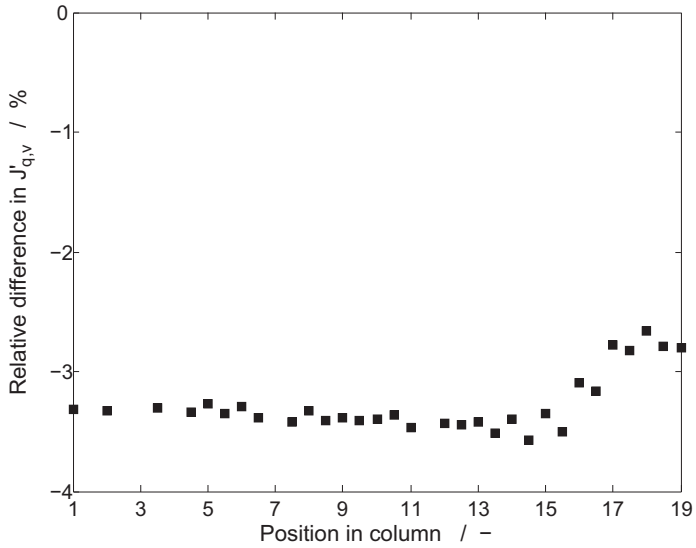

Figure 8.5: Effect of neglecting coupling on the measurable heat flux at the vapour boundary, as function of the position in the column.

8.5 Conclusions

Calculating fluxes from a combination of stage and point boundary conditions yields a consistent representation of how the fluxes vary along the length of the entire distillation column. The trend in the obtained nitrogen flux profile is similar to the one based on an equilibrium stage model, but the distribution of the nitrogen transfer over the two column halves does not agree. This disagreement can be partly explained by the use of a constant vapour film thickness. Including a dependency of the vapour film thickness on the vapour flow rate and viscosity is an important next step in the development of the model. The effect of neglecting coupling between thermal and mass fluxes on their calculated magnitudes is smaller when averaged for the entire column than it is for the single stage investigated earlier, but it is still considerable and should be considered in models used for optimization studies.

Acknowledgements

The research leading to these results has received funding from the European Community's 7th Framework Programme (FP7/2007-2013) under grant agreement number 211971 (The DECARBit project).

Nomenclature

H_j partial molar enthalpy of component j, J/mol

J_j	molar flux of component j, mol/(s m^2)
J_q	total heat flux, J/(s m^2)
J'_q	measurable heat flux, J/(s m^2)
L	liquid flow rate, mol/s
m	number of control volumes, dimensionless
r_{mn}	resistivity coupling driving force m with flux n, where $m, n \in q, N_2, O_2$
S_j	partial molar entropy of component j, J/(K mol)
T	temperature, K
V	vapour flow rate, mol/s
x	liquid mole fraction, dimensionless
y	vapour mole fraction, dimensionless
$\Delta_{ab}Y$	difference in property Y: $Y_b - Y_a$

Greek symbols

μ_j	chemical potential of component j, J/mol
σ	local entropy production, J/(K m^2)

Subscripts and superscripts

0	reference point
a, b	location indices
i, j	component indices
k	control volume index
l	liquid
n	stage index
N_2	nitrogen
O_2	oxygen
p	point
q	thermal energy
s	stage
tot	total
v	vapour

Chapter 9

Cryogenic total reflux experiments in a packed concentric HIDiC

Part A: Background and design

L.V. van der Ham[1] and M. Drescher[2]

1. Department of Chemistry
Norwegian University of Science and Technology
7491 Trondheim, Norway

2. SINTEF Energy Research
Kolbjørn Hejes vei 1D
7465 Trondheim, Norway

This chapter has been prepared for submission to
Separation and Purification Technology

Parts of this chapter have been published in
Book of abstracts of Trondheim CCS conference 2011, Trondheim, Norway
and
Proceedings of ICR 2011, Prague, Czech Republic

Abstract

Intensifying the heat integration of the distillation columns in a cryogenic air separation unit can yield a considerable reduction in its inefficiencies. Accurate predictions of the achievable reduction require more-detailed experimental input on the thermal energy transfer and the separation efficiency of a heat-integrated distillation column (HIDiC). The current work presents the design of an experimental concentric HIDiC that is separating a mixture of nitrogen and oxygen. Both the cylindrical inner column, having a diameter of 14 cm, and the ring-shaped outer column, having an outer diameter of 22 cm, are equipped with 1.6 m of structured packing, corresponding to approximately 6 theoretical equilibrium stages. The set-up is designed for total reflux operation at cryogenic temperatures and pressures up to 20 bar. Evaporating nitrogen is used in the condensers and electrical heaters are used as reboilers; the maximum total heat duty amounts to 25 kW. More details on the instrumentation and experiments are presented in part B of the publication series that the current work belongs to.

9.1 Introduction

The work presented in the current study is part of the European collaboration project DECARBit. The main aim of this project is to develop an Integrated Gasification Combined Cycle (IGCC) with pre-combustion CO_2 capture [Røkke and Langørgen, 2009]. An IGCC uses both purified oxygen and nitrogen, which are usually obtained by separating air. Within the DECARBit project, three different air separation technologies are investigated: high-temperature ceramic membranes, pressure-swing or temperature-swing adsorption, and cryogenic distillation. The current work is part of an effort to improve the efficiency of cryogenic air separation processes.
An essential part of the DECARBit project is the construction of several experimental set-ups. These set-ups, also called pilots, should bridge the gap between theoretical improvements and their commercial implementation. Within this context, a set-up has been developed that aims to enable the realistic design and evaluation of heat-integrated distillation columns (HIDiC) for the cryogenic separation of air. The design of this set-up is the main subject of the current work, being the first part in a series of publications. More details on the instrumentation and experiments are presented in the second part of this series [Van der Ham and Drescher, 2011b].

9.1.1 Cryogenic air separation

Cryogenic distillation of air is currently the most common technology for the production of large volumes of high purity oxygen and/or nitrogen [Smith and Klosek, 2001, Thorogood, 1991]. A cryogenic air separation unit (ASU) consists of four main process sections: a feed purification and pressurization section, a main heat exchanger, a distillation section, and a product pressurization section.
In the first section, air is compressed and stripped from water, carbon dioxide and other hydrocarbon contaminants. The cleaned air subsequently enters the main heat exchanger, where it is cooled to cryogenic conditions. The cryogenic air is fed to the

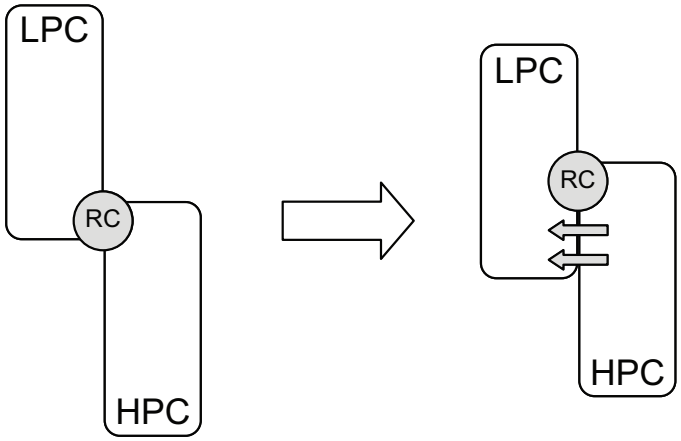

Figure 9.1: Schematic of heat-integrated air distillation columns.

distillation section, where it is separated into two or more product streams using a series of distillation columns that are equipped with structured packing. The products pass again through the main heat exchanger and are pumped or compressed to their desired final pressures.

9.1.2 Improving the distillation section efficiency

In a previous work, we compared the performance of two ASU designs using exergy analysis [Van der Ham and Kjelstrup, 2010]. Both designs had the same feed and product specifications, but they used a different number of distillation columns: either two or three. The three-column design was found to destroy 12% less exergy than the two-column design. Within the distillation section of the two-column design, which accounted for about one-quarter of the total exergy destruction, 75% of the exergy destruction was located in the distillation columns. Addition of the third column reduced this amount by 44%. The use of heat-integrated distillation columns (HIDiC) was suggested as another promising way to reduce the exergy destruction in the distillation section.
A recent study [Van der Ham and Kjelstrup, 2011c] showed that the exergy destruction in the distillation section of a two-column ASU can be reduced by approximately 25% when improving the heat integration between the distillation columns. In a conventional two-column desgin, the low-pressure column (LPC) is positioned on top of the high-pressure column (HPC). The combination of this configuration and the difference in operating pressures enables the use of a single heat exchanger that is functioning as reboiler for the LPC and as condenser for the HPC, the reboiler–condenser (RC). Improving the heat integration between the columns can be realized by moving the LPC down along or into the HPC, as schematically shown in Figure 9.1.
A similar configuration has previously been described by Nakaiwa et al. [1996], but

using two reboiler–condensers that are enclosing the heat-integrated column part, instead of one reboiler–condenser at the top of the HPC. They state that the energy requirement of the air separation unit can be reduced by 29% using this configuration. Iwakabe et al. [2006a] report a study that predicts an energy efficiency gain of 40% when using a plate-fin type HIDiC as part of a cryogenic air separation unit.

9.1.3 Heat-integrated distillation columns

The main characteristic of a heat-integrated distillation column (HIDiC) is that thermal energy is transferred between two column parts along an extended part of the integrated columns height. This distribution of the heat duties over a larger part of the column height can result into more reversible operation, as explained in detail by, for example, Nakaiwa and Ohmori [2009]. An extensive overview of numerically predicted reductions in the net energy input of a HIDiC, compared to a conventional distillation column, is given by Van der Ham [2011, section 3.2.1]. The possible reductions vary between 20% and 90%. So far, only two experimental investigations of a complete HIDiC have been done, both as part of a Japanese national research project. They showed reductions in the net energy input of 40% using a benzene–toluene mixture [Naito et al., 2000], and of 60% when using a 12-component hydrocarbon mixture [Horiuchi et al., 2008].
The thermal integration of the two column parts can in practise be realized using several types of configurations, an overview is given by De Rijke [2007]. The two Japanese HIDiCs are both based on concentrically-integrated columns that are equipped with structured packing. In such a configuration, a cylindrical inner column is surrounded by a ring-shaped outer column. The heat-transfer area is defined by the inner column wall. In order to provide for a sufficient amount of heat-transfer area, multiple parallel columns with a small diameter are used, instead of one column with a large diameter. For example, the second Japanese set-up contained seven parallel columns [Horiuchi et al., 2008].
As described in detail by Van der Ham [2011, section 3.2.4-6], there are several properties of a packed concentric HIDiC that might have a considerable effect on its performance but that have not yet been investigated experimentally. They are related to the overall heat-transfer coefficient that can be realized for varying operating conditions, to the performance of an annular distillation column, and to the effect that a radial heat flux has on the column performance. In previous numerical studies [Van der Ham et al., 2010, Van der Ham and Kjelstrup, 2011d], it was concluded that the interdependency of the diffusion and the heat fluxes should be explicitly included in distillation models, especially when modelling a HIDiC.

9.1.4 Objective

The main objective of the current work is to develop a design for an experimental set-up that can be used to investigate the following properties of an air separating HIDiC:

- Heat flux through the inner column wall
- Separation efficiency of the two column parts
- Radial temperature and composition gradients
- Interdependency of thermal and molar fluxes

The experimental results will provide data that is required for a detailed feasibility evaluation of using the HIDiC principle in a cryogenic ASU. The results will also yield insights that are valuable for the design and operation of packed HIDiCs and separation columns in general.

9.1.5 Outline

The current work is divided in three parts. In the first part, Section 9.2, the conceptual design of the set-up is defined along with a few key design variables. Next, the performance of this design is simulated in Section 9.3, in order to estimate the characteristics of several limiting operating cases. In the third part, the found operational characteristics are used to define the detailed dimensions and properties of the equipment that is part of the experimental set-up. They are described in detail in Section 9.4. More details on the instrumentation, the measurement strategy, and the experiments are included in Part B of this series of publications [Van der Ham and Drescher, 2011b].

9.2 Conceptual design

The main objective of the current experimental set-up is to gain more insight into various phenomena that occur inside a packed HIDiC. The two Japanese HIDiCs have already proven that it is possible to operate and control a complete HIDiC configuration, including compressor and throttle valve. The current set-up will not be used to repeat this.

9.2.1 Structural layout

In order to increase the operational freedom of the two HIDiC parts, it has been decided to operate the inner and the outer columns as two separate systems. Therefore, although they are integrated thermally, their mass streams are completely separated. The performance of structured packing is commonly evaluated using a column operating at total reflux [Olujić, 2009]. The current set-up will be based on total reflux operation as well. Figure 9.2 shows a schematic overview of the structural layout of the experimental HIDiC set-up.
The main components of the experimental set-up are the high-pressure column (HPC) and the low-pressure column (LPC). Each of them is equipped with a reboiler, a total condenser and a reflux drum. The reboilers are electrical heaters, and the condensers

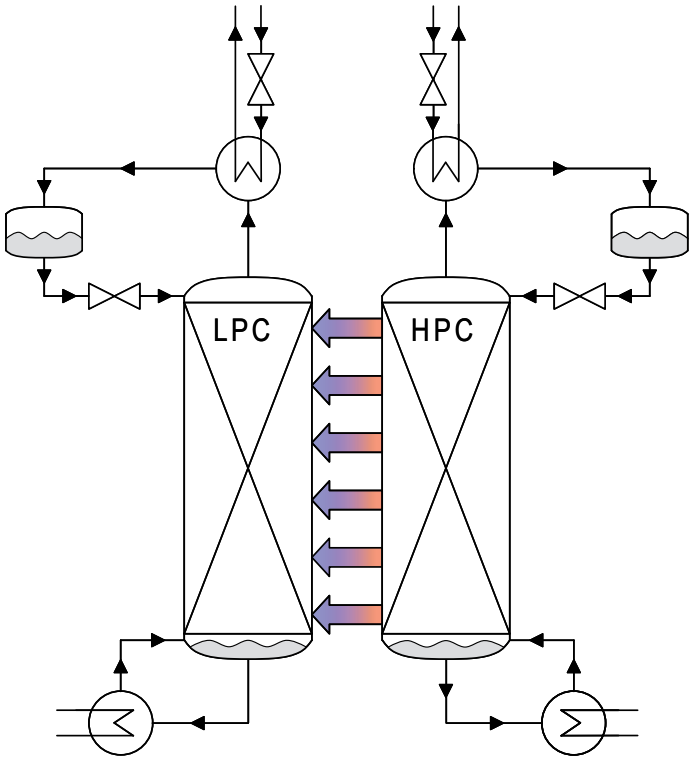

Figure 9.2: Schematic of the experimental HIDiC set-up.

use evaporating nitrogen as coolant. The liquid nitrogen is withdrawn from a common pressurized nitrogen storage tank. It is throttled to an ambient pressure before it enters the condensers.

9.2.2 Control strategy

The control structure is comparable for both columns and it consists of three parts. During normal operation, the absolute pressure is controlled using the condenser duty, by means of the coolant flow rate. A pressure relief valve is installed on top of each column as additional safety measure in case of a pressure build-up. The flow rates in the columns are controlled using the reboiler duties. The temperatures are directly related to the compositions; they will be controlled using the reflux flow rates.
The temperature control is based on the fact that each column contains a fixed amount of mass, which is divided over the reflux drum, the sump of the column (including the reboiler), and the column itself. The liquid in the reflux drum is enriched in nitrogen and the liquid in the sump of the column is enriched in oxygen. By adjusting the distribution of these amounts of liquid, it is possible to control the composition range inside the columns, and thus the temperatures. The temperature is used instead of the composition because temperature measurements are available continuously. Composition measurements are done periodically using gas chromatography and are therefore not continuously available.

9.2.3 Key design variables

This section discusses the most important design variables of the set-up: the column diameters and the structured packing that is used.

Column diameters

The column diameters have a big influence on the flow rates in the columns, which determine the required condenser and reboiler duties and thus the operating costs. In order to keep the operating costs at an acceptable level, the column diameters should not be too big. However, if they are designed too small, liquid maldistributions in the wall zones might become a serious issue. Small diameter columns might also be more difficult to construct accurately and equip with sufficient measurement instrumentation.
The inner column diameter determines how much heat-transfer area is available per cross-sectional area of the inner column. A smaller diameter results into more heat-transfer area per cross-sectional area, which is advantageous for the thermodynamic efficiency of a HIDiC. In order to keep the thermal energy transfer effect comparable for the inner and the outer columns, the ratio between their cross-sectional areas should not be too far away from unity.
Industrial pipes and flanges are readily available in certain standard dimensions. With the considerations above in mind, an outer column diameter of DN200 and an inner

column diameter of DN125 have been selected from the available standard diameters. The outer column has a wall thickness of 6.0 mm and the inner column has a wall thickness of 4.0 mm. These numbers result in an inner cross-sectional area that is equal to 74% of the outer cross-sectional area. The inter-wall distance between the inner and the outer walls is 33.7 mm. The chosen diameter characteristics are summarized in Table 9.1.

Table 9.1: Overview of the chosen inner-column and outer-column diameters.

Quantity		Inner column	Outer column
Inner wall-diameter	m	0.1317	0.2071
Outer wall-diameter	m	0.1397	0.2191
Cross-sectional area	m^2	0.0136	0.0184

Characteristics of the two previously built Japanese HIDiCs are given in Table 9.2 for comparison. The wall thicknesses that they used are unknown and neglected in the table.

Table 9.2: Dimensional characteristics of the two Japanese HIDiCs, given in mm. The top ones are for the first HIDiC [Naito et al., 2000], and the bottom ones for the second HIDiC [Horiuchi et al., 2008].

Column section	Top	Middle	Bottom
Outer column diameter	254	254	254
Inner column diameter	140	165	190
Inter wall distance	57.0	44.5	32.0
(Inner area / Outer area)	0.44	0.73	1.27
Outer column diameter	406	406	406
Inner column diameter	165	216	267
Inter wall distance	120.5	95.0	69.5
(Inner area / Outer area)	0.20	0.39	0.76

Structured packing

The most important design decisions with respect to the structured packing are the type of packing that is used and the total packing height. The combination of these two determines the total number of theoretical equilibrium stages in the column and column height.
A higher number of equilibrium stages means that higher top and bottom purities are obtained. The concentration difference corresponding to one equilibrium stage decreases towards the top and the bottom of a column. It is generally easier (more accurate) to measure large concentration (and temperature) differences than small

ones. So from this point of view is it advantageous to use a low number of equilibrium stages.
Using a low total packing height limits the construction costs related to the structured packing and the column walls. But using a low packing height (per theoretical stage) also means that there is less heat-transfer area available (per theoretical stage), which is disadvantageous for the thermodynamic efficiency of a HIDiC.
Sulzer Mellapak 250.Y and Montz B1-250 are types of structured packing that are commonly used for industrial air separation columns. They have about 3 theoretical stages per meter of packing. In consultation with Montz, it has been decided to use the B1-500 packing for the current set-up. The higher specific surface area is achieved by closer packed sheets, which results in a higher number of sheets in between the inner and outer walls. It also results into a lower maximum vapour flow rate. Table 9.3 gives an overview of the characteristics of the selected structured packing and Figure 9.3 shows a picture of the packing.

Table 9.3: Overview of the structured-packing characteristics.

Type of packing		Montz B1
Specific surface area	m^2/m^3	500
Corrugation angle	degrees	45
Height per element	mm	100
Wall wipers per element	-	2
Approximate efficiency	stages/m	4
Maximum F-factor	$\sqrt{\text{Pa}}$	2.0
Number of elements	-	16
Total packing height	m	1.60
Total number of stages	-	6

The performance characteristics of structured packing are often given as function of the F-factor, which is defined by the square root of the vapour density multiplied by the superficial gas velocity. The superficial gas velocity is given by the volumetric vapour flow divided by column cross-sectional area. Up the maximum F-factor, the separation efficiency is relatively constant. However, above this maximum, the efficiency diminished rapidly due to loading and flooding of the packing.
The dependency of the pressure drop over the packing on the F-factor is approximately linear on a log–log plot. In addition, the pressure drop depends slightly on the liquid load, which is given by the volumetric liquid flow rate divided by the column cross-sectional area. For a liquid load of 20 $m^3/(m^2h)$, the pressure drop is approximately 0.1 mbar/m at an F-factor of 0.3 $\sqrt{\text{Pa}}$, and approximately 3.0 mbar/m at an F-factor of 2.0 $\sqrt{\text{Pa}}$.

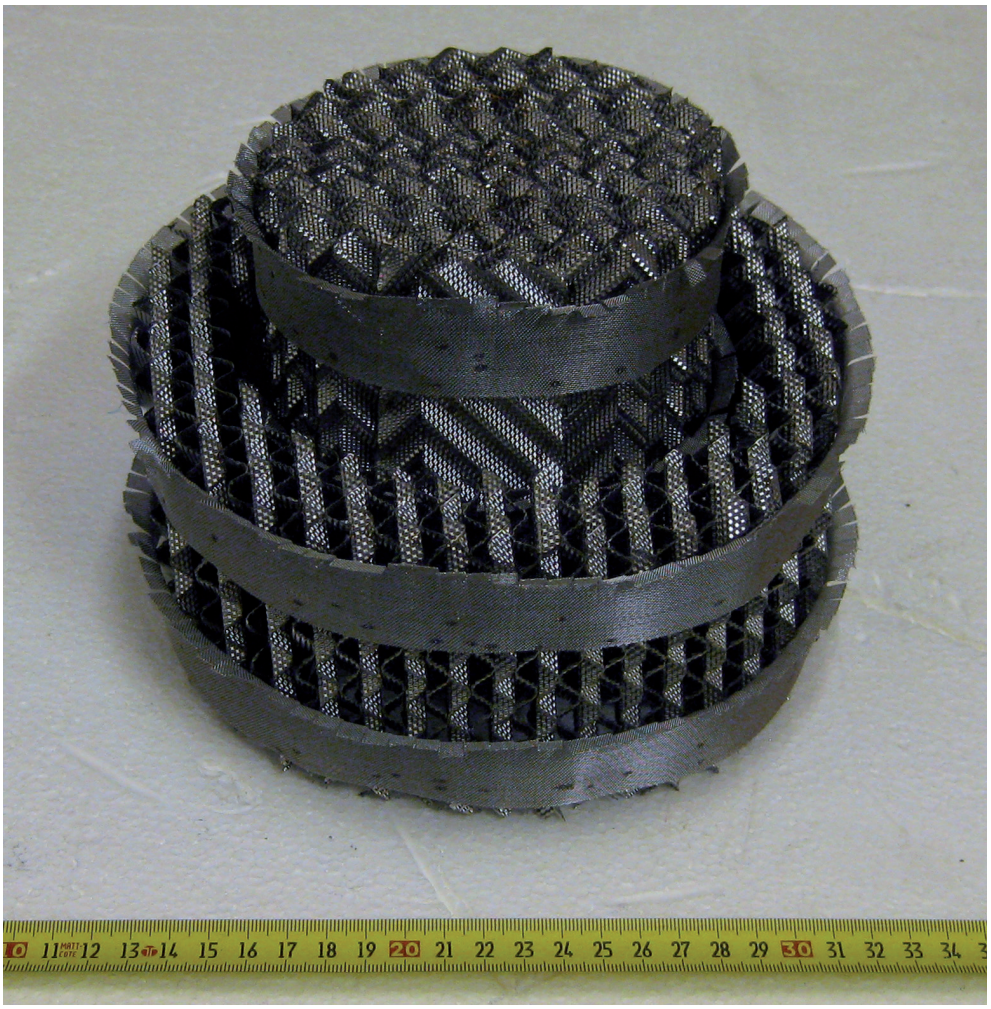

Figure 9.3: Picture of two packing elements: an element for the inner column that is partly placed inside an element for the outer column.
The scale shown at the bottom is in cm.

9.3 Simulations

In order to determine the maximum volumetric flow rates and the reboiler and condenser duties, several operating cases of the HIDiC set-up have been simulated. The distillation columns are simulated in HYSYS using a basic equilibrium stage model, which is described in more detail in Section 9.3.1. Section 9.3.2 describes how the maximum and minimum flow rates and operating pressures are determined. In Section 9.3.3, the combination of flow rates and pressures that minimizes the required total cooling duty is found, yielding the base case design. Three more extreme operating cases are identified as well. Some characteristic column profiles of the base case design are shown in Section 9.3.4. Based on the operating characteristics of all four cases, the volumetric flow rate limits and the maximum reboiler and condenser duties are finally determined in Section 9.3.5.

9.3.1 HYSYS model

The HIDiC set-up is simulated using a standard equilibrium stage model in HYSYS 2006. The model uses a fixed number of 6 equilibrium stages in both columns. The heat integration of the two columns is simulated by adding or removing amounts of thermal energy to the stages that are proportional to the difference in the stage temperatures of the two columns. Total reflux is mimicked by specifying a feed flow rates that is about 10^6 times smaller than the internal flow rates.
A constant overall heat-transfer coefficient of 500 W/(m^{2}K) is used in the simulations. The amount of heat-transfer area per equilibrium stage can be calculated using the diameter of the inner column wall and the number of theoretical stages per meter of packing. Possible vertical open spaces between packing elements are not included in the current model, neither is the thermal energy transfer between the sumps of the two columns. The loss of low temperature thermal energy to the surroundings is also neglected.
The use of a binary mixture of nitrogen and oxygen is assumed. This makes it easier to compare the experimental results with the numerical results obtained from theoretical models. The thermodynamic properties of this nitrogen–oxygen mixture are calculated using the Peng–Robinson equation of state modified by Stryjek and Vera and using Lee–Kessler vapour pressures (PRSV-LK).
The compositions at the top and bottom of a column are modelled such that the nitrogen stream at the top is as pure as the oxygen stream at the bottom. Operating around the centre of the total concentration range is advantageous because it results in bigger composition differences along the column height, which are easier to measure. In practise, this situation can be approximated by enforcing a purity of 50% half-way the column height.

9.3.2 Operating ranges

The detailed design of the experimental set-up requires estimates for the maximum required volumetric flow rates and reboiler and condenser duties. Those quantities

are mainly determined by four operating variables: the flow rates in the inner column, the flow rates in the outer column, the pressure in the outer column, and the pressure ratio. This section discusses the minimum and maximum flow rates and operating pressures that will be used during experiments.

Flow rates

As explained in Section 9.2.3, the maximum vapour flow rate is defined by the critical F-factor, above which regular operation becomes impossible. For Montz B1-500 packing, it is around 2.0 $\sqrt{\text{Pa}}$. The vapour flow rate is always equal to the liquid flow rate in a column that is operating at total reflux. So the upper operating limit of the liquid flow rate is also determined by the critical F-factor. However, the lower operating limit is determined by the liquid phase rather than the vapour phase.
The liquid flow rate is usually given as the amount of volumetric liquid flow per column cross-sectional area per unit of time, and is referred to as the liquid load. The use of structured packing makes is possible to operate within a very wide liquid load range, from about 0.2 to over 200 $\text{m}^3/(\text{m}^2\text{h})$. The lower limit of the operating range is related to dewetting of the packing. When the liquid load becomes too low, dry spots might be formed, causing a drop in the available vapour–liquid interface area and thus in the separation efficiency. Therefore, it is important that the liquid load is always above the minimum limit, at every location in the column. In a HIDiC, the liquid load varies significantly throughout the column, both in the longitudinal and radial directions. The variations in the longitudinal direction, caused by condensation and evaporation, can be estimated using conventional distillation column models. But the variations in the radial direction are harder to predict accurately. It is therefore important not to design too close to the regular minimum liquid load. The minimum allowable liquid load has been set at 1 $\text{m}^3/(\text{m}^2\text{h})$ for the current study. A preferred value of 5 $\text{m}^3/(\text{m}^2\text{h})$ will be used.

Pressure ratio

The pressure ratio between the two columns is responsible for the thermal energy transfer through the inner column wall. The amount of transferred energy is proportional to the temperature difference between the two columns, which has been found to be approximately proportional to the pressure ratio.
Pressure ratios used for HIDiC designs are typically in the order of 2 to 3. At higher ratios, the compression work that is required to create the pressure difference is becoming unfeasibly high. At lower ratios, the required amount of heat-transfer area is becoming too high. The optimal pressure ratio is different for each application. In a conventional air separation plant, the high-pressure and low-pressure columns operate with a pressure ratio of about 4.
With the above in mind, it has been decided to vary the pressure ratio between 1 and

4 during operation. A pressure ratio of 1 is included in order to enable comparisons with columns that do not involve heat integration.

Absolute pressures

In industrial processes, air is entering the distillation section at a pressure of about 5 bar. This pressure is defined by the air pre-purification step upstream of the distillation section. To keep the design as close to a practical implementation as possible, it has been decided to operate around this pressure level.
The minimum column operating pressure is related to the temperature level in the condensers. At an atmospheric pressure, liquid nitrogen evaporates at a temperature of about 77.3 K. In order to ensure a minimum temperature difference, we set the minimum operating pressure at 1.5 bar. This corresponds to a minimum temperature difference of about 4 K.
The maximum operating pressure is defined by the 5 bar pressure level and a maximum pressure ratio of 4, resulting in a maximum pressure of 20 bar.

Summarizing overview

Table 9.4 gives a summary of the conditions that define the minimum and maximum values of the flow rates and pressures in the inner and outer columns.

Table 9.4: Overview of the operating limits of the flow rates and pressures.

Variable	Minimum	Maximum
F_o & F_i	B = 1 $m^3/(m^2h)$	F-factor = 2.0 $\sqrt{Pa}$
P_R	1.0	4.0
P_o	1.5 bar	5.0 bar
P_i	3.0 bar	20.0 bar

9.3.3 Four operating cases

Because the operating costs of the set-up largely depend on the condenser duties, it is useful to get more insight in how the total cooling duty varies as function of the operating variables. This makes it possible to choose the combination of operating variables that yields the lowest cooling duties. It also allows for an estimation of the average required cooling duty.
In order to determine the optimal combination of operating variables, it needs to be decided at what pressures the flow rates will be varied, and vice versa. In Sections 9.A.1 and 9.A.2, the variation of the total condenser duty as function of both the inner and outer column flow rates is presented for several combinations of operating

pressures. It shows that the condenser duty is a linear function of the flow rates. That is why it is best to operate at low flow rates. In addition, it is best to operate at low absolute pressures and that the pressure ratio should be low but larger than unity. Based on these findings, four typical operating cases have been identified, which are listed in Table 9.5.

Table 9.5: Four typical operating cases.

Case		F_{min}	F_{max}	P_{min}	P_{max}
Min. liquid load	$m^3/(m^2h)$	1.0	-	5.0	5.0
Max. F-factor	$\sqrt{Pa}$	-	2.0	-	-
P_R	-	2.0	2.0	2.0	4.0
P_o	bar	1.5	1.5	1.5	5.0
P_i	bar	3.0	3.0	3.0	20.0

The operating ranges of the flow rates and of the pressures have one shared point: the minimum pressure case shown in Table 9.5. This operating case will be used as base case in the current study. The other three cases represent the most-extreme deviations from the base case conditions.

9.3.4 Base-case column profiles

Figures 9.4 to 9.7 show some characteristic column profiles for the base-case operating conditions. In these figures, the top of the column is given by position 1 and its bottom by position 7. The intermediate position numbers represent the locations in between two subsequent theoretical equilibrium stages.

Mass flow rates and compositions

Figure 9.4 shows how the mass flow rates and the nitrogen mole fractions in the inner and outer columns change along the height of the column. The shown profiles are by definition the same for the liquid and vapour phases, due to total reflux operation. When considering the liquid that is flowing down from the top to the bottom of the inner column, we see that the mass flow rate is increasing. This means that condensation is taking place in the inner column. Similarly, it can be seen that evaporation is taking place in the outer column. This makes sense because the inner column is operating at a higher pressure, and therefore at a higher temperature, than the outer column. As a result, thermal energy is transferred from the inner column to the outer column. The removal of thermal energy from the inner column is realized by the condensation of vapour, and the addition of thermal energy to the outer column causes liquid to evaporate.
The difference between the nitrogen mole fraction profiles of the inner and outer columns is caused by their different operating pressures. The shown influence of the

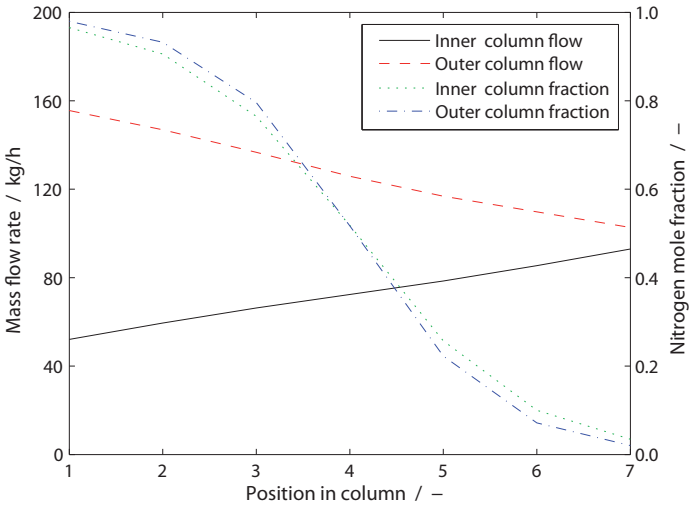

Figure 9.4: Column profiles of the mass flow rates and nitrogen mole fractions in the inner and outer columns. Position 1 represents the top of the column and position 7 its bottom.

pressure suggests that the product purities in general decrease when the operating pressure increases.

Liquid loads and F-factors

Figure 9.5 shows how the liquid loads and F-factors in the inner and outer columns change along the height of the column. The F-factor profiles are relatively linear and very similar to the mass flow rate profiles shown in Figure 9.4. The liquid load profiles have different trends; they are caused by the temperature and composition dependencies of the density. Using the F-factors shown in Figure 9.5 and the pressure drop characteristics of the structured packing, the total pressure drop in the two columns can be estimated: in the inner column it is approximately 0.25 mbar, and in the outer column approximately 0.70 mbar.

Liquid temperatures

Figure 9.6 gives an overview of how the liquid temperatures in the inner and outer columns change along the height of the column. The temperature difference between the top and the bottom of a column part is approximately 12 K. The profile of the difference between these two temperatures profiles is also shown in Figure 9.6; it varies between 7.2 and 7.6 K for the base case. However, the total radial temperature

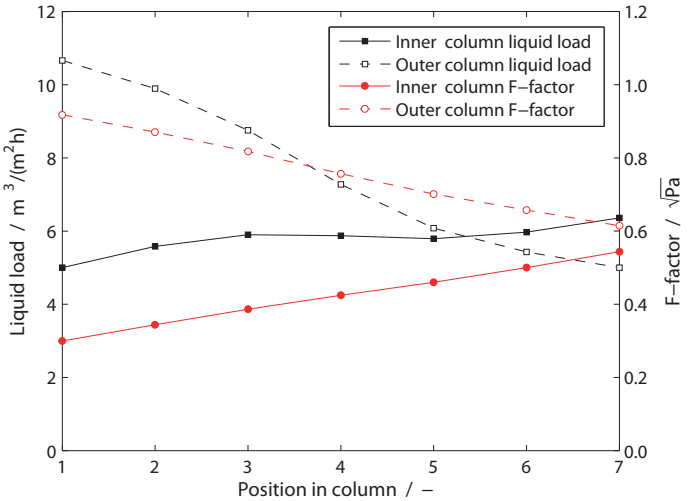

Figure 9.5: Column profiles of the liquid loads and the F-factors in the inner and outer columns. Position 1 represents the top of the column and position 7 its bottom.

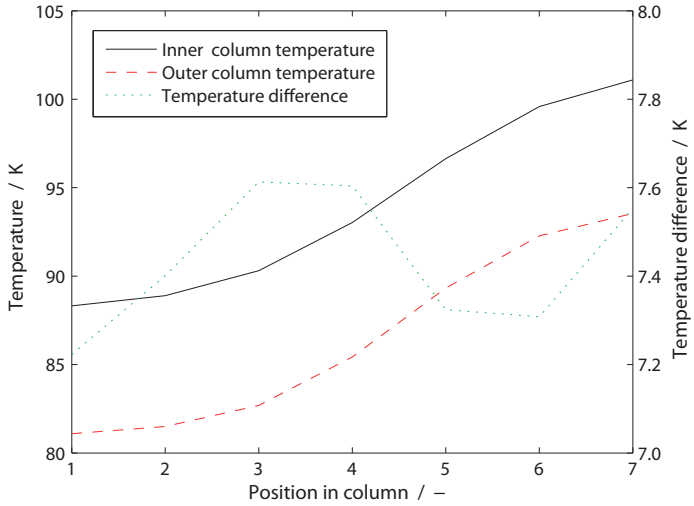

Figure 9.6: Column profiles of the liquid temperatures in the inner and outer columns, and of the difference between them. Position 1 represents the top of the column and position 7 its bottom.

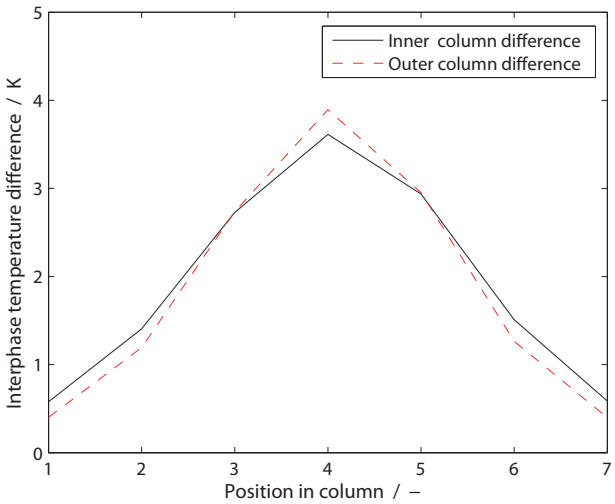

Figure 9.7: Column profiles of the temperature differences between the liquid and vapour phases in the inner and outer columns. Position 1 represents the top of the column and position 7 its bottom.

difference might be larger, because the temperature profiles represent averages of the total liquid phases.

Interphase temperature differences

Figure 9.7 shows the differences in temperature between the liquid and vapour phases in the two columns. It can be seen that these differences are the smallest at the top and bottom of the columns, about 0.5 K, and that they are the largest around the centre of the columns, about 3.5 K. The difference between the profiles of the inner and outer columns is caused by their different operating pressures. Extrapolating the influence of the pressure suggests that the temperature difference profile will be more constant at higher operating pressures.

9.3.5 Operating limits

The four operating cases described in Section 9.3.3 have been simulated using the model described in Section 9.3.1. Detailed simulation results are listen in Section 9.B. For each of the four cases, values for the mass flow rates, the liquid loads, the F-factors, the heat duties, the temperatures, the compositions, the vapour and liquid densities, and the vapour and liquid viscosities are listed for the top and the bottom of both the inner and outer columns.
Using these data, the operating limits of the volumetric vapour and liquid flow rates

and the maximum condenser and reboiler duties can be determined. The volumetric flow rates are arbitrative for dimensioning of piping, flow meters and control valves. The maximum heat duties are required for the design of the nitrogen supply system, the condensers and the reboilers. An overview of the volumetric vapour and liquid flow rates and the heat duties at the top and bottom of both the inner and outer column for all four operating cases is given in Table 9.6.
All volumetric liquid flow rates limits are defined by the maximum and minimum flow cases. The minimum volumetric vapour flow rates in the inner column are defined by the maximum pressure case. All other volumetric vapour flow rate limits are defined by the maximum and minimum flow conditions.
Because the flows in the two columns can be controlled independently, it is possible to combine any of the low-pressure inner column flow cases with any of the low-pressure outer column flow cases. As a result, it can be concluded that the total heat duties will vary between 8.5 and 25 kW when varying the inner column flow rate, and between 5.2 and 21 kW when varying the outer column flow rate. So overall, the total heat duties vary between 5.2 and 25 kW.

9.4 Detailed design

Based on the operating limits of the volumetric flow rates and the heat duties found in Section 9.3.5, detailed designs of all required components have been made. Their main properties and the rational behind them are presented in this section. A schematic of the entire set-up is shown in Figure 9.8.

9.4.1 Liquid nitrogen supply

The liquid nitrogen that is used as coolant in the condensers originates from a pressurized nitrogen tank. It is flowing through approximately 14 m of vacuum insulated piping, after which it is split in two streams, throttled down in pressure using two control valves (described in more detail in Section 9.4.8), and finally fed to the condensers where it is evaporated. Before being vented into the atmosphere, the two vaporized nitrogen streams are joined again and heated in a large heat exchanger in order to level the nitrogen temperature with the ambient temperature. The inner diameters of the vacuum insulated pipe are 26 mm for the process line and 60 mm for the vacuum jacket.

Storage tank

In order to determine the size of the nitrogen storage tank, the storage pressure and an estimate for the monthly nitrogen demand are required. The tank pressure determines what amount of liquid nitrogen is required for a given amount of cooling. A tank pressure of approximately 5 bar is used, which corresponds to a nitrogen requirement of 21.8 kg per kWh of cooling. A lower pressure results in a lower nitrogen demand,

Table 9.6: Overview of the top and bottom heat duties and volumetric flow rates of the four operating cases.

Case		Base		F_{max}		F_{min}		P_{max}	
Column		Inner	Outer	Inner	Outer	Inner	Outer	Inner	Outer
Top liquid flow rate	dm^3/h	68.1	196	419	426	13.6	85.2	68.1	349
Top vapour flow rate	m^3/h	17.1	23.6	25.5	51.5	0.83	10.3	0.48	12.6
Condenser duty	kW	2.68	8.45	16.5	18.4	0.54	3.68	1.46	12.5
Bottom liquid flow rate	dm^3/h	86.7	91.8	319	245	50.7	18.3	268	91.8
Bottom vapour flow rate	m^3/h	7.62	16.1	28.0	42.9	4.46	3.21	2.76	4.80
Reboiler duty	kW	5.16	5.97	19.0	15.9	3.02	1.19	8.98	5.01

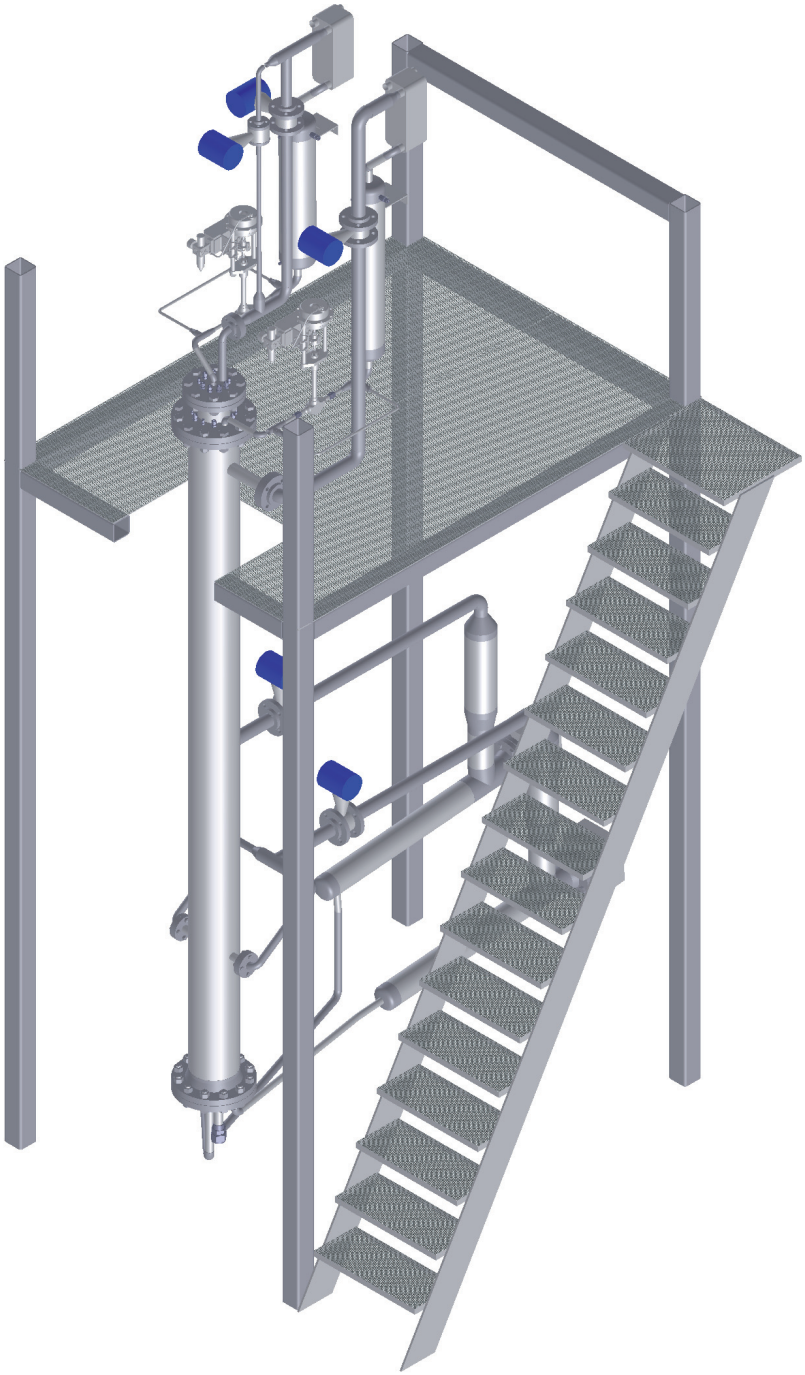

Figure 9.8: Three-dimensional schematic of the experimental set-up.

but it also increases the loss of low temperature thermal energy to the surroundings. Based on the cooling duties found in Section 9.A, three types of operating days can be identified: operation at the maximum duty of 25 kW, operation at a base case duty of 11 kW, and operation at a stand-by duty of 0.5 kW. The stand-by duty is the estimated cooling that is required to compensate for the loss of low temperature thermal energy to the surroundings when not operating. Assuming operating days of 8 hours, the daily cooling duty demands for the three types of days become 208, 96 and 12 kWh respectively, corresponding to daily nitrogen demands of 4.53, 2.09 and 0.26 ton.
In order to estimate the monthly nitrogen demand, one of the three operating day types needs to be assigned to each of the 30 days. It is assumed that 8.5 days are weekend days, which are stand-by days. For the remaining 21.5 days, it is assumed that one-fifth is maximum operating days, that two-fifths are base case operating days, and that the last two-fifths are stand-by days. This results in an approximate monthly nitrogen demand of 42 ton. Based on this estimate, a nitrogen storage tank with a volume of 11 m^3 has been installed.

Volumetric nitrogen flow rates

Using a nitrogen demand of 21.8 kg per kWh of cooling and the maximum condenser duties given in Section 9.3.5, the maximum nitrogen mass flow rate can be estimated to be 360 kg/h for the inner column, 401 kg/h for the outer column, and 544 kg/h for the combination of the two columns. Four different locations in the nitrogen circuit can be distinguished: (1) between the storage tank and the two cryogenic control valves, (2) between the control valves and the two condensers, (3) between the condensers and the after-heater, and (4) downstream of the after-heater. Table 9.7 gives an overview of the pressure, temperature, density, and resulting maximum volumetric flow rates at these four locations.

Table 9.7: Maximum volumetric nitrogen flow rates for four different locations in the nitrogen circuit.

Location		1	2	3	4
Pressure	bar	5.0	1.1	1.0	1.0
Temperature	K	T_{bub}	T_{bub}	T_{dew}	T_{amb}
Phase		L	L(+V)	V	V
Mass density	kg/m^3	723	802	4.54	1.13
Inner column flow	m^3/h	0.498	0.449	79.3	319
Outer column flow	m^3/h	0.555	0.500	88.3	355
Combined flow	m^3/h	0.752	0.678	120	481

9.4.2 Condensers

The condensers are copper-brazed plate heat exchangers from GEA of the type GBS 400H with 50 plates. Liquid nitrogen enters the heat exchangers at the bottom, evaporates, and leaves at the top outlets. The vapour streams from the columns enter at the top of the heat exchangers, condense, and leave at the bottom outlets. From the 49 channels, 25 are used for nitrogen flow in order to maximize the cooling duty. The condensers are sized based on the maximum flow rate conditions. During normal operation, most of the column side volume of the condensers is occupied by vapour.

9.4.3 Reflux drums

Kister [1990] and Seader and Henley [1998] recommend to size reflux drums based on a 2 to 5 minutes liquid residence time. In industrial installations, the main aims of a reflux drum are to serve as buffer for process fluctuations and to facilitate control. In the current set-up, its main aims are to provide a buffer volume required for changing operating conditions and to provide a pressure difference that ensures liquid flow from the reflux drum to the column.
Based on the maximum volumetric liquid flow rates listed in Table 9.6 and a residence time of 60 s, a first estimate for the required liquid volume has been calculated. Doubling this volume to ensure some buffer volume, and assuming vertical cylindrical drums with a height-to-diameter ratio of 4, approximate drum diameters of 0.16 m are found. Based on the available tube dimensions and on the expected liquid level changes during operation, (which are discussed in Section 9.D.4), the following reflux drum dimensions have been selected:

Table 9.8: Reflux drum dimensions.

Column		Inner	Outer
Liquid volume	dm^3	7.0	7.1
Drum diameter	m	0.155	0.137
Drum height	m	0.75	0.90
Total volume	dm^3	14.2	13.3

9.4.4 Liquid distributors

S-type liquid distribution systems from Montz are used for both columns. The distributor of the inner column has 20 drip points; 10 are located at distance of 32 mm from the column centre and 10 are located at a distance of 47 mm from the column centre. The distributor of the outer column has 36 drip points that are all located at a distance of 86 mm from the column centre. The inner column has a drip point density of almost 1500 points/m^2 and a maximum liquid capacity of about 400 dm^3/h. The outer column has a drip point density of almost 2000 points/m^2 and a maximum

liquid capacity of about 450 dm^3/h. Figure 9.9 shows a picture of the outer column distributor.

9.4.5 Column

High-pressure and low-pressure sides

It has been decided to operate the inner column at the high-pressure level and the outer column at the low-pressure level. There are several reasons why this is best configuration. Firstly, a column operating at a higher pressure requires a thicker column wall. When the outer column operates at the highest pressure, both walls need to be thick enough for the maximum operating pressure. If the inner column operates at the highest pressure, only the inner wall needs to be thick enough and the outer column can theoretically be thinner.
Secondly, the outer column is most sensitive to liquid maldistribution effects. It is therefore best to locate the evaporating side of the inner wall, which is the low-pressure side, at the outside. Because of condensation at the wall in the inner column, additional wall wipers might be desirable. The packing in the outer column has no wall wipers at the inner column wall, only at the outer column wall.
Another argument for locating the low-pressure side in the outer column is related to the thermal energy transfer through the outer wall. The low-pressure column is the column that needs to be heated along its height, and the high-pressure column needs to be cooled. Since thermal energy is entering the system through the outer wall, it is best to have it enter the low-pressure column.

Construction material

The material that is used to construct the inner column wall is important for the thermal resistance between the inner and outer columns. This resistance should in practise be as low as possible, because a lower resistance means that more thermal energy is transferred at a given temperature difference, or that a lower temperature difference (and thus pressure ratio) is needed to transfer the same amount of thermal energy. In an experimental situation, it is not essential to have an as low as possible resistance. It is more important to know the resistance accurately.
Industrial air distillation columns are nowadays constructed out of stainless steel or aluminium alloy; in the past copper has been used as well. At a temperature of 100 K, the thermal conductivity of copper, aluminium alloy and stainless steel are about 450, 200 and 10 W/(mK) respectively. Their current prices are about 6.8 \$/kg of copper, 2.0 \$/kg of aluminium, and 0.5 \$/kg of stainless steel. In general, stainless steel is roughly two times stronger than the other two materials. The exact values depend on the types of copper, aluminium and stainless steel that are considered.
From a thermal conductivity and cost point of view, it would be best to construct the inner wall out of aluminium alloy, and the outer column wall out of stainless

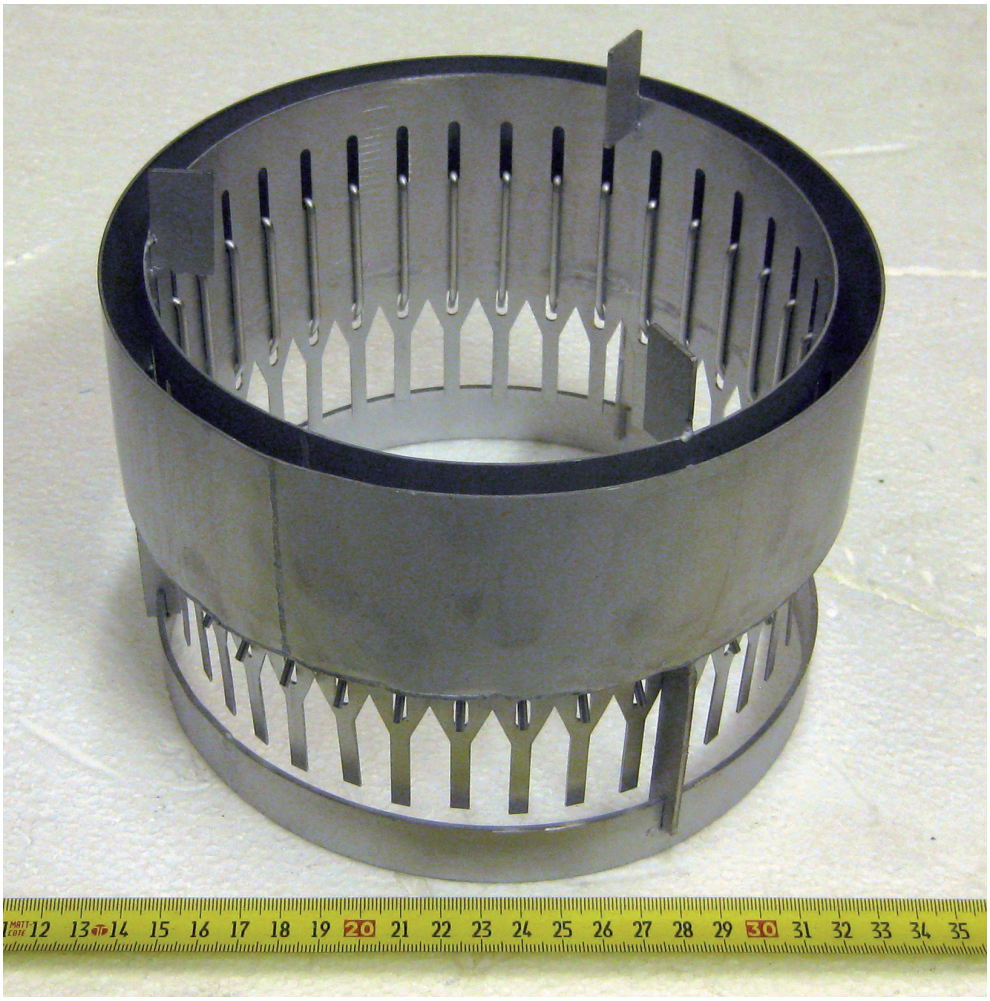

Figure 9.9: Picture of the liquid distributor of the outer column.
The scale shown at the bottom is in cm.

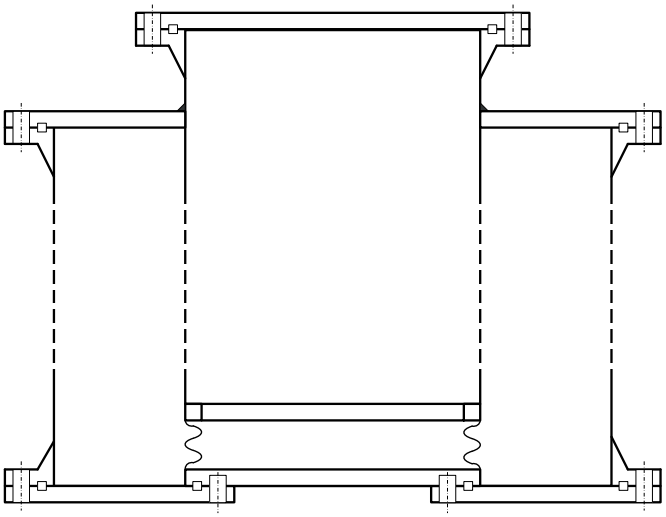

Figure 9.10: Schematic of the top and bottom flange configurations.

steel. However, the use of two construction materials with different thermal expansion coefficients can lead to unwanted complications. Therefore, it is more practical to construct the two columns walls out of the same material. Stainless steel has been chosen as construction material for the current columns, because stainless steel parts are more readily available in standard sizes and they are easier to process. For a commercial HIDiC, the use of aluminium or copper should be considered because of their superior thermal properties.

Top and bottom arrangements

Figure 9.10 shows how the top and the bottom of the set-up are arranged and how the column internals can be mounted.
The bottom of the inner column is welded to the column wall. The structured packing and other column internals are mounted from the top, where a flange is used. The top of the outer column is welded to the inner column wall. The internals and the shell of the outer column are mounted from the bottom. The bottom of the outer column is a flange that is attached to both the outer column wall and the bottom of the inner column. A metal bellows is used at the bottom of the set-up to prevent stresses in the longitudinal direction from occurring.

Column height

The total column height is defined by the total packing height, the space in between packing sections, the height of the liquid distribution system, and some additional open space at the top and the bottom of the column.
The 16 packing elements that are present in the column are installed in groups of four. In between these four packing sections, an open space of 2 cm is present to allow for instrumentation. The open spaces at the top of the column are approximately 0.50 m in the inner column and 0.35 m in the outer column, including the liquid distributors. The parts of the inner column wall that are located above and below the packing are surrounded by a polymer tube with a low thermal conductivity, in order to limit the thermal energy transfer to the packing section only.
Some guidelines for the open spaces in the bottom of a column are given by Kister [1990]. The vapour inlet should be positioned at least 30 cm above the maximum liquid level in the column sump, and the entering vapour should not be directed towards the liquid, in order to prevent liquid entrainment. The bottom packing section should be positioned at least 30 cm above the vapour inlet, to allow for proper vapour distribution. In order to prevent vapour entrainment into the reboiler, it is recommended that the liquid height in the sump of the column ensures a liquid residence time of at least one minute. In Section 9.D.4 it is shown that this results in a maximum liquid level of about 0.74 m in the inner column.
Combining all the above numbers results in a total column height of 3.5 m.

Support frame and insulation

The column, together with all other components, is positioned within a metal support frame that has an approximate height, width, and depth of 5, 1.5, and 2 m. All cold components are insulated by a layer of at least 15 cm of rockwool insulation. Parts of the open space within the support frame are also filled with rockwool insulation.

9.4.6 Reboilers

The reboilers are horizontal kettles with submerged electrical heating elements, each having a maximum duty of 20 kW. The heating compartment of each reboiler is a tube with an inner diameter of 0.11 m and a length of 1.10 m. It is equipped with 12 U-shaped heating elements with a length of about 1 m and an approximate diameter of 1 cm. The horizontal position of the reboiler is chosen such that the heating elements are always completely below the minimum liquid level in the column sumps.
The vapour flow rate at the outlets of the reboilers is measured in order to quantify the flow rates of the liquid and vapour that are leaving and entering at the bottom of the structured packing. Therefore, it is important that no entrainment is occurring in the streams that are entering and leaving the reboilers. If vapour is entrained in the liquid that is entering the reboiler, than a part of the vaporized liquid is recycled

back to the reboiler instead of flowing up through the packing. If liquid is entrained in the vapour that is leaving the reboiler, than a part of the flow through the reboiler leaves as liquid, which flows immediately back into the column sump. Both cases result in measured flow rates that are higher than the actual ones at the bottom of the structured packing.
Vapour entrainment is minimized by allowing for sufficient liquid residence time in the sump of the column and by sizing the liquid pipes for self-venting flow, as is discussed in more detail in Section 9.4.7. In order to limit the amount of liquid entrainment, the reboilers are equipped with vertical gravity separators having diameters and heights of approximately 0.14 m and 0.45 m. The sizing of these vapour–liquid separators is discussed in more detail in Section 9.C. Between the separators and the heating compartments, there is a height of about 0.30 m available to accommodate liquid level variations. This is slightly more than the expected maximum liquid level changes calculated in Section 9.D.4.

9.4.7 Piping

The properties of the piping going in and out of the columns have been determined based the maximum volumetric flow rates given in Section 9.3.5. Different criteria are used for vapour flow and the liquid flow, as explained in more detail below.

Vapour flow

The maximum volumetric vapour flow rates can be used to determine the diameter of the vapour tubes. Using a maximum allowable vapour velocity of 10 m/s [Simpson, 1968], the minimum inner diameters for the vapour tubes can be calculated. Based on the minimum inner diameters and an estimate for the wall thickness, tube sizes can be selected from the standard tube dimensions. For the annular outer column, two vapour inlets are used in order to promote a good vapour distribution. The results are shown in Table 9.9.

Table 9.9: Vapour tube characteristics, based on the maximum flow rate conditions given in Table 9.6.

Column	Location	Tubes	D_{min} (mm)	D (mm)
Inner	Top	1	30.0	35 x 2.0
Inner	Bottom	1	31.5	38 x 2.5
Outer	Top	1	42.7	60 x 2.0
Outer	Bottom	2	27.5	35 x 2.0

The vapour inlets and outlet of the outer column are positioned at the side of the column. For the inner column, the vapour inlet enters at the bottom and the vapour outlet leaves at the top. Because this vapour inlet tube passes through the liquid in

the sump of the column, some of the vapour might condense on the wall of the inlet tube. In order to prevent this from occurring, a tube with a slightly larger diameter is positioned around the inlet tube. In this way, the inlet tube is no longer in direct contact with the liquid. The top of the vapour inlet tube is shaped such that it directs the vapour flow to the side, instead of directing it upwards to the packing.

Liquid flow

In order to determine the size of the liquid tubes, the concept of self-venting flow has been used. This ensures that the bubbles that are present in a downflowing liquid are not entrained, but they flow up automatically. The absence of vapour bubbles in the liquid phase is important for correct flow measurements at the top and bottom of the column. In order to ensure self-venting flow, the following criterion should be obeyed [Simpson, 1968]:

$$\frac{v_L}{\sqrt{gD_i}}\sqrt{\frac{\rho_L}{\rho_L - \rho_V}} < 0.31 \tag{9.1}$$

Here, v_L is the superficial velocity of the liquid phase, based on a completely filled tube cross-section. The resulting minimum inner tube diameters are shown in Table 9.10, along with the selected standard tube types.

Table 9.10: Liquid tube characteristics, based on the maximum flow rate conditions given in Table 9.6.

Column	Location	D_{min} (mm)	D (mm)
Inner	Top	29.9	35 x 2.0
Inner	Bottom	26.7	35 x 2.0
Outer	Top	30.0	35 x 2.0
Outer	Bottom	24.0	30 x 2.0

The liquid enters both columns at the top. In the inner column, it is directly fed to the liquid distributor. However, in the outer column the liquid first enters a horizontal ring-shaped tube, from which it is transported into the liquid distributor using twelve vertical tubes.

9.4.8 Valves

The experimental set-up contains several types of valves. At the top of each column, a cryogenic ball valve is present that allows for the filling of working fluid. At both the top and the bottom of the two columns, a combination of a cryogenic ball valve and a needle valve is present that can be used to adjust the inventory of the columns. In addition, the set-up is equipped with several control valves and pressure relief valves.

Control valves

Four cryogenic control valves are used in the set-up. Two of them control the liquid flow from the reflux drums to the columns, the other two control the flow and throttling of the liquid nitrogen before it enters the condensers. The valves have been sized based on the International Standard IEC 60534-2-1 [IEC, 1998] and in correspondence with their manufacturers. The valves controlling the reflux are of the type WEKA PM-TGQV and have flow coefficient values of $K_v = 3.0$ for the inner column and $K_v = 2.6$ for the outer column. They have 1:20 modified equal percentage flow characteristics. The liquid nitrogen valves are of the type Samson Micro-flow Valve Type 3510. They have 1:50 equal percentage flow characteristics and K_v values of 0.63 for the inner column circuit and 1.6 for the outer column circuit.

Pressure relief valves

Both the inner and outer columns are equipped with pressure relief valves that designed using a maximum allowable operating pressure of 26 bar. The required discharge capacity of the valves is calculated based on EN 13648-3 [CEN, 2002], assuming fire conditions. Based on the dimensions and insulation configuration described in Section 9.4.5, minimum discharge capacities of 151 and 243 kg/h have been calculated for the inner and the outer columns. The dimensions of the valve have been decided on the bases of EN ISO 4126-1 [CEN, 2004]. The selected valves are all of the type Herose Type 06002, having a maximum discharge capacity of 587 kg/h, an orifice diameter of 6 mm, and a discharger coefficient of $K_d = 0.42$.

9.4.9 Mass inventory and liquid level limits

In order to determine the maximum and minimum liquid levels in the reflux drums and in the reboilers and column sumps, first the total amount of working fluid that is present in the system must be calculated. As part of this calculation, the total system volume must be calculated using the dimensions of the reflux drums, the columns, and the reboilers given in Sections 9.2.3, 9.4.3, 9.4.5 and 9.4.6. By evaluating the mass inventory in all these volumes at different operating conditions, the minimum amount of total mass inventory can be determined. The details of this calculation are presented in Sections 9.D.1 to 9.D.3. A summary of the results is shown in Table 9.11.

The liquid level limits can subsequently be determined by examining which liquid level changes are required in order to accommodate the total mass inventory at varying operating conditions. The details of this calculation are presented in Section 9.D.4 and the results are summarized in Table 9.12.

Table 9.11: Total system volume and mass inventory in both the inner and outer columns.

Column		Inner	Outer	Combined
Volume	dm^3	78.6	92.7	171
Nitrogen inventory	kg	6.98	7.18	14.2
Oxygen inventory	kg	18.6	18.5	37.1
Total inventory	kg	25.6	25.7	51.3

Table 9.12: Liquid level limits in the top and bottom of the inner and outer columns.

Column		Inner	Outer
Maximum top level	m	0.40	0.54
Minimum top level	m	0.14	0.48
Maximum bottom level	m	0.74	0.32
Minimum bottom level	m	0.46	0.22

9.5 Conclusions

The detailed design of an experimental set-up for the performance assessment of heat-integrated air distillation columns has been developed. First, a basic design was chosen that consists of two concentrically-integrated distillation columns with diameters of 14 and 22 cm. The high-pressure inner column operates between 1.5 and 20 bar and the low-pressure outer column operates between 1.5 and 5.0 bar. Both columns operate at total reflux and contain 6 theoretical stages of structured packing. Electrical heaters are used as reboilers and evaporating nitrogen provides cooling in copper-brazed plate heat exchangers that function as condenser. Using HYSYS simulations of several operating cases, the maximum volumetric flow rates have been determined at various locations in the set-up. The maximum total heat duty has been estimated to be 25 kW. Based on these operational limits, the dimensions of all other components have been selected. The resulting total column height is approximately 3.5 m. More details on the instrumentation and experiments are presented in the second part of this series of publications.

Notation

a	specific surface area, m^2/m^3
A_c	cross-sectional area, m^2
ASU	air separation unit
B	liquid load, $m^3/(m^2h)$
C_D	drag coefficient, dimensionless
D	diameter, m
f	volume fraction, dimensionless
F	flow rate, various units

g	gravitational constant, 9.81 m/s^2
h_p	packing height, m
HIDiC	heat-integrated distillation column
HPC	high-pressure column
IGCC	integrated gasification combined cycle
K_d	relief valve discharge coefficient, dimensionless
K_v	control valve flow coefficient
L	liquid
LPC	low-pressure column
m	mass inventory, kg
P	pressure, bar
RC	reboiler–condenser
v	velocity, m/s
V	vapour

Greek symbols

β	corrugation angle, degrees
δ	film thickness, m
ε	void fraction, dimensionless
η	viscosity, kg/(s m)
ρ	mass density, kg/m^3

Sub- and superscripts

amb	ambient conditions
bub	bubble point
dew	dew point
i	inner
L	liquid
max	maximum
min	minimum
o	outer
R	ratio
t	terminal
V	vapour

Acknowledgements

The research leading to these results has received funding from the European Community's 7th Framework Programme (FP7/2007-2013) under grant agreement number 211971 (The DECARBit project).

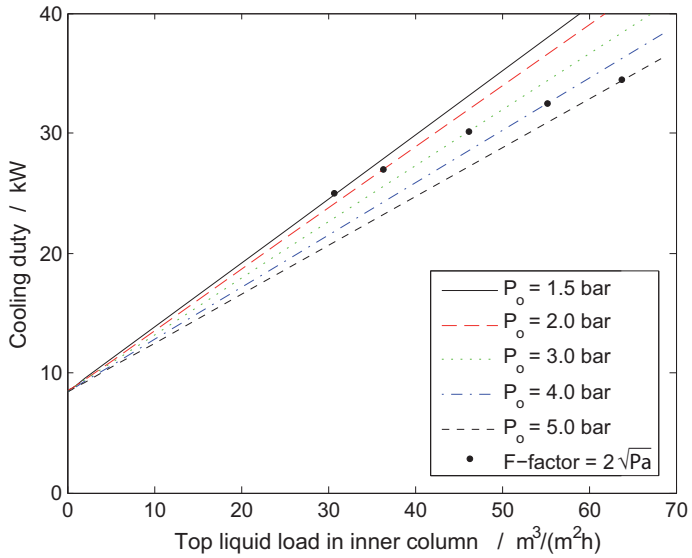

Figure 9.11: The cooling duty as function of the inner column top liquid load, using a fixed pressure ratio of 2 and for several outer column pressures.

9.A Cooling duties

9.A.1 Flow rates and outer column pressure

Figures 9.11 and 9.12 show how the cooling duty varies as function of the flow rate and the pressure in the outer column, for a fixed pressure ratio of 2. For each of the outer columns pressures, a black dot is used to indicate the point at which the F-factor is 2.0 $\sqrt{\text{Pa}}$. The figures show that the lowest condenser duty at which the critical F-factor value is reached corresponds to the lowest outer column pressure. So in order to minimize the condenser duty requirements during the experiments, it is best to operate at low absolute pressures.

9.A.2 Flow rates and pressure ratio

Figures 9.13 and 9.14 show how the cooling duty varies as function of the flow rate and the pressure ratio for an outer column pressure of 1.5 bar. The black dots indicate again the points at which the F-factor is 2.0 $\sqrt{\text{Pa}}$. Figure 9.13 suggests to use a pressure ratio as low as possible, and Figure 9.14 suggests to use a pressure ratio that is bigger than unity. From a practical point of view, it is also not desirable to operate at pressure ratio close to unity. The amount of thermal energy transfer will be very low in this case, making it more difficult to investigate the effects related to the heat integration.

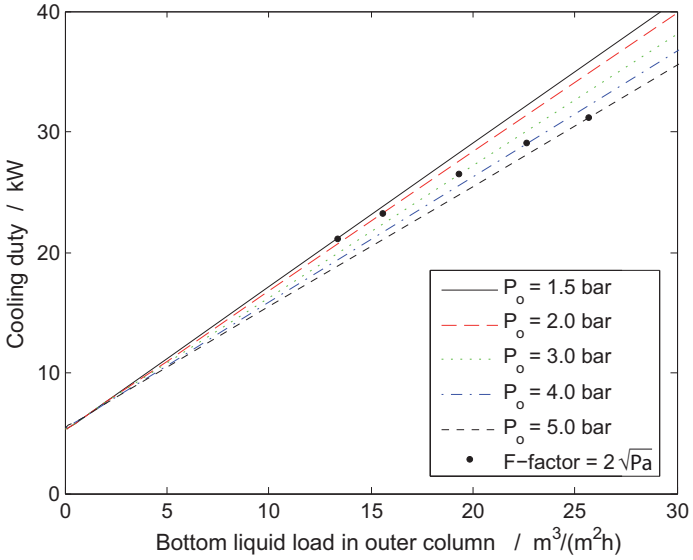

Figure 9.12: The cooling duty as function of the outer column bottom liquid load, using a fixed pressure ratio of 2 and for several outer column pressures.

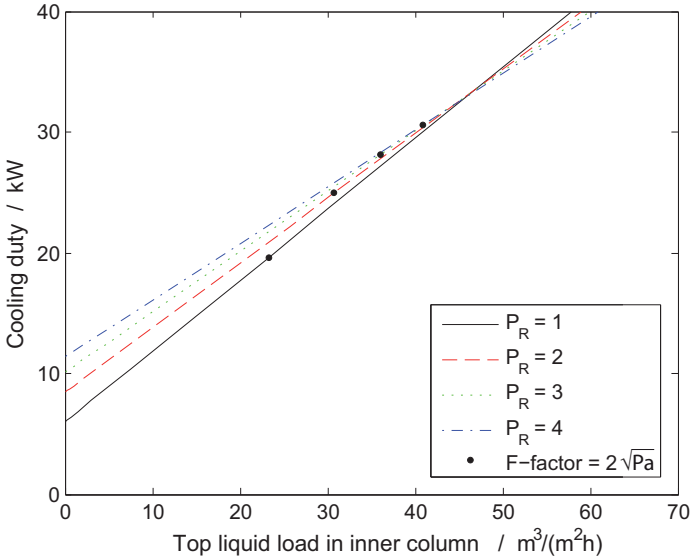

Figure 9.13: The cooling duty as function of the inner column top liquid load, at varying pressure ratios.

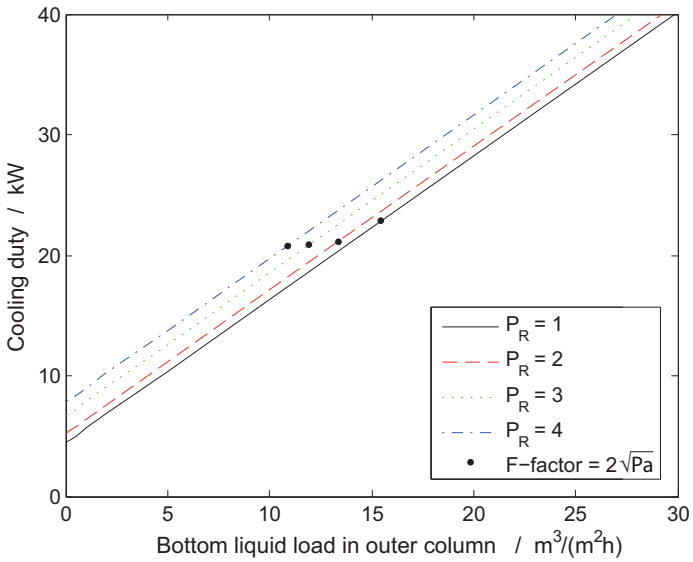

Figure 9.14: The cooling duty as function of the outer column bottom liquid load, at varying pressure ratios.

9.A.3 Variations from base case operation

The total base case cooling duty amounts to approximately 11 kW. In this section, it is investigated how this value changes for different operating conditions and for different values of some selected design variables.
Figure 9.15 shows how the condenser duty changes for different combinations of operating pressures. Based on all pressure combinations, the condenser duty will be between 8.7 and 14 kW.
Figure 9.16 shows the effect of varying the product purities on the required condenser duty. A general conclusion from this figure is that changing the composition ranges in the columns will slightly reduce the required condenser duties. This is related to a less constant temperature difference, and a decrease in the average temperature difference. The decrease in condenser duty is in the order of 1 to 2 kW.
Figure 9.17 shows how the cooling duty depends on the number of theoretical equilibrium stages, and thus on the separation efficiency of the packing. It can be seen that the cooling duty is practically independent of the the separation efficiency of the packing.
Figure 9.17 shows how the cooling duty depends on the overall heat-transfer coefficient of the inner wall. At very low values of the overall heat-transfer coefficient, the cooling duty is practically constant around 10 kW. At overall heat-transfer coefficients above 300 W/(m^{2}K), the condenser duty start to increase linearly with the overall heat-transfer coefficient. An increase of 100 W/(m^{2}K) in the overall heat-transfer coefficient corresponds to an increase of about 0.50 kW in the cooling duty.

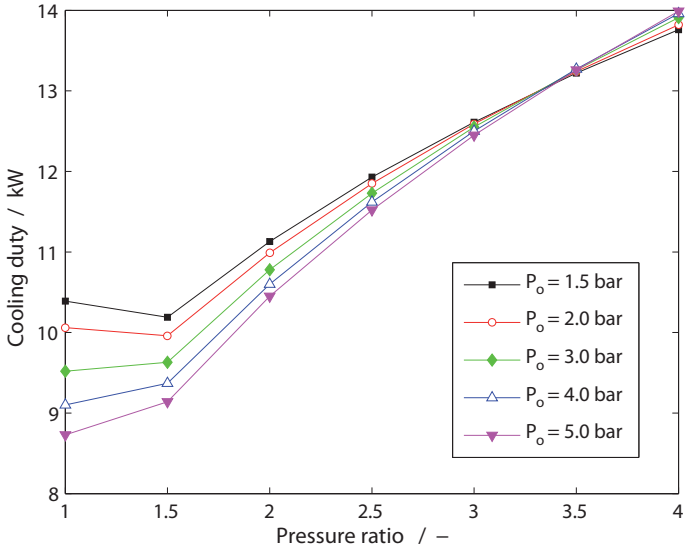

Figure 9.15: The cooling duty as function of the pressure ratio, at varying outer column pressures.

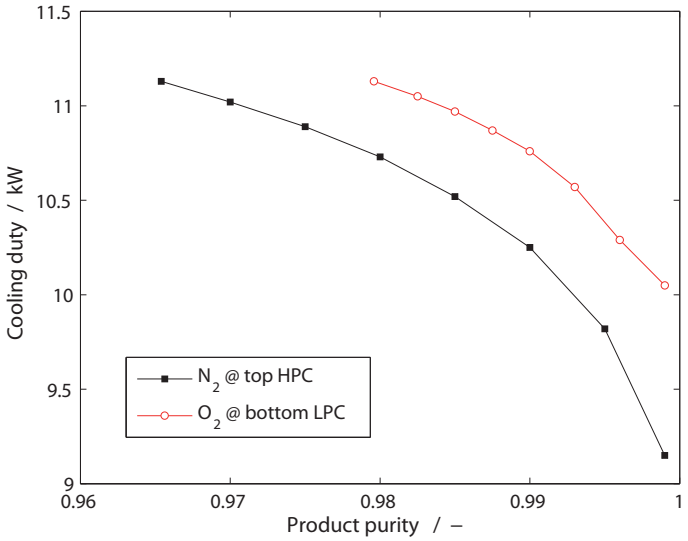

Figure 9.16: The cooling duty as function of the product purities.

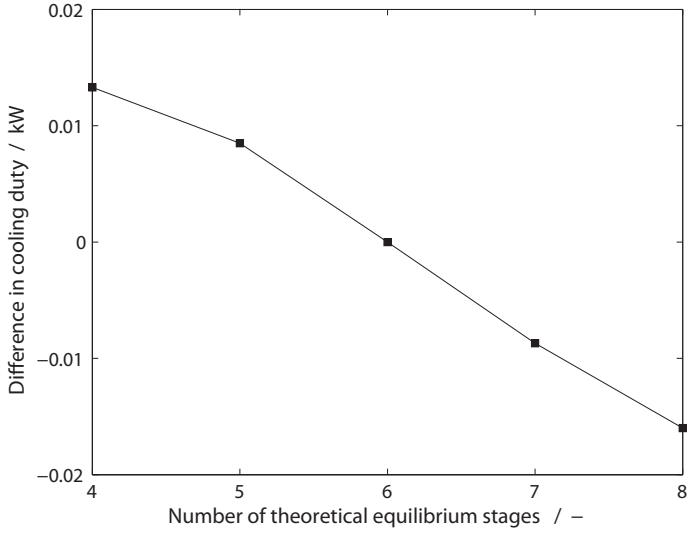

Figure 9.17: The cooling duty as function of the number of theoretical equilibrium stages, relative to the base case cooling duty.

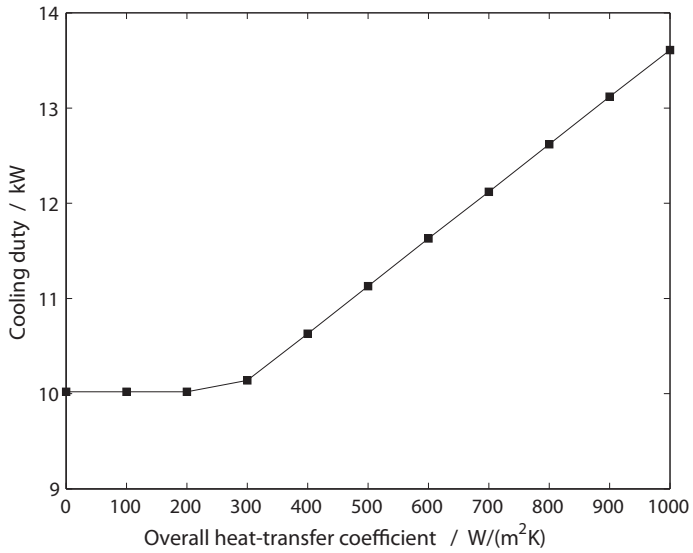

Figure 9.18: The cooling duty as function of the overall heat-transfer coefficient.

9.B Characteristics of the four operating cases

9.B.1 Flow rates and duties

This section summarizes the operating conditions of the four operating cases described in Section 9.3.3 in more detail.
Table 9.13 gives an overview of the base case operating conditions. The base case uses an inner column pressure of 3.0 bar, an outer column pressure of 1.5 bar, and it is based on minimum liquid loads of 5.0 $m^3/(m^2h)$ in both columns.

Table 9.13: Overview of the base case operating conditions for the inner and outer columns.

Quantity	Unit	Inner part	Outer part
Top flow rate	kg/h	52.1	155.6
Top liquid load	$m^3/(m^2h)$	**5.00**	10.67
Top F-factor	$\sqrt{Pa}$	0.300	0.918
Condenser duty	kW	2.68	8.45
Bottom flow rate	kg/h	93.0	102.7
Bottom liquid load	$m^3/(m^2h)$	6.36	**5.00**
Bottom F-factor	$\sqrt{Pa}$	0.544	0.616
Reboiler duty	kW	5.16	5.97

Table 9.14 shows the operating conditions of the inner and outer columns at their maximum flow conditions. They are defined by the maximum F-factor of 2.0 $\sqrt{Pa}$.

Table 9.14: Overview of the maximum flow operating conditions for the inner and outer columns.

Quantity	Unit	Inner part	Outer part
Top flow rate	kg/h	320.7	338.9
Top liquid load	$m^3/(m^2h)$	30.79	23.23
Top F-factor	$\sqrt{Pa}$	1.845	**2.000**
Condenser duty	kW	16.50	18.41
Bottom flow rate	kg/h	341.8	274.1
Bottom liquid load	$m^3/(m^2h)$	23.39	13.35
Bottom F-factor	$\sqrt{Pa}$	**2.000**	1.640
Reboiler duty	kW	18.98	15.92

Table 9.15 shows the operating conditions of the inner and outer columns at their minimum flow conditions. They are defined by a minimum liquid load of 1.0 $m^3/(m^2h)$.
Table 9.16 gives an overview of the maximum pressure operating conditions. The design uses an inner column pressure of 20.0 bar, an outer column pressure of 5.0 bar, and it is based on minimum liquid loads of 5.0 $m^3/(m^2h)$ in both columns.

Table 9.15: Overview of the minimum flow operating conditions for the inner and outer columns.

Quantity	Unit	Inner part	Outer part
Top flow rate	kg/h	10.4	67.7
Top liquid load	$m^3/(m^2h)$	**1.00**	4.64
Top F-factor	$\sqrt{Pa}$	0.060	0.399
Condenser duty	kW	0.54	3.68
Bottom flow rate	kg/h	54.4	20.5
Bottom liquid load	$m^3/(m^2h)$	3.72	**1.00**
Bottom F-factor	$\sqrt{Pa}$	0.318	0.123
Reboiler duty	kW	3.02	1.19

Table 9.16: Overview of the maximum pressure operating conditions for the inner and outer columns.

Quantity	Unit	Inner part	Outer part
Top flow rate	kg/h	42.2	257.5
Top liquid load	$m^3/(m^2h)$	**5.00**	19.02
Top F-factor	$\sqrt{Pa}$	0.092	0.862
Condenser duty	kW	1.46	12.53
Bottom flow rate	kg/h	223.3	94.5
Bottom liquid load	$m^3/(m^2h)$	19.78	**5.00**
Bottom F-factor	$\sqrt{Pa}$	0.506	0.323
Reboiler duty	kW	8.98	5.01

9.B.2 Physical properties

The physical properties of the base case, the maximum flow case, and the minimum flow cases are all equal, because they all use the same inner and outer column pressures. Table 9.17 gives an overview of the physical properties for the minimum pressure operating cases. The maximum operating pressure case, does involve different values for the physical properties. Table 9.18 gives an overview of the physical properties for the maximum pressure operating case.

Table 9.17: Overview of the base case physical properties for the inner and outer columns.

Quantity	Unit	Inner part	Outer part
Top temperature	K	88.9	81.5
Top N_2 fraction	mol/mol	0.965	0.980
Top L density	kg/m^3	765	795
Top V density	kg/m^3	12.6	6.58
Top L viscosity	Pa·s	$1.18{\cdot}10^{-4}$	$1.42{\cdot}10^{-4}$
Top V viscosity	Pa·s	$6.37{\cdot}10^{-6}$	$5.76{\cdot}10^{-6}$
Bottom temperature	K	101.1	93.5
Bottom O_2 fraction	mol/mol	0.965	0.980
Bottom L density	kg/m^3	1073	1119
Bottom V density	kg/m^3	12.2	6.39
Bottom L viscosity	Pa·s	$1.46{\cdot}10^{-4}$	$1.76{\cdot}10^{-4}$
Bottom V viscosity	Pa·s	$7.85{\cdot}10^{-6}$	$7.24{\cdot}10^{-6}$
Pressure	bar	3.0	1.5

9.C Sizing of the vapour–liquid separators

When designing a vapour–liquid separator, the required separator diameter can be determined using the terminal velocity (v_t) of a liquid droplet, which is given by

$$v_t = \sqrt{\frac{4gD}{3C_D}}\sqrt{\frac{\rho_L - \rho_V}{\rho_V}} \tag{9.2}$$

Here, C_D is the drag coefficient, which can be estimated for flow around a sphere and Reynolds numbers below $2 \cdot 10^5$ by:

$$C_D = \frac{24}{Re} + \frac{6}{1+\sqrt{Re}} + 0.4 \tag{9.3}$$

The first term of Equation (9.2) is sometimes referred to as the K-factor. In order to provide a margin of safety, it is recommended that the K-factor is at maximum between 0.05 and 0.1, depending on the properties of the system that is considered. The separator diameter can be determined by first assuming a certain value for the

Table 9.18: Overview of the maximum pressure physical properties for the inner and outer columns.

Quantity	Unit	Inner part	Outer part
Top temperature	K	119.2	95.4
Top N_2 fraction	mol/mol	0.831	0.948
Top L density	kg/m^3	620	738
Top V density	kg/m^3	88.2	20.5
Top L viscosity	Pa·s	$5.11{\cdot}10^{-5}$	$9.30{\cdot}10^{-5}$
Top V viscosity	Pa·s	$9.73{\cdot}10^{-6}$	$6.94{\cdot}10^{-6}$
Bottom temperature	K	128.9	107.5
Bottom O_2 fraction	mol/mol	0.831	0.948
Bottom L density	kg/m^3	828	1029
Bottom V density	kg/m^3	80.8	19.7
Bottom L viscosity	Pa·s	$6.89{\cdot}10^{-5}$	$1.24{\cdot}10^{-4}$
Bottom V viscosity	Pa·s	$1.06{\cdot}10^{-5}$	$8.38{\cdot}10^{-6}$
Pressure	bar	20.0	5.0

diameter. Based on this assumed diameter and the maximum volumetric vapour flow rate, the maximum superficial vapour velocity can be calculated. Next, the droplet size for which the terminal velocity equals the maximum vapour velocity is determined . This is called the critical droplet size: all droplets that are smaller than this critical size are entrained in the vapour, all droplets that are larger are pulled down by gravity back into the liquid phase. The K-factor that is calculated using the critical droplet size should be below 0.1. If it is higher, a larger separator diameter should be selected.
Once a suitable value for the separator diameter has been chosen, the critical droplet size can be used to calculate the maximum vertical distance that the droplet travels. This height gives an indication for the minimum required separator height. The calculation requires a value for the initial velocity of the droplet as input. A straightforward value would be to use the vapour velocity. In the current calculation, twice the vapour velocity is used in order to make a safe estimate.
For an inner separator diameter of 0.135 m, the following values are calculated:
The above calculation is based on the assumption that the vapour velocity is the same across the entire cross-section of the separator. An additional 0.30 m of height is added to make sure that this indeed is the case, similar to the design of the vapour inlets at the bottom of the columns. This results in a total separator height of about 0.45 m.

9.D Mass inventory and liquid level calculations

In order to calculate the required amount of working fluid in the columns and the liquid level limits during operation, first an estimate for the total volume of the system

Table 9.19: Vapour–liquid separator calculation characteristics.

Column Pressure Flow rate		Outer Min Max	Outer Max Base	Inner Min Max	Inner Max Base
Vapour velocity	m/s	0.832	0.093	0.544	0.054
Droplet diameter	mm	0.277	0.051	0.238	0.058
K-factor	-	0.063	0.013	0.058	0.018
Maximum height	mm	131.3	1.7	56.3	0.6

must be made. Using this volume, the maximum amount of required mass can be calculated. By evaluating the distribution of this amount of mass over the different parts of set-up for varying operating conditions, the maximum and minimum liquid levels in the reflux drums and column sumps can be determined.

9.D.1 System volumes

Table 9.20 gives an overview of the most important volumes that are needed for calculating the total mass inventory. The liquid in the system has the largest contribution to the total amount of mass, but large volumes of vapour should also be taken into account, especially at elevated pressures.

Table 9.20: System volumes, given in dm^3.

Column	Inner		Outer	
Reflux drum	14.2		13.3	
Column	43.3		58.4	
Top		6.8		6.4
Packing		20.4		27.4
Packing to V-inlet		4.1		5.5
V-inlet to bottom		12.1		19.0
Reboiler	19.7		19.7	
V/L-separator		6.4		6.4
Liquid buffer		2.9		2.9
Heating compartment		10.5		10.5
Piping	1.4		1.3	
Column to reboiler		0.6		0.5
Condenser to column		0.8		0.8
Total	78.6		92.7	

The reflux drum volumes are based on the dimensions described in Section 9.4.3. The column volumes are calculated using the properties described in Section 9.2.3. The

bottom part of the inner column contains the vapour inlet tube, which has an outer diameter of 50 mm and reduces the cross-sectional area of the column by about 15%. The reboiler volumes are based on the dimensions described in Section 9.4.6; the inner diameter of the liquid buffer volume is equal to the inner diameter of the heating compartment. The piping volumes are based only on the tubes containing liquid, their diameters are given in Section 9.4.7. Tube lengths of 1 m are assumed. The volumes of the vapour tubes and the condensers are not included. They are relatively small and contain mostly vapour, which results into relatively small contributions to the total mass inventory.

9.D.2 Mass inventory at maximum flow conditions

The maximum amount of working fluid is required at maximum flow conditions. This is related to the minimum liquid residence time requirements that are used for both the reflux drums and the column sumps. The first step of calculation the total mass inventory is to determine how much vapour and liquid is present in each of the volumes listed in Table 9.20. Once the volumes of vapour and liquid are know, the next step is to multiply them by the mass densities that correspond to their location and the operating pressure.
The top sections of the columns are assumed to contain vapour only. The packing sections contain both vapour and liquid, in addition to the packing itself. In the current calculations, it is assumed that the packing has a void fraction of 0.9. The vapour volume below the packing contains vapour and liquid that is falling down. In Section 9.D.3, it is described in detail how to calculate the amount of liquid that is present in a packing section and the vapour volume below it. The bottoms of the columns are occupied by liquid only. At the maximum flow conditions, half of the reflux drums is filled with liquid, and the liquid buffer volume of the reboilers is completely filled with vapour.
The physical properties in all volumes above the structured packing are assumed to be equal to the top conditions, as listed in Tables 9.17 and 9.18. In all volumes below the structured packing, they are equal to the bottom conditions. Average values are used for the packing section.
Table 9.21 gives an overview of the mass inventory in the different parts of the system at the maximum flow operating conditions.
The inner column contains 6.98 kg nitrogen and 18.62 kg oxygen, the outer column contains 7.18 kg nitrogen and 18.49 kg oxygen.

9.D.3 Mass inventory of the packing

During operation, the mass inventory in the structured packing and the vapour section below it consists of both vapour and liquid. The mass inventory of the vapour phase can be estimated by multiplying the total volume by the (average) vapour phase mass density and the void fraction of the structured packing (ε) minus the liquid fraction (f_L).

$$m_V = A_c h_p \left(\varepsilon - f_L\right) \rho_V \tag{9.4}$$

Table 9.21: Mass inventory at maximum flow conditions, given in kg.

Column	Inner		Outer	
Reflux drum	5.43		5.70	
Vapour		0.09		0.04
Liquid		5.34		5.65
Column	7.61		7.02	
Top		0.09		0.04
Packing		1.15		1.35
Packing to liquid		0.67		1.07
Liquid in sump		5.70		4.57
Reboiler	11.33		11.75	
V/L-separator		0.08		0.04
Liquid buffer		0.03		0.02
Heating compartment		11.21		11.70
Piping	1.24		1.19	
Column to reboiler		0.66		0.59
Condenser to column		0.58		0.60
Total	25.61		25.67	

Estimating the liquid inventory is more complicated, because it depends on the operating conditions. In order to get a reasonable estimate, we assume laminar flow of the liquid over the packing surface. At low liquid Reynolds numbers, the liquid film has negligible rippling, which means that the liquid film thickness is practically constant. The liquid film thickness can than be calculated using the Nusselt expression [Olujić et al., 2006]:

$$\delta_L = \sqrt[3]{\frac{3B\eta}{a\rho_L g \sin\beta}} \tag{9.5}$$

Here, B is the liquid load, η is the liquid viscosity, a is the specific surface area of the packing, ρ_L is the liquid density, g is the gravitational constant, and β is the corrugation angle of the packing with respect to the horizontal plane. The volumetric liquid fraction can subsequently be obtained by multiplying the calculated liquid film thickness by the specific surface area of the packing. In order to obtain the liquid mass inventory, multiplying by the total packing volume and the liquid density is required.

$$m_L = A_c h_p \left(\delta_L a\right) \rho_L \tag{9.6}$$

Because especially the liquid load is changing along the height of the column, the average of the top and bottom values of all variables have been used.
Table 9.22 gives an overview of the amounts of mass that are present in the structured packing section for the maximum flow and maximum pressure operating cases described in Section 9.3.3. The vapour, liquid and total amounts are shown, for both

Table 9.22: The liquid and vapour mass inventories in the structured packing section at the maximum flow and the maximum pressure operating conditions, for the inner and the outer columns.

Case		F_{max}		P_{max}	
Column		Inner	Outer	Inner	Outer
Liquid fraction	-	0.050	0.046	0.032	0.035
Liquid mass	kg	0.93	1.20	0.47	0.85
Vapour mass	kg	0.21	0.15	1.49	0.48
Total mass	kg	1.15	1.35	1.96	1.33

the inner and outer columns. A packing void fraction of 0.90 has been used.
The vapour mass inventory is practically independent of the flow rate. This is related to the fact that the liquid fraction is much smaller than the void fraction of the packing. Therefore, changes in the liquid fraction hardly influence the vapour volume. The vapour mass inventory does depend a lot on the operating pressure, because of the effect that is has on the vapour density.

9.D.4 Liquid level limits

It is important that the combination of the reflux drum, column sump and reboiler liquid buffer can accommodate the liquid level changes that are involved with different operating conditions. In order to investigate the maximum and minimum liquid levels in the system, the calculation performed in Section 9.D.2 has been repeated for different operating conditions. During these calculations, the top and bottom liquid levels were varied until the amounts of required nitrogen and oxygen were equal to ones found in Section 9.D.2.
Three additional operating cases have been investigated for both columns: maximum pressure operating conditions, stand-by operation at 5 bar, and stand-by operation at 1.5 bar. Tables 9.23 and 9.24 give an overview of the mass distribution and the liquid levels for these three cases. The maximum flow operating conditions are also shown for comparison.
It can be concluded that bottom liquid level limits in the inner column are 0.46 and 0.74 m, in the outer column they are 0.22 and 0.32 m. The maximum difference in bottom liquid level is 0.28 m. The reflux drum liquid level limits in the inner circuit are 0.14 and 0.40 m, in the outer circuit they are 0.48 and 0.54 m.

Table 9.23: Mass inventory and liquid levels in the inner column at various flow conditions.

Flow	-	max	base	off	off
Pressure	bar	3	20	5	1.5
Reflux drum	kg	5.43	2.67	5.61	6.10
Column	kg	7.61	10.53	7.11	6.33
Reboiler	kg	11.33	11.43	11.69	11.88
Piping	kg	1.24	0.98	1.19	1.29
Top liquid level	m	0.37	0.14	0.39	0.40
Bottom liquid level	m	0.46	0.74	0.53	0.47

Table 9.24: Mass inventory and liquid levels in the outer column at various flow conditions.

Flow	-	max	base	off	off
Pressure	bar	1.5	5	5	1.5
Reflux drum	kg	5.70	5.36	5.77	6.29
Column	kg	7.02	7.65	6.94	5.90
Reboiler	kg	11.75	11.55	11.85	12.28
Piping	kg	1.19	1.10	1.10	1.19
Top liquid level	m	0.48	0.49	0.53	0.54
Bottom liquid level	m	0.22	0.29	0.32	0.27

Chapter 10

Cryogenic total reflux experiments in a packed concentric HIDiC

Part B: Instrumentation and experiments

L.V. van der Ham[1] and M. Drescher[2]

1. Department of Chemistry
Norwegian University of Science and Technology
7491 Trondheim, Norway

2. SINTEF Energy Research
Kolbjørn Hejes vei 1D
7465 Trondheim, Norway

This chapter has been prepared for submission to
Separation and Purification Technology

Parts of this chapter have been published in
Book of abstracts of Trondheim CCS conference 2011, Trondheim, Norway
and
Proceedings of ICR 2011, Prague, Czech Republic

Abstract

Intensifying the heat integration of the distillation columns in a cryogenic air separation unit can yield a considerable reduction in its inefficiencies. Accurate predictions of the achievable reduction require more-detailed experimental input on the thermal energy transfer and the separation efficiency of a heat-integrated distillation column (HIDiC). Part A of the current series of publications [Van der Ham and Drescher, 2011a] presents the detailed design of a packed concentric HIDiC that has been developed for this purpose. The current work describes in detail what instrumentation and experiments are required in order to obtain the desired experimental data on the overall heat-transfer coefficient, the performance of a ring-shaped distillation column, and the effects of a radial heat flux. The results of these experiments will be added to the publication series as soon as they become available.

10.1 Introduction

The current work is the second part of a series of publications concerning an experimental set-up that is used to investigate the properties of a packed concentric heat-integrated distillation column (HIDiC). This research is part of the DECARBit project, which is a European collaboration project that aims to enable the use of an Integrated Gasification Combined Cycle (IGCC) with pre-combustion CO_2-capture [Røkke and Langørgen, 2009].
One of the research topics of the DECARBit project is the application of novel distillation techniques to a cryogenic air separation unit (ASU), which is typically used to supply the purified oxygen and nitrogen that are required in an IGCC. Within this context, the use of heat-integrated distillation stages is being investigated. As explained in more detail by, for example, [Nakaiwa and Ohmori, 2009], the use of a HIDiC can improve the thermodynamic efficiency of a distillation process by allowing more reversible operation. Detailed simulations of a two-column ASU have shown that the irreversibilities in its distillation section can be reduced by approximately 25% due to the use of heat-integrated distillation stages [Van der Ham and Kjelstrup, 2011c].
Integration of the two distillation columns is realized by using a concentric configuration, meaning that a cylindrical inner column is surrounded by a ring-shaped outer column. A difference in operating pressure causes thermal energy to be transferred from the high-pressure column (HPC) through the inner column wall to the low-pressure column (LPC). This type of integration has also been used in the only two experimental HIDiCs that have been constructed so far [Horiuchi et al., 2008, Naito et al., 2000]. These two set-ups have proven the technical feasibility of a packed concentric HIDiC, but the detailed performance properties of such a configuration have not been reported. Therefore, the detailed design of such a HIDiC is still subject to several uncertainties in its thermal energy and mass transfer performance.
The main aim of the experimental set-up that is presented in the current series of publications is to try and remove those uncertainties. The development and the properties of the design for the set-up are discussed in detail in the first part of the series

[Van der Ham and Drescher, 2011a]. The current work focuses on the instrumentation that is used and on the required experiments. The experimental results will be added to the series of publications once they become available.

10.1.1 Uncertain design properties

The uncertainties that are currently present in the design of a packed concentric HIDiC are discussed in more detail by Van der Ham [2011, Section 3.2]. They are here summarized for the sake of convenience.

Overall heat-transfer coefficient

The amount of thermal energy that is transferred between the two column parts of a HIDiC is one of the key design parameter. In order to model this thermal energy transfer, current HIDiC models often assume a value for the overall heat-transfer coefficient, which is used for the entire column. At the moment, there are only three experimental values of the overall heat-transfer coefficient that can be used as basis for this estimation. Typically, an estimate based on the average value is used.
In reality, the value of the overall heat-transfer coefficient depends on quantities like the liquid flow rates on both sides of the inner column wall, the pressures, the temperatures, and the compositions. These quantities are different for each distillation process and, in addition, most of them vary significantly along the height of a HIDiC. Therefore, more experimental investigations are required on the value of the overall heat-transfer coefficient as function of the operating variables.

Performance of a ring-shaped column

Two important properties of a distillation column that is equipped with structured packing are the separation efficiency per amount of packing height and the maximum allowable vapour flow rate. These quantities might be lower in a ring-shaped column than in a conventional cylindrical column. This is related to an increase in the amount of wall area per column volume, and to a higher sensitivity for angular maldistributions. The extent of these potential performance reductions is unknown and it should thus be quantified.

Effects of a radial heat flux

The heat integration of the two column parts causes a heat flux in the radial direction of the columns that is not present in a conventional column. The heat flux can affect the performance of both column parts in two ways. Firstly, it creates radial temperature gradients in the columns, which might lead to radial composition gradients that

can affect the separation performance of the columns. The severity of these gradients should be assessed.
The second effect is related to the interdependency that exists between the thermal and molar fluxes, as given by the theory of irreversible thermodynamics (see, for example, Kjelstrup and Bedeaux [2008]). Numerical studies [Van der Ham et al., 2010, Van der Ham and Kjelstrup, 2011d] have shown that the influence of this coupling effect is considerable. Therefore, a change in the heat flux might have a significant effect on the diffusion fluxes. The extent of this effect must be investigated experimentally.

10.1.2 Objective

The main objective of the current work is to describe in detail what instruments and experiments are required in order to characterize the following aspects in a packed concentric HIDiC:

- Heat flux through the inner column wall
- Separation efficiency of the two column parts
- Radial temperature and composition gradients
- Interdependency of thermal and molar fluxes

The experimental results will provide data that is required for a detailed feasibility evaluation of using the HIDiC principle in a cryogenic ASU. The results will also yield insights that are valuable for the design and operation of separation columns in general.

10.1.3 Outline

This work starts with a presentation of the theory background that is needed when quantifying the heat flux through the inner wall, the separation efficiency, the radial gradients, and the interdependency of thermal and molar fluxes. In order to do so, first a simplified representation of a packed concentric HIDiC is introduced in Section 10.2, describing three different types of sub-systems. Each of these sub-systems is subsequently discussed in more detail. After that, they are used in Section 10.3 to explain how to calculate the heat flux and the coupling effect based on experimental measurements. The required experimental and theoretical inputs are identified. Section 10.4 discusses in more detail what kind of experimental instrumentation is used. The required experiments are finally explained and listed in Section 10.5.

10.2 Simplified HIDiC model

Figure 10.1 shows a very simplistic representation of a HIDiC. In this representation, the HIDiC consists of an inner wall, two liquid phases that are flowing down along the

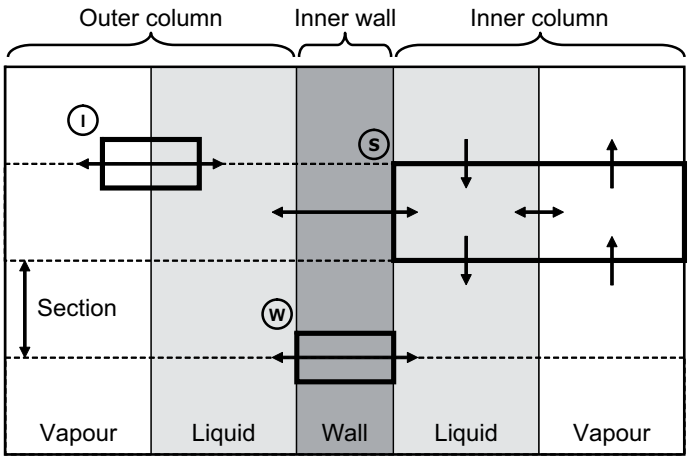

Figure 10.1: Schematic of the different types of sub-systems within HIDiC.

inner wall, and two vapour phases that are rising up next to the liquids. The side at the left of the wall represents the outer column, and the side at the right represents the inner column. For the vapour and liquid properties, values are used that are averages over the entire cross-sections of the columns. This means that in the current representation, the vapour and liquid properties only change along the height of the columns.
The system shown in Figure 10.1 consists of four sections, which are separated by horizontal dotted lines. Experimental measurements are typically performed in between these sections, and at the top and bottom of the columns. The use of four sections results in a total of five measurement heights. Three types of sub-systems are indicated in the schematic: an inner-wall region Ⓦ, a vapour–liquid section Ⓢ, and a vapour–liquid interface region Ⓘ.

10.2.1 Inner-wall region

The inner-wall region has a width equal to the wall thickness, and a height equal to a differential element of the height of the column. Figure 10.2 shows a more detailed overview of the inner-wall region.
The inner-wall region is characterized by four quantities: the wall temperatures at the sides of the outer ($T_{W,o}$) and the inner ($T_{W,i}$) columns, the wall thickness (d_W), and the local thermal flux through the wall ($J_{q,W}$).

10.2.2 Vapour–liquid section

A vapour–liquid section has a height that is equal to the vertical distance between two measurement locations; its width is representing the entire cross-section of a column. Figure 10.3 shows a more detailed overview of a vapour–liquid section.

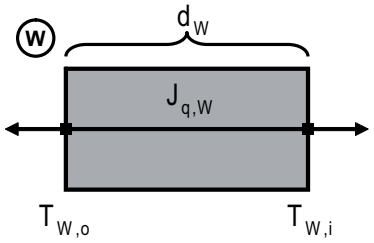

Figure 10.2: Schematic of an inner-wall region.

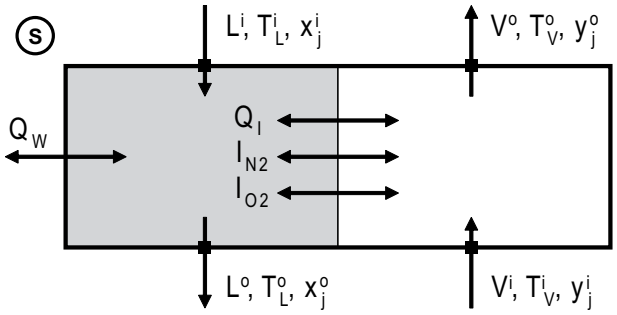

Figure 10.3: Schematic of a vapour–liquid section.

In case of a binary mixture, a vapour–liquid section is characterized by seventeen quantities. The first six are related to the vapour phase: the vapour flow rates in and out of the section (V^i and V^o), their temperatures (T_V^i and T_V^o), and their compositions (y_j^i and y_j^o). The second six are related to the liquid phase: the liquid flow rates in and out of the section (L^i and L^o), their temperatures (T_L^i and T_L^o), and their compositions (x_j^i and x_j^o). The next three are the total amounts of thermal energy (Q_I), nitrogen (I_{N_2}), and oxygen (I_{O_2}) that are transferred through the vapour–liquid interface. And the last ones are the total amount of thermal energy that is transferred through the inner-wall (Q_W), and the pressure (P). The pressure drop over a section is relatively small, meaning that the pressure is practically constant.

10.2.3 Vapour–liquid interface region

A vapour–liquid interface region has a height equal to a differential element of the height of the column, and a width equal to the sum of the vapour and liquid interface film thicknesses. These interface films are hypothetical regions in which it is assumed that all transfer processes between the vapour and liquid phases take place. The properties at the outer boundaries are equal to the properties of the adjacent bulk phases. Figure 10.4 shows a more detailed overview of an interface region.
A vapour–liquid interface region is characterized by ten quantities: the vapour boundary temperature (T_V) and composition (y_j), the liquid boundary temperature (T_L)

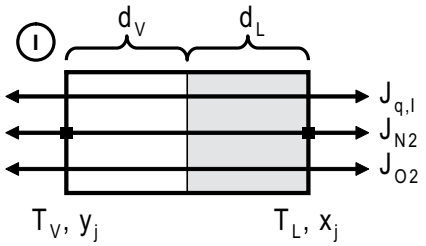

Figure 10.4: Schematic of a vapour–liquid interface region.

and composition (x_j), the local total energy flux ($J_{q,I}$), the local molar nitrogen flux (J_{N_2}), the local molar oxygen flux (J_{O_2}), the thicknesses of the vapour (d_V) and liquid (d_L) interface films, and the pressure.

10.3 Calculations

This section explains how the four aspects listed in Section 10.1.2 are being quantified based on measurements of the quantities introduced in Section 10.2. The calculations make use of the fact that the vapour and liquid flow rates are by definition equal to each other at every height in a column that is operating at total reflux. This is also true for the vapour and liquid compositions. Applied to the top and bottom of a column (section), this is written as:

$$V^o = L^i = F^{top} \tag{10.1}$$

$$y^o = x^i = z^{top} \tag{10.2}$$

$$V^i = L^o = F^{bot} \tag{10.3}$$

$$y^i = x^o = z^{bot} \tag{10.4}$$

The most important prerequisite for equal flow rates and compositions is steady state operation. It is important to realize that only the total flow rates and the average compositions are equal. Local variations might still occur in the radial and angular directions.

10.3.1 Thermal energy transfer

The transfer of thermal energy through the inner wall is evaluated at two levels of detail: the total amount of transferred energy and the local flux of thermal energy through the inner wall. The first one is easier to measure accurately, but the second one provides more insight in what exactly is happening inside the column.

Total amount of transferred energy

The total amount of thermal energy that has been removed from a column through the inner column wall (Q_W^{tot}) can be calculated in two ways. It is given by the difference between the reboiler and condenser duties (Q_R and Q_C), and by the difference between the enthalpy contents of the ingoing and outgoing vapour and liquid streams:

$$Q_W^{tot} = Q_R - Q_C \tag{10.5}$$

$$= (F^{bot}H_V^{bot} + F^{top}H_L^{top}) - (F^{top}H_V^{top} + F^{bot}H_L^{bot}) \tag{10.6}$$

When considering the outer column, the cold that is lost through the outer wall to the environment (Q_{lost}) should also be taken into account. Since this is equivalent to the addition of thermal energy, this term appears with a positive sign on the right-hand side of the equation.
The reboiler duty is obtained by direct measurements of the duty of the electrical heater. The condenser duty is calculated based on the coolant flow rate and values for the temperatures and pressures both upstream and downstream of the condenser. In the current set-up, the coolant is evaporating nitrogen that is supplied from a pressurized storage tank. Before it is fed to the condenser it is first throttled down in pressure. The upstream temperature and pressure are measured before the liquid nitrogen is being throttled. Assuming that the coolant circuit is adiabatic and that the upstream and downstream measurements do not involve two-phase conditions, the condenser duty is given by:

$$Q_C = F^{N_2}\left(H_V^{N_2} - H_L^{N_2}\right) \tag{10.7}$$

In order to calculate the total vapour and liquid enthalpies at the top and bottom of the column, the compositions are being be measured in addition to the temperatures, pressures and flow rates. At steady state conditions, the compositions of the vapour and liquid streams are equal, similar to their flow rates.
The difference between the vapour and liquid enthalpies at the column top should be equal to the condenser duty. Similarly should the reboiler duty be equal to the difference between the vapour and liquid enthalpies at the bottom of the column:

$$Q_C = F^{top}\left(H_V^{top} - H_L^{top}\right) \tag{10.8}$$

$$Q_R = F^{bot}\left(H_V^{bot} - H_L^{bot}\right) \tag{10.9}$$

The energy transfer through the wall can be determined in two independent ways per column. So in total, there are four independent sets of measurements that all yield a value for the total amount of transferred energy. The consistency of these values gives an indication of the accuracy of the measurements.

Local thermal energy flux

The local thermal energy flux through the column wall is relatively easy to calculate using the inner-wall region shown in Figure 10.2. Going from the inner to the outer

column, it is given by:

$$J_{q,W} = \frac{\lambda_W}{d_W} \left(T_{W,i} - T_{W,o}\right) \tag{10.10}$$

Here, λ_W is the thermal conductivity of the wall material, which is obtained from literature. The wall thickness is specified as part of the design. The two wall temperatures are measured during operation. This allows for the calculation of the thermal energy flux at the height where the temperature measurements are done.
By measuring the wall temperatures at several locations along the height of the wall, profiles can be constructed that represent the wall temperatures along the entire height of the column. Consequently, a profile can be obtained for the local thermal energy flux through the wall.
Integrating this local thermal energy flux profile over a part of the column height yields the amount of thermal energy that is transferred in that part of the column. When integrating over the entire column height, the total amount of transferred energy can again be calculated:

$$Q_W^{tot} = \pi D \int_{bot}^{top} J_{q,W}\left(h\right) dh \tag{10.11}$$

10.3.2 Separation efficiency

The separation efficiency of structured packing is often characterized using the packing height that corresponds to a single theoretical stage (HETP). Calculating the separation efficiency of an entire column follows the same procedure as calculating it for a section of a column. Measurements of the compositions at the top and the bottom of the column or section are the main inputs for determining the total number of theoretical stages (N). For a binary mixture, this number is given by the Fenske equation:

$$N = \frac{\ln\left[\left(\frac{x}{1-x}\right)^{top}\left(\frac{1-x}{x}\right)^{bot}\right]}{\ln \alpha} \tag{10.12}$$

Here, x is the mole fraction of the most volatile component, which is nitrogen in a nitrogen–oxygen mixture, and α is the relative volatility of the two components [Seader and Henley, 1998]. Because the relative volatility changes along the height of a column or section, the geometric mean of the top and bottom values is often used as representative value:

$$\alpha = \sqrt{\alpha^{top}\alpha^{bot}} \tag{10.13}$$

Relative volatilities are calculated using thermodynamic models. So temperature and pressure measurements are required in addition to the composition measurements. The average HETP of a column or section is calculated by dividing the packing height (h_p) by the corresponding number of theoretical stages:

$$\mathrm{HETP} = \frac{h_p}{N} \tag{10.14}$$

10.3.3 Radial and angular gradients

The radial and angular gradients in the vapour and liquid temperatures and compositions are investigated by direct measurements of these variables at several locations on a single height of the column. In order to determine at which locations it is most useful to measure, first the most common reasons for these gradients, or maldistributions, are considered.

Common maldistribution causes

In a heat integrated column, the presence of an additional heat flux can cause maldistribution in both the vapour and the liquid phases. Kister [1990] lists various reasons for vapour and liquid maldistributions in regular packed distillation columns.
Vapour maldistributions have two major causes. They are caused either by a bad initial feed distribution, or by the combination of a liquid maldistribution and a high flow rate. A bad initial vapour distribution usually flattens out within a few packing elements. A higher pressure drop over the packing promotes a more uniform vapour distribution.
Liquid maldistributions have more possible causes. Similar to vapour maldistributions, they can be caused by a bad initial feed distribution. In the case of structured packing, liquid tends to accumulate in the wall-zones at the ends of the corrugated sheet channels. Another reason for liquid maldistributions is a possible non-verticality of the entire column. Liquid maldistributions are usually more persistent than vapour maldistributions. They can be partly countered by using liquid wall-wipers, and by positioning subsequent packing elements with an angular difference of 90 degrees.

Measuring vapour maldistributions

A bad initial vapour distribution can cause maldistributions in both the radial and the angular directions, but the additional heat flux will only cause maldistributions in the radial direction. So in case of a proper initial vapour distribution, only radial maldistributions can be expected along the column height. Therefore, the vapour temperature and composition are measured at several locations in the radial direction at all measurement heights. To ensure a proper initial distribution, it is sufficient to check the variation in the angular direction at only one height, preferably above the bottom packing section. It is not necessary to investigate the angular variation in the radial variation.

Measuring liquid maldistributions

Similar to the vapour, the liquid temperature and compositions are measured at several locations in the radial direction at all measurement heights. Angular liquid

maldistributions can be caused by a bad initial distribution, by the packing geometry and by column non-verticality. Therefore, they can occur even in case of a proper initial liquid distribution. It is therefore also useful to investigate the angular variation in the radial variation. Maldistributions in the liquid flow tend to increase rather than decrease when going down, so the angular variation is best evaluated near the bottom of a packed bed.

Combined measurement strategy

Summarizing, the vapour and liquid properties are measured at several locations in the radial direction at all measurement heights. At least three locations are measured per height, in order to detect non-linear gradients. The measurements are done in the same angular direction at all heights. It is sufficient to investigate the angular variation in the vapour and liquid properties only at the height level above the bottom packing section. The radial variation in the liquid properties is measured in all angular measurement directions at this height. It is sufficient to measure the radial variation in the vapour properties in only one angular direction.

Measurement locations

The experimental set-up contains five measurements heights. At height levels 1, 2, 3 and 5, counting from top to bottom, only one angular measurement direction is used for all measurement types. At height level 4, six angular measurement directions are used for all liquid measurements and for the vapour measurements in the outer column. For the vapour measurements in the inner column, only three measurement directions are used.
At the top measurement height, all liquid has the same properties because it all originates from the same source and it has not passed through any packing yet. Therefore, the liquid temperature and composition only need to be measured once per column at this height, including the measurement at the outer wall. Similarly, all vapour has the same properties at the bottom measurement height, requiring only one vapour temperature and composition measurement per column at this height. The inner wall temperatures is measured at all measurement heights, because they are used to calculate the energy transfer through the wall.
The temperature measurement locations for all five measurement heights are schematically shown in Figure 10.5. The grey squares are measurement locations that are in the wall zone of the inner column wall. They are located directly at the wall and are positioned in the liquid phase during normal operation. The white squares are regular liquid phase measurements locations. White circles represent locations where both liquid and vapour properties are measured and white diamonds are vapour phase measurement locations.

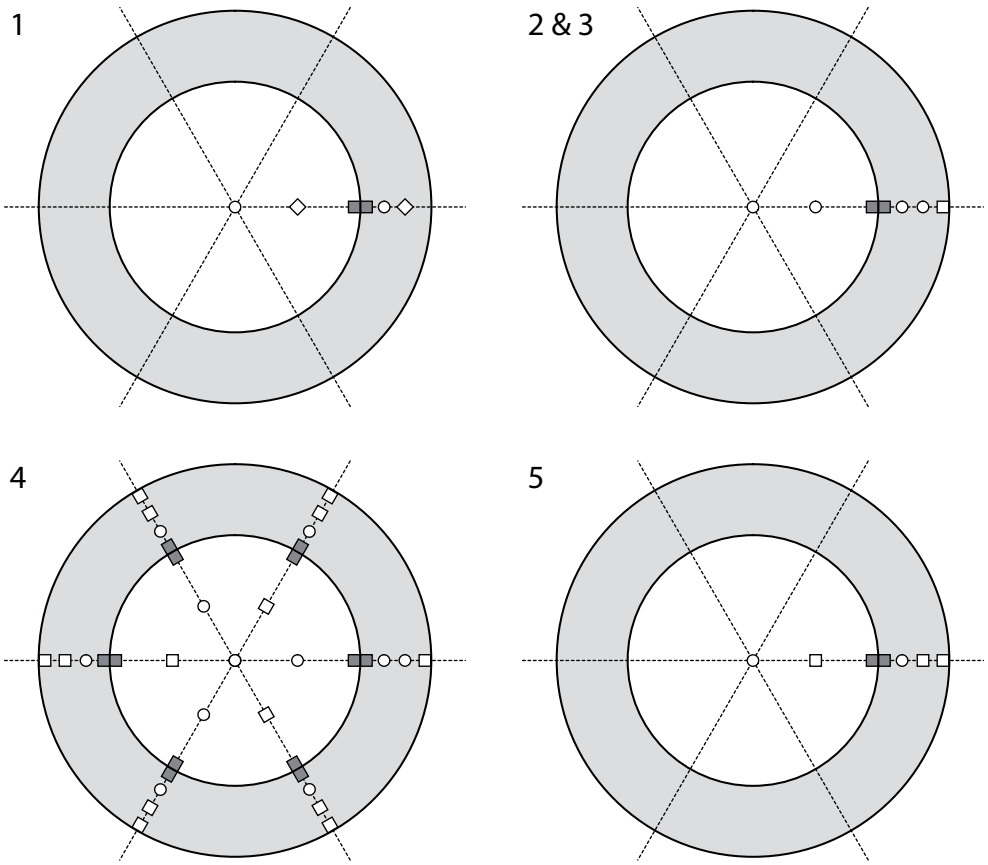

Figure 10.5: Cross-sectional overviews of the internal temperature measurement positioning at each of the five measurement heights, counting from top to bottom. Each dashed line represents an angular measurement direction and the symbols on the lines indicate measurement locations.

The locations of the composition measurements are the same as those for the temperature measurements, with one exception: there is no need to measure the liquid phase compositions at the inner wall of measurement height 1.

10.3.4 Interdependency of thermal and molar fluxes

Determining the extent of coupling between thermal and molar fluxes requires the most complicated calculation. It is based on the vapour–liquid interface region that is shown in Figure 10.4 and uses the theory of irreversible thermodynamics [Kjelstrup and Bedeaux, 2008]. The aim of the calculation is to find the values of the resistivities that are coupling the thermal and molar fluxes. In case of a binary mixture of nitrogen and oxygen, the force-flux relations for the vapour–liquid interface region are given by [Van der Ham and Kjelstrup, 2011d]:

$$\Delta_{LV}\frac{1}{T} = r^{tot}_{qq}J'_{q,V} + r^{tot}_{qN_2}J_{N_2} + r^{tot}_{qO_2}J_{O_2} \tag{10.15}$$

$$-\frac{\Delta_{LV}\mu_{N_2}(T_L)}{T_L} = r^{tot}_{N_2q}J'_{q,V} + r^{tot}_{N_2N_2}J_{N_2} + r^{tot}_{N_2O_2}J_{O_2} \tag{10.16}$$

$$-\frac{\Delta_{LV}\mu_{O_2}(T_L)}{T_L} = r^{tot}_{O_2q}J'_{q,V} + r^{tot}_{O_2N_2}J_{N_2} + r^{tot}_{O_2O_2}J_{O_2} \tag{10.17}$$

Here, $\mu_j(T)$ is the chemical potential of component j evaluated at constant temperature T, $J'_{q,V}$ is the local measurable heat flux at the vapour boundary of the interface region, and r_{mn} represents the resistivity that is coupling driving force m with flux n. The notation Δ_{LV} is used to indicate the difference between the liquid and vapour boundaries of the system, and the superscript *tot* indicates the total resistivity of the entire vapour–liquid interface region. The matrix containing all the total resistivities is symmetric, which means that $r_{mn} = r_{nm}$. Formulae for the total resistivities are given by Van der Ham and Kjelstrup [2011d]. The resistivities that we would like to calculate from our measurements are $r_{qN_2} = r_{N_2q}$ and $r_{qO_2} = r_{O_2q}$. The other resistivities can be obtained relatively accurately from theoretical relations for the thermal conductivity (r_{qq}) and the diffusion coefficients ($r_{N_2N_2}$, $r_{O_2O_2}$ and $r_{N_2O_2} = r_{O_2N_2}$). The calculation of these resistivities is explained in more detail by Van der Ham et al. [2010].

The bulk vapour and liquid temperatures should both be measured. The bulk composition needs to be measured in only one phase, because it is the same in both phases under total reflux conditions. When the pressure is also known, the driving forces can be calculated using a suitable thermodynamic model. The local fluxes through the interface are calculated using evaluations of the vapour–liquid sections. This is discussed below in more detail.

In addition to the coupling resistivities, the experimental results will also yield calculated values for the vapour and liquid interface film thicknesses. An additional relation between the relevant variables is obtained by requiring the entropy production calculated both using an entropy balance and using irreversible thermodynamics to be the same [Van der Ham et al., 2010].

Finding the local fluxes

Values for the local fluxes are derived from values for the total amounts of thermal energy and components that are transferred in the vapour–liquid sections. These total amounts can be determined using an energy balance around a vapour–liquid section. The energy balance can be rewritten in such a way that it allows for the calculation of the bottom flow rate of a column or section, when the top flow rate is known:

$$F^{bot} = \frac{F^{top}\left[H_L\left(T_L^i\right) - H_V\left(T_V^o\right)\right]_{z^{top}} - Q_W}{\left[H_V\left(T_V^i\right) - H_L\left(T_L^o\right)\right]_{z^{bot}}} \tag{10.18}$$

The energy transferred through the wall is here positive when it is added to the section. If we subsequently consider one of two phases separately, it is possible to determine the amounts of energy and components that are transferred through the vapour–liquid interface. Based on the vapour phase and defining transfer from the liquid to the vapour phase as positive, they become:

$$Q_I = F^{top}H_V\left(T_V^o, z^{top}\right) - F^{bot}H_V\left(T_V^i, z^{bot}\right) \tag{10.19}$$

$$I_j = F^{top}z_j^{top} - F^{bot}z_j^{bot} \tag{10.20}$$

Once the total amounts of transferred energy and components are determined for all sections of a column, the final step is to construct flux profiles based on them. This step requires a value for the vapour–liquid interfacial area, which can be calculated from the specific surface area of the structured packing in combination with the column geometry. These flux profiles give the values of the local fluxes at every location along the height of the column.

Calculation routine

The routine for calculation of the coupling coefficients can be summarized as follows, using a bold font for quantities that are varying along the column height:

1. Determine $\boldsymbol{J_{q,W}}$ and $\boldsymbol{Q_W}$ as described in Section 10.3.1.
2. Measure $\boldsymbol{z_j}$, $\boldsymbol{T_V}$, $\boldsymbol{T_L}$, $\boldsymbol{P}$, and F^{top} or F^{bot}.
3. Calculate $\boldsymbol{H_V}$ and $\boldsymbol{H_L}$ for $\boldsymbol{T_V}$, $\boldsymbol{T_L}$, $\boldsymbol{z_j}$ and $\boldsymbol{P}$.
4. Calculate $\boldsymbol{F}$ using Equation (10.18).
5. Calculate $\boldsymbol{Q_I}$ and $\boldsymbol{I_j}$ using Equations (10.19) and (10.20).
6. Determine $\boldsymbol{J'_{q,I}}$ and $\boldsymbol{J_j}$ from $\boldsymbol{Q_I}$ and $\boldsymbol{I_j}$.
7. Calculate $\boldsymbol{\mu_{j,V}}$ and $\boldsymbol{\mu_{j,L}}$ for $\boldsymbol{T_V}$, $\boldsymbol{T_L}$, $\boldsymbol{z_j}$ and $\boldsymbol{P}$.

8. Calculate $\boldsymbol{\lambda_V}$, $\boldsymbol{\lambda_L}$, $Đ_{\boldsymbol{V}}$ and $Đ_{\boldsymbol{L}}$ for $\boldsymbol{T_V}$, $\boldsymbol{T_L}$, $\boldsymbol{z_j}$ and $\boldsymbol{P}$.

9. Calculate $\boldsymbol{r_{qj}}$, $\boldsymbol{d_V}$ and $\boldsymbol{d_L}$ using Equations (10.15) to (10.17), and the entropy balance.

10.3.5 Theoretical inputs

The calculations require several thermodynamic and transport properties as input. The thermal conductivity of the wall material should be provided by the column manufacturer and verified experimentally. The thermodynamic properties α, H, S and μ_j can be calculated very accurately using the reference equation of state for nitrogen–argon–oxygen mixtures by Lemmon et al. [2000]. The thermal conductivity and viscosity of these mixtures can be calculated using the works of Shan et al. [2000] and Lemmon and Jacobsen [2004]. The liquid phase Maxwell-Stefan diffusion coefficient can be calculated using a modified Stokes–Einstein relation proposed by Rutten [1992]. And the vapour phase Maxwell–Stefan diffusion coefficient can be calculated by combining kinetic theory, see for example Hirschfelder et al. [1964], and the thermodynamic model by Lemmon et al. [2000]. These relations often require the temperature, pressure and composition as input.

10.4 Instrumentation

All measurements are done during steady state operation. The experimental instrumentation that is used in the set-up is divided in two groups: instrumentation that is present inside the two columns, and instrumentation that is located outside the columns. This section presents the details of all the instruments that are used.

10.4.1 Internal instrumentation

The instrumentation inside the HIDiC is used for measurements of the pressure (drop), the temperature and the composition. The required instrumentation is positioned in between structured packing sections. A number of four sections results into five possible measurement heights. The temperature and composition are measured at several locations at each measurement height, in order to investigate their radial and angular variations. The pressures are only measured once per column at each measurement height, so the radial and angular variation in the pressure (drop) is not investigated. A more detailed overview of the measurement locations is given in Section 10.3.3. A quantitative summary of the internal measurements is given in Table 10.1.
When measuring properties of the vapour phase, it is important to ensure that indeed the vapour phase properties are measured, and not the liquid phase properties. In order to do so, the vapour phase measurements are shielded from the down-flowing liquid using a umbrella-like configuration. Similarly, the liquid phase measurements are shielded from up-flowing vapour. This configuration is shown in Figure 10.6.

Table 10.1: Number of internal measurements locations for all measurement heights (from top to bottom) and measurement types.

Height level	1	2	3	4	5	Total
Inner column						
$T_{W,i}$	1	1	1	6	1	10
T_L	1	2	2	7	2	14
T_V	2	2	2	4	1	11
x	1	3	3	13	3	23
y	2	2	2	4	2	11
$(\Delta)P$	1	1	1	1	1	5
Outer column						
$T_{W,i}$	1	1	1	6	1	10
$T_{W,o}$	0	1	1	6	1	9
T_L	1	2	2	12	1	19
T_V	2	2	2	7	2	14
x	1	4	3	24	4	37
y	2	2	2	7	1	14
$(\Delta)P$	1	1	1	1	1	5
Total						
T	8	11	11	48	9	87
$x + y$	6	11	11	48	9	85
$(\Delta)P$	2	2	2	2	2	10

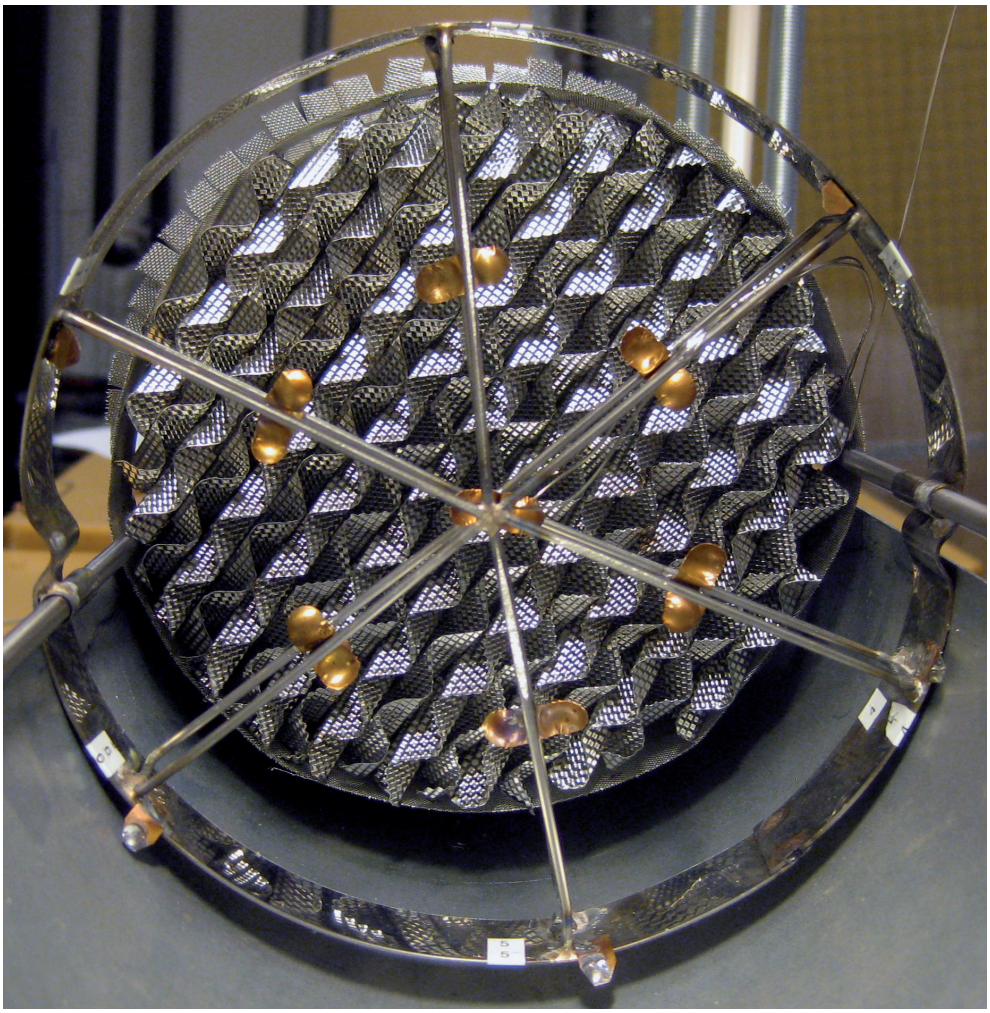

Figure 10.6: Picture of measurement level 4 in the inner column, showing the umbrella-like and cup-like configurations that are designed for performing single phase measurements.

Temperature sensors

The temperature sensors that are used for the internal temperature measurements are Type E thermocouples (chromel–constantan) supplied by Omega. They have ungrounded junctions, a stainless steel sheath with a diameter of 0.020 inch, and varying wire lengths. These thermocouples have a high voltage output per unit of temperature. They have a tolerance of approximately 1.5% within the relavant operating range of the set-up.
In the set-up, the temperature measurements are used to obtain temperature profiles in the longitudinal, the radial and the angular directions of the two columns. They are also used to measure differences between the vapour and liquid phases at the same location, and differences between the temperatures at the two sides of the inner wall. These temperature differences might be as small as the tolerance of a single temperature measurement, resulting in inaccurate values for the differences. In order to improve the accuracy of the relative values, temperature differences can also be measured directly.
A temperature sensor can only be used to measure one relative temperature at the same time, so either relative to a reference temperature, or relative to another temperature sensor. It is possible to switch between different relative measurements by changing the connections to the signal interpreter, so without requiring any actions inside the columns.

Composition measurements

The composition measurements are done by withdrawing very small samples of working fluid from the columns and analysing them using gas chromatography (GC). An Agilent 3000 Micro GC is used with a PLOT U/MS-5A column, using argon as carrier gas, and using a backflush injector. It can detect concentrations below 20 ppm for many components.

Absolute pressure measurements

The absolute pressures in the two columns are measured above the packing section using Cerabar S PMP71 pressure transmitter supplied by Endress+Hauser. They have a recommended measuring range up to 100 bar and an accuracy of 0.075% of the set measuring span. Using a span of 0 to 25 bar, which corresponds to a turndown of 4, results in an accuracy of approximately +/- 19 mbar.

Pressure difference measurements

The pressure differences over the four sections of structured packing are measured using Deltabar S PMD75 differential pressure transmitters supplied by Endress+Hauser.

They have an operating range between 0 and 10 mbar and an accuracy of approximately 0.15% of the set measuring span.

10.4.2 External instrumentation

The external instrumentation is similar for both columns. It can be divided into three groups: one related to the coolant circuit, one related to the column top flow, and one related to the column bottom flow.
Three properties of the coolant flow are measured: the temperature of the liquid before it enters the control valve, the temperature of the vapour after it has passed through the condenser, and the vapour flow rate.
At the top of the column, five quantities are measured: the vapour composition, the vapour flow rate, the temperature of the vapour before it enters the condenser, the temperature of the liquid after it has passed through the condenser, and the pressure difference between the top and bottom of the reflux drum.
At the bottom of the column, six quantities are measured: the pressure difference between the bottom of the packing and the bottom of the column, the liquid composition, the temperature of the liquid before it enters the reboiler, the reboiler duty, the vapour flow rate, and the temperature of the vapour after it has passed through the reboiler.
Figure 10.7 shows the piping and instrumentation diagram of the experimental set-up, indicating all external instrumentation. Unfortunately, the full details of the diagram are only observable when viewed as a digital document.

Volumetric gas flow meters

The volumetric gas flows at the top and bottom of the columns and of the vaporized nitrogen streams are measured using vortex flow meters supplied by Endress+Hauser. All meters are of the type Proline Prowirl 72W, but different sizes are used at different locations, depending on the expected flow rates.
The meters in the nitrogen circuits have a size of DN25, allowing a maximum flow rate of approximately 110 m^3/h. The top of the inner column is equipped with both a DN15 and a DN40 meter in parallel, in order to cover the entire expected flow rate range. The maximum flows of these meters are approximately 35 and 270 m^3/h. The bottom of the inner column and both the top and bottom of the outer column are equipped with DN50 meters, allowing a maximum flow rate of approximately 430 m^3/h.
The minimum flow rates depend on the density of the vapour streams and on the Reynolds numbers. The vapour velocity should be higher than seven divided by the square root of the density, and the Reynolds number should be higher than 4000. For Reynolds numbers above 20000 the accuracy of the measurements increases, resulting in a maximum deviation of 1% of the reading.

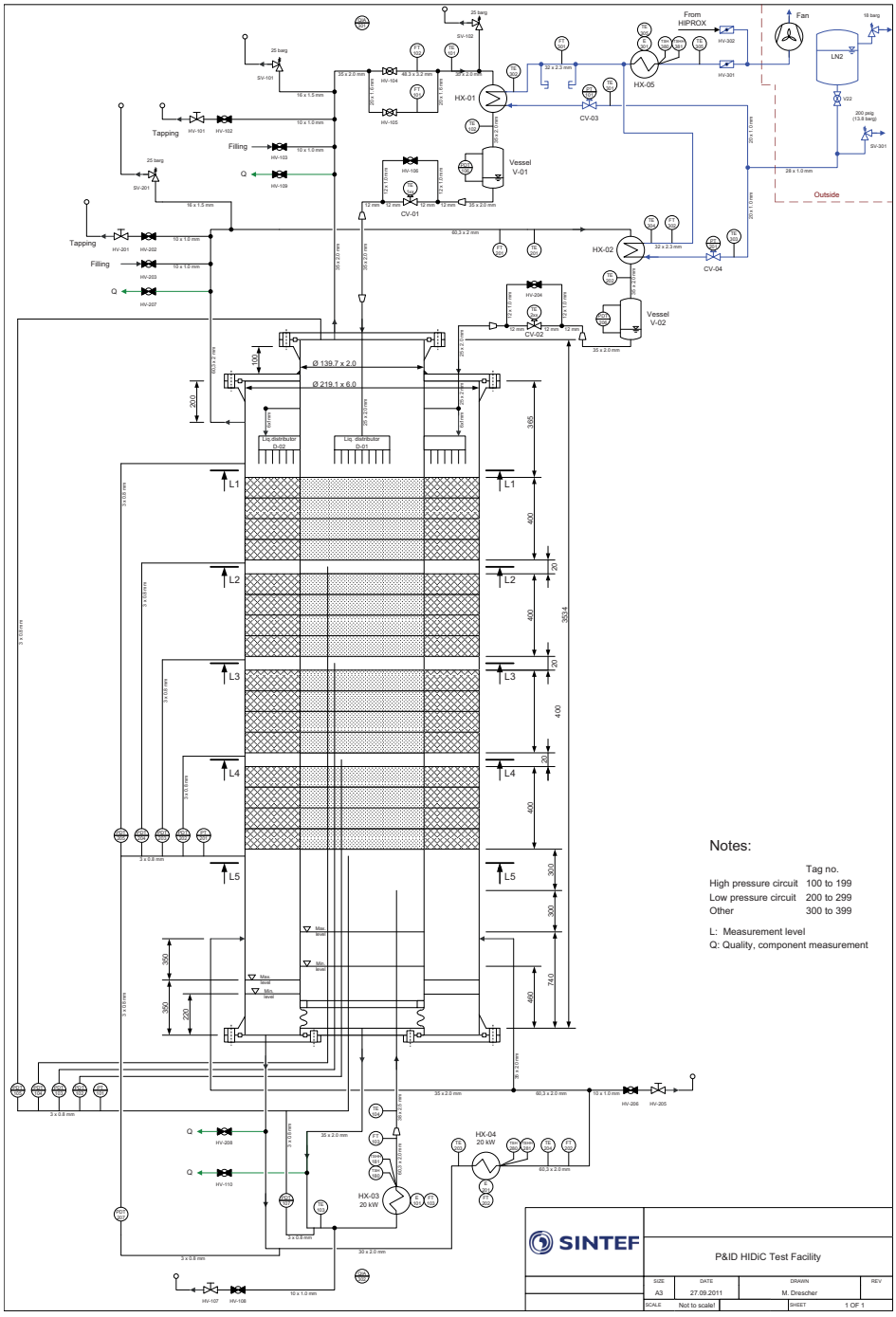

Figure 10.7: Piping and instrumentation diagram of the experimental set-up.

Electrical duty transmitters

The electrical duty that is used by the reboilers is measured using clamp-on power analysers supplied by Hioki, type 3166. They have an accuracy of 0.6% of the reading plus 0.4% of the selected measurement range.

Temperature sensors

The external temperature measurements are done using Class A RTD-PT100 sensors with a diameter of 3 mm, supplied by Teck-Skotselv.

Composition measurements

The composition of the streams entering and leaving the top and bottom of the two columns is measured as described in Section 10.4.1.

Pressure difference measurements

The pressure differences over the liquid levels in the reflux drums and the column sumps are measured using Deltabar S PMD75 pressure sensors supplied by Endress+Hauser. They have an operating range between 0 and 100 mbar and an accuracy of approximately 0.15% of the set measurement span. For a span of 0 to 50 mbar, the accuracy becomes +/- 0.075 mbar. The main function of these measurements is to provide high and low levels alarms.

10.5 Experiments

The experiments can be considered as specific combinations of the six operating variables that can be controlled in the set-up: the flow rates, the pressures and the compositions (or temperatures) in the two columns. The experiments have been divided into fifteen items, which are summarized in Table 10.2 and discussed in more detail in Section 10.5.1 to 10.5.10.

10.5.1 Experiment 1

The first experiment is mainly used to characterize the angular and radial gradients under operation without energy transfer. In case of proper initial liquid and vapour distributions, no angular gradients should be detected. This will be verified. Radial gradients might be present because of wall flow. The extent of these gradients will be determined, so that it can be used for comparison with operating cases that do

Table 10.2: Summary of the experimental planning. The minimum, base and maximum flow rates correspond to 1.0 $m^3/(m^2h)$, 5.0 $m^3/(m^2h)$ and 2.0 $\sqrt{Pa}$. The minimum and maximum outer column pressures are 1.5 and 5.0 bar, and the minimum and maximum pressure ratios amount to 1 and 4. The base mole fractions are chosen such that the top N_2 fraction is equal to the bottom O_2 fraction. These numbers are discussed in more details in Part A of this series of publications [Van der Ham and Drescher, 2011a].

	F_i	F_o	P_o	P_R	x_o	x_i	comments
1	base	base	min	1	base	base	no energy transfer
2	min→max	off	min	1	base	base	flow range
3	off	min→max	min	1	base	base	flow range
4	base	base	min	2	base	base	base case, energy transfer
5	min→max	base	min	2	base	base	
6	base	min→max	min	2	base	base	
7	base	base	min	min→max	base	base	increased T-difference
8	min→max	off	$2 \cdot P_o^{min}$	1	base	base	no energy transfer, incr. P
9	off	min→max	$2 \cdot P_o^{min}$	1	base	base	
10	min→max	off	$P_R^{max} \cdot P_o^{min}$	1	base	base	maximum pressure
11	off	min→max	$P_R^{max} \cdot P_o^{min}$	1	base	base	
12	base	base	min→max	2	base	base	increased P, energy transfer
13	base	base	min	2	base→O_2	base	increased oxygen purity
14	base	base	min	2	base	base→N_2	increased nitrogen purity
15	max	max	min	3	O_2	N_2	industrial case

involve energy transfer, such as experiment 4.
In case of considerable radial gradients, it will be assessed whether there is a direct correlation between the temperature and composition gradients, both for the liquid and the vapour phases. It will also be investigated in what way the cross-sectional average temperatures and composition can best be derived from the available measurements. The coupling effect in the absence of thermal integration can be determined as part of these experiments.

10.5.2 Experiments 2 & 3

These experiments are used to assess the structured packing performance as function of the column shape: either cylindrical or angular. The performance will be evaluated by measuring the separation efficiency and the pressure drop of the packing as function of the column loading. As part of the experiments, the minimum and maximum operable column loadings are determined: the dewetting and the flooding points.
Because the columns are not influencing each other in the absence of a pressure difference, it is possible to perform experiments in one of the columns while the other column operates at zero or minimum column loading. This limits the required heat duties of the set-up. The found column loading limits are used to decide on the base-case column loadings for the subsequent experiments.

10.5.3 Experiment 4

This experiments is similar to the one described in Section 10.5.1. The main difference is the presence of thermal energy transfer. The radial gradients and the best representation of the cross-sectional averages are again determined. A comparison with the results of experiment 1 is made. The findings from experiments 2 & 3 can be used as basis for the column loadings.

10.5.4 Experiments 5 & 6

These experiments are similar to the ones described in Section 10.5.2, again with the presence of thermal energy transfer as the main difference. The performance of the structured packing in both columns is evaluated as function of the column loading. Because the columns are now thermally coupled, the column loadings should always be sufficiently large to ensure proper thermal energy transfer.
A comparison between the findings from experiments 3 and 6 gives more insight into the effect of heat integration on the column loading limits and packing performance of the outer column. Experiments 2 and 5 cannot be compared to each other to assess the same effect, because the operating pressure of the inner column is different for the two experiments.

10.5.5 Experiment 7

This experiment investigates the effect of the pressure ratio, and thus the temperature difference, on the thermal energy transfer and separation efficiency. The column

loadings will be based on a combination of the results from experiments 2 & 3 and 5 & 6. At the maximum pressure ratio, the radial gradients and the coupling effect will be determined.

10.5.6 Experiments 8 & 9

These experiments are again done in the absence of thermal energy transfer. They are similar to the ones described in Section 10.5.2, but at an elevated pressure. A comparison between the findings from experiments 5 and 8 gives more insight into the effect of heat integration on the column loading limits and packing performance of the inner column. Comparing the results of experiments 8 and 9 can again be used to assess the influence of the different column geometries.

10.5.7 Experiments 10 & 11

These experiments are similar to the ones described in Section 10.5.6, but at an even higher pressure. The main aim of the experiments is to serve as comparison for the maximum pressure ratio results from experiment 7. The influence of the different column geometries is assessed as well.

10.5.8 Experiment 12

In this experiment, the influence of the absolute pressure in the presence of a thermal energy transfer is assessed. Its effect on the thermal energy transfer and the separation efficiency is investigated. The findings from experiments 5 & 6 can be used as basis for the column loadings.

10.5.9 Experiments 13 & 14

These experiments serve to investigate the influence of having different composition profiles in each of the columns. Different composition profiles result in a less constant temperature difference profile throughout the set-up. The findings from experiments 5 & 6 can be used as basis for the column loadings.

10.5.10 Experiment 15

The last experiment is mimicking an industrial implementation of the set-up. This means that the pressure ratio is around 3 and that the composition profiles are shifted towards pure products. The column loadings are as high as is achievable with the set-up.

10.6 Conclusions

The instrumentation and experiments that are required to investigate the uncertain properties currently present in the designs of packed concentric HIDiCs have been

presented. These uncertainties are related to: the value of the overall heat-transfer coefficient, the performance of a ring-shaped column, and the effects of a radial heat flux. It has also been discussed how the uncertain design properties can be quantified based on the measurements that are performed.
Radial and angular temperature and composition gradients inside the columns will be measured directly in both the vapour and liquid phases. The separation efficiency of the columns will be calculated using composition measurements at their tops and bottoms. The total amount of thermal energy transfer will be determined based on two independent measurements of the condenser and reboiler duties of both the column parts. In combination with measurements at several height levels of the temperature difference over the inner column wall, a heat flux profile can be determined. Based on this heat flux profile and on several other previously mentioned measurements, the effect of coupling between thermal and mass fluxes can be assessed.

Notation

ASU	air separation unit
D	inner-column diameter, m
d	(film) thickness, m
F	molar flow rate, mol/s
h	height, m
H	molar enthalpy, J/mol
HETP	height equivalent to a theoretical stage, m
HIDiC	heat-integrated distillation column
HPC	high-pressure column
I	interfacial transfer rate, mol/s
IGCC	integrated gasification combined cycle
J	molar flux, mol/s m^2
J_q	total heat flux, J/(s m^2)
J'_q	measurable heat flux, J/(s m^2)
L	liquid flow rate, mol/s
LPC	low-pressure column
N	number of theoretical stages, dimensionless
P	pressure, bar
Q	heat rate, J/s
r_{mn}	local resistivity coupling driving force m with flux n, where $m, n \in q, N_2, O_2$
T	temperature, K
V	vapour flow rate, mol/s
x	liquid mole fraction, dimensionless
y	vapour mole fraction, dimensionless
$\Delta_{LV}Y$	difference in property Y between the liquid and vapour boundaries: $Y_V - Y_L$
z	mole fraction, dimensionless

Greek symbols

α	relative volatility, dimensionless

λ	thermal conductivity, J/(s K m)
μ	chemical potential, J/mol

Sub- and superscripts

bot	bottom of a column (section)
C	condenser
I	interface
i	in(ner)
j	component index
L	liquid
N_2	nitrogen
O_2	oxygen
o	out(er)
p	(structured) packing
q	thermal energy
R	reboiler
top	top of a column (section)
tot	total
V	vapour
W	wall

Acknowledgements

The research leading to these results has received funding from the European Community's 7th Framework Programme (FP7/2007-2013) under grant agreement number 211971 (The DECARBit project).

Chapter 11

Discussion and future work

11.1 Air separation unit design

In Chapters 5 and 6, two possible changes in the design of a cryogenic air separation unit (ASU) have been investigated. The potential performance improvement of these changes depends on the required product pressures of the ASU. When an ASU has to deliver high-pressure products, the required product pressure can be obtained either by the compression of gas at an ambient temperature or by the pumping of liquid at a cryogenic temperature. The second option is known as a pumped liquid cycle; this is the option used in the ASUs studied in Chapters 4 and 6.
Compared to the total energy requirement of a vapour compression cycle, a pumped liquid cycle performs comparable or slightly worse. The pumping energy is much less than the compression energy, but because the pumping occurs at a cryogenic temperature, additional refrigeration is required. This refrigeration is often provided for by the compression and expansion of a part of the feed air. When high-pressure oxygen is produced, the use of a pumped liquid cycle is nowadays preferred because it results in safer operation of the air separation unit [Dawson et al., 2004].

11.1.1 Hot heat exchanger

In Chapter 6, it is shown that the addition of a hot heat exchanger can significantly improve the efficiency of the studied ASU. This efficiency improvement is the largest for ASUs that use a pumped liquid cycle. In a pumped liquid cycle, the high pressure of the product(s) require that a part of feed is compressed to a high pressure, in order to maintain proper temperature profiles in the main heat exchanger. This compression step generates the heat of compression that the hot heat exchanger is transferring from the feed to the products. In case of vapour compression instead of liquid pumping, the energy is directly added to the products, so no additional hot heat exchanger is required for this purpose.

However, in the pre-purification step of an ASU, air is usually compressed to approximately 5 bars. This compression step also involves heat of compression that can be used to pre-heat some of the ASU products. In case of a pumped liquid cycle, this heat of compression should be used before the products are heated against the heat of compression of the booster, because it has a lower temperature.

11.1.2 Lowering the pressure in the HPC

In Chapter 5 it is shown that the use of HI stages in combination with a lower operating pressure in the high-pressure column (HPC) can considerably reduce the irreversibilities in the distillation section of an ASU. However, in Chapter 6 it was found that not all of these efficiency gains are translated into an efficiency increase of the entire ASU. Section 6.6.2 discusses several possible reasons for this. Another reason is related to the use of a pumped liquid cycle, which requires the compression of a part of the feed to a fixed pressure level. Only the part of the feed that is directly fed to the HPC involves less compression. This is why the use of HI stages is most attractive in ASUs that do not have a pumped liquid cycle, for example the ASU of an oxy-fuel combustion process, which requires oxygen at a low pressure.

11.2 Heat-integrated distillation stages

The overview of reported efficiency gains given in Section 3.2.1 shows that the use of heat-integrated distillation stages and columns has a large potential for efficiency improvements in various applications. The results presented in Chapter 5 confirm that this is also the case for air distillation. The further development of these HI stages should focus at two important subjects, in order to accelerate their industrial implementation. They are related to the modelling of HIDiCs and to the value of the heat-transfer capacity.

11.2.1 More-accurate HIDiC models

Before HIDiCs can be used in industrial processes, it is important to have reliable models that can give an accurate prediction of their performance. The work presented in Chapters 7 to 10 shows good examples of efforts that aim to achieve this. In addition to the four aspects that the experimental efforts presented in Chapters 9 and 10 focus on, attention should also be paid to the pressure drop characteristics of a HIDiC. It is of course imperative to use the obtained model as basis for economic evaluations.

11.2.2 Increasing the heat-transfer capacity

In order to increase the efficiency of a HIDiC as much as possible, it is important to maximize the heat-transfer capacity of the HI stages. This means that both the heat-transfer area and the overall heat-transfer coefficient should be increased. Several possible options to achieve this are discussed in detail in Section 5.6.2. These options should be investigated in more detail, preferably both numerically and experimentally.

11.3 Integrated-interface transfer model

Chapters 7 and 8 concern the further development of the integrated-interface transfer model introduced in Section 3.3.2. The theoretical background and mathematical description that are required to represent the interface region by a series of connected control volumes have been given. In Chapter 7, the model is used to simulate the transfer processes at a single position in a nitrogen–oxygen distillation column. In Chapter 8, it has been applied to sets of boundary conditions that represent the entire height of a distillation column.
The final goal of developing this model is to predict the performance of an entire separation column with a higher accuracy and flexibility than currently existing models can do. Several further developments of the model are required before this goal can be reached; they are related to the simulation of a complete column, to the simulation of different types of systems, and to the experimental verification of the model.

11.3.1 Simulating a complete separation column

The calculations that have been performed so far all focus on the transfer at a single height or cross-section of a packed column. Those single heights need to be connected to each other, transforming the model to a one-dimensional form. This will involve the use of differential height elements, representing small parts of the total column height. As shortly discussed in Sections 7.6.4 and 8.4.2, there are several quantities that need to be added to the model, because they vary along the height of the column. They can affect both the thickness of the interface region and the effective interface area.

Thickness of the interface region

In rate-based distillation models, it is assumed that the resistance against mass and energy transfer between the well-mixed vapour and liquid bulk phases is completely located in the vapour–liquid interface region, as explained in Section 3.3.2. So the thickness of the interface region is an important model parameter. The vapour–liquid interface region consists of a vapour film, the interface, and a liquid film, as discussed in Section 7.2.
In the conventional rate-based models by Agrawal et al. and Egoshi et al., which are discussed in more detail in Section 3.3.3, the mass transfer relations contain the Reynolds and Schmidt numbers. These dimensionless numbers depend amongst others on the velocity, density, and viscosity: quantities that typically change along the height of a distillation column.
The liquid velocity depends mainly on the liquid flow rate and the type of packing that is used; it also depends slightly on the liquid density and viscosity. The vapour velocity depends on the vapour flow rate, the vapour density, and the free cross-sectional area of the column, which is given by the total area minus the area occupied by the packing and by the liquid phase. Both the densities and viscosities of the two

phases vary mainly due to the changing composition and temperature. Pressure drop in the column can also have a minor influence on mainly the vapour density.
Figure 11.1 shows a first crude attempt to include some of these dependencies in the results presented in Section 8.4.2. As shown in Section 7.5.1, most of the transfer resistance is located in the vapour film. In addition, Table 9.17 shows that the vapour density is relatively constant, compared to the vapour viscosity and the vapour flow rates shown in Table 8.1. Therefore, the original results have been adjusted based on changes in the vapour flow rate and the vapour viscosity only. The relative nitrogen transfer has been multiplied by the change in viscosity and it has been divided by the change in vapour flow rate.

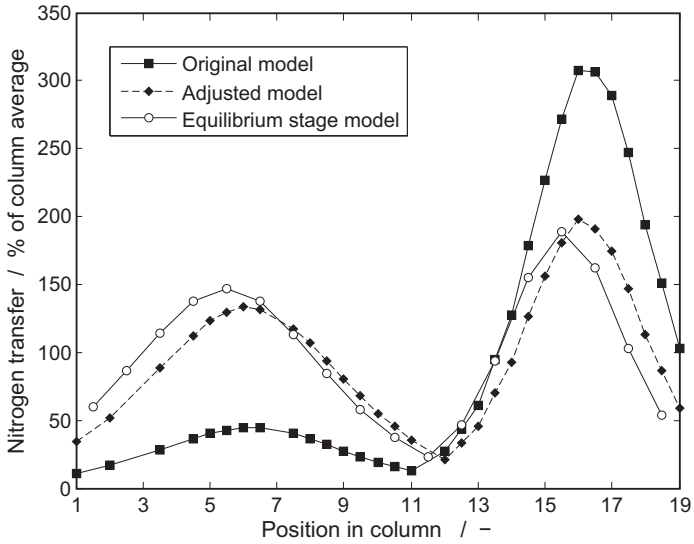

Figure 11.1: Comparison between the nitrogen fluxes calculated with the original model and the adjusted model, and the total amounts of transferred nitrogen calculated from the equilibrium stage model.

The resulting adjusted nitrogen transfer profile shows much closer resemblance with the transfer profile of the equilibrium stage model than the profile of the original model does. This confirms that including dependencies of the interface region thickness on quantities like the velocities, viscosity, and density can yield a more realistic transfer profile. Of course, the model should be based on and compared to experimental data rather than other models. This is discussed in more detail Section 11.3.3.

Effective interface area

Another important variable that should be included in the model is the effective interface area per column volume. This variable is also required in conventional

rate-based models. It was recently concluded by Tsai et al. [2011] that the effective interface area mainly depends on the type of packing that is used and on the liquid flow rate, it also slightly depends on the surface tension. The liquid viscosity and gas velocity were reported to have little influence on the effective interface area. The ratio between the effective interface area and the packing area was found to vary between 0.5 and 1.2. At values below unity, the packing is thought to be not entirely wetted. Values above unity can be related to ripples in the liquid surface and to the presence of droplets.

Minimizing the difference in entropy production

In Section 8.4.1, it is discussed that for some sets of boundary conditions it was impossible to find a liquid film thickness that yields a thermodynamically consistent solution for the fluxes. When simulating an entire distillation column, it is important to obtain values for the fluxes for every set of boundary conditions. In order to achieve this, it is possible to minimize the absolute difference between the entropy production calculated using the fluxes and forces and entropy production calculated using the entropy balance, instead of requiring this difference to be exactly zero. For the sets of boundary conditions that already did yield a solution, this change will not have any effect. However, for the other ones, it will now yield a solution too. Naturally, the value of the difference should be monitored in those cases, to ensure that it is not getting too big.

11.3.2 Simulating different systems

So far, the use of the integrated-interface transfer model has been focussed on a packed distillation column that is separating a binary mixture. The range of systems that the model is applied to should be extended in order to include trayed columns and other (types of) mixtures.

Trayed columns

The main differences between applying the integrated-interface transfer model to a packed column and applying it to a trayed column are the same as for a conventional rate-based model. They are mainly related to the different flow patterns of the two phases and the different models used for the effective interface area. In packed columns, the two phases are flowing counter-currently throughout the entire column, but in trayed columns the two phases flow cross-currently over the trays.
In a packed column, the interface area is related to the specific area of the packing. On a tray, the interface area is provided by bubbles in the liquid phase and droplets in the vapour phase. The amount of interface area depends on the amounts and sizes of the bubbles and droplets, and on the height of the liquid and the froth on a tray.

Therefore, the model for a trayed column is more elaborate than the model for a packed column, but this is not related to type of transfer model that is used.

Other mixtures

So far, the integrated-interface model has only been applied to binary vapour–liquid mixtures of either water and ethanol [De Koeijer and Kjelstrup, 2004, Kjelstrup and De Koeijer, 2003, Mendoza and Kjelstrup, 2011] or nitrogen and oxygen [Chapters 7 and 8]. It should be applied other binary mixtures, also including liquid-liquid mixtures, and multi-component mixtures as well. Compared to binary mixtures, the only complication involved with simulating multi-component mixtures is related to the heats of transfer calculation. How to perform this calculation is described in detail by Kempers [2001]. Adding argon as the third component to a nitrogen–oxygen mixture could be an interesting system to start with.

11.3.3 Experimental verification

In Sections 8.4.2 and 11.3.1, the integrated-interface transfer model is compared to an equilibrium stage model. This can be used as a first assessment of the model performance. A better comparison would be to a four-film transfer model. However, the only correct comparison that can be made should be based on experimental data.

Model for the thickness of the interface region

In order to compare the model to experimental data, three steps need to be taken. Firstly, experimental data needs to be used as basis for the development of a model that relates the thickness of the interface region to the flow rates, temperatures, compositions, and pressures of the two phases (which then also define the densities, viscosities and surface tension). The second step is to simulate various other distillation column cases, based on the developed model for the thickness of the interface region. Finally, the simulation results can be compared to experimental data. The columns cases used in the second and third step should be different from the ones used in the first step.

Coupling between heat and diffusion fluxes

One of the main differences between the integrated-interface transfer model and the four-film transfer model is the inclusion of the direct coupling between heat and diffusion fluxes. In Sections 5.6.1 and 7.6.2, it is discussed that the influence of this coupling effect can be especially significant when modelling a heat-integrated distillation column (HIDiC). Experimental investigations using a HIDiC can be used

to verify the importance of the coupling effect. In Section 10.3.4, it is explained how the coupling effect can be quantified using the experimental set-up described in Chapters 9 and 10. It is also possible to perform a more-qualitative evaluation.
Experimental distillation columns often operate at total reflux. From a modelling perspective, this is advantageous because it results in very well-defined vapour and liquid phase compositions. In the experimental HIDiC set-up described in Chapters 9 and 10, it is possible to control the pressure ratio, and thus the temperature difference, between the two column parts. The experimentally observed relation between the temperature difference and the separation efficiency of the two columns (experiment 7, described in Section 10.5.5) can be compared to simulation results. The required simulations should calculate the molar fluxes for changing values of the temperature driving force, both including and excluding the coupling effect and using equal values of the vapour and liquid compositions. Comparing the experimentally observed trend to the coupled and non-coupled ones can give a qualitative indication about which of the two is closest to reality.

Chapter 12

Conclusions

Several options to improve the Second law efficiency of a cryogenic air separation unit (ASU) as part of an integrated gasification combined cycle (IGCC) have been investigated. Based on the exergy analysis of two state-of-the-art ASUs with a pumped liquid cycle, three process parts have been identified as the most inefficient ones: the compressor after-coolers, the distillation section, and the main heat exchanger. In a conventional two-column ASU design, their contributions to the overall exergy destruction amount to 39%, 26%, and 17%. Within the distillation section, approximately 75% of the destruction is located in the distillation columns. The exergy efficiency, defined by the desired change in exergy content of the products divided by the net added work, is 35% for this process.

The exergy destruction in the compressor after-coolers is caused by the use of cooling water. By replacing the cooling water with the ASU product streams, it is possible to almost completely eliminate this contribution, increasing the exergy efficiency of the process towards 70%. This ASU performance improvement is translated via increased product temperatures to an increased hydrogen production in the gasifier and water-gas shift unit of the IGCC and to an increased net work output in the turbines of the combined cycle. The reduction in exergy destruction of 1.6 kJ/mol air corresponds to a 0.74% increase in the net electric efficiency of the IGCC. The performance improvement caused by the use of this hot heat exchanger is the largest for ASUs that use a pumped liquid cycle.

Two alternatives for decreasing the exergy destruction of the distillation section have been examined: the addition of a third distillation column, and the combination of using heat-integrated stages (HI stages) and decreasing the ratio between the pressures in the two columns. The first option can reduce the exergy destruction in the distillation section by approximately 30%, resulting in a 7% reduction in the ASUs work input. When applying the second option, reductions in the distillation section

exergy destruction of 20% to 30% are possible, depending on the amount of heat-transfer capacity that is present per theoretical equilibrium stage.
In addition to this uncertainty in the heat-transfer capacity, which is partly related to the absence of detailed knowledge on the overall heat-transfer coefficient, three other uncertainties exist in the model that has been used to perform the numerical evaluations. They are related to the use of a ring-shaped distillation column, to the presence of radial gradients in the HI stages, and to the interdependency of heat and diffusion fluxes.

In order to assess these four aspects experimentally, a concentric heat-integrated distillation column (HIDiC) has been designed that can be used to perform total reflux experiments at cryogenic temperature and elevated pressures. The designed set-up has inner and outer column diameters of 14 and 22 cm, and a total column height of approximately 3.5m. Both the inner and the outer column will be equipped with electrical reboilers that have a maximum duty of 20 kW. Copper-brazed plate heat exchangers will be used as condensers. They will be fed with up to 550 kg/h of liquid nitrogen as coolant.
The total amount of thermal energy that is being transferred from the high-pressure column to the low-pressure column will be quantified by two independent measurements of the reboiler and condenser duties of both column parts. Over 80 composition and temperature measurements will enable characterization of the phenomena that are occurring inside the columns. These measurements will cover the longitudinal, the radial, and the angular directions of the columns, in both the vapour phase and the liquid phase.
The experimental results obtained with this set-up will not only be useful for more-detailed feasibility evaluations of heat-integrated air distillation columns, but they will be beneficial for the accurate design and simulation of separation columns in general. Various other distillation processes can benefit from using HI stages. In addition to the mentioned experimental investigations and the development of more-accurate models, future research on the use of HI stages should focus on maximization of the heat-transfer capacity.

As another way to improve the accuracy of models for (heat-integrated) distillation columns, efforts have been used on the further development of the integrated-interface transfer model. A new formulation has been developed, that represents the interface region by a series of $2n + 1$ connected control volumes. Based on this formulation, a calculation method has been developed that can be used to obtain values for the thermal and molar fluxes based on input values for the overall driving forces. The ratio between the thicknesses of the vapour and liquid films is found by requiring consistency between the entropy production calculated using the entropy balance and using the product-sum of conjugate fluxes and driving forces.
A nitrogen–oxygen mixture has been used to investigate the properties of this new model. It was found that the calculated values of the fluxes converge when increasing the number of control volumes per film (n). For the lowest possible value of $n = 1$, some of the calculated fluxes differed by a factor of 2 from their converged values. In

order to ensure that the deviation from the converged values is within 0.1%, a value of at least $n = 32$ should be used.
Most of the transfer resistivities are located in the vapour film. Uncertainties in the calculation results are mainly caused by uncertainties in the Maxwell–Stefan diffusion coefficients and in the liquid phase heat of transfer. The calculated value for the measurable heat flux at the liquid boundary of the interface region is most sensitive to these uncertainties, as well as to the effects of neglecting the interface resistance and neglecting the direct coupling between heat and diffusion fluxes. Accurate values for the heat flux are especially important when modelling HIDiCs and diabatic distillation columns.
The importance of the coupling effect has been found to be significant along the entire height of a distillation column. It should always be included in accurate models for the simultaneous transfer of thermal energy and mass. The effect of the interface resistivities is relatively small. Further developments of the integrated-interface transfer model should focus on three main points: simulation of an entire separation column, simulation of more various types of systems, and experimental verification of the model.

This work has presented several options to improve the Second law efficiency of a cryogenic ASU. Some of them are mainly applicable to cryogenic ASUs, or even only to a special type of cryogenic ASU. The use of HI stages, however, has the potential to improve the efficiency of many other separation processes. All of the options can contribute to limit future CO_2 emissions and climate changes.

Appendix A

An empirical Helmholtz energy based model for the calculation of thermodynamic properties of N_2–Ar–O_2-mixtures

L.V. van der Ham

Department of Chemistry
Norwegian University of Science and Technology
7491 Trondheim, Norway

This chapter is based on a report written for the PhD-course
KP8108 – Phase Equilibria
NTNU, December 2008

Abstract

A Matlab model has been created that can be used to calculate various single phase thermodynamic properties and vapour–liquid equilibrium conditions of nitrogen–argon–oxygen mixtures. The model can be used during the design of cryogenic air distillation columns. It is based on an empirical equation of state that is explicit in Helmholtz energy and describes the real mixture properties as an excess contribution to the Helmholtz energy. The accuracy of the Matlab model is around 0.1% for the relevant single phase thermodynamic properties and around 0.5% for vapour–liquid equilibrium conditions.

A.1 Air distillation

Distillation of air is currently the most commonly used technique for the production of pure oxygen and nitrogen on an industrial scale. Atmospheric air is a mixture of nitrogen, oxygen, argon, carbon dioxide, water and other trace elements. In an air separation process, carbon dioxide and water are typically removed from this mixture before it enters the distillation unit. The air that is fed to a distillation column can therefore be properly considered as a mixture of nitrogen, oxygen and argon only; their mole fractions are given in Table A.1 [Hausen and Linde, 1985].

Table A.1: Composition of air

Component	Mole fraction
N_2	0.7812
O_2	0.2096
Ar	0.0092
Total	1.0000

The design of a distillation column depends heavily on the thermodynamic data that is used as basis. It is therefore desired to use thermodynamic data that is as accurate as possible. The aim of this essay is to present a model for the calculation of accurate thermodynamic data for nitrogen–argon–oxygen mixtures.

A.2 Equations of state

The thermodynamic state of a pure component is defined when its temperature (T), pressure (P) and specific volume (v) are defined. These three variables are often referred to as the state variables. The relation between three state variables can be captured in an equation of state, which allows calculating the third variable when the other two are known. All other thermodynamic properties, like the entropy (S) and the enthalpy (H), can be determined using the equation of state as well.

A.2.1 Early equations of state

Classically, an equation of state gives the pressure as a function of the temperature and specific volume, or alternatively its reciprocal; the density (ρ). Various functional forms of such a pressure explicit equation of state have been developed in the course of time [Hausen and Linde, 1985, Jacobsen et al., 1997]. The simplest and less accurate one is the ideal gas law

$$P = \frac{RT}{v} = \rho RT \tag{A.1}$$

Here, R is the universal gas constant. Other well-known pressure explicit functional forms are the virial equation, with temperature dependent constants B, C, D, ...,

$$P = \frac{RT}{v} + \frac{B}{v^2} + \frac{C}{v^3} + \frac{D}{v^4} + \dots \tag{A.2}$$

the Van der Waals equation, with constants a and b,

$$P = \frac{RT}{v-b} - \frac{a}{v^2} \tag{A.3}$$

the Soave–Redlich–Kwong equation, with constant b and temperature dependent a,

$$P = \frac{RT}{v-b} - \frac{a(T)}{v(v+b)} \tag{A.4}$$

the Peng–Robinson equation, with constant b and temperature dependent a,

$$P = \frac{RT}{v-b} - \frac{a(T)}{v(v+b)+b(v-b)} \tag{A.5}$$

and the Benedict–Webb–Rubin equation, with constants A_0, A_0, A_0, a, b, c, α and γ,

$$P = \frac{RT}{v} + \frac{B_0 RT - A_0 - \frac{C_0}{T^2}}{v^2} + \frac{bRT - a}{v^3} + \frac{a\alpha}{v^6} + \frac{c}{v^3 T^2}\left(1 + \frac{\gamma}{v^2}\right) e^{\frac{-\gamma}{v^2}} \tag{A.6}$$

The virial equation of state describes the deviation from ideal gas behaviour as an infinite power series expansion in terms of the volume. The Van der Waals, Soave–Redlich–Kwong and Peng–Robinson equations of state are also knows as cubic equations of state, because they describe the non-ideal part with a term that is cubic in

the specific volume.
These equations of state can also be used to describe mixtures, although the results are generally less accurate than for pure components. For mixtures, the constants that are used become composition dependent. They can be calculated using certain mixing rules and additional binary interaction parameters.

A.2.2 Modern equations of state

During the development of the early equations of state, the main aim was to obtain more accurate expressions without increasing the complexity too much, because calculations were often still executed without a computer. The wide-spread availability of computational speed opened they way for more complex and accurate equations of state, based on an empirical rather than an analytical approach [Jacobsen et al., 1997, Span, 2000]. The number of model parameters increased to more than 30, which resulted in the name multi-parameter equations of state. This name is a bit misleading though, because the early equations of state also use multiple parameters, although less. The term 'empirical equations of state' will be used in this work.
Along with the change to empirical equations of state came the change from a pressure explicit functional form to a Helmholtz energy explicit functional form. The main advantage of using the Helmholtz energy is that all other thermodynamic properties can be determined by differentiation only, which makes the equation of state a fundamental equation. If a pressure explicit expression is used, integration is required too. When translating this difference into practise, it means that more complex functional forms can be used if an equation of state is explicit in Helmholtz energy.
The first developments in the field of empirical equations of state were aimed at optimising the function form that was used. The goal was to obtain a very high accuracy while using as less parameters as possible. When developing a high accuracy equation of state for a wide range of conditions, a large number of experimental results is required to fit it to. The first efforts were therefore mainly focused on well-measured substances, and several very high accuracy equations of state have been developed in this way. Because the accuracy of calculated thermodynamic properties is within the experimental error of experiments, they can be used as reference for these properties. This is why these equations of state are also called reference equations of state.
The functional forms of reference equations of state are rather substance specific. Because there is also a desire for equations of state for less well-measured substances, more general functional forms have been being developed as well. This has been done by optimising the functional form using the experimental data of a group of relatively similar and well-measured substances, and applying this functional form to other less well-measured substances of the same group. These equations of state are called technical equations of state. Their accuracy is still high, but not as high as is the case for the reference equations of state. The number of parameters used in technical equations of state is typically less than for reference equations of state.
Another development within field of empirical equations of state is the extension of its application from pure substances to multi-component mixtures, again using certain mixing rules and additional binary interaction parameters.

A.2.3 Equations of state for N_2, Ar, O_2 and mixtures thereof

In the near past, early equations of state for nitrogen, argon, oxygen and mixtures of these components still received some attention in literature; see for example the work of Asami and Ebisu for the pure components [Asami, 1990, Asami and Ebisu, 1989, 1990], and the work of Hwang for mixtures [Hwang, 1987]. But today, publications on the subject concern empirical equations of state only. In contrary, most commercial simulation software still uses the early equations of state as basis for its calculations. Both technical as well as reference equations of state are available for pure nitrogen, argon and oxygen [Schmidt and Wagner, 1985, Span and Wagner, 2003a,b, Stewart et al., 1991, Tegeler et al., 1999]. Technical equations of state are easier to implement in calculations because the functional form is exactly the same for each substance and because less parameters are involved. This makes them more attractive than the reference equations of state. On the other hand, the reason for developing technical equations of state was to provide an equation of state for substances that are less well-measured, not because the calculations involved with reference equations of state are too demanding. So if both are available, one should always choose to use reference equations of state. They are simply more accurate.
Several empirical equations of state for air and mixtures of nitrogen, argon and oxygen in general have been published. The first ones modelled the mixture properties based on an extended corresponding states approach. This means that the mixture is modelled as if it is a pure substance, using mixing rules and composition dependent shape factors to relate the mixture to a reference substance [Clarke et al., 1993]. Later equations of state quantify the deviation of the real mixture properties from the ideal mixture properties in terms of an excess contribution, again using mixing rules and composition dependent shape factors.
Some of the most recent equations of state are limited to a fixed ternary mixture composition [Panasiti et al., 1999], to variable compositions for binary mixtures only [Estela-Uribe, 2006], or to the liquid phase only [Goharshadi and Moosavi, 2008]. This makes them unsuitable for use in the current work, since variable ternary mixture compositions for both liquid and vapour phase are required during distillation column modelling. There are only two publications that satisfy these criteria; one is focused on nitrogen–argon–oxygen mixtures only [Lemmon et al., 2000], and the other is a more general model that can be used for mixtures of more varied substances [Lemmon and Jacobsen, 1999]. The former one can be interpreted as the reference equation of state for the nitrogen–argon–oxygen mixture, and the latter as a technical equation of state for this mixture. It is therefore the former one that is used as basis for the current work.

A.3 A Helmholtz energy based mixture model

As explained in Section A.2.2, modern equations of state are typically explicit in Helmholtz energy. The independent variables that are used in the chosen model are the temperature and density. In addition, the model uses reduced variables instead of normal ones. It relates the dimensionless Helmholtz energy of a pure component

(α_i) to the reciprocal reduced temperature (τ) and the reduced density (δ),

$$\alpha_i(\tau,\delta) = \alpha_i\left(\frac{T_{c,i}}{T}, \frac{\rho}{\rho_{c,i}}\right) = \frac{a_i(T,\rho)}{RT} \tag{A.7}$$

Here, $T_{c,i}$ is the critical temperature, $\rho_{c,i}$ the critical pressure and a_i the molar Helmholtz energy of a pure component. The dimensionless Helmholtz energy of a mixture (α_{mix}) is built up out of two parts; a part that is related to the ideal mixture properties and a part that is related to the non ideal mixture properties:

$$\alpha_{mix} = \sum_{i=1}^{n} x_i(\alpha_i + \ln x_i) + \alpha^E \tag{A.8}$$

Here, x_i are the mole fractions of the n components. The last term is called the excess dimensionless Helmholtz energy (α^E) and is discussed in more detail in Section A.3.2. The dimensionless Helmholtz energy of a pure component is also built up out of an ideal and a non-ideal part:

$$\alpha_i = \alpha_i^0 + \alpha_i^r \tag{A.9}$$

Here, α_i^0 is the dimensionless ideal gas Helmholtz energy and α_i^r the dimensionless residual Helmholtz energy of a pure component. They are discussed in more detail in Section A.3.1.
The dimensionless Helmholtz energy of a mixture can also be split up into an overall ideal part, containing the ideal mixture as well as the ideal gas parts, and an overall real part, containing the residual as well as the excess parts:

$$\alpha_{mix} = \alpha_{mix}^{ideal} + \alpha_{mix}^{real} = \left(\sum_{i=1}^{n} x_i\left(\alpha_i^0 + \ln x_i\right)\right) + \left(\sum_{i=1}^{n} x_i\alpha_i^r + \alpha^E\right) \tag{A.10}$$

A.3.1 Pure component contributions

As discussed in Section A.1, distillation of air involves three pure components; nitrogen, argon and oxygen. The equations of state used to model their thermodynamic properties have big similarities, but because reference equations of state are used they are still slightly different. Each equation of state is discussed in detail in Section A.3.1. First, some fixed physical properties of these components are presented in Table A.2. Throughout this work, the components are ordered based on their normal boiling points.

Table A.2: Fixed physical properties of the pure components

Physical property	(unit)	Nitrogen	Argon	Oxygen
Molecular mass	(g/mol)	28.0135	39.9480	31.9988
Critical temperature	(K)	126.192	150.687	154.581
Critical pressure	(MPa)	3.396	4.863	5.043
Critical density	(mol/dm^3)	11.184	13.407	13.630
Triple point temperature	(K)	63.151	83.806	54.361
Triple point pressure	(kPa)	12.523	68.891	0.1463
Triple point liquid density	($mmol/dm^3$)	24.07	101.5	0.3237
Triple point vapour density	(mol/dm^3)	30.957	35.465	40.816
Normal boiling point	(K)	77.355	87.302	90.188

Nitrogen

The equation of state used for nitrogen is described by Span et al. [2000]. The dimensionless ideal gas Helmholtz energy is given by

$$\alpha^0 = \ln\delta + N_1 \ln\tau + N_2 + N_3\tau + \frac{N_4}{\tau} + \frac{N_5}{\tau^2} + \frac{N_6}{\tau^3} + N_7 \ln\left(1 - e^{-N_8\tau}\right) \qquad \text{(A.11)}$$

Here, N_k are empirical parameters. The dimensionless residual Helmholtz energy is given by

$$\alpha^r = \sum_{k=1}^{6} N_k \delta^{i_k} \tau^{j_k} + \sum_{k=7}^{32} N_k \delta^{i_k} \tau^{j_k} e^{-\delta^{l_k}} + \sum_{k=33}^{36} N_k \delta^{i_k} \tau^{j_k} e^{-\phi_k(\delta-1)^2 - \beta_k(\tau-\gamma_k)^2} \qquad \text{(A.12)}$$

Here, N_k, i_k, j_k, l_k, ϕ_k, β_k and γ_k are empirical parameters. Terms 33 till 36 are used to improve the accuracy in the critical region.

Argon

The equation of state used for argon is described by Tegeler et al. [1999]. The dimensionless ideal gas Helmholtz energy is given by

$$\alpha^0 = \ln\delta + N_1 + N_2\tau + 1.5\ln\tau \qquad \text{(A.13)}$$

Here, N_k are empirical parameters. The dimensionless residual Helmholtz energy is given by

$$\alpha^r = \sum_{k=1}^{12} N_k \delta^{i_k} \tau^{j_k} + \sum_{k=13}^{37} N_k \delta^{i_k} \tau^{j_k} e^{-\delta^{l_k}} + \sum_{k=38}^{41} N_k \delta^{i_k} \tau^{j_k} e^{-\phi_k (\delta-1)^2 - \beta_k (\tau-\gamma_k)^2} \quad \text{(A.14)}$$

Here, N_k, i_k, j_k, l_k, ϕ_k, β_k and γ_k are empirical parameters.

Oxygen

The equation of state used for oxygen is described by Schmidt and Wagner [1985]. The dimensionless ideal gas Helmholtz energy is given by

$$\begin{aligned} \alpha^0 = &\ln \frac{\delta}{\delta_0} + N_1 \tau^{1.5} + \frac{N_2}{\tau^2} + N_3 \ln \tau + N_4 \tau \\ &+ N_5 \ln \left(e^{N_7 \tau} - 1\right) + N_6 \ln \left(1 + \frac{2}{3} e^{-N_8 \tau}\right) + N_9 \end{aligned} \quad \text{(A.15)}$$

Here, N_k are empirical parameters. Further, δ_0 is the reduced density, evaluated at the standard temperature and pressure of $T_0 = 298.15$ K and $P_0 = 1.01325$ bar. The dimensionless residual Helmholtz energy is given by

$$\alpha^r = \sum_{k=1}^{13} N_k \delta^{i_k} \tau^{j_k} + \sum_{k=14}^{24} N_k \delta^{i_k} \tau^{j_k} e^{-2} + \sum_{k=25}^{32} N_k \delta^{i_k} \tau^{j_k} e^{-4} \quad \text{(A.16)}$$

Here, N_k, i_k and j_k are empirical parameters.

Ancillary equations

In addition to the equations of state described above, also some ancillary equations are given that can be used to determine thermodynamic properties at phase changes. The values of these pure component properties can be used to obtain initial guesses for vapour–liquid equilibrium calculations of mixtures. The ancillary equations for nitrogen and argon are described in the references given above; those for oxygen are described by Stewart et al. [1991]. The ancillary equations can be used to calculate the

saturated vapour pressure (P_σ), the saturated liquid density (ρ') and the saturated vapour density (ρ''):

$$\ln \frac{P_\sigma}{P_c} = \frac{T_c}{T} \sum_{k=1}^{n} N_k \theta^{i_k} \tag{A.17}$$

$$\ln \frac{\rho'}{\rho_c} = \sum_{k=1}^{n} N_k \theta^{i_k} \tag{A.18}$$

$$\frac{\rho'}{\rho_c} = 1 + \sum_{k=1}^{n} N_k \theta^{i_k} \tag{A.19}$$

$$\ln \frac{\rho''}{\rho_c} = \frac{T_c}{T} \sum_{k=1}^{n} N_k \theta^{i_k} \tag{A.20}$$

Equations (A.17) and (A.20) can be used for nitrogen, argon as well as oxygen. Equation (A.18) should be used for nitrogen and argon only, and Equation (A.19) for oxygen only. Here, N_k and i_k are empirical parameters, and further

$$\theta = 1 - \frac{T}{T_c} \tag{A.21}$$

A.3.2 Mixture contributions

The equation of state for mixtures of nitrogen, argon and oxygen is described by Lemmon et al. [2000]. It is based on Equation (A.10), with the dimensionless excess Helmholtz energy given by

$$\alpha^E = \left(\sum_{i=1}^{2} \sum_{j=i+1}^{3} x_i x_j F_{ij} \right) \left(0.00871334 \delta^2 \tau^{1.5} - 0.00195245 \delta^2 \tau^{-1.4} \right) \tag{A.22}$$

Here, F_{ij} are empirical mixture parameters. Equation (A.22) involves the reduced density and reciprocal reduced temperature. When considering pure components the calculation of these quantities uses the critical density and critical temperature. But when considering mixtures, composition dependent reducing parameters for the density (ρ_{red}) and for the temperature (T_{red}) should be used:

$$T_{red} = \sum_{i=1}^{3} x_i T_{c,i} + \sum_{i=1}^{2} \sum_{j=i+1}^{3} x_i x_j \zeta_{ij} \tag{A.23}$$

$$\rho_{red} = \left(\sum_{i=1}^{3} \frac{x_i}{\rho_{c,i}} + \sum_{i=1}^{2} \sum_{j=i+1}^{3} x_i x_j \xi_{ij} \right)^{-1} \tag{A.24}$$

Here, ζ_{ij} and ξ_{ij} are empirical mixture parameters. Only the real part of Equation (A.22) should be evaluated using these reducing parameters to calculate the

reduced density and temperature. The ideal part still uses the critical densities and temperatures, resulting into

$$\begin{aligned}\alpha_{mix} = &\sum_{i=1}^{n} x_i \left[\alpha_i^0\left(\frac{T_{c,i}}{T}, \frac{\rho}{\rho_{c,i}}\right) + \ln x_i\right] \\ &+ \sum_{i=1}^{n} x_i \alpha_i^r\left(\frac{T_{red}}{T}, \frac{\rho}{\rho_{red}}\right) + \alpha^E\left(\frac{T_{red}}{T}, \frac{\rho}{\rho_{red}}\right)\end{aligned} \tag{A.25}$$

A.4 Calculation routines

The model explained in Section A.3 gives the Helmholtz energy as a function of temperature and density. As described in Section A.2, all thermodynamic properties can be calculated using derivatives of the Helmholtz energy. The calculation of some common single phase thermodynamic properties is discussed in more detail in Section A.4.1. Section A.4.2 focuses on calculations involving vapour–liquid equilibrium in mixtures.

A.4.1 Single phase thermodynamic properties

The single phase thermodynamic properties that are most relevant when modelling a distillation column are the pressure, the molar enthalpy (h) and the molar entropy (s); they are given by

$$\frac{P}{\rho RT} = 1 + \delta\left(\frac{\partial \alpha^r}{\partial \delta}\right)_\tau \tag{A.26}$$

$$\frac{h}{RT} = \tau\left(\left(\frac{\partial \alpha^0}{\partial \tau}\right)_\delta + \left(\frac{\partial \alpha^r}{\partial \tau}\right)_\delta\right) + \delta\left(\frac{\partial \alpha^r}{\partial \delta}\right)_\tau + 1 \tag{A.27}$$

$$\frac{s}{R} = \tau\left(\left(\frac{\partial \alpha^0}{\partial \tau}\right)_\delta + \left(\frac{\partial \alpha^r}{\partial \tau}\right)_\delta\right) - \alpha^0 - \alpha^r \tag{A.28}$$

Other thermodynamic properties that are often used to verify calculation routines are the molar internal energy (u), the isochoric molar heat capacity (C_v), the isobaric molar heat capacity (C_p) and the speed of sound (w). They are given by

$$\frac{u}{RT} = \tau\left(\left(\frac{\partial \alpha^0}{\partial \tau}\right)_\delta + \left(\frac{\partial \alpha^r}{\partial \tau}\right)_\delta\right) \tag{A.29}$$

$$\frac{C_v}{R} = -\tau^2\left(\left(\frac{\partial^2 \alpha^0}{\partial \tau^2}\right)_\delta + \left(\frac{\partial^2 \alpha^r}{\partial \tau^2}\right)_\delta\right) \tag{A.30}$$

$$\frac{C_p}{R} = -\tau^2 \left(\left(\frac{\partial^2 \alpha^0}{\partial \tau^2} \right)_\delta + \left(\frac{\partial^2 \alpha^r}{\partial \tau^2} \right)_\delta \right) + \frac{\left(1 + \delta \left(\frac{\partial \alpha^r}{\partial \delta} \right)_\tau - \delta\tau \left(\frac{\partial^2 \alpha^r}{\partial \delta \partial \tau} \right) \right)^2}{1 + 2\delta \left(\frac{\partial \alpha^r}{\partial \delta} \right)_\tau - \delta^2 \left(\frac{\partial^2 \alpha^r}{\partial \delta^2} \right)_\tau} \tag{A.31}$$

$$\frac{w^2 M_w}{RT} = 1 + 2\delta \left(\frac{\partial \alpha^r}{\partial \delta} \right)_\tau + \delta^2 \left(\frac{\partial^2 \alpha^r}{\partial \delta^2} \right)_\tau - \frac{\left(1 + \delta \left(\frac{\partial \alpha^r}{\partial \delta} \right)_\tau - \delta\tau \left(\frac{\partial^2 \alpha^r}{\partial \delta \partial \tau} \right) \right)^2}{\tau^2 \left(\left(\frac{\partial^2 \alpha^0}{\partial \tau^2} \right)_\delta + \left(\frac{\partial^2 \alpha^r}{\partial \tau^2} \right)_\delta \right)} \tag{A.32}$$

Equations (A.26) to (A.32) concern the calculation of thermodynamic properties of a pure component, they are written using α^0 and α^r. If a mixture is concerned instead of pure component, the structure of all equations remains the same, but all α^0 and α^r should be replaced by α_{mix}^{ideal} and α_{mix}^{real}, and the derivatives should be taken at constant composition.

A.4.2 Vapour–liquid equilibrium

The basic principle on which the distillation concept is built, is that the most volatile component in the mixture concentrates in the vapour phase and the least volatile component in the liquid phase. It is therefore essential for the modelling of a distillation column to know how each of the components gets distributed over the two phases. In practise this distribution is often expressed using equilibrium constants (K_i), they are defined as the ratios between the mole fractions in the vapour phase (y_i) and the mole fractions in the liquid phase (x_i)

$$K_i = \frac{y_i}{x_i} \tag{A.33}$$

A three component two phase system involves ten variables, namely a temperature, a pressure and three mole fractions in each of the phases. Since the mole fractions in a single phase must add up to one, there are only eight independent variables. When two phases are at chemical equilibrium, this means that the temperature, pressure and chemical potentials of the components (μ_i) are equal in both phases. These five dependencies leave three degrees of freedom. This derivation is known as the phase rule for non-reacting systems. It can be used to determine four practical equilibrium calculations. In each of the calculations, the composition of one phase is fixed in combination with either the temperature of the pressure. The result of the calculation is given by the composition of the other phase and the pressure if the temperature was fixed or the temperature if the pressure was fixed. Each type of calculation has been given a name based on the quantities that are calculated; an overview is given in Table A.3.

As can be seen in Table A.3, a fifth common calculation type exists; the flash calculation. In this calculation, the total mole fractions (z_i) are fixed in addition to the temperature and pressure, and the vapour and liquid phase mole fractions are calculated in combination with the molar vapour fraction (f_v).

Table A.3: Five types of vapour–liquid equilibrium calculations

Calculation type	Fixed quantities	Calculated quantities
Dew point temperature	P, y_i	T, x_i
Dew point pressure	T, y_i	P, x_i
Bubble point temperature	P, x_i	T, y_i
Bubble point pressure	T, x_i	P, y_i
Flash	T, P, z_i	x_i, y_i, f_v

General solving strategies

Unfortunately, the equilibrium calculations are not as straightforward as the single phase thermodynamic property calculations. An iteration scheme is required to find the solution. Two iteration schemes are often used in practise; one is based on a direct substitution method and is known as the K-value method, the other is based on Newton's method. The K-value method is especially useful for mixtures that have constant K-values, but the more the K-values start to differ as a function of composition the worse this methods works. Newton's method works for both constant as well as varying K-values, but its disadvantage is that a good initial guess of the solution has to be provided. It can be difficult to find a routine that always yields sufficient accurate initial guesses. Because the K-values of the nitrogen–argon–oxygen mixture are not constant, Newton's method has been chosen as the method to use in this work.
The primary aim of Newton's method is to adjust the compositions of the phases in such a way that the chemical potentials of all components become equal in both phases. In terms of Helmholtz energy (A), the chemical potential of a component is defined as the partial derivative with respect to the number of moles of the component (n_i) at constant temperature, total volume (V) and number of moles of all other components (n_j)

$$\mu_i = \left(\frac{\partial A}{\partial n_i}\right)_{T,V,n_j} \tag{A.34}$$

All derivatives with respect to the numbers of moles are calculated numerically in this work, as suggested by Lemmon et al. [2000].
Using Newton's method, the numbers of moles of the components are continuously updated until the chemical potentials are equal. In the case of a flash calculation, the total composition is given and the distribution of the components over both phases is solved for. The vector containing the changes in number of moles for each iteration step (Δn_i) is then given by

$$\Delta n_i^v = -\Delta n_i^l = -\left(\frac{\partial \mu_i^v}{\partial n_j^v} + \frac{\partial \mu_i^l}{\partial n_j^l}\right)^{-1} \left(\mu_i^v - \mu_i^l\right) \quad \text{with } i = j = 3 \tag{A.35}$$

Here, the first right-hand side term is a three-by-three matrix containing the partial derivatives of the chemical potentials with respect to all components. Similar to the change vector, the second right-hand side term is a vector with length three.
In the other four types of calculations listed in Table A.3 the composition of one phase is fixed and the composition of the other phase is solved for. If the vapour phase composition is fixed, the changes in number of moles for the liquid phase can be calculated using

$$\Delta n_i^l = -\left(\frac{\partial \mu_i^l}{\partial n_j^l}\right)^{-1} \left(\mu_i^l - \mu_i^v\right) \quad \text{with } i = j = 3 \tag{A.36}$$

A complication for all calculations is that the total number of moles in one or both phases changes, which changes the pressures of the affected phases. An obvious way to obtain or keep the desired pressure is to vary the volumes (or densities) of the affected phases. In theory it is possible to include the required volume changes in the iteration scheme as well. The additional partial derivatives that are needed are those for the chemical potentials and pressures with respect to the volumes.
However, in practise this approach proves to require a very accurate initial guess, making it unsuitable for the current work. Therefore a different solution strategy has been used. It is explained in more detail for the case of a bubble point pressure calculation below; and it can be applied to all calculations except the flash. But, with the results of the other calculations, an accurate initial guess can be made for a flash calculation based on Newton's method with simultaneous updates in all numbers of moles and volumes, as is discussed below.

Bubble point pressure calculation

The aim of a bubble point pressure calculation is to find the pressure and liquid phase composition that are in equilibrium with a given vapour phase composition at a given temperature.
The chosen strategy to find the solution is to start by picking two pressures, based on an estimation of the mixture its saturated vapour pressure. At these two chosen pressures, Newton's method is used to find the numbers of moles in the liquid phase that result into chemical equilibrium. Next, the found liquid composition is normalized and the chemical potentials in the liquid phase are calculated using this new composition. The difference between these chemical potentials and the fixed chemical potentials in the vapour phase can then be translated into a quantity that represents

the overall deviation (d). At the bubble point pressure this deviation is zero. It is relatively easy to find the zero point, because the deviation is almost a perfect linear function of the pressure. A schematic of the calculation routine is shown below, Matlab code for this routine can be found in Section A.A.

1. Estimate P_σ at T, y_i using Equation (A.17).
2. Find n_i^l at equilibrium for $P_\sigma + dP_1$ and $P_\sigma + dP_2$, using Equation (A.35).
3. Normalize n_i^l.
4. Calculate $d = \sum_i \left(1 - \frac{\mu_i^v}{\mu_i^l}\right)$
5. Estimate P at which $d = 0$
6. Find n_i^l at equilibrium for P, normalize n_i^l, and calculate d.
7. Check whether $|d| < \varepsilon$ at P; return to step 5 if needed.
8. $P_{bub} = P$ and $x_i = n_i^l$

In practise, an accurate bubble point pressure is often found after a single iteration. The accuracy of this value is checked by calculating the overall deviation at this estimated pressure. If the accuracy is too low, the first estimation can be used to obtain a more accurate estimate for the bubble point pressure. The accuracy can continuously be improved by adding more pressures, but in practise the maximum number of required iterations for $\varepsilon = 10^{-4}$ is two.
For a dew point pressure calculation, the liquid and vapour phase compositions should simply be swapped. If a bubble point temperature calculation is performed, the pressure and temperature should be swapped. And in the case of a dew point temperature calculation, both liquid and vapour phase compositions, and pressure and temperature should be swapped.

Flash calculation

Using routines for bubble and dew point temperature calculations similar to the routine discussed above, a flash calculation becomes straightforward. A schematic of the calculation routine is shown below, Matlab code for the entire routine can be found in Section A.B.

1. Calculate T_{bub} and T_{dew} at P, z_i.
2. Check whether $T_{bub} < T < T_{dew}$; if not, stop.
3. Estimate f_v using Equation (A.37).

4. Estimate n_i^v and n_i^l using Equations (A.38) to (A.41).
5. Calculate V^v and V^l.
6. Find n_i^v, n_i^l, V^v and V^l at equilibrium for P and T.
7. Calculate y_i, x_i and f_v.

The first step is to check whether the specified input lies in the two-phase region of the mixture. This is done by calculating the bubble and dew point temperatures of the mixture at the specified pressure. If the specified temperature does not lie in between these two temperatures the calculation is terminated because the specified conditions lie in a single phase region. Otherwise, an estimation for the vapour phase fraction is made based on the calculated and specified temperatures, using an empirical equation

$$f_v = \left(\frac{T - T_{bub}}{T_{dew} - T_{bub}} \right)^{0.6} \tag{A.37}$$

Using this vapour phase fraction, estimations for the vapour and liquid phase compositions are made. The composition of the smallest phase is estimated using the difference between the overall composition and the bubble or dew point composition. The composition of the largest phase is then obtained by subtracting the smallest phase from the total composition. If the vapour phase is the smallest one, the compositions are estimated using

$$n_i^v = f_v \left(z_i + \left(y_i^{bub} - z_i \right) (1 - f_v) \right) \tag{A.38}$$

$$n_i^l = z_i - n_i^v \tag{A.39}$$

Here it is assumed that the total number of moles equal unity. If the liquid phase is the smallest phase, the compositions are estimated using

$$n_i^l = (1 - f_v) \left(z_i + \left(x_i^{dew} - z_i \right) f_v \right) \tag{A.40}$$

$$n_i^v = z_i - n_i^l \tag{A.41}$$

Using these estimates for the compositions, estimates for the volumes of the phases can be calculated via the densities. Then the final step is to find the compositions and volumes at which the two phases are at equilibrium, using Newton's method for all the compositions and volumes simultaneously. The result of this iteration step then simply leads to the desired values of the vapour phase fraction and the vapour and liquid phase mole fractions.

A bubble point data table

A common method to solve distillation columns models is the bubble-point method. This iterative method is especially useful for mixtures with relatively constant equilibrium constants. Each iteration step requires the calculation of all stage temperatures using bubble point data. A bubble point temperature calculation as described above takes about 1.4 seconds. This means that it would take about 14 minutes to obtain the solution of a column with 20 trays that requires 30 iterations. A strategy to substantially decrease the simulation time is to use a table with pre-generated bubble point data. Instead of calculating the bubble point data numerous times during the simulation, they can be obtained from the pre-generated table by interpolation, which is much faster.
A bubble point temperature calculation of air requires three independent variables as input; the pressure and two of the three liquid mole fractions. If the distillation column is assumed to operate at a constant pressure, a simple two-dimensional table is sufficient to cover the required range of possible input data. But if the pressure drop over the stages is taken into account, a three-dimensional table is required, resulting in a three-dimensional interpolation to obtain the bubble point data.
Matlab contains the 'interpn'-function to perform multi-dimensional interpolations. This function does not allow extrapolation and it needs an equally spaced grid, typically created using the 'meshgrid'-function. The nitrogen and oxygen mole fraction range from 0 to 1 and the argon mole fraction typically ranges from 0 to 0.2. The combination of the grid requirements and the mole fraction ranges causes the sum of the mole fractions to exceed 1 in some cases. In order to constrain the bubble point to data to realistic values, a normalisation of the mole fractions is executed prior to the calculation of the bubble point. It is therefore also necessary to 'un-normalize' the input mole fractions before they are used as input to interpolate in the pre-generated table. It has been verified that this procedure does not affect the accuracy of the bubble point data. Interpolation at the grid point values yielded exactly the tabulated values of the grid points.
The strategy proves to decrease the simulation time considerably in practise. The simulation of a distillation column with 18 trays requiring 41 iterations now takes only 23 seconds. So the simulation is about 50 times faster if a table with pre-generated bubble point data is used. A three-dimensional table with 7 pressure grid points, 21 argon mole fraction grid points and 51 oxygen (and nitrogen) grid points has been used for this particular simulation. The average difference between interpolated off-grid values and their corresponding calculated values is $5 \cdot 10^{-4}\%$ of the calculated value, so the interpolated values are fairly accurate. If desired, the accuracy of the interpolation results can be increased by adding more grid points, but this will also slow the simulation somewhat down.

A.5 Comparing Matlab model results to literature

This section compares the results of the Matlab model that has been developed to execute the calculation discussed in Section A.4 to literature values of the calculated

properties as reported by Lemmon et al. [2000], and to two cubic equations of state. Section A.5.1 compares the results for the single phase thermodynamic properties of air and Sections A.5.2 and A.5.3 compare vapour–liquid equilibrium results of air. In order to compare calculated values to reference values, Lemmon et al. use the average absolute deviation (AAD), which is defined as

$$AAD = \frac{1}{n}\sum_{i=1}^{n}\left|1 - \frac{X_i^{calc}}{X_i^{ref}}\right| \tag{A.42}$$

Here, X is any thermodynamic property. When fitting a model to experimental data, the superscript ref refers to the experimental value. In the current work, this superscript refers to the literature values reported by Lemmon et al..

A.5.1 Single phase thermodynamic properties of air

The performance of the developed Matlab model has been assessed in the state space region that is most relevant for air distillation; temperatures between 60 and 120 K, at intervals of 10 K, and pressures of 1 atm, 2 bar, 5 bar and 10 bar. Because the model is explicit in density and not in pressure, the first step of each calculation was to find the density that corresponds to the required pressure and temperature. The next step was to calculate the isochoric heat capacity, the isobaric heat capacity, the speed of sound, the internal energy, the enthalpy and the entropy at the specified temperature and the found density. All calculations use the composition of air as given in Table A.1. An overview of the calculation results is given in Section A.C. A summarized comparison of these results to the literature values is shown in Table A.4.

Table A.4: Overview of the average absolute deviations for thermodynamic properties of air

P (Pa)	101325	200000	500000	1000000	Combined	Literature
AAD in ρ	0.0004	0.0004	0.0004	0.0003	0.0004	0.0010
AAD in u	0.0009	0.0007	0.0005	0.0004	0.0006	0.0010
AAD in h	0.0007	0.0006	0.0005	0.0004	0.0005	0.0010
AAD in s	0.0005	0.0005	0.0004	0.0004	0.0004	0.0010
AAD in C_v	0.0067	0.0096	0.0116	0.0108	0.0097	0.0078
AAD in C_p	0.0051	0.0074	0.0082	0.0067	0.0069	0.0175
AAD in w	0.0033	0.0031	0.0035	0.0039	0.0035	0.0045
AAD	0.0025	0.0032	0.0036	0.0033	0.0031	0.0048

Table A.4 shows the average absolute deviations for each thermodynamic property at different pressures. Each value is the average over the entire temperature range, including both liquid and vapour phases. The average over all thermodynamic properties is given in the last column. At the bottom of the table, the averages over all

pressures are given as well; they can be compared to the shown literature values. The AADs of the isochoric heat capacity and the velocity of sound are comparable, but the AADs for the other calculated thermodynamic properties are about half of the literature values. This means that in the worst case the accuracy of the Matlab model calculations is only slightly lower than the accuracy of the literature values.

A.5.2 Bubble and dew point pressures of air

The performance of the vapour–liquid part of the developed Matlab model has been assessed by comparing calculated bubble and dew point pressures to literature values. These literature values are not obtained by a method similar to the method used in this work; they are obtained using ancillary equations that have been fitted to experimental data. Table A.5 shows a comparison between the literature and calculated values of the bubble and dew point pressures at various temperatures, along with the absolute deviations (AD), which is the non-averaged AAD.

Table A.5: Overview of the literature (Lit.) and calculated (Calc.) bubble and dew point pressures

T (K)	P_{bub} (MPa)			P_{dew} (MPa)		
	Lit.	Calc.	AD	Lit.	Calc.	AD
60	0.00555	0.00555	0.0008	0.00258	0.00261	0.0106
65	0.01432	0.01432	0.0003	0.00776	0.00781	0.0063
70	0.03191	0.03191	0.0000	0.01943	0.01950	0.0036
75	0.06333	0.06333	0.0000	0.04228	0.04231	0.0007
80	0.11462	0.11461	0.0001	0.08232	0.08223	0.0012
85	0.19262	0.19266	0.0002	0.14665	0.14627	0.0026
90	0.30475	0.30478	0.0001	0.24320	0.24226	0.0039
95	0.45886	0.45882	0.0001	0.38047	0.37887	0.0042
100	0.66313	0.66319	0.0001	0.56742	0.56484	0.0046
105	0.92606	0.92534	0.0008	0.81341	0.80952	0.0048
110	1.25642	1.25441	0.0016	1.12824	1.12265	0.0050
115	1.66327	1.65902	0.0026	1.52226	1.51475	0.0050
120	2.15573	2.14825	0.0035	2.00674	1.99777	0.0045
AAD	-	-	0.0008	-	-	0.0044

The absolute deviations averaged over all temperatures are given at the bottom of the table. The accuracy of the literature values for the bubble point pressures that is given by Lemmon et al. amounts 0.0057. So the Matlab model, which is based on the mixture model described in Section A.3, performs well compared to the literature values, which are obtained from an equation explicitly fitted for the bubble point pressure of air as a function of temperature.

A.5.3 Comparison to SRK and PRSV-LK equations of state

It is also interesting to get an idea about how the empirical Helmholtz based model discussed in this work behaves compared to cubic equations of state that are commonly used in commercial simulation software. Therefore, a comparison has been made to the Soave–Redlich–Kwong equation of state (SRK), and to the Peng–Robinsons equation of state modified by Stryjek and Vera and using Lee–Kessler vapour pressures (PRSV-LK).
A basic air distillation column is used as basis for the comparison. In this way, a good representation of the compositions and temperatures relevant for air distillation is obtained. The column is modelled using Aspen HYSYS 2006. It has 16 trays, a total condenser (tray 0) and a reboiler (tray 17). It operates at a constant pressure of and the vapour phase feed is added to the column at tray 10. An oxygen recovery of 98% and an oxygen purity of 95% are used as specifications.
First, the column is solved twice in HYSYS, using the SRK and the PRSV-LK equations of state. The resulting liquid and vapour phase compositions are then used to calculate bubble and dew point temperatures and compositions using the Matlab routines discussed in Section A.4.2. The differences between the calculated temperatures give an indication about how the models differ.
Figure A.1 shows the temperature differences for the liquid and vapour phases between the empirical Helmholtz based equation of state and the SRK equation of state, Figure A.2 shows the differences between the Helmholtz based equation of state and the PRSV-LK equation of state.
Both figures show the largest temperature differences in the middle part of the column, at the columns' tops and bottoms the differences are the smallest. At the feed stage, the compositions inside the column are almost equal to the composition of air. Because the empirical Helmholtz based model is especially accurate for this composition, it is most likely that the temperature differences are caused by the inaccuracy of the cubic equations of state when used for multi-component mixtures. Near the columns' tops and bottoms the compositions change towards a binary mixtures and pure components, this is why the temperature differences can become smaller.

A.6 Conclusion

A modern empirical equation of state for mixtures of nitrogen, argon and oxygen has successfully been implemented in a Matlab model. The equation of state is explicit in Helmholtz energy and describes the real mixing properties as an excess Helmholtz energy. The Matlab model can be used to calculate various single phase thermodynamic properties and vapour–liquid equilibrium conditions. The accuracy of the Matlab model is comparable to the accuracy of the literature model that is used as basis. The average absolute deviation of the relevant single phase thermodynamic properties is below 0.1% and the average absolute deviation of the vapour–liquid equilibrium conditions is below 0.5%. The Matlab model is suitable for use during the design of an air distillation column. The differences between the empirical equations of state and cubic equations of state are the largest for multi component mixtures.

Figure A.1: Comparison between vapour and liquid phase temperatures of the empirical Helmholtz based equation of state and the Soave–Redlich–Kwong equation of state.

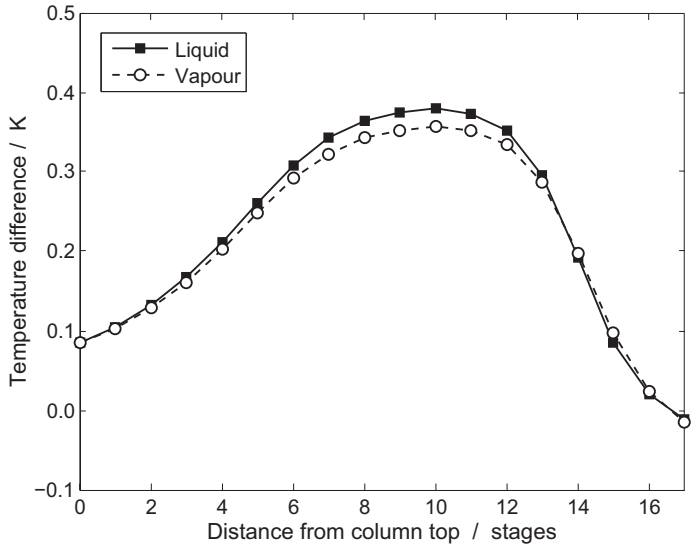

Figure A.2: Comparison between vapour and liquid phase temperatures of the empirical Helmholtz based equation of state and the modified Peng–Robinsons equation of state by Stryjek & Vera with Lee–Kessler vapour pressures.

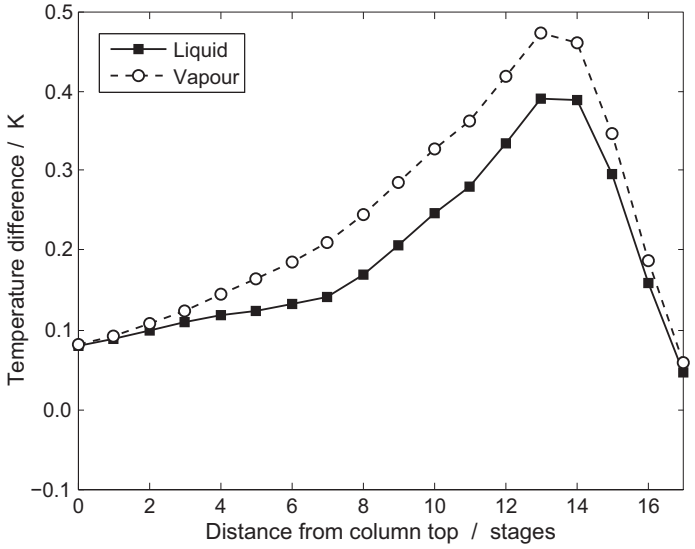

A.A Matlab code for a bubble point pressure calculation

```
function [ Pbub, yi ] = FIND_Pbub( T, zi )
%Bubble point pressure and vapour composition
% This function calculates the bubble point pressure [Pa] and mole fractions
% in the vapour phase [-] for a given temperature [K] and overall mole
% fractions [-] (which are equal tot the mole fractions in the liquid phase).

global k

% A rough estimate for the mixture's boiling pressure at the given
% temperature is obtained using the saturated vapour pressures. This
% pressure is used to generate estimates for the bubble point pressure.
xi = zi;
Pb = sum(CALC_Psati(T).*xi);

% A quite accurate value for the bubble point pressure is obtained by
% calculating the errors in chemical potentials for multiple pressure
% estimates, and interpolating at which pressure the error becomes zero.
% Because the error is an almost linear function of the pressure, two
% estimates are sufficient. More estimates can be added to increase the
% accuracy, but it also increases the calculation time.
Pb = linspace(0.8*Pb,Pb,2);
for i = 1:length(Pb)
    [yi(i,:),dx(i)] = FIND_yi(T,Pb(i),xi);
end
Pbub = spline(dx,Pb,0);

% The accuracy of the estimated bubble point pressure is checked, and if
% needed a more accurate value is obtained. In practice only one or even
% zero updates are required.
iter = 0;
cnv = 0;
while iter < 5 && ~cnv
   [yi,dx] =  FIND_yi(T,Pbub,xi);
   if abs(dx) < 1E-4
        cnv = 1;
   else
        Pbub(2) = Pbub*1.01;
        [yi(2,:),dx(2)] =  FIND_yi(T,Pbub(2),xi);
        Pbub = spline(dx,Pbub,0);
   end
   iter = iter + 1;
end

% Display a warning message if the calculation did not converge properly
if dx > 1E-4
    disp('Warning: unconverged bubble point pressure.')
end
```

```
function [ yi, dx ] = FIND_yi( T, P, xi )
%Vapour phase mole fractions and total deviation in chemical potentials
% This function finds the vapour phase composition that is in equilibrium with
% given liquid phase mole fractions [-] at given temperature [K] and
% pressure [Pa]. The found numbers of moles in the vapour phase are normalised
% to yield the vapour phase mole fractions [-] and the total deviation between
% the chemical potential of the liquid and vapour phase [-] is calculated.
% This function is used in FIND_Pbub and FIND_Tbub.

global k

% Initialise some variables
n_l = xi;                           % number of moles in the liquid phase
rho_l = FIND_rhol(T,P,xi);          % molar density in the liquid phase
V_l = sum(n_l) / rho_l;             % volume of the liquid phase
mu_l = CALC_dAdni(T,V_l,n_l)';      % chemical potential of the liquid phase
yi = xi;                            % vapour phase mole fractions
n_g = yi;                           % number of moles in vapour phase
rho_g = FIND_rhog(T,P,yi);          % molar density in the vapour phase
V_g = sum(n_g) / rho_g;             % volume of the vapour phase

% Find the equilibrium compositions using Newton steps
iter = 0;
cnv = 0;
while iter < 10 && ~cnv
    mu_g = CALC_dAdni(T,V_g,n_g)';
    if max(abs(1-mu_g./mu_l)) < 1E-4
        cnv = 1;
    else
        d2Adn2 = CALC_d2Adni2(T,V_g,n_g);
        dn = -(d2Adn2\(mu_g-mu_l));
        for i = 1:length(dn)
            while n_g(i) ~=0 && n_g(i)+dn(i) <= 1E-8
                  dn = dn*0.2;
                  disp('reduce step size to 20 percent of old value');
            end
        end
        n_g = n_g + dn';
        iter = iter + 1;
    end
end
% Normalise the found solution
yi = n_g / sum(n_g);

% Calculate the error when using new mole fractions
n_g = yi;
rho_g = FIND_rhog(T,P,yi);
V_g = sum(n_g) / rho_g;
mu_g = CALC_dAdni(T,V_g,n_g)';
dx = sum(1-mu_g./mu_l);
```

A.B Matlab code for a flash calculation

```
function [ yi, xi, f_g, cnv ] = FLASH( T, P, zi, varargin )
%Vapour and liquid phase mole fractions, and molar gas fraction
% This function finds the equilibrium compositions for a mixture of given
% total composition at specified temperature [K] and pressure [Pa]. First a
% rough initial guess of the molar gas fraction is calculated, using the
% bubble and dew point temperatures. An initial guess for the distribution
% of a fixed number of moles over the phases and components is made, as
% well as for the volumes. Equilibrium conditions are solved based on equal
% chemical potentials and that both pressures should be equal to the target
% pressure. The volumes and mole numbers are updated using newton steps.

global k

% The total number of moles in the system
ntot = 1000;

% The bubble and dew point conditions can either be provided as input to
% the function in order to save time or they can be calculated.
if nargin > 3
    Tbub = varargin{1};
    yi_bub = varargin{2};
    Tdew = varargin{3};
    xi_dew = varargin{4};
else
    [Tbub, yi_bub] = FIND_Tbub(P,zi);
    [Tdew, xi_dew] = FIND_Tdew(P,zi);
end

% Check whether the given conditions are inside the two-phase region. If
% so, estimates for the vapour and liquid phase mole compositions are
% calculated, based on the estimated molar gas fraction.
if T < Tbub
    disp('Warning: conditions out two-phase region, single liquid phase');
    yi = [0,0,0];
    xi = zi;
    f_g = 0;
    cnv = -1;
    return
elseif T > Tdew
    disp('Warning: conditions out two-phase region, single gas phase');
    yi = zi;
    xi = [0,0,0];
    f_g = 1;
    cnv = -1;
    return
else
    f_g = ((T - Tbub) / (Tdew - Tbub))^0.6;
    if f_g < 0.5
        yi = zi + (yi_bub-zi)*(1-f_g);
        n_g = ntot*yi*f_g;
        n_l = ntot*zi - n_g;
        xi = n_l / sum(n_l);
    else
        xi = zi + (xi_dew-zi)*(f_g);
        n_l = ntot*xi*(1-f_g);
        n_g = ntot*zi - n_l;
        yi = n_g / sum(n_g);
    end
end
```

```
% Estimates for the volumes using the molar densities
rho_g = FIND_rhog(T,P,yi);
rho_l = FIND_rhol(T,P,xi);
V_g = sum(n_g) / rho_g;
V_l = sum(n_l) / rho_l;

% Find the equilibrium volumes and compositions at the specified pressure,
% using Newton steps.
iter = 0;
cnv = 0;
while iter < 15 && ~cnv
    P_g = -CALC_dAdV(T,V_g,n_g);
    P_l = -CALC_dAdV(T,V_l,n_l);
    mu_g = CALC_dAdni(T,V_g,n_g)';
    mu_l = CALC_dAdni(T,V_l,n_l)';
    if abs(P-P_g) < 1 && abs(P-P_l) < 1 && iter > 0 && max(abs(1-mu_g./mu_l)) < 1E-3
        cnv = 1;
    else
        g1 = [-P_g;-P;mu_g];
        H1 = [CALC_d2AdV2(T,V_g,n_g),0,CALC_d2AdVdni(T,V_g,n_g); ...
              0,0,0,0,0,;                                        ...
              CALC_d2AdVdni(T,V_g,n_g)',[0;0;0],CALC_d2Adni2(T,V_g,n_g)];
        g2 = [-P;-P_l;mu_l];
        H2 = [0,0,0,0,0,;                                        ...
              0,CALC_d2AdV2(T,V_l,n_l),CALC_d2AdVdni(T,V_l,n_l); ...
              [0;0;0],CALC_d2AdVdni(T,V_l,n_l)',CALC_d2Adni2(T,V_l,n_l)];
        dg = (g1 - g2);
        H = H1 + H2;
        dx = -(H\dg);
        st1 = [V_g,V_l,n_g];
        st2 = [V_g,V_l,n_l];
        for i = 3:length(dx)
            while st1(i)+dx(i) <= 1E-8 || st2(i)-dx(i) <= 1E-8
                  dx = dx*0.2;
                  disp('reduce step size to 20 percent of old value');
            end
        end
        V_g = V_g + dx(1);
        V_l = V_l - dx(2);
        if V_g < 0 || V_l < 0
            disp('Warning: negative volume encountered');
        end
        n_g = n_g + dx(3:end)';
        n_l = n_l - dx(3:end)';
        iter = iter + 1;
    end
end

% Return results
yi = n_g / sum(n_g);    % vapour phase mole fractions
xi = n_l / sum(n_l);    % liquid phase mole fractions
f_g = sum(n_g) / ntot;  % molar gas fraction

% Display a warning message if the calculation did not converge properly
if ~cnv
    disp('Warning: unconverged flash calculation')
end
```

A.C Single phase thermodynamic properties

Table A.6: Single phase thermodynamic properties of air at $P = 1$ atm.

T (K)	ρ $\left(\frac{mol}{dm^3}\right)$	u $\left(\frac{J}{mol}\right)$	h $\left(\frac{J}{mol}\right)$	s $\left(\frac{J}{molK}\right)$	C_v $\left(\frac{J}{molK}\right)$	C_p $\left(\frac{J}{molK}\right)$	w $\left(\frac{m}{s}\right)$
60.00	33.039	-6566.7	-6563.6	26.807	33.74	54.92	1043.8
70.00	31.590	-6016.0	-6012.8	35.298	31.76	55.31	952.2
78.90	30.220	-5520.9	-5517.6	41.957	30.27	56.07	867.6
81.72	0.15504	-241.3	412.2	116.094	21.35	31.01	177.4
90.00	0.13938	-60.9	666.0	119.053	21.11	30.39	187.3
100.00	0.12446	153.7	967.8	122.233	20.99	29.99	198.3
110.00	0.11256	366.1	1266.3	125.078	20.91	29.74	208.6
120.00	0.10281	577.2	1562.8	127.658	20.85	29.57	218.3

Table A.7: Single phase thermodynamic properties of air at $P = 2$ bar.

T (K)	ρ $\left(\frac{mol}{dm^3}\right)$	u $\left(\frac{J}{mol}\right)$	h $\left(\frac{J}{mol}\right)$	s $\left(\frac{J}{molK}\right)$	C_v $\left(\frac{J}{molK}\right)$	C_p $\left(\frac{J}{molK}\right)$	w $\left(\frac{m}{s}\right)$
60.00	33.044	-6567.5	-6561.4	26.795	33.75	54.90	1044.4
70.00	31.597	-6017.0	-6010.7	35.283	31.77	55.29	952.8
80.00	30.053	-5460.6	-5453.9	42.716	30.11	56.18	857.7
85.39	29.165	-5155.9	-5149.0	46.405	29.34	57.03	804.7
87.99	0.29156	-148.9	537.0	112.192	21.71	32.36	181.5
90.00	0.28376	-103.1	601.7	112.919	21.59	32.04	184.1
100.00	0.25111	120.2	916.7	116.239	21.28	31.06	195.9
110.00	0.2258	338.5	1224.2	119.171	21.11	30.50	206.8
120.00	0.20545	553.8	1527.3	121.808	21.00	30.13	216.9

Table A.8: Single phase thermodynamic properties of air at $P = 5$ bar.

T (K)	ρ $\left(\frac{mol}{dm^3}\right)$	u $\left(\frac{J}{mol}\right)$	h $\left(\frac{J}{mol}\right)$	s $\left(\frac{J}{molK}\right)$	C_v $\left(\frac{J}{molK}\right)$	C_p $\left(\frac{J}{molK}\right)$	w $\left(\frac{m}{s}\right)$
60.00	33.060	-6569.8	-6554.6	26.756	33.76	54.87	1046.1
70.00	31.617	-6020.1	-6004.3	35.239	31.79	55.24	954.7
80.00	30.079	-5464.8	-5448.2	42.663	30.13	56.10	860.1
90.00	28.401	-4896.8	-4879.2	49.363	28.75	57.91	760.9
96.12	27.270	-4537.6	-4519.3	53.232	28.06	59.88	695.8
98.36	0.69445	-35.8	684.2	106.834	22.66	36.30	185.5
100.00	0.67801	5.7	743.2	107.429	22.47	35.67	187.9
110.00	0.59595	247.9	1086.8	110.706	21.81	33.36	200.9
120.00	0.53467	478.6	1413.8	113.551	21.47	32.13	212.5

Table A.9: Single phase thermodynamic properties of air at $P = 10$ bar.

T (K)	ρ $\left(\frac{mol}{dm^3}\right)$	u $\left(\frac{J}{mol}\right)$	h $\left(\frac{J}{mol}\right)$	s $\left(\frac{J}{molK}\right)$	C_v $\left(\frac{J}{molK}\right)$	C_p $\left(\frac{J}{molK}\right)$	w $\left(\frac{m}{s}\right)$
60.00	33.085	-6573.6	-6543.4	26.692	33.78	54.82	1048.9
70.00	31.649	-6025.3	-5993.7	35.165	31.81	55.16	957.8
80.00	30.122	-5471.8	-5438.6	42.575	30.16	55.96	864.0
90.00	28.461	-4906.6	-4871.5	49.254	28.78	57.67	766.1
100.00	26.581	-4317.0	-4279.4	55.489	27.70	61.18	659.2
106.22	25.224	-3926.7	-3887.0	59.294	27.21	65.37	584.3
108.10	1.38310	6.9	730.0	102.412	24.08	43.69	185.8
110.00	1.33793	63.8	811.2	103.157	23.63	41.90	189.2
120.00	1.15664	336.6	1201.2	106.554	22.46	36.89	204.3

Bibliography

Agrawal, R., Woodward, D. W., 1991. Efficient cryogenic nitrogen generators: An exergy analysis. Gas Separation and Purification 5, 139–150.

Agrawal, R., Woodward, D. W., Ludwig, K. A., Bennett, D. L., 1993. Impact of low pressure drop structure packing on air distillation. Institution of Chemical Engineers Symposium Series 128, A125–A138.

Arman, B., Nguyen, T. C., Bonaquist, D. P., Wong, K. K., 2001. Cryogenic air separation system using an integrated core. US Patent 6237366.

Asami, T., 1990. Thermodynamic properties of argon calculated from the BWR equation of state with eight newly determined coefficients. Cryogenics 30, 968–971.

Asami, T., Ebisu, H., 1989. Thermodynamic properties of nitrogen calculated from the BWR equation of state. Cryogenics 29, 995–997.

Asami, T., Ebisu, H., 1990. Thermodynamic properties of oxygen calculated from the BWR equation of state with eight newly determined coefficients. Cryogenics 30, 113–115.

Asano, K., 2006. Mass transfer. From fundamentals to modern industrial applications. Wiley-VCH.

Bedeaux, D., Kjelstrup, S., 2004. Irreversible thermodynamics – a tool to describe phase transitions far from global equilibrium. Chemical Engineering Science 59, 109–118.

Bejan, A., 1982. Entropy generation through heat and fluid flow. Wiley, New York, United States of America.

Bejan, A., Tsatsaronis, G., Moran, M., 1996. Thermal design and optimization. Wiley, New York, United States of America.

Biddulph, M. W., 1975. Multicomponent distillation simulation – distillation of air. AIChE Journal 21, 327–335.

Bolland, O., Booth, N., Franco, F., Machhi, E., Manzoli, G., Naqvi, R., Pfeffer, A., Rezvani, S., Abu Zara, M., May 2009. Common framework definition document. Deliverable 1.4.1, DECARBit project, public report.

Briesch, M. S., Deen, P. G., Sullivan, T. B., 2007. Advanced integration for improved integrated gasification combined cycle efficiency. US Patent 20070181854.

Brugerolle, J. R., Ha, B., 2009. Thermal integration of oxygen plants. US Patent 20090178408.

Cabrera-Ruiz, J., Jiménez-Gutiérrez, A., Segovia-Hernández, J. G., 2011. Assessment of the implementation of heat-integrated distillation columns for the separation of ternary mixtures. Industrial & Engineering Chemistry Research 50, 2176–2181.

Campbell, J. C., Wigal, K. R., Van Brunt, V., Kline, R. S., 2008. Comparison of energy usage for the vacuum separation of acetic acid/acetic anhydride using an internally heat integrated distillation column (HIDiC). Separation Science and Technology 43, 2269–2297.

Castle, W. F., 2002. Air separation and liquefaction: recent developments and prospects for the beginning of the new millenium. International Journal of Refrigeration 25, 158–172.

CEN, 2002. EN 13648-3. Cryogenic vessels – Safety devices for protection against excessive pressure – Part 3: Determination of required discharge – Capacity and sizing. Comité Européen de Normalisation, Brussels, Belgium.

CEN, 2004. EN ISO 4126-1. Safety devices for protection against excessive pressure – Part 1: Safety valves. Comité Européen de Normalisation, Brussels, Belgium.

Chen, H., Huang, K., Wang, S., 2010. A novel simplified configuration for an ideal heat-integrated distillation column (ideal HIDiC). Separation and Purification Technology 73, 230–242.

Cipolla Jr., J. W., Lang, H., Loyalka, S. K., 1974. Kinetic theory of condensation and evaporation II. Journal of Chemical Physics 61 (1), 69–77.

Clarke, W., Jacobsen, R., Beyerlein, S., Penoncello, S., 1993. An Extended corresponding states model for predicting thermodynamic properties of the N2-Ar-O2 mixture. Fluid Phase Equilibria 88, 13–24.

Cornelissen, R. L., 1997. Thermodynamics of sustainable development - The use of exergy analysis and the reduction of irreversibility. Ph.D. thesis, Universiteit Twente, Enschede, The Netherlands.

Darde, A., Prabhakar, R., Tranier, J. P., Perrin, N., 2009. Air separation and flue gas compression and purification units for oxy-fuel combustion systems. Energy Procedia 1, 527–534.

Dawson, B. K., Siegmund, S. C., Yonggui, Z., 2004. Flowsheet optimization for multi-product air separation units. In: Proceedings of the 1st Baosteel Annual Academic Conference; Shanghai, China, 27-28 May 2004.

De Groot, S. R., Mazur, P., 1962. Non-equilibrium thermodynamics. North-Holland publishing company, Amsterdam, the Netherlands.

De Koeijer, G. M., 2002. Energy efficient operation of distillation columns and a reactor applying irreversible thermodynamics. Ph.D. thesis, Norwegian University of Science and Technology, Trondheim, Norway.

De Koeijer, G. M., Kjelstrup, S., 2004. Application of Irreversible Thermodynamics to Distillation. International Journal of Thermodynamics 7 (3), 107–114.

De Koeijer, G. M., Kjelstrup, S., Salamon, P., Siragusa, G., Schaller, M., Hoffmann, K. H., 2002. Comparison of Entropy Production Rate Minimization Methods for Binary Diabatic Distillation. Industrial & Engineering Chemical Research 41, 5826–5834.

De Koeijer, G. M., Røsjorde, A., Kjelstrup, S., 2004. Distribution of heat exchange in optimum diabatic distillation columns. Energy 29, 2425–2440.

De Rijke, A., 2007. Development of a concentric internally heat integrated distillation column. Ph.D. thesis, Delft University of Technology, Delft, The Netherlands.

Egoshi, N., Kawakami, H., Asano, K., 1999. Mass transfer in ternary distillation of nitrogen–argon–oxygen system in wetted-wall column. Journal of Chemical Engineering of Japan 32, 409–416.

Egoshi, N., Kawakami, H., Asano, K., 2000. Mass transfer in binary distillation of nitrogen–oxygen and argon–oxygen systems by packed column with structured packings. Journal of Chemical Engineering of Japan 33, 245–252.

Egoshi, N., Kawakami, H., Asano, K., 2001. Heat and mass transfer model approach to prediction of separation performance of cryogenic air separation plant by packed columns with structured packing. Journal of Chemical Engineering of Japan 34, 22–29.

Egoshi, N., Kawakami, H., Asano, K., 2002. Heat and mass transfer model approach to optimum design of cryogenic air separation plant by packed columns with structured packing. Separation and Purification Technology 29, 141–151.

Egoshi, N., Kusuno, T., Kawakami, H., 1997. Mass transfer in binary distillation of nitrogen–oxygen and argon–oxygen systems in a wetted-wall column. Journal of Chemical Engineering of Japan 30, 7–12.

Emun, F., Gadalla, M., Majozi, T., Boer, D., 2010. Integrated gasification combined cycle (IGCC) process simulation and optimization. Computers and Chemical Engineering 34, 331–338.

Estela-Uribe, J., 2006. A Helmholtz energy model for air and binary mixtures of nitrogen, oxygen and argon. Fluid Phase Equilibria 243, 171–182.

Fonyó, Z., 1974a. Thermodynamic analysis of rectification I. Reversible model of rectification. International Chemical Engineering 14, 18–27.

Fonyó, Z., 1974b. Thermodynamic analysis of rectification II. Finite cascade models. International Chemical Engineering 14, 203–210.

Freshwater, D. C., 1951. Thermal economy in distillation. Transactions of the Institution of Chemical Engineers 29, 149–160.

Frey, H. C., Zhu, Y., 2006. Improved system integration for Integrated Gasification Combined Cycle (IGCC) systems. Environmental Science and Technology 40 (5), 1693–1699.

Glavatskiy, K., 2009. Multicomponent interfacial transport as described by the square gradient model; evaporation and condensation. Ph.D. thesis, Norwegian University of Science and Technology, Trondheim, Norway.

Günster, W., Wolf, E., Zimmermann, G., 2010. Method for increasing the efficiency of a combined gas/steam power station with integrated gasification combined cycle. US Patent 20100146929.

Goharshadi, E., Moosavi, M., 2008. Prediction of thermodynamic properties of liquid air. International Journal of Thermophysics 29, 656–663.

Hausen, H., Linde, H., 1985. Tieftemperaturtechnik: Erzeugung sehr tiefer Temperaturen, Gasverflüssigung und Zerlegung von Gasgemischen. Springer-Verlag, Berlin, Germany.

Higginbotham, P., Agrawal, R., Herron, D. M., 2001. Process for the production of oxygen and nitrogen. US Patent 6227005.

Hirschfelder, J. O., Curtiss, C. F., Bird, R. B., 1964. Molecular theory of gases and liquids. Structure of Matter Series. Wiley, New York, USA.

Horiuchi, K., Yanagimoto, K., Kataoaka, K., Nakaiwa, M., Iwakabe, K., Matsuda, K., 2008. Energy saving characteristics of the internally heat integrated distillation column (HIDiC) pilot plant for multicomponent petroleum distillation. Journal of Chemical Engineering of Japan 41, 771–778.

Huang, K., Shan, L., Zhu, Q., Qian, J., 2007. Design and control of an ideal heat-integrated distillation column (ideal HIDiC) system separating a close-boiling ternary mixture. Energy 32, 2148–2156.

Huber, M., Hiltbrunner, R., 1966. Füllkörperrektifizierkolonnen mit Maldistribution. Chemical Engineering Science 21 (9), 819–832.

Hwang, S.-C., 1987. Vapor-liquid equilibrium calculations for N2-Ar-O2 mixtures with modified B-W-R equation of state and a corresponding state principle. Fluid Phase Equilibirua 37, 153–167.

Ibbs, T. L., Grew, K. E., Hirst, A. A., 1929. Thermal diffusion at low temperatures. Proceedings of the Physical Society 41, 456–475.

IEC, 1998. International Standard 60534-2-1. Industrial-process control valves – Part 2-1: Flow-capacity – Sizing equations for fluid flow under installed conditions. International Electrotechnical Commission, Geneva, Switzerland.

International Energy Agency, 2010. CO_2 emissions from fuel combustion - 2010 Edition. IEA Statistics. International Energy Agency, Paris, France.

Iwakabe, K., Nakaiwa, M., Huang, K., Matsuda, K., Nakanishi, T., Ohmori, T., Endo, A., Yamamoto, T., 2006a. An internally heat-integrated distillation column (HIDiC) in Japan. In: Distillation and Absorption 2006. pp. 900–911.

Iwakabe, K., Nakaiwa, M., Huang, K., Nakanishi, T., Røsjorde, A., Ohmori, T., Endo, A., Yamamoto, T., 2006b. Energy saving in multicomponent separation using an internally heat-integrated distillation column (HIDiC). Applied Thermal Engineering 26, 1362–1368.

Iwakabe, K., Nakaiwa, M., Huang, K., Nakanishi, T., Røsjorde, A., Ohmori, T., Endo, A., Yamamoto, T., 2006c. Performance of an internally heat-integrated distillation column (HIDIC) in separation of ternary mixtures. Journal of Chemical Engineering of Japan 39, 417–425.

Jacobsen, R., Penoncello, S., Lemmon, E., 1997. Thermodynamic properties of cryogenic fluids. Plenum Press, New York, USA.

Jimenez, E. S., Salamon, P., Rivero, R., Rendon, C., Hoffmann, K. H., Schaller, M., Andresen, B., 2004. Optimization of a diabatic distillation column with sequential heat exchangers. Industrial & Engineering Chemistry Research 43, 7566–7571.

Johannessen, E., 2004. The state of minimum entropy production in an optimally controlled system. Ph.D. thesis, Norwegian University of Science and Technology, Trondheim, Norway.

Johannessen, E., Kjelstrup, S., 2004. Minimum entropy production in plug flow reactors: An optimal control problem solved for SO_2 oxidation. Energy 29, 2403–2423.

Johannessen, E., Kjelstrup, S., 2005. A highway in state space for reactors with minimum entropy production. Chemical Engineering Science 60 (12), 3347–3361.

Johannessen, E., Røsjorde, A., 2007. Equipartition of entropy production as an approximation to the state of minimum entropy production in diabatic distillation. Energy 32, 467–473.

Kempers, L. J. T. M., 2001. A comprehensive thermodynamic theory of the Soret effect in a multicomponent gas, liquid, or solid. Journal of Chemical Physics 115 (14), 6330–6341.

Kerry, F. G., 2007. Industrial Gas Handbook: Gas Separation and Purification. CRC Press, Boca Raton, Florida, USA.

Kister, H. Z., 1990. Distillation Operation. McGraw-Hill, New York, United States of America.

Kjelstrup, S., Bedeaux, D., 2008. Non-equilibrium thermodynamics of heterogeneous systems. World Scientific Publishing, Singapore.

Kjelstrup, S., Bedeaux, D., Johannessen, E., Gross, J., 2010. Elements of Irreversible Thermodynamics for Engineers. World Scientific Publishing, Singapore.

Kjelstrup, S., De Koeijer, G. M., 2003. Transport equations for distillation of ethanol and water from the entropy production rate. Chemical Engineering Science 58, 1147–1161.

Kjelstrup Ratkje, S., Sauar, E., Hansen, E., Lien, K., Hafskjold, B., 1995. Analysis of entropy production rates for design of distillation columns. Industrial & Engineering Chemistry Research 34 (9), 3001–3007.

Kotas, T. J., 1985. The exergy method of thermal plant analysis. Butterworths, London, United Kingdom.

Krishnamurty, R., Andrecovich, M. J., 1989. Application of a nonequilibrium stage model to cryogenic process simulation. In: Proceedings of the International Symposium on Gas Separation Technology; Antwerp, Belgium, 10-15 September 1989. pp. 599–608.

Latimer, R. E., 1967. Distillation of air. Chemical Engineering Progress 63 (2), 35–59.

Leites, I. L., Sama, D. A., Lior, N., 2003. The theory and practice of energy saving in the chemical industry: some methods for reducing thermodynamic irreversibility in chemical technology processes. Energy 28 (1), 55–97.

Lemmon, E., Jacobsen, R., 1999. A generalized model for the thermodynamic properties of mixtures. International Journal of Thermophysics 20, 825–835.

Lemmon, E. W., Jacobsen, R. T., 2004. Viscosity and thermal conductivity equations for nitrogen, oxygen, argon, and air. International Journal of Thermophysics 25 (1), 21–69.

Lemmon, E. W., Jacobsen, R. T., Penoncello, S. G., Friend, D. G., 2000. Thermodynamic properties of air and mixtures of nitrogen, argon, and oxygen from 60 to 2000 K at pressures to 2000 MPa. Journal of Physical Chemistry 29 (3), 331–385.

Liu, X., Qian, J., 2000. Modeling, control, and optimization of ideal internal thermally coupled distillation columns. Chemical Engineering and Technology 23, 235–241.

Mah, R. S. H., Nicholas, Jr., J. J., Wodnik, R. B., 1977. Distillation with secondary reflux and vaporization: A comparative evaluation. AIChE Journal 23, 651–658.

Matsuda, K., Iwakabe, K., Huang, K., Nakaiwa, M., Nakanishi, T., Kataoka, K., Takamatsu, T., Ohmori, T., Endo, A., Yamamoto, T., Kataoka, S., 2006. Simulation of Ternary Distillation in a Heat Integrated Distillation Column (HIDiC) with a Rate-Based model. Journal of the Chinese Institute of Chemical Engineers 37 (5), 467–474.

Mendoza, D. F., Kjelstrup, S., 2011. Modeling a non-equilibrium distillation stage using irreversible thermodynamics. Chemical Engineering Science 66, 2713–2722.

Naito, K., Nakaiwa, M., Huang, K., Endo, A., Aso, K., Nakanishi, T., Nakamura, T., Noda, H., Takamatsu, T., 2000. Operation of a bench-scale ideal heat integrated distillation column (HIDiC): an experimental study. Computers and Chemical Engineering 24, 495–499.

Nakaiwa, M., Akiya, T., Owa, M., Tanaka, Y., 1996. Evaluation of an energy supply system with air separation. Energy Conversion and Management 37, 295–301.

Nakaiwa, M., Huang, K., Endo, A., Ohmori, T., Akiya, T., Takamatsu, T., 2003. Internally heat-integrated distillation columns: a review. Chemical Engineering Research and Design 81, 162–177.

Nakaiwa, M., Huang, K., Owa, M., Akiya, T., Nakane, T., Sato, M., Takamatsu, T., 1997. Energy savings in heat-integrated distillation columns. Energy 22, 621–625.

Nakaiwa, M., Ohmori, T., 2009. Innovation in distillation processes: Process intensification for energy savings through concept of "detuning" from ideal state. Synthesiology - English edition 2 (1), 55–63.

Nakanishi, T., Adachi, N., Nishida, N., Iwakabe, K., Horiuchi, K., Nakaiwa, M., 2008. Basic design of a double-pipe unit type internally heat integrated distillation column (HIDiC). In: Proceedings of the AIChE Annual Meeting 2008; Philadelphia, USA, 16-21 November 2008. pp. 1–6.

Nakano, A., Maeda, T., 2008. Study on thermal diffusion in artificial air near the critical point. AIP Conference Proceedings 985, 780–787.

Niggemann, G., Hiller, C., Fieg, G., 2010. Experimental and Theoretical Studies of a Dividing-Wall Column Used for the Recovery of High-Purity Products. Industrial & Engineering Chemistry Research 49, 6566–6577.

Olujić, Ž., 1999. Effect of column diameter on pressure drop of a corrugated sheet structured packing. Chemical Engineering Research and Design 77, 505–510.

Olujić, Ž., 2009. Standardization of structured packing efficiency measurements - version 2. An open document, Delft University of Technology.

Olujić, Ž., Fakhri, F., de Rijke, A., de Graauw, J., Jansens, P. J., 2003. Internal heat integration – the key to an energy-conserving distillation column. Journal of Chemical Technology and Biotechnology 78, 241–248.

Olujić, Ž., van Baak, R., Haaring, J., Kaibel, B., Jansen, H., 2006. Liquid distribution properties of conventional and high capacity structured packings. Chemical Engineering Research and Design 84, 867–874.

Panasiti, M., Lemmon, E., Penoncello, S., Jacobsen, R., Friend, D., 1999. Thermodynamic properties of air from 60 to 2000 K at pressures up to 2000 MPa. International Journal of Thermophysics 20, 217–228.

Rackley, S. R., 2010. Carbon Capture and Storage. Butterworth-Heinemann.

Raney, S. M., Thorogood, R. M., 1997. Optimisation of thermally integrated distillation for low purity oxygen production. In: Distillation and Absorption '97. Vol. 2. pp. 521–530.

Rastogi, R. P., Madan, G. L., 1966. Cross-Phenomenological Coefficients. Part 6.– Dufour Effect in Gases. Transactions of the Faraday Society 62, 3325–3330.

Rivero, R., 2001. Exergy simulation and optimization of adiabatic and diabatic binary distillation. Energy 26, 561–593.

Røkke, N. A., Langørgen, Ø., 2009. Enabling pre-combustion plants - the DECARBit project. Energy Procedia 1, 1435–1442.

Røsjorde, A., 2004. Minimization of entropy production in separate and connected process units. Ph.D. thesis, Norwegian University of Science and Technology, Trondheim, Norway.

Røsjorde, A., Kjelstrup, S., 2005. The second law optimal state of a diabatic binary tray distillation column. Chemical Engineering Science 60 (5), 1199–1210.

Rutten, W. M., 1992. Diffusion in liquids. Ph.D. thesis, Delft University of Technology, Delft, The Netherlands.

Sauar, E., Kjelstrup Ratkje, S., Lien, K. M., 1996. Equipartition of Forces: A new principle for process design and optimization. Industrial & Engineering Chemistry Research 35 (11), 4147–4153.

Schaller, M., 2007. Numerically Optimized Diabatic Distillation Columns. Ph.D. thesis, Chemnitz University of Technology, Chemnitz, Germany.

Schaller, M., Hoffmann, K. H., Siragusa, G., Salamon, P., Andresen, B., 2001. Numerically optimized performance of diabatic distillation columns. Computers and Chemical Engineering 25, 1537–1548.

Schmidt, R., Wagner, W., 1985. A new form of the equation of state for pure substances and its application to oxygen. Fluid Phase Equilibria 19, 175–200.

Seader, J. D., Henley, E. J., 1998. Separation Process Principles. John Wiley and Sons, Inc., New York, USA.

Shah, M. M., 2003. Three column cryogenic air separation system with dual pressure air feeds. US Patent 6536234.

Shah, M. M., Drnevich, R. F., Lynch, N. J., Mahoney, K. W., 2001. Cryogenic air separation and gas turbine integration using heated nitrogen. US Patent 6295838.

Shan, Z., Jacobsen, R. T., Penoncello, S. G., 2000. A generalized model for the transport properties of air components and mixtures. Advances in Cryogenic Engineering 45, 1229–1236.

Shenvi, A. A., Herron, D. M., Agrawal, R., 2011. Energy efficiency limitations of the conventional heat integrated distillation column (HIDiC) configuration for binary distillation. Industrial & Engineering Chemistry Research 50, 119–130.

Simpson, L. L., 1968. Sizing piping for process plants. Chemical Engineering (17 June), 192–214.

Smith, A. R., Klosek, J., 2001. A review of air separation technologies and their integration with energy conversion processes. Fuel Processing Technology 70 (2), 115–134.

Span, R., 2000. Multiparameter equations of state: an accurate source of thermodynamic property data. Springer, Berlin, Germany.

Span, R., Lemmon, E., Jacobsen, R., Wagner, W., Yokozeki, A., 2000. A reference equation of state for the thermodynamic properties of nitrogen for temperatures from 63.151 to 1000 K and pressures to 2200 MPa. Journal of Physical and Chemical Reference Data 29, 1361–1433.

Span, R., Wagner, W., 2003a. Equations of state for technical applications. I. Simultaneously optimized functional forms for nonpolar and polar fluids. International Journal of Thermophysics 24, 1–39.

Span, R., Wagner, W., 2003b. Equations of state for technical applications. II. Results for nonpolar fluids. International Journal of Thermophysics 24, 41–109.

Stewart, R., Jacobsen, R., Wagner, W., 1991. Thermodynamic properties of oxygen from the triple point to 300 K with pressures to 80 MPa. Journal of Physical and Chemical Reference Data 20, 917–1021.

Suphanit, B., 2010. Design of internally heat-integrated distillation column (HIDiC): Uniform heat transfer area versus uniform heat distribution. Energy 35, 1505–1514.

Taylor, R., Krishna, R., 1993. Multicomponent mass transfer. John Wiley and Sons, Inc., New York, USA.

Tegeler, C., Span, R., Wagner, W., 1999. A new equation of state for argon covering the fluid region for temperatures from the melting line to 700 K at pressures up to 1000 MPa. Journal of Physical and Chemical Reference Data 28, 779–850.

Thorogood, R. M., 1991. Developments in air separation. Gas Separation and Purification 5, 83–94.

Tondeur, D., Kvaalen, E., 1987. Equipartition of entropy production. An optimality criterion for transfer and separation processes. Industrial & Engineering Chemistry Research 26 (1), 50–56.

Tsai, R. S., Seibert, A. F., Eldridge, R. B., Rochelle, G. T., 2011. A Dimensionless Model for Predicting the Mass-Transfer Area of Structured Packing. AIChE Journal 57, 1173–1184.

Tung, H. H., Davis, F. J., Mah, R. S. H., 1986. Fractionating Condensation and Evaporation in Plate-Fin Devices. AIChE Journal 32, 1116–1124.

Van der Ham, L. V., 2011. Improving the Second law efficiency of a cryogenic air separation unit. Ph.D. thesis, Norwegian University of Science and Technology, Trondheim, Norway.

Van der Ham, L. V., Bock, R., Kjelstrup, S., 2010. Modelling the coupled transfer of mass and thermal energy in the vapour–liquid region of a nitrogen–oxygen mixture. Chemical Engineering Science 65, 2236–2248.

Van der Ham, L. V., Drescher, M., 2011a. Cryogenic total reflux experiments in a packed concentric HIDiC. Part A: Background and design. In preparation.

Van der Ham, L. V., Drescher, M., 2011b. Cryogenic total reflux experiments in a packed concentric HIDiC. Part B: Instrumentation and experiments. In preparation.

Van der Ham, L. V., Gross, J., Kjelstrup, S., 2011. Two performance indicators for the characterization of the entropy production in a process unit. Energy 36, 3727–3732.

Van der Ham, L. V., Gross, J., Verkooijen, A. H. M., Kjelstrup, S., 2009. Efficient conversion of thermal energy into hydrogen: Comparing two methods to reduce exergy losses in a sulfuric acid decomposition reactor. Industrial & Engineering Chemistry Research 48, 8500–8507.

Van der Ham, L. V., Kjelstrup, S., 2010. Exergy analysis of two cryogenic air separation processes. Energy 35, 4731–4739.

Van der Ham, L. V., Kjelstrup, S., 2011a. Distributing the heat integration of distillation columns for air separation. In: Proceedings of the 24th International Conference on Efficiency, Cost, Optimization, Simulation and Environmental Impact of Energy Systems; Novi Sad, Serbia, 4-7 July 2011.

Van der Ham, L. V., Kjelstrup, S., 2011b. Improving the heat integration of distillation columns in a cryogenic air separation unit. In: Proceedings of the 23rd IIR International Congress of Refrigeration; Prague, Czech Republic, 21-26 August 2011.

Van der Ham, L. V., Kjelstrup, S., 2011c. Improving the heat integration of distillation columns in a cryogenic air separation unit. Industrial & Engineering Chemistry Research 50, 9324–9338.

Van der Ham, L. V., Kjelstrup, S., 2011d. The importance of coupling between thermal and molar fluxes in a nitrogen–oxygen distillation column. International Journal of Thermodynamics, accepted.

Van Itterbeek, A., De Rop, W., 1956. Measurements on the velocity of sound in air under pressures up to 20 atm combined with thermal diffusion. Applied scientific research 6, 21–28.

Waldmann, L., 1944. Eine neue Messmethode für Thermodiffusions- und Diffusionskoeffizienten in Gasen. Naturwissenschaften 32, 223–224.

Waldmann, L., 1949. Über die Druck- und Temperaturabhängigkeit der Wärmeerscheinung bei der Diffusion. Zeitskrift für Naturforschung 4a, 105–117.

Wilhelmsen, Ø., Johannessen, E., Kjelstrup, S., 2010. Energy efficient reactor design simplified by second law analysis. International Journal of Hydrogen Energy 35, 13219–12231.

Yong, P. S., Moon, H. M., Yi, S. C., 2002. Exergy analysis of cryogenic air separation process for generating nitrogen. Journal of Industrial and Engineering Chemistry 8 (6), 499–505.